

Digital Twin of Cardiovascular Systems

Using Artificial Intelligence and Computational Haemodynamics



Neeraj Kavan Chakshu

College of Engineering
Swansea University

Submitted to Swansea University in fulfilment of the requirements for
the Degree of Doctor of Philosophy

2021

Copyright: The Author, Neeraj K. Chakshu, 2023

Distributed under the terms of a Creative Commons Attribution-ShareAlike
4.0 International License (CC-BY-SA).

Abstract

Patient specific modelling using numerical methods is widely used in understanding diseases and disorders. It produces medical analysis based on the current state of patient's health. Concurrently, as a parallel development, emerging data driven Artificial Intelligence (AI) has accelerated patient care. It provides medical analysis using algorithms that rely upon knowledge from larger human population data. AI systems are also known to have the capacity to provide a prognosis with overall accuracy levels that are better than those provided by trained professionals. When these two independent and robust methods are combined, the concept of human digital twins arise. A Digital Twin is a digital replica of any given system or process. They combine knowledge from general data with subject oriented knowledge for past, current and future analyses and predictions. Assumptions made during numerical modelling are compensated using knowledge from general data. For humans, they can provide an accurate current diagnosis as well as possible future outcomes. This allows for precautions to be taken so as to avoid further degradation of patient's health.

In this thesis, we explore primary forms of human digital twins for the cardiovascular system, that are capable of replicating various aspects of the cardiovascular system using different types of data. Since different types of medical data are available, such as images, videos and waveforms, and the kinds of analysis required may be offline or online in nature, digital twin systems should be uniquely designed to capture each type of data for different kinds of analysis. Therefore, passive, active and semi-active digital twins, as the three primary forms of digital twins, for different kinds of applications are proposed in this thesis. By the virtue of applications and the kind of data involved in each of these applications, the performance and importance of human digital twins for the cardiovascular system are demonstrated. The idea behind these twins is to allow for the application of the digital twin concept for online analysis, offline analysis or a combination of the two in healthcare. In active digital twins active data, such as signals, is analysed online in real-time; in semi-active digital twin some of the components

being analysed are active but the analysis itself is carried out offline; and finally, passive digital twins perform offline analysis of data that involves no active component.

For passive digital twin, an automatic workflow to calculate Fractional Flow Reserve (FFR) is proposed and tested on a cohort of 25 patients with acceptable results. For semi-active digital twin, detection of carotid stenosis and its severity using face videos is proposed and tested with satisfactory results from one carotid stenosis patient and a small cohort of healthy adults. Finally, for the active digital twin, an enabling model is proposed using inverse analysis and its application in the detection of Abdominal Aortic Aneurysm (AAA) and its severity, with the help of a virtual patient database. This enabling model detected artificially generated AAA with an accuracy as high as 99.91% and classified its severity with acceptable accuracy of 97.79%. Further, for active digital twin, a truly active model is proposed for continuous cardiovascular state monitoring. It is tested on a small cohort of five patients from a publicly available database for three 10-minute periods, wherein this model satisfactorily replicated and forecasted patients' cardiovascular state. In addition to the three forms of human digital twins for the cardiovascular system, an additional work on patient prioritisation in pneumonia patients for ITU care using data-driven digital twin is also proposed. The severity indices calculated by these models are assessed using the standard benchmark of Area Under Receiving Operating Characteristic Curve (AUROC). The results indicate that using these models, the ITU and mechanical ventilation can be prioritised correctly to an AUROC value as high as 0.89.

Declaration

This work has not previously been accepted in substance for any degree and is not being concurrently submitted in candidature for any degree.

Signed: Neeraj Kavan Chakshu

9 November 2021

This thesis is the result of my own investigations, except where otherwise stated. Other sources are acknowledged by footnotes giving explicit references. A bibliography is appended.

Signed: Neeraj Kavan Chakshu

9 November 2021

I hereby give consent for my thesis, if accepted, to be available online in the University's Open Access repository and for inter-library loan, and for the title and summary to be made available to outside organisations.

Signed: Neeraj Kavan Chakshu

9 November 2021

The University's ethical procedures have been followed and, where appropriate, that ethical approval has been granted.

Signed: Neeraj Kavan Chakshu

9 November 2021

Acknowledgements

First and foremost, I am grateful to my parents for everything in life as my journey of life wouldn't be possible without them, especially my mother for all her inspiration and support throughout my student life. I owe my highest gratitude to my supervisors Dr Igor Sazonov and Prof. Perumal Nithiarasu for all their support and guidance throughout my PhD. The freedom and encouragement they provided me to explore different ideas made it possible for me to achieve every objective I had in my mind for this PhD with great satisfaction. Further, I would like to express my gratitude to the College of Engineering, Swansea University, for admitting me and providing me with the College of Engineering Centenary Scholarship to pursue my PhD and also to the entire staff, particularly the PGR team, for providing all the support required to complete my PhD.

I also would like to thank Dr Jason Carson for providing access to the enhanced trapezoidal rule solver based 1D haemodynamic model. I also owe a great deal of gratitude to my colleagues and friends from Zienkiewicz Centre for Computational Engineering(ZCCE) for their invaluable inputs and moral support during the course of my PhD. I would also like to thank my undergraduate supervisor, Dr V.Krishna, PES University, Bangalore, India, without whom my journey to Swansea University wouldn't have been possible. The work presented in this thesis is partially supported by HDRUK and Medical Research Council, Grant/Award Number: MR/S004076/1, and Global Challenges Research Fund (GCRF), Grant/Award Number: RB1819APM003SWANKARU.

"You can't make bricks without straw", the support and contribution of every teacher at various stages of my life, all the way from kindergarten to PhD, has helped me become the person I am, therefore I am grateful to every teacher and mentor in my life.

Table of contents

List of figures	x
List of tables	xv
Nomenclature	xviii
1 Introduction	1
1.1 The concept of digital twins	1
1.2 The origins and current usage of digital twins	2
1.3 The role of human digital twins in healthcare	3
1.4 The objectives and outline of this thesis	4
2 One Dimensional Haemodynamic modelling	7
2.1 Model equations	8
2.1.1 Governing equations for an elastic vessel	8
2.1.2 Velocity profile	9
2.1.3 Constitutive relations	9
2.1.4 Characteristic Analysis	10
2.2 Boundary conditions	12
2.2.1 Heart function	12
2.2.2 Terminal vessels	13
2.3 Arterial network	14
2.4 Numerical schemes	14
2.4.1 Locally Conservative Galerkin (LCG) method	14
2.4.2 Enhanced trapezoidal method	18
2.5 Summary	21

3	Artificial Intelligence	23
3.1	An overview of machine learning algorithms	24
3.1.1	Supervised learning	25
3.1.2	Unsupervised learning	33
3.2	Application : An AI based digital-twin for prioritizing pneumonia patient treatment	34
3.2.1	Methodology	36
3.2.2	Results and Discussion	43
3.2.3	Conclusion	47
3.3	Summary	47
4	Passive Digital Twin	49
4.1	Introduction	50
4.2	Geometry of coronary arteries	51
4.2.1	Segmentation	52
4.3	Estimation of Lumen size for mesh generation	58
4.4	Haemodynamic modelling	59
4.5	Results and Discussions	63
4.5.1	Limitations	67
4.6	Conclusions	69
4.7	Summary	70
5	Semi-Active Digital Twin	71
5.1	Introduction	71
5.2	Detection of head oscillations	75
5.2.1	Assumptions and guidelines	76
5.2.2	Facial recognition and region of interest (ROI)	76
5.2.3	Feature points tracking and filtering	77
5.2.4	Principal component analysis	79
5.3	Mechanical modelling of head oscillations	80
5.3.1	One dimensional haemodynamic model	81
5.3.2	Determination of axial force on the wall	82
5.3.3	Dynamic equation of head-neck system	86
5.3.4	Coupling moments calculated from haemodynamic model with the dynamic equation	87
5.3.5	Modeling stenoses	88

5.4	Results and discussions	89
5.4.1	Sensitivity analysis	92
5.4.2	Discussions	92
5.5	Limitations	94
5.6	Conclusions	95
5.7	Summary	96
6	Active Digital Twin	97
I	Enabler model	98
6.1	Inverse analysis of human systemic circulation	99
6.2	Introduction	99
6.3	Methodology	103
6.3.1	Virtual Patient Database	104
6.3.2	Application of inverse analysis in Abdominal Aortic Aneurysm (AAA) detection	108
6.3.3	Deep learning for inverse pressure wave form calculation and AAA classification	111
6.4	Results and Discussion	116
6.4.1	Analysis of the virtual database	116
6.4.2	Inverse analysis using Neural Networks	117
6.4.3	Application of inverse analysis to the classification of Aortic Abdominal Aneurysm (AAA)	120
6.5	Conclusions	122
II	Truly active model	124
6.6	Data driven forecasting	125
6.6.1	Data selection and processing	125
6.6.2	Neural network architecture and training	126
6.7	Continuously adapting 1D haemodynamic modelling system	127
6.7.1	Closed loop system	127
6.7.2	An example of sepsis	131
6.7.3	Results and discussions	133
6.8	Conclusions	135

6.9	Summary	136
7	Conclusions and future research	138
7.1	Passive digital twins	138
7.2	Semi-active digital twins	139
7.3	Active digital twins	140
7.4	Final remarks	141
Appendix A Neural network architectures used for prioritising pneumonia patients		142
A1:	MLP models	142
A2:	RNN based models	143
Appendix B Workflow proposed and vascular dimensions observed for Fractional Flow Reserve application in Chapter 4		149
B1	: Workflow summary	149
B2	Vessel geometry of coronary arteries with stenosis	149
Appendix C Peer-reviewed journal papers published during PhD candidature		156
References		157

List of figures

1.1	The data flow in human digital twins.	4
2.1	Lumped model used to represent flow in one side of the heart	13
2.2	A three-element Windkessel model with two resistive elements (R_1 and R_2) and a compliance element C . P_{art} and P_{veins} are arterial pressure and venous pressure respectively.	14
2.3	The arterial tree presented in Table 2.1. This network has been adapted from [39]	15
3.1	Classification of artificial intelligence.	24
3.2	An artificial neuron.	27
3.3	A multilayer layer perceptron model. The colours in edges represent their weights.	28
3.4	Kernel convolution, where the kernel h is multiplied with the input matrix f by striding though it to generate a feature map G	28
3.5	A typical convolutional neural network	29
3.6	A Recurrent Neural Network (RNN) cell where the output from previous step is concatenated with input for the current step in a sequence.	32
3.7	A Long Short-Term Memory (LSTM) Cell.	32
3.8	Three tiered patient prioritisation strategy to reduce mortality rate in intensive care units.	35
3.9	Multilayer Perceptron (MLP) and Recurrent Neural Networks (RNN) for calculating severity indices.	40
3.10	AUROC (shaded area) curve for MLP models used to predict the probability of death and the probability of requiring mechanical ventilation support.	44

3.11	AUROC (shaded area) curve for RNN based model results of the probability of death for patients and the probability of requiring mechanical ventilation support.	45
3.12	ROC curve for RNN based model used to predict probability of death for patients in Tier Three	46
4.1	Workflow proposed in the present work for automatic calculation of FFR from a CT Scan.	51
4.2	Filtering processes carried out on each of the CCTA slices to extract pixels corresponding to coronary arteries. In subfigure [b], in clockwise order, Non-local means Denoising filtering, Frangi filtering, Binary thresholding, Contour detection and removal are carried out to extract parts of interest	54
4.3	Automatic detection of aorta using Hough circle transform. The detected aorta is encircled in black.	55
4.4	Density-based spatial clustering of applications with noise (DBSCAN). Points within each other's vicinity, with a search radius of ϵ are grouped together as a single cluster. Blue and grey points belong to one cluster, where the former ones are core points. The grey points are reachable but make up the outer points of the cluster. The orange point is a noise point as it cannot be reached by any other point.	57
4.5	Detected clusters of voxels of coronary arteries. The left cluster and right cluster are of right and left coronary arteries respectively.	57
4.6	Skeleton obtained from voxel cluster is used as centreline along which lumen radii is calculated.	59

4.7	The closed-loop used to estimate the boundary conditions for the coronary system. Detailed description is available in previous studies [143, 32, 144]. Here, CO is the cardiac output, SBP is the systolic blood pressure, DBP is the diastolic blood pressure, HR is the heart rate, C_{art} is the arterial compliance, R_{beds} is the peripheral resistance, V_{blood} is the blood volume, Q_{cor} is the coronary inflow, P_{LV} is the left ventricular pressure, and P_{RV} is the right ventricular pressure. R_{beds} and C_{art} refer to peripheral resistance from various capillary beds and arterial compliance in the ETM model (described in Chapter 2). R_{beds} is representative of various capillary beds across the arterial network in the ETM model and must not be confused with R_{cor} described below, which is the resistance pertaining to the coronary system. The cardiac cycle uses the heart lumped model proposed in [30].	61
4.8	Inflow boundary conditions used for left and right coronary arteries. . .	62
4.9	A lumped-parameter model connected to the outlets of the patient specific coronary network to represent the micro-circulation. Part connects to the 1D domain, R_1 is the characteristic impedance, R_2 is the resistance of the micro-circulation at the arterial side, R_3 is the micro-circulatory resistance at the venous side, C_1 is the micro-circulatory arterial compliance, C_2 is the intra-myocardial compliance, P_{LV} is a scaled pressure from the left ventricle (or right ventricle for the right coronary artery [RCA]), and P_{ven} represents the pressure in the venous system which is set to 5mmHg	63
4.10	cFFR values obtained from models using automatically and manually segmented coronary geometries are compared against invasively measured FFR. The cases for which invasive FFR values were not available have been excluded from the graph to avoid any confusion, however, cFFR values for such cases are available in Table 4.4.	65
5.1	Diagnosis of carotid stenosis by comparing results of computer vision and biomechanical model (digital twin).	74
5.2	Region of interest.	77
5.3	Energy at different frequencies for the results of blood-flow-driven-head-neck vibration predicted by the proposed mechanical model.	78

5.4	Workflow used in the present work to detect carotid stenosis and its severity	78
5.5	Force exerted by blood flow in a single finite element of two major inter-cranial arteries with respect to time.	81
5.6	Cerebral arteries used in the one dimensional model	82
5.7	Element of the vessel of length h . Here, \mathbf{t} is the unit vector acting along the element axis, \mathbf{n}_1 and \mathbf{n}_2 are the normals to the element inlet and outlet, respectively	83
5.8	The head-neck system employed in the present work.	87
5.9	Comparison of synthetic and measured head vibration for healthy volunteers	90
5.10	Comparison of synthetic and measured head vibration for a patient suffering from severe carotid occlusions.	91
5.11	Sensitivity analysis of different input parameters on head-neck vibration when other quantities have been kept constant	93
6.1	A schematic representation of envisaged digital twin.	100
6.2	Schematic of inverse analysis to determine wave-forms at different locations using three measurements at accessible locations as input.	101
6.3	Example of personalised model generation using patient profiles. This includes three parallel workflows: for generation of the geometrical mesh parameters (left), for generation the inlet boundary conditions (centre) and for generation of elastic parameters of the mesh segments	105
6.4	An artificial neuron used in Multilayer Perceptron model (MLP).	106
6.5	A model of an Abdominal Aortic Aneurysm.	108
6.6	Blood pressure waveforms (simulated) in abdominal aorta computed close to its distal end for healthy, Large AAA and critical AAAs (where the vessel is about to rupture) cases.	110
6.7	Volumetric Blood Flow Rate (simulated) in in abdominal aorta computed close to its distal end for healthy, Large AAA and critical AAA (where the vessel is about to rupture) cases.	110
6.8	LSTM based inverse analysis and AAA classification.	111
6.9	Long Short-Term Memory (LSTM) cell consisting of cell state as well as forget, input and output gates	113
6.10	1D Convolutional Neural Network used to detect severity of AAA.	114

6.11	Input blood pressure waveforms measured at three different locations. . .	119
6.12	Outputs calculated for inputs in Figure 6.11 by RNN in healthy subjects at different locations.	120
6.13	Output calculated at the distal end of abdominal aorta by LSTM based neural network for inverse analysis in a human patient for Large AAA condition.	121
6.14	Confusion matrix to understand the performance of the model for virtual patients in the entire database.	122
6.15	Preprocessing of blood pressure waveform data to split it into samples of 10 minutes.	126
6.16	Flowchart for the warm-up phase.	130
6.17	Flowchart for the active phase.	131
6.18	An example of best matched waveform generated by digital twin model(1D model), after fine tuning the control parameters, with the input (MGH/MF waveform).	132
A1.1	Neural network architecture used for MLP models.	143
A1.2	Loss observed over epochs during training.	144
A1.3	Calibration curves for MLP models.	144
A2.1	Neural network architecture used for RNN based models in Tier 2) . .	146
A2.2	Neural network architecture used for RNN based models in Tier 3 . . .	147
A2.3	Loss observed over epochs during training.	148
A2.4	Loss observed over epochs during training.	148

List of tables

2.1	The basic arterial tree and properties used by the LCG model , adapted from [39]. Here, L is the vessel length, D1, D2 and D3 are daughter vessels, β_i and β_f are the material properties of the vessel wall at the proximal and distal end of the vessel respectively, and A_i and A_f are the vessel's cross-sectional area at the proximal and distal end respectively.	22
3.1	Baseline characteristics of subset selected from eICU Collaborative Research Database v2.0	38
3.2	Baseline characteristics of subset selected from MIMIC-III [87][88]. Note: Since every field in this table is not measured for the entire population of the subset, the 95% CI provided in the brackets are representative of only those patients in whom the respective field was measured and recorded.	39
4.1	Filter settings used in de-noising and Frangi filters for preprocessing of images.	53
4.2	A summary of steps followed in this chapter for haemodynamic modelling of the coronary artery geometries obtained using the proposed automatic method.	64
4.3	Coronary geometry detected from the proposed automatic segmentation workflow is compared against manually segmented coronary arteries. L , R_0 and R_f , are average vessel length, radius at the start of the vessel and radius at the end of the vessel respectively. R_s is the average minimum vessel radius at the stenosis location. Detailed data for each patient case is available in B2.	66

4.4	cFFR values calculated using geometries obtained automatically and manually on test patient cohort is compared against actual invasively measured FFR.	68
5.1	Values for K_s and C_s from Wang and Rahmatalla [166]	87
5.2	Parameters of the sensitivity analysis for different ages, where PWV is the pulse wave velocity [172], MAP is the mean arterial pressure, and HR is the heart rate	94
6.1	Architecture of Deep learning model I	114
6.2	Architecture of Deep learning model II	116
6.3	Baseline characteristics of virtual patients (without AAA) used in the virtual database [199, 200, 172, 201].	117
6.4	Baseline characteristics (average, 95% CI in brackets) of virtual patients (with AAA) used in the virtual database.	118
6.5	Parameters used to train neural networks for forecasting of BP values. .	126
6.6	Range of physiological values used to generate the reference waveform database .* A_{0i} is the initial area at the start of the terminal vessels. .	129
6.7	Systolic blood pressure obtained after fine tuning digital twin models for three 10-minute periods, with values averaged over 3 cardiac cycles chosen within a 10 minute time period.	134
6.8	Diastolic blood pressure obtained after fine tuning digital twin models for three 10-minute periods, with values averaged over 3 cardiac cycles chosen within a 10 minute time period.	134
6.9	Mean arterial blood pressure (MAP) obtained after fine tuning digital twin models for three 10-minute periods, with values averaged over 3 cardiac cycles chosen within each 10 minute time period.	135
6.10	Estimated cardiac outputs calculated from tuned digital twin models for three 10-minute periods.	135
6.11	BP values forecasted and that obtained by calibrating digital twin using the forecasted values, compared against actual measured BP values from Period 3.	136
A1.1	Neural network parameters used in architecture and training of MLP models	142

A2.2	Neural network parameters used in architecture and training of RNN based models.	145
B1	Workflow proposed in the present work to automate cFFR calculation from CT scans.	150
B2	Values obtained from the proposed workflow for left coronary geometry is compared against values obtained from manual segmentation carried out using VMTK(Vascular Modelling toolkit).	151
B3	Initial vessel radius obtained from the proposed workflow for left coronary geometry is compared against values obtained from manual segmentation carried out using VMTK(Vascular Modelling toolkit).	152
B4	Final vessel radius obtained from the proposed workflow for left coronary geometry is compared against values obtained from manual segmentation carried out using VMTK(Vascular Modelling toolkit).	153
B5	Minimum vessel radius at stenosis location obtained from the proposed workflow for left coronary geometry is compared against values obtained from manual segmentation carried out using VMTK(Vascular Modelling toolkit).	154
B6	Values obtained from the proposed workflow for left coronary geometry is compared against values obtained from manual segmentation carried out using VMTK(Vascular Modelling toolkit).	154
B7	Initial vessel radius obtained from the proposed workflow for right coronary geometry is compared against values obtained from manual segmentation carried out using VMTK(Vascular Modelling toolkit).	155
B8	Final vessel radius obtained from the proposed workflow for right coronary geometry is compared against values obtained from manual segmentation carried out using VMTK(Vascular Modelling toolkit).	155
B9	Minimum vessel radius at stenosis location obtained from the proposed workflow for right coronary geometry is compared against values obtained from manual segmentation carried out using VMTK(Vascular Modelling toolkit).	155

Nomenclature

Abbreviations

AAA	Abdominal Aortic Aneurysm
AI	Artificial intelligence
AUROC	Area Under Receiving Operating Characteristic Curve
BCG	Ballistocardiography
BP	Blood pressure
CAD	Computer-aided design
CAD	Coronary artery disease
CCTA	Coronary Computerised Tomography Angiography
CHD	Coronary heart disease
CNN	Convolutional neural network
CO	Cardiac output
CT	Computerised tomography
DBP	Diastolic blood pressure
DBSCAN	Density-based spatial clustering of applications with noise
DICOM	Digital Imaging and Communications in Medicine (digital image format)
DTW	Dynamic time warping
ECG	Electrocardiogram

ETM	Enhanced trapezoidal rule method
FFR	Fractional Flow Reserve
HR	Heart rate
ITU	Intensive therapy unit
LCG	Locally conservative Galerkin
LSTM	Long short-term memory
MGH/MF	Massachusetts General Hospital / Marquette Foundation waveform database
MLP	Multilayer perceptron model
MP	Mega pixels
MRI	Magnetic resonance imaging
PCA	Principal Component Analysis
PCHIP	Piecewise Cubic Hermite Interpolating Polynomial
PWV	Pulse wave velocity
ReLU	Rectified linear unit
RNN	Recurrent neural network
ROI	Region of interest
SBP	Systolic blood pressure
TanH	Hyperbolic tangent
TIA	Transient ischemic attack
UMLS	Unified Medical Language System

Common symbols

α	Momentum correction factor
β	Material properties of the vessel wall

Γ	Wall viscosity coefficient
μ	Dynamic viscosity
ρ	Blood density
σ	Output activation function
τ	Wall shear stress
θ	Angle
ξ	Radial coordinate
ζ	Velocity profile constant
A	Vessel cross-sectional area
c_0	Reference wave speed
E	Young's modulus
f	Friction force
h	Wall thickness
L	Length
m	Mass
P	Fluid pressure
Q	Volumetric flow rate
R	Vessel radius
t	Time
u	Flow velocity
Z	Characteristic impedance

Chapter 1

Introduction

The three forms of digital twins for the human cardiovascular system, passive, semi-active and active, are conceptualised and developed in this thesis. Utilising a combination of computational mechanics and state-of-the-art artificial intelligence, each of the three proposed forms of digital twins is envisioned for potentially diagnosing cardiovascular diseases and monitoring of cardiovascular state in human patients. This chapter introduces the concept of digital twins, provides an overview of the origins and current usage of digital twins and explains the role of human digital twins in healthcare. The outline and objectives of this thesis are presented at the end of this chapter.

1.1 The concept of digital twins

The term ‘unique’ is pertinent to each system, process, living being and inanimate object. No two of these entities are the same, even if they are similar in shape, size and make. Distinct microscopic variations exist even if macroscopic similarities can be observed. For example, consider two cars of the same make, with the same configurations and delivered at the same time at the same location. In addition, let us assume that these cars are from the same batch and are manufactured parallelly at the same production unit. At the time of delivery, even with such high levels of similarity, if the materials in each of these cars are to be observed microscopically, features such as crystal structure, microscopic cracks and their locations will be observed to be distinct.

As mentioned above, not just objects but also their life-cycle is unique. Every individual object is subjected to different levels, forms and durations of mechanical forces during its life-cycle. Of the two similar cars in the example above, let us assume that one of them is bought by Subject A, who lives in a geographically flat urban

environment and the other car is bought by Subject B, who lives in a mountainous rural region. After three years of regular use by each of the subjects, it will be observed that the clutch plates and brake pads would have worn out to a much higher degree in Subject B's car than Subject A's car. This exemplifies the fact that every individual object is both physically unique as well as subjected to a unique life-cycle.

As a need to analyse, monitor and predict the above-mentioned uniqueness in every object and process, digital twins were conceptualised. Digital twins are virtual or digital replicas of objects and processes. These replicas digitally capture information such as features, trends, functions and various other fields from the physical entity and use them to build its representation in the current state. Past information from the physical entity in combination with the knowledge of artificial intelligence models, trained on vast amounts of general data, is utilised by these twins to predict the future state of the entity.

1.2 The origins and current usage of digital twins

The origins of the term 'Digital Twin' can be traced back to a description of the concept by John Vickers in NASA's 2010 road map [1]. The concept, however, has existed since 2002 when Michael Grieves introduced it with the title 'Conceptual Ideal for PLM' in a University of Michigan presentation [2], where PLM stands for Product Lifecycle Management. The term has since been bolstered with usage in multiple publications spanning various disciplines [3]. To prevent any ambiguity, it is worth noting that digital twins are also sometimes referred to as 'Virtual twins'.

When the question of a formal definition for digital twins arises, IBM defines it as "A digital twin is a virtual representation of an object or system that spans its lifecycle, is updated from real-time data, and uses simulation, machine learning and reasoning to help decision-making" [4]. Over the years, this concept has been adopted by various disciplines, likes those of which range from aerospace and manufacturing to healthcare and IoT. To begin with, the digital twin concept has been used in recent publications such as Zhao *et al* [5], to reduce carbon emission in machining; Thies *et al* [6], for use in AR/VR training; Joos *et al* [7], for the design of Lithium-Ion battery cathodes; and Rjabtvšikov *et al* [8], in service unit for AC motor stator inter-turn short circuit fault detection. For larger-scale applications, usage of this concept has been proposed for Industry 4.0 by Uhlemann *et al* [9], Qi and Tao [10] and Vachálek *et al* [11]; for smart cities by Shirowzhan *et al* [12] and Ford and Wolf [13].

1.3 The role of human digital twins in healthcare

Similar to all objects in this universe, every individual human being, including those who have identical twins, have a unique physical, mental and emotional form as a result of their unique genetic code [14]. General medical treatments in such a genetically variegated human population tend to have low levels of efficacy. The emergence of human digital twins in healthcare provides a platform for patient-specific analysis for accurate diagnosis and patient care. For patient care, digital twins have potential in six critical applications: personalised diagnosis, monitoring, drug development, surgery and implant manufacturing. These twins are generally designed to either replicate any one particular organ/organ system or the overall body as one system. Human digital twins, such as those proposed by Liu *et al*[15] capture and record patient data, as signals using sensors such as accelerometers, oximeters and Holter monitor; as images such as MRI and CT scans; and as discrete data such as physiological data (height, weight etc.) and patient's medical history. This data is modelled and analysed for understanding the current state of the patient and use for personalising care in the above-mentioned applications (See Figure 1.1). In the Figure 1.1, representing an ideal digital twin system, the data flow starts from the measurement of the patient's vitals and other parameters, which then is fed to a computational system that uses the input data to modify or update a personalised virtual replica of the patient. The virtual replica then can be used by the computational system to diagnose any problem in the patient as well as calculate an estimate of the patient's health in future.

The widely accepted definition of digital twins mentioned in Section 1.2 encapsulates the essence of ideal digital twins, however, in the case of healthcare most of the existing forms of human digital twins cannot still replicate the physics in action behind the physical entities being twinned in a human interpretable form. Most of these existing forms rely on the-state-of-the-art artificial intelligence models, such as deep neural networks, that use compounded multidimensional mapping of parameters to model the body functions and provide a diagnosis or prediction. These models, when trained to replicate or twin a human being, provide a highly accurate representation as well as predictions for the individual and their health state. However, owing to the complex mapping, the reasoning behind an analysis or prediction from these AI models is in some cases not possible to comprehend using human intelligence. To resolve this issue, in this thesis, each of the three forms of digital twin being proposed utilise a combination

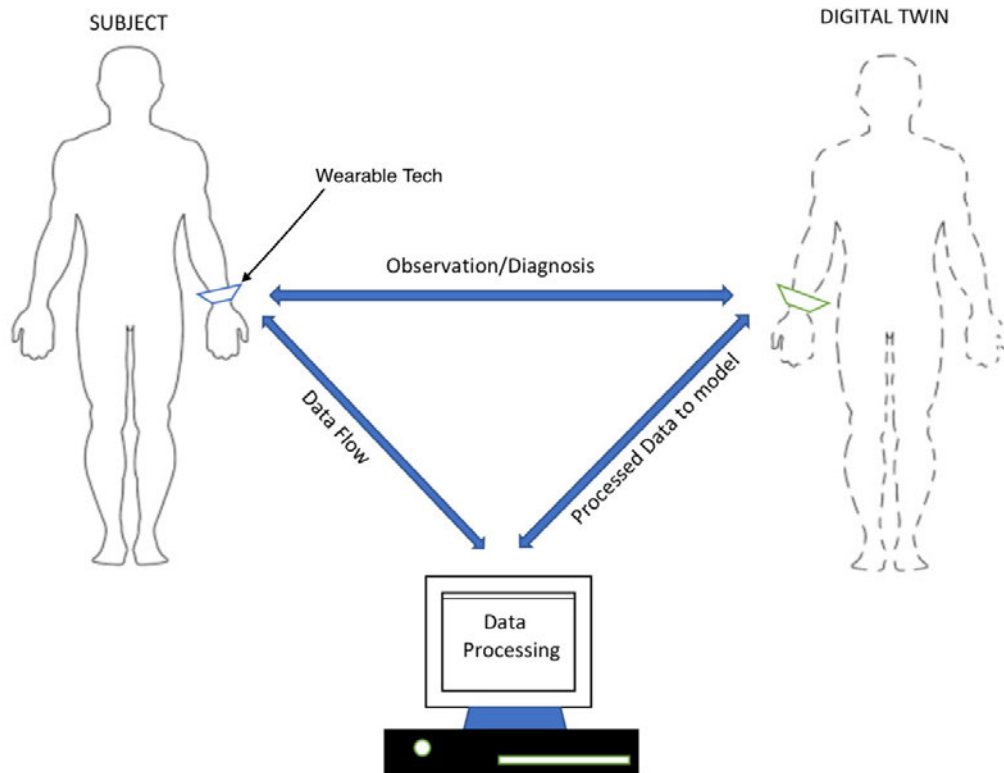


Fig. 1.1 The data flow in human digital twins.

of computational mechanics with artificial intelligence so as to provide patient-oriented diagnosis of cardiovascular diseases and monitoring of the cardiovascular system.

1.4 The objectives and outline of this thesis

In this thesis, three forms of human digital twins, passive, semi-active and active twins, for different kinds of applications are proposed. By the virtue of applications and the kind of data involved in each of these applications, the performance and importance of human digital twins for the cardiovascular system are demonstrated. The idea behind these twins is to allow for the application of the digital twin concept for online analysis, offline analysis or a combination of the two in healthcare. In active digital twins active data, such as signals, is analysed online in real-time; in semi-active digital twin some of the components being analysed are active but the analysis itself is carried out offline; and finally in passive digital twins perform offline analysis of data that involves no active component (for example, image-based modelling).

The outline of this thesis is as follows:

Chapter 2: In this chapter, the one-dimensional haemodynamic models used in this thesis are explained. The different numerical schemes for solving the differential equations and various configurations of the haemodynamic model used in this thesis are described. This chapter ends with information on the scaling of the arterial network for personalised representation of the patient's haemodynamic model.

Chapter 3: The chapter begins with a comprehensive review of existing artificial intelligence (AI) methods and their usage in healthcare. Then the popular trends of AI usage within the healthcare industry, standards and current performance are discussed. To exemplify the digital twins in healthcare that are purely data-driven, a three-tiered strategy to prioritize ICU care for pneumonia patients is proposed. Results from this example are presented at the end of the chapter.

Chapter 4: The passive digital twin, the first of the three forms of human digital twins is presented in this chapter. A workflow for automating the calculation of Fractional Flow Reserve (FFR) from CT scans, a critical parameter to analyse the functional relevance of coronary stenoses, is proposed as an example of a passive digital twin. The proposed workflow is tested with retrospective CT scan data from twenty-five patients and their results are presented and discussed at the end of the chapter.

Chapter 5: In this chapter, head-neck vibration due to the pulsatile nature of blood flow is exploited to detect carotid stenosis and its severity. To analyse this vibration, a coupled computer vision and computational mechanics method is proposed, which introduces the second form of the human digital twin, the semi-active digital twins. Preliminary results of this method on healthy subjects and a patient with carotid stenosis are presented at the end of this chapter. Work presented in this chapter is available as a peer-reviewed article, Chakshu *et al*[16].

Chapter 6: The final form of a human digital twin, active digital twin, is presented in this chapter. It begins with purely data-driven digital twins trained to perform forward analysis using *in vivo* measurements as well as inverse analysis using *in silico* data. The generation of *in silico* data and potential application for inverse analysis in detection of Abdominal Aortic Aneurysms(AAA), published in Chakshu *et*

al[17], is described in detail within this chapter. Then a system to adapt parameters of a one-dimensional haemodynamic model in real-time for replication of blood waveforms measured *in vivo* is proposed. At the end of this chapter, a combination of purely data-driven digital twins and the actively adaptive one-dimensional haemodynamic model is presented as a complete active digital twin capable of replicating the current cardiovascular state as well as predicting it for the near future.

Chapter 7: In this chapter, the forms of human digital twins developed in this thesis are summarised and conclusions are drawn from their results. Future research for this topic is also discussed at the end of this chapter.

Chapter 2

One Dimensional Haemodynamic modelling

The circulatory system in the human body is an organ system critical for the circulation of blood, which is essential for the transportation of oxygen, carbon dioxide and other nutrients such as electrolytes to every cell of the body. This system primarily consists of the cardiovascular and lymphatic system, with the former made up of blood, heart and blood vessels and the latter made up of lymph, lymph nodes and lymph vessels. The cardiovascular system further can be divided into the systemic circulation and pulmonary circulation, where the former is responsible for the supply of oxygenated blood from the heart to the tissues of the body and returning of deoxygenated blood from these tissues to the heart and the latter is responsible for transporting deoxygenated blood from the heart to the lungs and returning oxygenated blood back to the heart. In this work, within the systemic circulation, only the arterial network is being analysed in all proposed forms of the human digital twin.

In order to analyse blood circulation in the arterial system or parts of it under healthy conditions as well as when affected by diseases or medical intervention, various numerical models have been proposed over the years [18–30]. Analysis of the entire arterial tree is carried out using 1D modelling in most of the published models as complete 3D modelling of the entire tree is computationally challenging. Factors such as modelling of fluid-structure interaction between the blood and vessel walls, lack of material data and others severely affect the computational analysis in 3D modelling. Additionally, blood flow can be considered quasi-1D as wavelengths of the pressure-flow waves generated by the heart are much greater than the diameter of the blood vessels. Thus, taking all these factors into account and recognising the need for greater

computational speeds in our work, 1D modelling has been adopted for all proposed forms of digital twins in this work.

Primarily two forms of 1D modelling have been adopted in this work. The first model referred to as **ETM model** in this thesis, utilises a coupled 1D-0D model and incorporates enhanced trapezoidal rule as the numerical scheme. The second model referred to as **LCG model** in this thesis, uses a 1D model with tapered vessels for terminal vessels and incorporates locally conservative Taylor-Galerkin as the numerical scheme.

2.1 Model equations

In this section, the equations used to model blood flow in one dimension is described. It starts by describing governing equations for an elastic vessel and its numerous formulations. Then, the velocity profile used in this thesis is explained before ending the section with an overview of constitutive relations used by models in this thesis.

2.1.1 Governing equations for an elastic vessel

The flow in elastic vessels, cylindrical vessels with elastic walls, in one-dimensional flow for a vessel section can be represented using continuity and momentum equations [31, 32, 29] given as,

$$\frac{\partial A}{\partial t} + \frac{\partial Q}{\partial x} = 0 \quad (2.1)$$

$$\frac{\partial Q}{\partial t} + \frac{\partial(\alpha \frac{Q^2}{A})}{\partial x} = -\frac{A}{\rho} \frac{\partial P}{\partial x} + \frac{f}{\rho} \quad (2.2)$$

respectively, where A is the vessel cross-sectional area, u is the average flow velocity, P is the pressure, Q is the volumetric flow rate ($Q = Au$), u_x is the axial component of the flow velocity, x is the coordinate in the axial direction, f is the friction force per unit length, and α is a momentum correction factor given by

$$\alpha = \frac{\int_{CS} u_x^2 d\sigma}{Au^2}, \quad u = \frac{\int_{CS} u_x d\sigma}{A} \quad (2.3)$$

It accounts for the non-uniform velocity distribution along the radial direction.

The above set of equations (2.1 and 2.2) are generally represented in three formulations, AU, AQ and PQ. Out of which AU and PQ formulations are used by the models

in this thesis and shown below in Equations (2.4) and (2.5) respectively.

$$\begin{cases} \frac{\partial A}{\partial t} + \frac{\partial Au}{\partial x} = 0 \\ \frac{\partial u}{\partial t} + (2\alpha - 1)u \frac{\partial u}{\partial x} + (1 - \alpha) \frac{u^2}{A} \frac{\partial A}{\partial x} + \frac{1}{\rho} \frac{\partial P}{\partial x} - \frac{f}{\rho A} = 0 \end{cases} \quad (2.4)$$

$$\begin{cases} \frac{\partial A}{\partial P} \frac{\partial P}{\partial t} + \frac{\partial Q}{\partial x} = 0 \\ \frac{\rho}{A} \frac{\partial Q}{\partial t} + \frac{\rho}{A} \frac{\partial(\alpha \frac{Q^2}{A})}{\partial x} + \frac{\partial P}{\partial x} - \frac{f}{A} = 0 \end{cases} \quad (2.5)$$

2.1.2 Velocity profile

In the above equations, the term f , representing frictional forces on the fluid, is derived for both models used in this thesis using an axi-symmetric velocity profile given as

$$u_x(x, \xi, t) = U \frac{\zeta + 2}{\zeta} \left[1 - \left(\frac{\xi}{R} \right)^\zeta \right] \quad (2.6)$$

where $u_x(x, \xi, t)$ is the axial velocity profile, $U = Q/A$ is the average axial velocity in the cross-section, R is the vessel radius, ξ is the radial coordinate, and ζ is a constant pertaining to a chosen velocity profile. In this work, ζ is taken as 2. This gives f as

$$f = -2(\zeta + 2)\mu\pi U \quad (2.7)$$

where μ is the dynamic viscosity and is considered to be constant. Here, $u_x(x, \xi, t)$ is the x -component of the velocity vector, $u(t) = \frac{1}{A} \int_A (u_x(x, \xi, t) dA)$ is the average velocity (averaged over cross-section).

2.1.3 Constitutive relations

To provide a relationship between a vessel's cross-sectional area and transmural pressure, difference between pressure inside the vessel to pressure outside the vessel (from the surrounding tissue), is given by a constitutive relation. It helps close the set of governing equations, continuity and momentum equations (Equations (2.1) and (2.2)). Various linear and non-linear equations have been proposed for this relation [18, 33, 34]. In this thesis, the **LCG model** uses a non-linear relation [35, 22, 31, 29] given as

$$P - P_{ext} = P_0 + \frac{\beta}{A_0} (\sqrt{A} - \sqrt{A_0}), \quad \beta(x) = \frac{4}{3} \sqrt{\pi} E h \quad (2.8)$$

where P_{ext} is the external pressure on the vessel from surrounding tissue, $P - P_{ext}$ is the transmural pressure, A_0 and P_0 refer to stress free vessel area and diastolic pressure respectively, and $\beta(x)$ accounts for the material properties of the vessel wall with thickness $h(x)$ and elastic modulus $E(x)$.

In the **ETM model**, however, a visco-elastic relation is used which combines power law (for elastic term) [30, 36, 37] and a Voigt model for the viscous wall term [38, 30], and is given as

$$P - P_{ext} - P_0 = \frac{2\rho c_0^2}{b} \left(\left(\frac{A}{A_0} \right)^{b/2} - 1 \right) + \frac{\Gamma}{A_0 \sqrt{A_0}} \frac{\partial A}{\partial t}, \quad b = \frac{2\rho c_0^2}{P_0 - P_{collapse}} \quad (2.9)$$

where $P_{collapse}$ is the pressure at which the vessel is fully collapsed and c_0^2 is the wave speed.

2.1.4 Characteristic Analysis

A characteristic system is required to numerically solve the set of equations given by Equations (2.1) and (2.2). To develop such a system, the chain rule is often applied on the pressure term in the momentum equation. An example from [32] is presented to show such a derivation. Consider Equation (2.5) written in the form

$$\begin{cases} \frac{\partial A}{\partial P} \frac{\partial P}{\partial t} + \frac{\partial Q}{\partial x} = 0 \\ \frac{\rho}{A} \frac{\partial Q}{\partial t} + \frac{\rho}{A} \frac{\partial(\alpha \frac{Q^2}{A})}{\partial x} + \frac{\partial P}{\partial x} - \frac{f}{A} = 0 \end{cases} \quad (2.10)$$

along with Equation (2.9). With application of chain rule on the pressure term, we get,

$$\frac{\partial P}{\partial x} = \frac{\partial P}{\partial A} \frac{\partial A}{\partial x} + \frac{\partial P}{\partial \beta} \frac{\partial \beta}{\partial x} + \frac{\partial P}{\partial A_0} \frac{\partial A_0}{\partial x} \frac{\partial P}{\partial P_{ext}} \frac{\partial P_{ext}}{\partial x} \quad (2.11)$$

which allows for a quasi-linear representation of the system of equations as,

$$\frac{\partial \mathbf{U}}{\partial t} + \mathbf{H} \frac{\partial \mathbf{U}}{\partial x} = \mathbf{C} \quad (2.12)$$

where

$$U = \begin{bmatrix} A \\ Q \end{bmatrix} \quad H = \begin{bmatrix} 0 & 1 \\ \frac{\beta \sqrt{A}}{2\rho A_0 - \frac{Q^2}{A^2}} & 2\frac{Q}{A} \end{bmatrix}$$

and

$$\mathbf{C} = \begin{bmatrix} 0 \\ -\frac{\zeta\pi\mu Q}{\rho A} - \frac{A}{\rho} \frac{\partial P}{\partial P_{ext}} \frac{\partial P_{ext}}{\partial x} - \frac{A}{\rho} \frac{\partial P}{\partial A_0} \frac{\partial A_0}{\partial x} - \frac{A}{\rho} \frac{\partial P}{\partial \beta} \frac{\partial \beta}{\partial x} \end{bmatrix}$$

For the above equation, by solving $|\Lambda I - H| = 0$, eigenvalues Λ are calculated as

$$\Lambda = \begin{bmatrix} \lambda_1 \\ \lambda_2 \end{bmatrix} = \begin{bmatrix} u + \sqrt{\frac{\beta\sqrt{A}}{2\rho A_0}} \\ u - \sqrt{\frac{\beta\sqrt{A}}{2\rho A_0}} \end{bmatrix} = \begin{bmatrix} u + c \\ u - c \end{bmatrix} \quad (2.13)$$

where λ_1 and λ_2 are forward and backward propagation speeds respectively and c is the wave speed. Under physiological arterial flow conditions, maximum velocity U is smaller compared to the pulse wave velocity c ,

Left eigenmatrix can be determined using $l_i H = \lambda_i l_i$ as

$$L = \begin{bmatrix} l_1^T \\ l_2^T \end{bmatrix} = \begin{bmatrix} -u + c & 1 \\ -u - c & 1 \end{bmatrix}$$

Noting that H can be represented as $H = L^{-1} \bar{\Lambda} L$, where

$$\bar{\Lambda} = \begin{bmatrix} \lambda_1 & 0 \\ 0 & \lambda_2 \end{bmatrix} \quad (2.14)$$

Equation (2.12) can be written as

$$L \frac{\partial U}{\partial t} + \bar{\Lambda} L \frac{\partial U}{\partial x} - LC = 0 \quad (2.15)$$

Then characteristic variables w_1 and w_2 , from $\frac{\partial w_1}{\partial U} = l_1$ and $\frac{\partial w_2}{\partial U} = l_2$ respectively, in the form $W = [w_1, w_2]$ can be used to write Equation (2.15)

$$\frac{\partial W}{\partial t} + \bar{\lambda} \frac{\partial W}{\partial x} = 0 \quad (2.16)$$

Note that the term \mathbf{C} has been ignored as A_0 and β are assumed to be constant and the viscous resistance term is small enough to be neglected.

The characteristic variables, w_1 and w_2 , can be calculated from

$$w_{1,2} = u - u_0 + \int_{A_0}^A \frac{c}{A} dA = u - u_0 + \int_{P_0}^P \frac{1}{\rho c} dP \quad (2.17)$$

$$w_1 = u - u_0 + 4(c - c_0) \quad w_2 = u - u_0 - 4(c - c_0) \quad (2.18)$$

by manipulating the characteristic variables, primitive variables A and u can be found as

$$A = \left(\frac{w_1 - w_2}{8} \right)^4 \left(\frac{2\rho A_0}{\beta} \right)^2, \quad u = \frac{w_1 + w_2}{2} \quad (2.19)$$

2.2 Boundary conditions

2.2.1 Heart function

In 1D haemodynamic modelling, the heart function has been modelled using numerous approaches, with some using heart model in a closed-loop framework [30, 34] while others taking only ventricular activity [29] into consideration to calculate cardiac outflow into the aorta. The heart function used in thesis varies for different applications. For example, in **LCG model**, used in **Chapter 6** for active digital twin, uses an aortic valve and ventricular pressure approach [29]. In this approach, modelling is carried out with respect to the aortic valve, which opens for uni-directional blood when the ventricular pressure is higher than the aortic pressure during systole and remains closed during diastole.

The input for this model starts a point in the left ventricle, just before the aortic valve. Two sigmoid waveforms, each in the form shown below in Equation (2.20) are fused at mid-ejection to form a realistic pressure waveform.

$$p_{sig}(t) = a_1 + \frac{(a_2 - a_1)}{1 + e^{-\frac{a_3 - t}{a_4}}} \quad (2.20)$$

where $a_1 = p_{ed} - 9.11 \times 10^{-4} p_{peak}$, $a_2 = p_{peak}$, $a_3 = 7t_c$, $a_4 = t_c$, where p_{ed} is pressure at the end of diastole, p_{peak} is peak ventricular pressure and t_c is a time constant that controls isovolumic upstroke or downstroke.

However, in the **ETM model**, a lumped model, proposed by Mynard and Smolich [30], is used to represent the function of the heart, as shown below in Figure 2.1 where R_s and E_{nat} are source resistance and native elastance of the chamber. In valves, B , R and L are Bernoulli's resistance, viscous resistance and inertance respectively. Detailed description of the lumped models and their implementation are available in [32] [30].

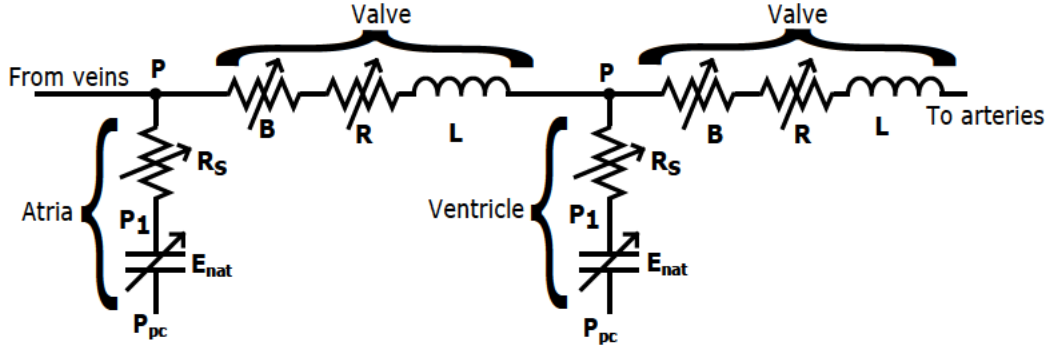


Fig. 2.1 Lumped model used to represent flow in one side of the heart

2.2.2 Terminal vessels

Towards the end of the arteries, they split into a large number of small arterioles and then into capillaries that supply blood to almost every part of the body at the tissue level. The network of capillaries makes up what is known as vascular capillary beds. These beds provide resistance to the flow and also have a compliance component in them. To model them, two different approaches are adopted by the models used in this work.

The **LCG model** uses a tapered vessel for terminal vessels, whose gradient both in terms of A_0 and β from the start of the vessel to the end of the vessel is representative of the resistance provided to the flow by the capillary bed and its compliance to which the vessel is connected to. By altering the terminal vessels' A_0 for the end node, in turn affecting the gradient of the taper, systemic vascular resistance is controlled in this thesis [29].

In the **ETM model**, the capillary bed properties are modelled using Windkessel models, a form of lumped models. These models use resistance, compliance and inertance elements (analogous to resistive, capacitive and inductive elements respectively in an electric circuit) are used to model the characteristics of the capillary beds (for example see Figure 2.2). The function of each of the element is given as

$$R = \frac{\Delta P}{Q}(\text{resistance}), Q_{net} = C \frac{\partial P_{tm}}{\partial t}(\text{capacitance}), \Delta P = L \frac{\partial Q}{\partial t}(\text{inductance}) \quad (2.21)$$

where ΔP is change in blood pressure, Q is the blood volumetric flow rate, C is the compliance of the capillary bed, P_{tm} is the transmural pressure, L is the fluid inertia in a volume and t is the time. Different forms of this model are used for various

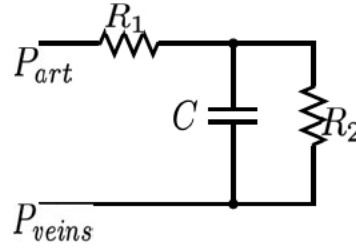


Fig. 2.2 A three-element Windkessel model with two resistive elements (R_1 and R_2) and a compliance element C . P_{art} and P_{veins} are arterial pressure and venous pressure respectively.

applications in this thesis. The variation used for each application is detailed in their respective chapters.

2.3 Arterial network

The two haemodynamic models used in this thesis use arterial tree information that is significant for the application in which they are being adopted. However, for completeness, the arterial tree used by the **LCG model**, adapted from [39] is described below in Table 2.1 and Figure 2.3. The values in this section correspond to a general human model. However, in order to modify vessel length and area to a patient's physiology, for patient-oriented simulations (a crucial component for digital twins), empirical equations derived or observed by various studies [40–43] on general population is used.

2.4 Numerical schemes

In this section, the two numerical schemes, the Locally conservative Taylor-Galerkin and the enhanced trapezoidal methods, used to solve the equations shown in Section 2.1 are described. The solutions described in this section have already been described in [29] and [44], however, for ease of reading all equations have been presented below.

2.4.1 Locally Conservative Galerkin (LCG) method

The LCG method is based on a standard finite element Galerkin procedure. The derivation of this method begins with discretisation of AU formulation, which can be

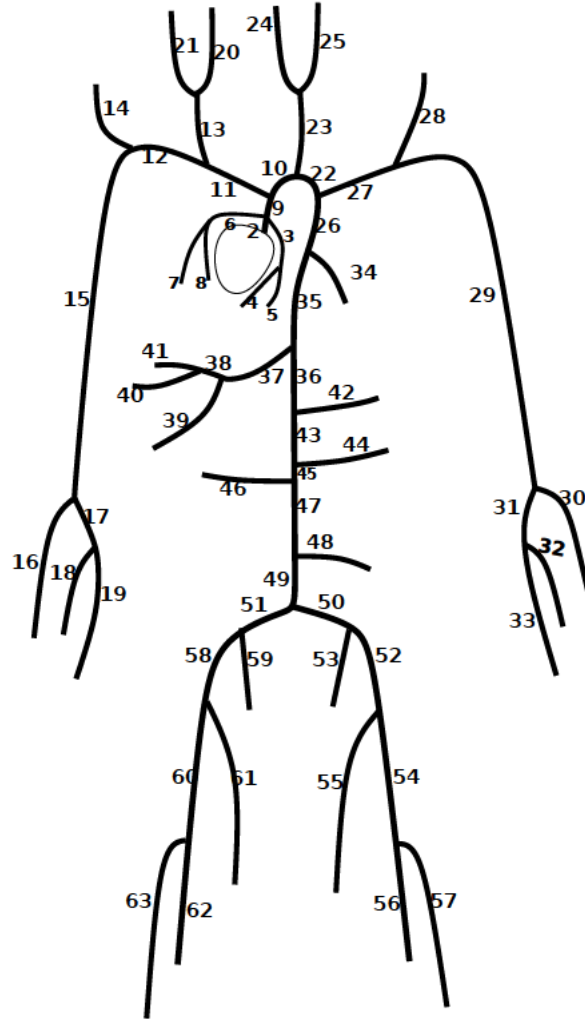


Fig. 2.3 The arterial tree presented in Table 2.1. This network has been adapted from [39]

represented as

$$\frac{\partial \mathbf{U}}{\partial t} + \frac{\partial \mathbf{F}}{\partial x} = \mathbf{S} \quad (2.22)$$

where

$$\mathbf{U} = \begin{bmatrix} A \\ u \end{bmatrix}, \quad \mathbf{F} = \begin{bmatrix} uA \\ \frac{u^2}{2} + \frac{p}{\rho} \end{bmatrix} \quad \text{and} \quad \mathbf{S} = \begin{bmatrix} 0 \\ -\frac{2(\zeta+2)\mu\pi u}{\rho} \end{bmatrix}$$

By differentiating (2.22) with respect to time and applying the chain rule, we get

$$\frac{\partial^2 \mathbf{U}}{\partial t^2} = \frac{\partial \mathbf{S}}{\partial \mathbf{U}} \frac{\partial \mathbf{U}}{\partial t} - \frac{\partial}{\partial x} \left(\frac{\partial \mathbf{F}}{\partial \mathbf{U}} \mathbf{U} \right) \quad (2.23)$$

then, substituting (2.22) into (2.23) , we get

$$\frac{\partial^2 \mathbf{U}}{\partial t^2} = \frac{\partial \mathbf{S}}{\partial \mathbf{U}} \left(\mathbf{S} - \frac{\partial \mathbf{F}}{\partial x} \right) - \frac{\partial (F_U \mathbf{S})}{\partial x} + \frac{\partial}{\partial x} \left(F_U \frac{\partial \mathbf{F}}{\partial x} \right) \quad (2.24)$$

where $F_U = \frac{\partial F}{\partial U}$. Further, the Taylor series expansion in time gives,

$$\mathbf{U}^{n+1} = \mathbf{U}^n + \Delta t \frac{\partial \mathbf{U}^n}{\partial t} + \frac{\Delta t^2}{2} \frac{\partial^2 \mathbf{U}^n}{\partial t^2} + O(\Delta t^3) \quad (2.25)$$

where n is the current time step and Δt is the time step. The final explicit semi-discrete form can be obtained by substituting Equations (2.22) and (2.24) in the above Taylor expansion, after ignoring higher order terms,

$$\frac{\mathbf{U}^{n+1} - \mathbf{U}^n}{\Delta t} = \mathbf{S}^n - \frac{\partial \mathbf{F}^n}{\partial x} - \frac{\Delta t}{2} \left[\frac{\partial}{\partial x} \left(F_U^n \mathbf{S}^n - F_U^n \frac{\partial \mathbf{F}^n}{\partial x} \right) - S_U^n \frac{\partial \mathbf{F}^n}{\partial x} - S_U^n \mathbf{S}^n \right] \quad (2.26)$$

The above discrete form (Equation (2.26)) helps in formulation of a residual equation for finite element method, explained below.

Global Taylor-Galerkin method For finite element method, standard spacial discretisation is performed over the global domain Ω , with boundaries Γ . A residual equation is possible by using Galerkin weighting \mathbf{N}^T along with linear spatial discretisation, which is given as,

$$\int_{\Omega} \left(\mathbf{N}^T \frac{\Delta \hat{\mathbf{U}}^n}{\Delta t} - \mathbf{N}^T \hat{\mathbf{R}}^n \right) d\Omega = 0 \quad (2.27)$$

where \mathbf{R} is RHS of Equation (2.26), and hat signifies that the respective variables are approximated by the finite element method. Using this Equation (2.27), the following equation in compact matrix form may be derived,

$$[\mathbf{M}]\{\Delta \mathbf{U}\} = \Delta t([\mathbf{K}]\{\mathbf{F}\}^n + [\mathbf{L}]\{\mathbf{S}\}^n + \{\mathbf{f}_{\Gamma}\}^n) \quad (2.28)$$

where $[\mathbf{M}]$ is the mass matrix, $[\mathbf{K}]$ and $[\mathbf{L}]$ are coefficient matrices for convection, Taylor-Galerkin and source terms and \mathbf{f} accounts for boundary fluxes.

Locally conservative Taylor-Galerkin method Introduced by Thomas and Nithiarasu [45, 46], LCG is a method that treats element as a sub-domain with its own boundaries.

Using this method, Equation (2.28), can be written as

$$[\mathbf{M}_e]\{\Delta\mathbf{U}\} = \Delta t([\mathbf{K}_e]\{\mathbf{F}\}^n + [\mathbf{L}_e]\{\mathbf{S}\}^n + \{\mathbf{f}_{\Gamma_e}\}^n) \quad (2.29)$$

Here, $[\mathbf{M}_e]$, $[\mathbf{K}_e]$ and $[\mathbf{L}_e]$ are all elemental matrices, i.e for each element, and this system of equations solved within the element. A neumann boundary condition is applied with the flux term which represents the information transmitted between the elements.

To derive this method for inviscid cases, terms dealing with S and S_U are removed and the following reduced form is obtained,

$$\int_{\Omega_e} \mathbf{N}^T \frac{\Delta \hat{\mathbf{U}}^n}{\Delta t} = - \int_{\Omega_e} \mathbf{N}^T \frac{\Delta \hat{\mathbf{F}}^n}{\Delta x} + \frac{\Delta t}{2} \int_{\Omega_e} \mathbf{N}^T \frac{\partial}{\partial x} \left(\hat{F}_U^n \frac{\partial \hat{\mathbf{F}}^n}{\partial x} \right) d\Omega_e = 0 \quad (2.30)$$

Solving the above equation we get an element mass matrix as,

$$[\mathbf{M}_e] = \frac{l_e}{6} \begin{bmatrix} 2 & 1 \\ 1 & 2 \end{bmatrix} \quad (2.31)$$

where l_e is the element length. The lumped matrix for this may be written as,

$$[\mathbf{M}_e] = \frac{l_e}{2} \begin{bmatrix} 1 & 0 \\ 0 & 1 \end{bmatrix} \quad (2.32)$$

Further, integrating the convection term we get,

$$- \int_{\Omega_e} \mathbf{N}^T \frac{\partial \hat{\mathbf{F}}^n}{\partial x} d\Omega_e = \int_{\Omega_e} \frac{\partial \mathbf{N}^T}{\partial x} \hat{\mathbf{F}}^n d\Omega_e - \int_{\Gamma_e} \mathbf{N}^T \hat{\mathbf{F}}^n \mathbf{n} d\Gamma_e \quad (2.33)$$

where $\hat{\mathbf{F}}$ is computed in a small post-processing step as the average value of \mathbf{F} from adjacent elements. The Taylor-Galerkin term is also integrated as,

$$\int_{\Omega_e} \mathbf{N}^T \frac{\partial}{\partial x} \left(F_U^n \frac{\partial \hat{\mathbf{F}}^n}{\partial x} \right) d\Omega_e = - \int_{\Omega_e} \frac{\partial \mathbf{N}^T}{\partial x} F_U^n \frac{\partial \hat{\mathbf{F}}^n}{\partial x} d\Omega_e + \int_{\Gamma_e} \mathbf{N}^T \bar{F}_U^n \frac{\partial \hat{\mathbf{F}}^n}{\partial x} d\Gamma_e \quad (2.34)$$

$[\mathbf{K}_e]$ is obtained by solving Equations (2.33) and (2.34), along with source terms as,

$$[\mathbf{K}_e] = \left(\frac{1}{2} + \frac{\Delta t}{4} \check{\mathbf{S}}_U^n \right) \begin{bmatrix} -1 & -1 \\ 1 & 1 \end{bmatrix} - \frac{\Delta t}{2l_e} \check{F}_U^n \begin{bmatrix} 1 & -1 \\ -1 & 1 \end{bmatrix} \quad (2.35)$$

where $\check{\mathbf{S}}_U$ and \check{F}_U are average values over the elemental sub-domain. Similarly, $[\mathbf{L}_e]$ is obtained as

$$[\mathbf{L}_e] = \left(\frac{l_e}{6} + \frac{\Delta t l_e}{12} \check{\mathbf{S}}_U^n \right) \begin{bmatrix} 2 & 1 \\ 1 & 2 \end{bmatrix} + \frac{\Delta t}{4} \check{F}_U^n \begin{bmatrix} -1 & -1 \\ 1 & 1 \end{bmatrix} \quad (2.36)$$

We get the flux term as

$$\{\mathbf{f}_e\} = \left\{ \begin{array}{c} \check{\mathbf{F}}_i^n \\ \check{\mathbf{F}}_j^n \end{array} \right\} \quad (2.37)$$

since the Taylor-Galerkin terms, that arise from the numerical technique, are not included as they will be zero on the boundaries.

In this scheme, flow in vessel junctions is solved by evaluating outgoing characteristics, conservation of mass, given as

$$Q = A_p u_p = \sum_{i=1}^N A_i u_i \quad (2.38)$$

where p is the parent vessel and N is the number of daughter vessels, and Continuity of total pressure (solved using Newton-Raphson method), given as

$$\frac{\rho u_p^2}{2} + p_{ext(p)} + \beta(\sqrt{A_p} - \sqrt{A_{p0}}) = \frac{\rho u_i^2}{2} + p_{ext(i)} + \beta(\sqrt{A_i} - \sqrt{A_{i0}}) \quad (2.39)$$

Detailed information on implementation of this scheme as well as the above derivation are available in [29].

2.4.2 Enhanced trapezoidal method

Enhanced trapezoidal method (ETM) is developed by enhancing the Simplified trapezoidal rule method (STM) proposed by Kroon *et al* [47]. In STM, all flows Q are directed inwards, towards element the element center. It is developed by solving PQ formulation, shown in Equation (2.5), for a domain discretised into non-overlapping two noded elements. To achieve this, following steps are used. To begin with, the PQ formulation is linearised as,

$$\begin{aligned} C_a^{n+1} &\approx C_a^{n+1,k}, Q^{n+1} \approx Q^{n+1,k+1}, P^{n+1} \approx P^{n+1,k+1}, \\ \frac{Q^{2^{n+1}}}{A} &\approx \frac{Q^{2^{n+1,k}}}{A}, \frac{\rho^{n+1}}{A} \approx \frac{\rho^{n+1,k}}{A}, \\ \left(\frac{2(\zeta+2)\mu\pi Q}{A^2} \right)^{n+1} &\approx \left(\frac{2(\zeta+2)\mu\pi Q}{A^2} \right)^{n+1,k} \end{aligned} \quad (2.40)$$

where k is the iteration level, giving a system of equations with continuity

$$C_A^n \frac{\partial P}{\partial t} + \frac{\partial Q^{n+1}}{\partial x} = 0, \quad C_A = \frac{\partial A}{\partial P} \quad (2.41)$$

and momentum

$$\frac{\rho}{A^n} \frac{\partial Q}{\partial t} + \frac{\partial P^{n+1}}{\partial x} = \left(-\frac{2(\zeta + 2)\mu\pi Q}{A^2} - \frac{\rho}{A} \frac{\partial \left(\frac{Q^2}{A} \right)}{\partial x} \right)^n \quad (2.42)$$

equations. The domain Ω is then split into smaller elements (e) with two nodes each. Using trapezoidal rule, the system is integrated in space, giving continuity equation as,

$$\int_e \left(C_A^n \frac{\partial P}{\partial t} \right) dx = \frac{\Delta x}{2} \left(C_{A,1}^n \frac{\partial P_1}{\partial t} + C_{A,2}^n \frac{\partial P_2}{\partial t} \right) \quad (2.43)$$

$$\int_e \left(\frac{\partial Q^{n+1}}{\partial x} \right) dx = (Q_2^{n+1} - Q_1^{n+1}) \quad (2.44)$$

and momentum equation as,

$$\int_e \left(\frac{\rho}{A^n} \frac{\partial Q}{\partial t} \right) dx = \frac{\Delta x}{2} \left(\frac{\rho}{A_1^n} \frac{\partial Q_1}{\partial t} + \frac{\rho}{A_2^n} \frac{\partial Q_2}{\partial t} \right) \quad (2.45)$$

$$\int_e \left(\frac{\partial P^{n+1}}{\partial x} \right) dx = (P_2^{n+1} - P_1^{n+1}) \quad (2.46)$$

for LHS terms and taking RHS term as h

$$h = \left(\frac{-2(\zeta + 2)\pi\mu Q}{A^2} - \frac{\rho}{A} \frac{\partial \left(\frac{Q^2}{A} \right)}{\partial x} \right)^n \quad (2.47)$$

integration gives

$$\int_e (h)^n dx = \frac{\Delta x}{2} (h_1 + h_2)^n \quad (2.48)$$

Further, by using second-order backward difference for the time derivatives, given as

$$\frac{\partial U}{\partial t} \approx \frac{3}{2\Delta t} U^{n+1} - \frac{2}{\Delta t} U^n + \frac{1}{2\Delta t} U^{n-1} \quad (2.49)$$

the above integrated system can be written as

$$\begin{aligned} \begin{bmatrix} \frac{3}{2\Delta t} \frac{\Delta x}{2} C_{A,1}^n & \frac{3}{2\Delta t} \frac{\Delta x}{2} C_{A,2}^n \\ -1 & 1 \end{bmatrix} \begin{bmatrix} P_1 \\ p_2 \end{bmatrix}_e^{n+1} + \begin{bmatrix} -1 & 1 \\ \frac{3}{2\Delta t} \frac{\Delta x}{2} \frac{\rho}{A_1^n} & \frac{3}{2\Delta t} \frac{\Delta x}{2} \frac{\rho}{A_2^n} \end{bmatrix} \begin{bmatrix} Q_1 \\ Q_2 \end{bmatrix}_e^{n+1} = \begin{bmatrix} 0 \\ \frac{\Delta x}{2} (h_1^n + h_2^n) \end{bmatrix}_e \\ + \begin{bmatrix} \frac{\Delta x}{2} \left(C_A^n \frac{2}{\Delta t} P^n - C_A^n \frac{2}{\Delta t} P^{n-1} \right)_1 \\ \frac{\Delta x}{2} \left(\frac{\rho}{A^n} \frac{2}{\Delta t} Q^n - \frac{\rho}{A^n} \frac{2}{\Delta t} Q^{n-1} \right)_1 \end{bmatrix}_e + \begin{bmatrix} \frac{\Delta x}{2} \left(C_A^n \frac{2}{\Delta t} P^n - C_A^n \frac{2}{\Delta t} P^{n-1} \right)_2 \\ \frac{\Delta x}{2} \left(\frac{\rho}{A^n} \frac{2}{\Delta t} Q^n - \frac{\rho}{A^n} \frac{2}{\Delta t} Q^{n-1} \right)_2 \end{bmatrix}_e \end{aligned} \quad (2.50)$$

which can be generalised as,

$$\mathbf{F}_e \mathbf{P}_e^{n+1} + \mathbf{G}_e^c \mathbf{Q}_e^{c,n+1} = \mathbf{h}_e^n \quad (2.51)$$

where c represents conventional discretisation and e represents elemental domain.

At this point, flow direction is towards the element center, which leads to the changing of sign for Q at second node, thereby changing the sign of the second column of G_e^c , giving the matrix G_e^c as

$$\mathbf{G}_e = \begin{bmatrix} G_{11} & -G_{12} \\ G_{21} & -G_{22} \end{bmatrix} \quad (2.52)$$

and Q_e^c as $Q_e = [Q_1, -Q_2]^T$. Matrix \mathbf{G}_e is then inverted to give a final elemental system of equations, given as

$$\begin{bmatrix} -\mathbf{G}_e^{-1} & \mathbf{F}_e \end{bmatrix} \mathbf{P}_e^{n+1} = \begin{bmatrix} -\mathbf{G}_e^{-1} & \mathbf{h}_e^n \end{bmatrix} + \mathbf{Q}_e^{n+1} \quad (2.53)$$

These elemental systems are assembled to form a global system matrix, in which it can be observed that continuity of mass is automatically satisfied. Since this scheme uses the same pressure node at vessel junction for parent and daughter vessels, static pressure is also conserved. This is enhanced by the ETM scheme, where constraints are put at the vessel junction, using Lagrange multipliers to conserve total pressure, and not just static pressure. For more detailed information on implementation and Lagrange multipliers, please refer to [44].

2.5 Summary

In this chapter, the different haemodynamic models used in this thesis are described. The governing equations behind these models, boundary conditions applied, arterial networks employed, and numerical schemes used to solve them are briefly explained. The models described in this chapter are employed in Chapters 4, 5 and 6 along with machine learning algorithms (described in Chapter 3) to develop three primary forms of digital twin for cardiovascular systems.

Table 2.1 The basic arterial tree and properties used by the **LCG model**, adapted from [39]. Here, L is the vessel length, D1, D2 and D3 are daughter vessels, β_i and β_f are the material properties of the vessel wall at the proximal and distal end of the vessel respectively, and A_i and A_f are the vessel's cross-sectional area at the proximal and distal end respectively.

Ves. No.	Vessel Name	$L(\text{cm})$	D1	D2	D3	$\beta_i(\text{dyne/cm}^3)$	$\beta_f(\text{dyne/cm}^3)$	$A_i(\text{cm}^2)$	$A_f(\text{cm}^2)$
1	LV Outflow Tract	1	2	0	0	226955	226955	7.01	7.01
2	Aortic Root	1	3	6	9	226955	226955	7.01	7.01
3	Left Coronary Artery	3	4	5	0	7202352	7202352	0.21	0.21
4	Left Endocardial	7	0	0	0	12604116	25208233	0.12	0.06
5	Left Epicardial	7	0	0	0	12604116	25208233	0.12	0.06
6	Right Coronary Artery	3	7	8	0	8402744	8402744	0.18	0.18
7	Right Endocardial	7	0	0	0	14684407	29368815	0.103	0.0515
8	Right Epicardial	7	0	0	0	14684407	29368815	0.103	0.0515
9	Ascending Aorta I	4	10	11	0	226974	236530	6.7887	6.5144
10	Aortic Arch I	2	22	23	0	302244	302244	3.9408	3.9408
11	Brachiocephalic	3.5	12	13	0	640973	704503	1.3273	1.2076
12	Right Subclavian I	3.5	14	15	0	837109	912790	0.5675	0.5204
13	Right Carotid	9.4	20	21	0	780114	1547491	1.4314	0.3848
14	Right vertebral	13.5	64	0	0	5500848	5500848	0.1257	0.1257
15	Right Subclavian II	39.8	16	17	0	912790	1905517	0.5204	0.1662
16	Right Radius	22	65	0	0	6865458	9076928	0.0962	0.0616
17	Right Ulnar I	6.7	18	19	0	4491547	4491547	0.1452	0.1452
18	Right Interosseous	7	66	0	0	29488309	29488309	0.0314	0.0314
19	Right Ulnar II	17	67	0	0	9236815	10680132	0.1295	0.1018
20	Right Int. Carotid	17.8	68	0	0	2708944	3661587	0.2552	0.1452
21	Right Ext. Carotid	10.2	69	0	0	3285840	5158305	0.1963	0.0962
22	Aortic Arch II	3.9	26	27	0	302241	302241	3.5968	3.5968
23	Left Carotid	13.9	24	25	0	921510	1843019	1.131	0.2827
24	Left Int. Carotid	17.8	70	0	0	3133271	4027528	0.2206	0.132
25	Left Ext. Carotid	10.2	71	0	0	3718696	5158305	0.1735	0.0962
26	Thoracic Aorta I	5.2	34	35	0	331654	331654	3.1353	3.1353
27	Left subclavian I	3.5	28	29	0	824615	899167	0.5675	0.5204
28	Left vertebral	13.5	72	0	0	5500848	5500848	0.1257	0.1257
29	Left subclavian II	39.8	30	31	0	912790	1905517	0.5204	0.1662
30	Left radius I	22	73	0	0	6865458	9076928	0.0962	0.0616
31	Left ulnar I	6.7	32	33	0	4491547	4491547	0.1452	0.1452
32	Left interosseous	7.9	74	0	0	29488309	29488309	0.0314	0.0314
33	Left ulnar II	17	75	0	0	9236815	10680132	0.1295	0.1018
34	Intercostals	8	76	0	0	383563	511417	1.2076	0.6793
35	Thoracic Aorta II	10.4	36	37	0	660414	723277	1.4314	1.307
36	Abdominal Aorta I	5.3	42	43	0	727791	727791	1.169	1.169
37	Celiac I	1	38	39	0	1266119	4814418	0.4778	0.1257
38	Celiac II	1	40	41	0	4814418	4814418	0.1257	0.1257
39	Hepatic	6.6	77	0	0	3046313	3046313	0.1521	0.1521
40	Gastric	6.3	78	0	0	4179182	4179182	0.1018	0.1018
41	Splenic	7.1	79	0	0	2148583	2148583	0.2376	0.2376
42	Sup. Mesenteric	5.9	80	0	0	2306909	2306909	0.2827	0.2827
43	Abdominal Aorta II	1	44	45	0	691528	691528	1.0936	1.0936
44	Left Renal	3.2	81	0	0	2359136	2359136	0.2124	0.2124
45	Abdominal Aorta III	1	46	47	0	691528	691528	1.0936	1.0936
46	Right Renal	3.2	82	0	0	2359136	2359136	0.2124	0.2124
47	Abdominal Aorta IV	10.6	48	49	0	670856	751491	1.0568	0.9434
48	Inf. Mesenteric	5	83	0	0	5054198	5054198	0.0804	0.0804
49	Abdominal Aorta V	1	50	51	0	723320	723320	0.8495	0.8495
50	Left Com. Iliac	5.9	52	53	0	1128379	1318778	0.5027	0.4301
51	Right Com. Iliac	5.8	58	59	0	1128379	1318778	0.5027	0.4301
52	Left Ext. Iliac	14.4	54	55	0	2329841	3234971	0.4301	0.3097
53	Left Int. Iliac	5	84	0	0	12036044	12036044	0.1257	0.1257
54	Left Femoral	44.3	56	57	0	3051859	3978858	0.3097	0.2376
55	Left Deep Femoral	12.6	85	0	0	7071176	14142352	0.1257	0.1257
56	Left Post. Tibial	32.1	86	0	0	17685616	17685616	0.0962	0.0962
57	Left Ant. Tibial	34.3	87	0	0	6207018	7510492	0.2376	0.1963
58	Right Ext. Iliac	14.5	60	61	0	2329841	3234971	0.4301	0.3097
59	Right Int. Iliac	5	88	0	0	12036044	12036044	0.1257	0.1257
60	Right Femoral	44.4	62	63	0	3051859	3978858	0.3097	0.2376
61	Right Deep Femoral	12.7	89	0	0	7071176	14142352	0.1257	0.1257
62	Right Post. Tibial	32.2	90	0	0	17685616	17685616	0.0962	0.0962
63	Right Ant. Tibial	34.4	91	0	0	6207018	7510492	0.2376	0.1963

Chapter 3

Artificial Intelligence

From multi-speciality hospitals to community centres, healthcare infrastructure generates large amounts of medical data. Starting from inpatient records, medical history to diagnosis, monitoring, care charts and discharge summary, every patient generates large volumes of data. Generation of this patient data takes place in various types and volumes across different healthcare settings. The primary types of which are:

- **Text :** Data such as inpatient details, medical history, clinicians' notes and so on are generally generated in textual form.
- **Time series (signals) :** Patient data such as Electrocardiogram (ECG), blood pressure waveforms, SpO_2 (Oxygen saturation) and so on are generated as time-dependent information. Apart from patient data, signals from medical devices and equipment are also generated, analysis of which is necessary for their maintenance.
- **Image :** Every scan used to analyse patients' internals such as Computerised Tomography(CT), Magnetic Resonance Imaging(MRI) and ultrasound are generated as image matrices (2-D and 3-D images).

A brief overview of the current machine learning algorithms, working principles and their use in the analysis of the above patient data is discussed in the first half of this chapter. In the second half, an application with these algorithms in a three-tiered strategy to prioritise ITU treatment for pneumonia patients is presented to exemplify the capacity of AI algorithms.

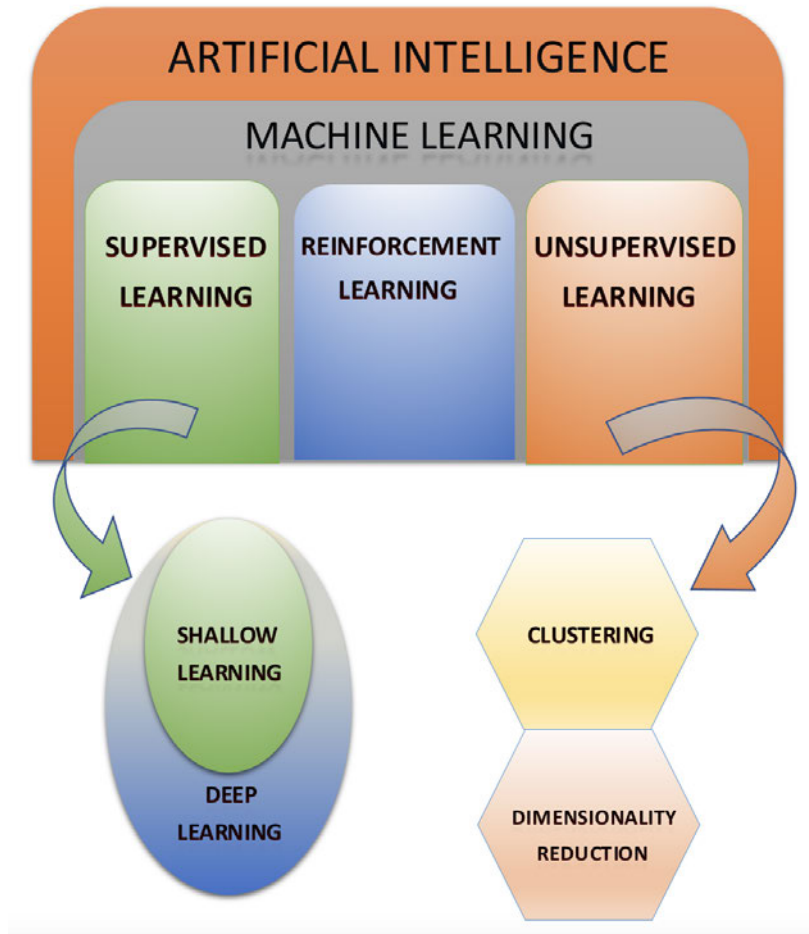


Fig. 3.1 Classification of artificial intelligence.

3.1 An overview of machine learning algorithms

Artificial intelligence is synonymous with machine learning. However, artificial intelligence is the science of mimicking intelligence using machines and machine learning is the means of achieving this. Machine learning can broadly be divided into supervised, unsupervised and reinforcement learning, as shown in Figure 3.1. The following subsections will explain the first two types of learning, supervised and unsupervised learning, their sub-classifications, examples of their use in medical analysis and working principles. The last type of learning, reinforcement learning, is not adopted in any of the digital twins presented in this thesis therefore not being discussed in this chapter to avoid any ambiguity.

3.1.1 Supervised learning

In supervised learning labelled data is provided, using which machine learning algorithms are adapted or fit to provide an output for a given task. The majority of machine learning based biomedical applications adopt this kind of learning. These algorithms are predominantly used for classification and prediction, therefore are used for the diagnosis and prognosis of diseases.

Based on the complexity or depth of knowledge captured in these algorithms, supervised machine learning can be divided into shallow and deep learning. The depth of knowledge required for an application is heavily influenced by the amount of available training data, required efficacy, computational constraints and data type.

Shallow learning

In shallow learning, also known as traditional machine learning, data defined by predefined features are trained upon by lower-dimensional algorithms. In other words, features manually extracted from any given data is used to perform actions such as classifications and regressions. For biomedical usage, multiple applications using such algorithms have been developed and deployed over the last two decades [48–51].

Within shallow supervised learning, following types of algorithms are widely adopted:

- Regression algorithms: In these algorithms, to get predictions using a univariate or multivariate function, the relationship between the variables are iteratively refined using a measure of error. Examples of such algorithms are:
 - Linear regression,
 - Logistic regression and
 - Multivariate Adaptive Regression Splines (MARS)
- Decision tree based algorithms: These algorithms use flowchart-like models of decisions and their possible consequences to model outcomes in any given task. Examples of such algorithms are:
 - Conditional Decision trees
 - Classification and Regression Tree (CART)
 - Random Forests

- Instance based algorithms: In such algorithms, comparison of new data with existing database using a measure of similarity is used to perform any given task. Examples of such algorithms are:
 - K-Nearest Neighbour (KNN)
 - Support Vector Machine (SVM)
 - Locally weighted learning [52]

Deep learning

In deep learning, algorithms with multiple layers of weighted non-linear or linear mapping are used to progressively extract features of the given data and learn its higher-dimensional representation, representative of both recognisable features as well as hidden or not easily deducible features within the data. Owing to their efficacy and speed, these algorithms are widely being proposed and adopted in almost every part of healthcare. Multiple examples of such applications have been proposed for patient record management [53, 54], diagnosis [55, 56], prognosis [57, 58] and drug development [59, 60].

Deep learning predominantly consists of artificial neural networks. These artificial neural networks use units known as artificial neurons (see Figure 3.2)(inspired by the real human neurons) as their building blocks. These deep neural networks use vast amounts of data to train and perform various tasks. Primary forms of such deep neural networks include Feedforward neural networks and recurrent neural networks. The sections below will provide an overview of each of these types of neural networks and suitable applications for them in healthcare.

Feedforward neural network In this form of neural networks, the information flow from input to output is forward and unidirectional during calculations. Multilayer perceptron (MLP) and convolution neural networks (CNN) are widely used feedforward neural networks in healthcare. Owing to their unidirectional information flow, these networks are preferred for diagnostic applications.

Multilayer Perceptron In an artificial neural network, several of the artificial neurons, similar to the neuron shown in Figure 3.2, are put together parallelly to form a neural layer. In Multilayer Perceptron (MLP) models, multiple such layers are connected progressively, such that neurons from each layer are connected to each

neuron in the previous layer. In other words, every neuron in one layer is connected to every neuron in the next layer. The outputs from one layer to the next are generally mapped or activated using non-linear or linear functions. As shown in Figure 3.3, in an MLP, the first layer which accepts the input data is known as the input layer, the final layer which provides an output is known as the output layer and every layer in between them are usually known as hidden layers. Such a network allows for different higher-dimensional features to be identified in input data. Some of the widely used activation functions in an MLP are:

- ReLU (Rectified linear unit): $\sigma = \max(0, x)$
- TanH (Hyperbolic tan): $\sigma = \frac{e^x - e^{-x}}{e^x + e^{-x}}$
- Sigmoid: $\sigma = \frac{1}{1 + e^{-x}}$

Equations (3.1) and (3.2) represent the calculation of output in an artificial neuron, as shown in Figure 3.2, where w_i are the weights, b is the bias, σ is the activation function, O is the output and x_i are the inputs.

$$z = \sum_{i=1}^n x_i w_i + b \quad (3.1)$$

$$O = \sigma(z) \quad (3.2)$$

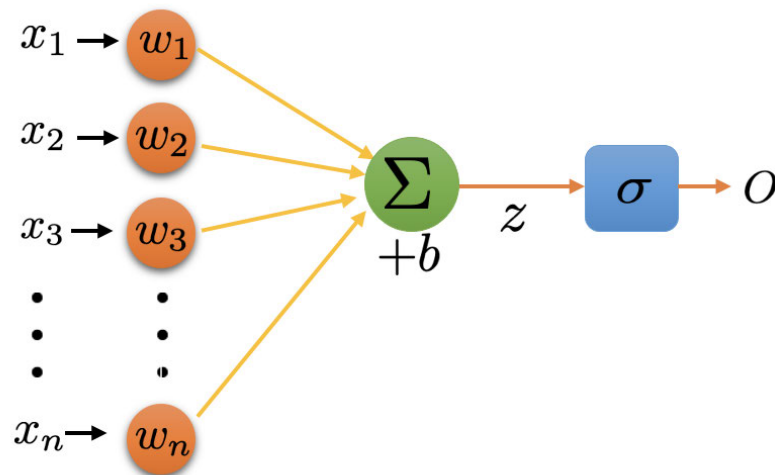


Fig. 3.2 An artificial neuron.

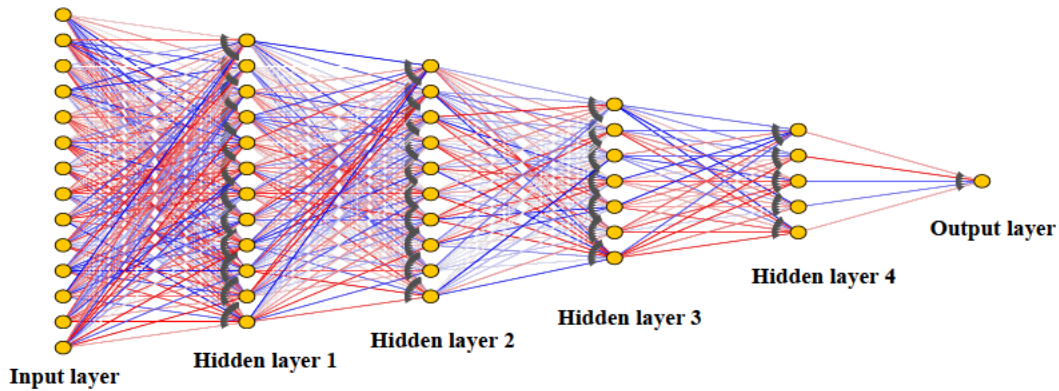


Fig. 3.3 A multilayer layer perceptron model. The colours in edges represent their weights.

Convolutional neural networks Convolutional neural networks (CNN) are another type of feedforward neural network that relies on kernel convolution to extract features from matrices. In kernel convolution, as shown in Figure 3.4 and Equation (3.3), filters or kernels are multiplied with an input matrix by striding through it, to extract a certain kind of feature depending on the weights in the kernel.

$$G[x, y] = (f * h)[x, y] = \sum_j \sum_k h[j, k] f[x - j, y - k] \quad (3.3)$$

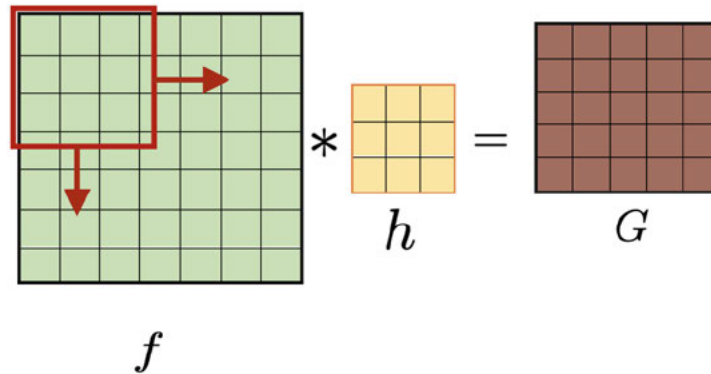


Fig. 3.4 Kernel convolution, where the kernel h is multiplied with the input matrix f by striding through it to generate a feature map G .

In a CNN, multiple such convolutions are carried out on input data using multiple filters. Outputs from which are further propagated through multiple layers of higher-level feature extraction through further convolutions, aggregation of features and non-linear mapping [61]. In most of these networks, feature aggregation is carried out

in addition to convolution using max-pooling and global pooling. In max pooling, a given input matrix is downsized, just like convolution, but the values in the output are maximum values in the search areas corresponding to the kernel, striding through the input matrix. In global pooling, the entire input matrix is downsized to a single value, which could either be the average or maximum of the values from the input matrix. At the end of these networks, features extracted through the above multiple layers are passed onto an MLP like dense layers, formally known as fully connected layers, to perform classification or prediction. Figure 3.5, shows a typical CNN consisting of multiple layers of convolutions, pooling and finally coupling with fully connected layers to perform any given task.

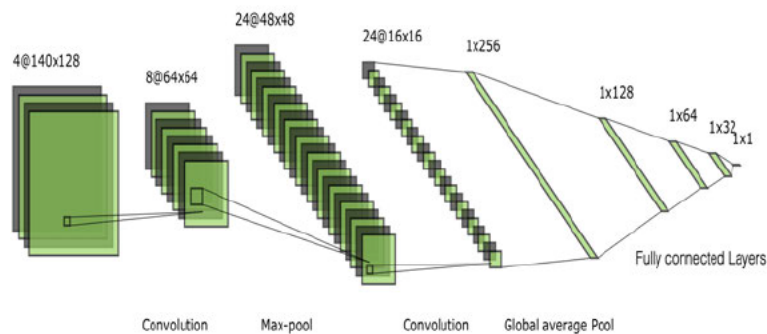


Fig. 3.5 A typical convolutional neural network

CNNs are widely used for applications involving images. Thus, for biomedical applications involving scans of a patient, CNN's can provide good levels of efficacy [55].

Training feed forward neural networks In training, the weights and biases of a neural network are optimised with the help of training data in order for the network to perform any given task. To begin, the weights and biases of any neural network are first initialised. Initialisation may be carried out using methods such as,

- **Constant initialisation**, where all weights or biases are initialised to a constant value. Popularly, the value is chosen to be 1.0.
- **Random initialisation**, where the weights or biases are initialised using sample drawn from distributions such as uniform and normal distributions.

Once initialised, the outputs generated by the network for input training data are compared against expected output. Quantification of the error between the predicted output and the expected output is carried out using loss or cost functions (C) such as absolute mean error

$$C = \frac{1}{n} \sum_{i=1}^n |y_i - \hat{y}_i| \quad (3.4)$$

and mean squared error

$$C = \frac{1}{n} \sum_{i=1}^n (y_i - \hat{y}_i)^2, \quad (3.5)$$

where y , \hat{y} and n are the predicted value, expected value and number of training samples respectively, for applications such as prediction, where numerical output is required. For applications such as classification where probabilities are involved, cost functions such as binary cross-entropy

$$C = \frac{1}{n} \sum_{i=1}^n [y_i \log(\hat{y}_i) + (1 - y_i) \log(1 - \hat{y}_i)] \quad (3.6)$$

is used. In Equation (3.6), y is the expected label, a 0 or 1, and \hat{y} is the calculated value, which in practice lies between 0 and 1. The output from cost functions is then used to optimize the weights and biases.

Popularly neural networks are trained using backpropagation, a technique that uses simple chain rule to optimise weights and biases, however, various other optimisation algorithms such as extended Kalman filter [62], difference target propagation [63] also are available to train neural networks. In this thesis, all neural networks are trained using backpropagation. In this algorithm, the derivatives of the cost function with respect to weights and biases in the last layer is used to propagate and consequently optimise weights and biases, using the chain rule, of the previous layers, extending back up to the first hidden layer (the one after input layer). For example in the output layer,

$$\frac{\partial C}{\partial w_n} = \frac{\partial C}{\partial \sigma} \frac{\partial \sigma}{\partial z} \frac{\partial z}{\partial w_n} \quad (3.7)$$

where C is the cost, w_n are the weights in the output layer, z is the output from the output layer (prior to output activation) and σ is the output activation.

The steps followed in backpropagation could be generalised as:

Calculate the derivatives of the cost function with respect to weights and biases in the output layer.

↓

Calculate the derivatives of the cost function with respect to weights and biases in the hidden layer before the output layer.

↓
⋮

Calculate the derivatives of the cost function with respect to weights and biases in the first hidden layer after the input layer.

The gradients calculated in this manner are then used by algorithms, known as optimisers, such as Adam [64] and stochastic gradient descent (SGD), to update the weights and biases.

Further, training of neural networks involves the usage of multiple techniques and methods to optimally train the network to prevent problems such as overfitting and increase the overall performance of neural networks. Overfitting is a condition where the network is optimised strongly with respect to the training data such that their performance drops when inputs not in the training dataset are given. Generally, the training dataset is divided into training and validation subsets. Neural networks are trained on the training subset and concurrently tested using the validation subset, monitoring of losses between the two subsets allows for tracking of the networks' performance. This allows for monitoring of networks for overfitting and allows for early stopping of training if required. To prevent overfitting, apart from early stopping, multiple methods such as regularisation, K-fold cross-validation are also available. In this thesis, multiple methods and various combinations of parameters have been used to train neural networks for different applications. The particular configuration of neural networks and their respective configurations used during training in each instance have been provided.

Recurrent neural network Recurrent neural networks are a class of neural networks designed to handle sequential data such as time series. In each recurrent cell, the building block for this type of neural network, the input for each sequential step is concatenated with the cell's output from the previous step (as shown in Figure 3.6). This type of close-looped architecture allows for these networks to perform dynamically in any given sequential input.

In biomedical applications, these networks are best suited for places where time series data are generated such as signals (ECG, ABP etc., as explained in the beginning of this chapter).

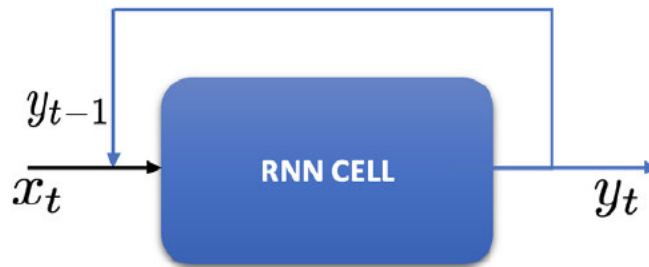


Fig. 3.6 A Recurrent Neural Network (RNN) cell where the output from previous step is concatenated with input for the current step in a sequence.

Long Short-Term Memory (LSTM) A simple recurrent neural network, using cells as shown in Figure 3.6, performs well for applications where long term dependencies in sequence are not involved. In other words, short sequences are well handled by simple or regular RNN cells. However, when long-term retention of features in a sequence are required for such cells to perform, a modified form of RNN cell known as Long Short-Term Memory (LSTM) [65–67] cell is required.

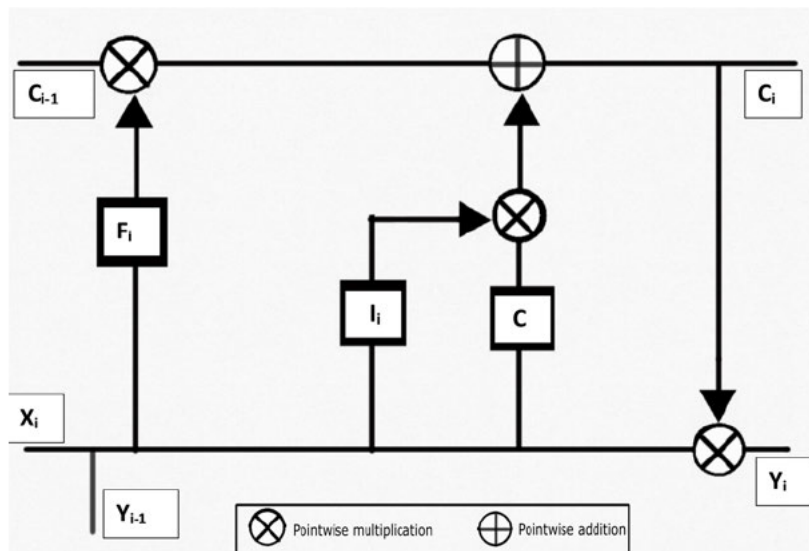


Fig. 3.7 A Long Short-Term Memory (LSTM) Cell.

In LSTM a cell state is introduced, which is a parallel flow of data within a cell. It allows for certain information to be carried in parallel to actual data to track various dependencies between elements. In Figure 3.7, the cell state (C_i) is passed through the upper channel and a concatenated signal, consisting of input from the current step

(X_i) and output from the previous step (Y_{i-1}) , is passed through the lower channel. Gates F_i , I_i and C are used to learn from previous steps and predict the next one. Each of these gates refers to a combination of neural layer connected to the cell state through a logical operator or combination of logical operator and other gates. Based on the logical operation carried at the end of their respective neural layer, gates can be identified for their functions such as to forget, retain, select or modify cell state which in turn affects the output value.

Transfer learning

Many times, in biomedical research, a minimal amount of data is available or is generated at the sites of research, for example in a rare or novel disease. Developing deep learning based applications in such situations is very hard as deep learning needs vast amounts of data during training. To alleviate, a concept known as transfer learning is adopted. In this method neural networks pre-trained on data, in most of the cases similar to the desired application, are adopted and re-trained on the available small amounts of data. In this way, a lot of features present in the current data are already identified and smaller novel features, specific to the current data are extracted.

3.1.2 Unsupervised learning

In unsupervised learning, unlabelled data is provided, upon which an analysis is carried out without any guidance. This form of learning is widely used for the analysis and identification of data. This kind of learning is in general carried out using either clustering or dimensionality reduction.

- In **clustering**, data points similar to one another are grouped or clustered. These algorithms are used for applications such as big data analysis. In this form of unsupervised learning, three widely used algorithms are:
 - K-means
 - Hierarchical clustering
 - density-based clustering
- **Dimensionality Reduction** is used to detect patterns within the provided data. This form of analysis is widely used for applications such as object or face detection and big data visualisation. Widely used dimensionality reduction algorithms include:

- Independent Component Analysis (ICA)
- Self Organising Maps (SOM)
- Principal Component Analysis (PCA)

3.2 Application : An AI based digital-twin for prioritizing pneumonia patient treatment

In this section, a data-driven digital twin based three-tiered system is proposed to prioritise patients for urgent intensive care and ventilator support. The deep learning methods are used to build patient-specific digital-twins to identify and prioritise critical cases amongst severe pneumonia patients. The three-tiered strategy is proposed to generate severity indices to: 1) identify urgent cases, 2) assign critical care and mechanical ventilation, and 3) discontinue mechanical ventilation and critical care at the optimal time. The severity indices calculated in the present study are the probability of death and the probability of requiring mechanical ventilation. These enable the generation of patient prioritisation lists and facilitates the smooth flow of patients in and out of Intensive Therapy Units (ITUs). The proposed data-driven digital-twin is built on pre-trained deep learning models using data from more than 1895 pneumonia patients. The severity indices calculated in the present study are assessed using the standard benchmark of Area Under Receiving Operating Characteristic Curve (AUROC). The results indicate that the ITU and mechanical ventilation can be prioritised correctly to an AUROC value as high as 0.89. This model may be employed in its current form to COVID-19 patients, but transfer learning with COVID-19 patient data will improve the predictions. The digital-twin model developed and tested for this application is available in a public repository, that can be found [here](#).

The COVID-19 pandemic [68] put an unprecedented stress on the already strained healthcare infrastructure [69, 70]. This situation forced the healthcare providers to prioritise patients in critical need to access Intensive Therapy Units (ITU) and mechanical ventilation. Some of the currently used scoring systems for patient prioritisation include SOFA (Sepsis-related Organ Failure Assessment) [71], APACHE (Acute Physiology and Chronic Health Evaluation) [72], and SAPS II (simplified acute physiology score) [73]. These systems have been validated over time for analysis of intensive care treatments [74–77]. In recent past, several works have been published on severity scoring using neural networks and other machine learning algorithms [78–80]. Majority of these

algorithms were trained on large ITU datasets to calculate severity scores, covering a wide range of diseases and medical conditions. Such systems, though valuable during normal times, may not be sufficiently specific to address the COVID-19 pandemic. In the case of COVID-19 (and in other similar forms of influenza), more precise and dynamically evolving system may be necessary to address the sudden increase in severity and the need for mechanical ventilation. With more mutations of the virus being identified over time [81], an evolving knowledge of the disease severity of each virus variant has become extremely important. A robust and dynamically adaptable model that takes into account the progression of severity over the course of care, which may be different for different variants of the disease, is therefore needed.

A data-driven digital twin can provide real-time feedback on how patients are likely to behave based on their current known condition using periodic input data from the patient's vitals (such as heart rate, respiration rate). The severity scores calculated by these models can form the basis for prioritising potential pneumonia patients for ITU and mechanical ventilation. The three-tiered strategy of identify,

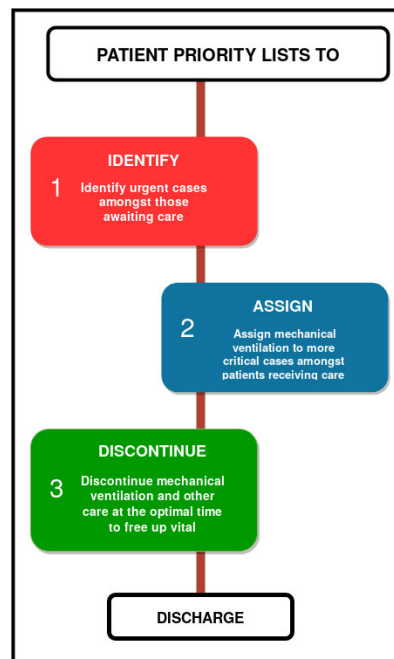


Fig. 3.8 Three tiered patient prioritisation strategy to reduce mortality rate in intensive care units.

assign and discontinue, as shown in Figure 3.8, is employed in this application to produce a patient priority list. The three-tiers are: 1) identify urgent cases amongst those awaiting care, 2) assign mechanical ventilation to critical cases amongst patients

receiving care, and 3) discontinue mechanical ventilations and other care at the optimal time, thereby freeing-up vital resources. In this application, each of these steps are enabled by artificial neural network models, a type of artificial intelligence system, that are well established for complex diagnosis with unprecedented levels of accuracy [82–85]. These methods require significant amount of data for training and testing. However, acquiring, de-identifying and indexing huge amounts of COVID-19 patient data from ITU is currently challenging. Hence, to expedite progress, a transfer learning [86] approach may be adopted. In such approaches, as explained in Section 3.1.1, artificial neural networks are trained using large amounts of data from similar backgrounds to that of COVID-19. The trained model can be bolstered with smaller amounts of COVID-19 data, when available, to improve accuracy. Since the background data used here is from pneumonia patients, the model proposed should be representative of severe COVID-19 patients. All the artificial neural networks used in the three tiers of Figure 3.8 together forms an individual patient’s digital-twin system.

3.2.1 Methodology

An interconnected system, comprising multiple independent neural networks, designed to assist a concerted decision making process, is proposed. Independent severity indices are calculated at the three tiers shown in Figure 3.8 to assist in identifying cases that are severe but with a high chance of survivability. The indices used in each of the tiers are as follows (see Figure 3.8):

- (i) Tier One, Patients awaiting intensive care - (a) Difference between probabilities of death with and without mechanical ventilation support and (b) Probability of requiring mechanical ventilation.
- (ii) Tier Two, Intensive care inpatients awaiting mechanical ventilation support - (a) Probability of death (based on data from continuous monitoring of vitals), (b) Probability of requiring mechanical ventilation support (based on data from continuous monitoring of vitals) and (c) Severity indices used in Tier One.
- (iii) Tier Three, Discontinuation of mechanical ventilation support amongst inpatients - (a) Probability of requiring mechanical ventilation support (based on data from continuous monitoring of vitals) and (b) Probability of death (with consideration of mechanical ventilation data).

Within each tier, based on probabilities calculated, thresholds can be set by the ITU professionals for decision making. Independent severity score thresholds can be set within each tier to allow situations in which different stages of ITU care may be needed at different healthcare units or settings (Example - A patient moving from one hospital to another).

Data Selection and Pre-Processing

Primary sources of data used in this application are from MIMIC-III [87][88] and eICU Collaborative Research Database v2.0 [89] [90], obtained from PhysioNet [91]. MIMIC III is a publicly-available database comprising de-identified health-related data associated with approximately sixty thousand admissions of patients who stayed in critical care units of the Beth Israel Deaconess Medical Center between 2001 and 2012. eICU Collaborative Research Database v2.0 is multi-center database comprising de-identified health data associated with over 200,000 admissions to ITUs across the United States between 2014-2015 (see Table 3.1). Both of these databases consist of various vital sign measurements, de-identified information on patient stay, diagnosis information, records of medical procedures carried out, drugs administered and various other intensive care information.

Since severe COVID-19 patients suffer from pneumonia [92], the selection and aggregation of data here is based on critical symptom of pneumonia. Therefore, various subsets of MIMIC-III and eICU databases with pneumonia are chosen for training. All patient data with missing vital information are ignored. The subsets chosen are:

- (a) Pneumonia Mortality subset - Patients who suffered from any form of pneumonia. This subset included both survived and died cases at the time of discharge.
- (b) Pneumonia Ventilator subset - This consists of all survived patients at the time of discharge, but suffered from some form of pneumonia.

In the case of MIMIC-III database, a total of 493 ITU stays of pneumonia patients were considered. Patient data with available matching and admissible quality waveform data (collected from MIMIC-III matched waveform subset) were considered. Out of which, 211 (42.79%) stays required mechanical ventilation and 95 (19.26%) stays resulted in death.

Table 3.1 Baseline characteristics of subset selected from eICU Collaborative Research Database v2.0

Overall population, n=1895	
Age	68 [56-79]
Gender(Male)	994
On Mechanical ventilation	1155 (60.94%)
HR (bpm)	112 [98-128]
MAP(mmHg)	62 [51-123]
RR (cpm)	33 [25-41]
Na (mmol/l)	138 [133-141]
Glucose (mmol/l)	146 [96-201]
WBC ($10^3/mm^3$)	9.7 [5.33-15.06]
PaO_2/FiO_2	1.66 [1.12-2.37]
Bilirubin (mg/dl)	0.6 [0.4-0.9]
Dead	230 (12.13%)

Neural Networks and Architecture

The proposed three-tiered system is constructed primarily using multiple independent neural networks. However, the type of neural networks used can be classified into two categories, Multilayer Perceptron (MLP) and Recurrent Neural Networks (RNN). Artificial neural networks may be used to perform functions such as classification and prediction. As explained in Section 3.1.1, MLP models use a series of cascaded non-linear transformations of weighted coefficients, as shown in Figure 3.9 (a), to perform these functions. The MLPs typically accept discrete values as inputs. In the case of patient data, some examples of discrete inputs are patient gender, blood glucose level and sodium levels. These input values can be used to calculate the probability of death and the probability of a patient requiring mechanical ventilation.

In ITU, waveforms (time series) of body vitals measured are examples of sequential input. In order to predict or classify patients, LSTM cells (explained in Section 3.1.1) are designed to ‘retain’ and/or ‘forget’ parts of input data sequence(s). These abilities make them the appropriate choice of neural networks to calculate severity indices and assess patient criticality continuously or at regular time intervals. The RNN based models used in this application use a combination of sequential and discrete value inputs. As seen in Figure 3.9 (b), a combination of LSTM cell layer and additional MLP model is used to predict severity index of interest using fully connected neural layers. All models were built using Tensorflow library [93], using Keras [94] library, on Python.

Table 3.2 Baseline characteristics of subset selected from MIMIC-III [87][88]. Note: Since every field in this table is not measured for the entire population of the subset, the 95% CI provided in the brackets are representative of only those patients in whom the respective field was measured and recorded.

Overall population, n=493	
Age	67 [66-69]
Gender (Male)	264
HCO ₃ (mmol/l)	23 [22-25]
Carboxyhaemoglobin (%)	2.34 [1.51-3.17]
Chloride (mmol/l)	102 [100-104]
Calcium (mmol/l)	1.10 [1.04-1.07]
Glucose (mg/dL)	154 [143-165]
Hematocrit (%)	33 [32-34]
Haemoglobin (g/dL)	11 [10.54-11.46]
Lactate (mmol/l)	1.88 [1.72-2.05]
Methemoglobin (g/dL)	0.38 [0.21-0.56]
K (mmol/l)	4.05 [3.93-4.18]
Na (mmol/l)	136 [134-139]
Temperature (°C)	36.73 [36.52-36.95]
On Mechanical ventilation	211 (42.79%)
FiO ₂	0.68 [0.64-0.72]
SO ₂ (%)	86 [84-88]
PCO ₂ (mmHg)	39 [37-40]
PEEP (cmH ₂ O)	6 [6-7]
Ph	7.31 [7.30-7.33]
PO ₂ (mmHg)	114 [104-123]
O ₂ flow (lpm)	14.21 [8.11-20.31]
Tidal volume (mL)	505 [488-523]
Dead	95 (19.26%)

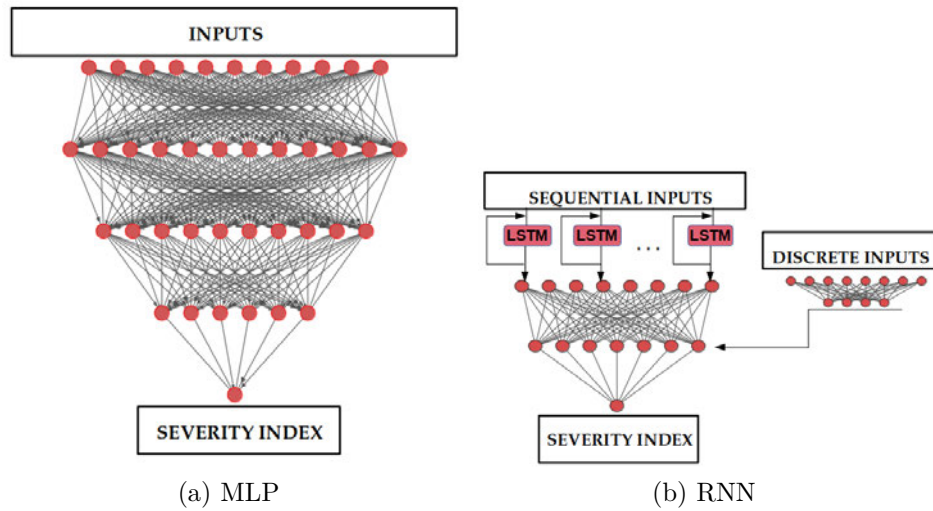


Fig. 3.9 Multilayer Perceptron (MLP) and Recurrent Neural Networks (RNN) for calculating severity indices.

The MLP Models consisted of three dense hidden layers. These layers are non-linearly activated using Rectified Linear Unit (ReLU) functions. Depending on the severity index to be predicted, the input layer consisted of 21-22 input parameters. As the final value being predicted in these models is a single value between 0 and 1, an output layer with single neuron and sigmoid activation is used. Detailed architecture of MLP models and training parameters are provided in Appendix A.

In the case of RNN based models, sequential input data is processed by a network model with single or double LSTM layer(s). These layers use input arrays with 8 input parameters. Discrete inputs are processed by an independent network model with a 21-26 input parameters, depending on the severity index. The outputs of these networks are then merged and fed to final model activated with 'ReLU' functions. Similar to the MLP models, the final model has an output neuron with sigmoid activation. Dropouts and activity regularizers, were used in these models to avoid over-fitting. A detailed description of RNN based model architectures and training parameters have been provided in the Appendix A.

The discrete input data was standardised within a similar range. All MLP models were trained and cross-validated on data subsets chosen from eICU Collaborative Research Database v2.0. All RNN based models were trained on the MIMIC-III database, owing to the waveform datasets available in them. Datasets were split into training (80%) and testing dataset (20%). Cross-validation of models were carried out on the training to tune the hyper parameters and analyse model performance using

K-fold method, for which the training dataset was divided into 10 folds. The K-fold validation method splits the training dataset into K-folds or K bins, from which one of the folds is held out for validation and the remaining folds are used for training. The neural network is independently trained K times, one for each fold held out as the validation fold. The results obtained by training over K cycles are averaged to analyse model performance and tune the hyper parameters. The final model selection is based on best accuracy obtained for the testing dataset, which is never used during training.

Tier One-"Identify": Identification of ill patients amongst those awaiting intensive care

Since this class of patients are not monitored continuously, data obtained within 24 hours of hospital admission is used. A subsystem of two MLP models were trained on a subset containing pneumonia patient data from eICU Collaborative Research Database v2.0 database. One was used to predict the probability of death, and the other for calculating the probability of requiring mechanical ventilation.

The first model was trained on ‘Pneumonia mortality subset’, consisting of 1895 patients and the second model was trained on ‘Pneumonia ventilator subset’, consisting of 1665 patients. The twenty input fields chosen for the first MLP are age, gender, ventilation status (a binary value), intubation status (a binary value), dialysis status (a binary value), heart rate, respiration rate, Glasgow coma scale, white blood cells (WBC) count, blood glucose levels, PaO_2 , $PaCO_2$, mean blood pressure, body temperature, sodium, potassium, bicarbonate, bilirubin, FiO_2 , chronic diseases (Metastatic cancer, AIDS or Haematologic malignancy) and Blood Urea Nitrogen (BUN) levels. These inputs are also used by APACHE IV scale. The second MLP for predicting probability of requiring mechanical ventilation used the same input parameters as the first except for ventilation status, which is now added as additional parameter. To remind the reader, the data set used for this model consists of only patients who survived at the time of discharge. Thus, the training criteria should include mechanical ventilation support data to successfully discharge the patient alive.

Using the predicted severity indices, a patient priority list may be generated to admit patients with more urgent need for care into ITU. Since mechanical ventilation is the indication of severity in COVID-19 patients, probability of requiring mechanical ventilation is the primary severity index in preparing such a list. The patients with similar probabilities of requiring ventilation are prioritised using difference between probabilities of death, with and without ventilation. The probability of death with

mechanical ventilation may also be used to further refine the prioritisation list. The prioritised patients in Tier One may be admitted to the ITU and the prioritisation list may be further refined in Tier Two for providing mechanical ventilation.

Tier Two-"Assign": Identifying and providing mechanical ventilation support amongst intensive care patients

The patients selected from Tier One to go into ITU can now be continuously monitored. However, with limited number of mechanical ventilators it becomes a necessity to provide this support to the more urgent cases. To identify urgent cases amongst the inpatients in an ITU, a continuous monitoring based severity index is required. The primary severity indices used here are probability of requiring mechanical ventilation support (based on continuous monitoring) and Probability of death (based on continuous monitoring). The RNN based model shown in Figure 3.9 (b) is used to predict these severity indices. The sequential (continuous) inputs used here are heart rate, pulse, systolic and diastolic blood pressures, respiration rate and SpO_2 , in addition to multiple discrete input fields[95], AADO2 (alveolar-arterial difference of oxygen partial pressure), HCO_3 , carboxyhaemoglobin, chloride, calcium, base excess, glucose, haematocrit, haemoglobin, sodium, potassium, SO_2 , FiO_2 , PO_2 , methemoglobin, temperature, age and gender. The lowest measured discrete input value in a 24 hour period is used in the training. A direct allocation of ventilation support at the first tier is also possible when required.

Tier Three-"Discontinue": Identifying patients who can discontinue mechanical ventilation support

The patients identified in Tier Two to receive mechanical ventilation can now undergo continuous monitoring to decide when to discontinue treatment. The probability of requiring mechanical ventilation support (based on continuous monitoring of patient) and probability of death (considering continuous ventilation support) are used as the indices to safely remove the mechanical ventilation support. The RNN used in Tier Two with similar inputs is continued here to observe the probability of still requiring mechanical ventilation support. The patients with probability of requiring mechanical ventilation lower than a set threshold may be removed from the ventilator support. To reduce the risk of false negatives, probability of death is also monitored in this tier. An additional RNN based model is trained to take ventilator settings along with the inputs used in Tier Two to predict probability of death. The additional input fields

include PEEP, required O_2 and tidal volume. The person with probability of requiring mechanical ventilation less than the set limit must also have a probability of death lower than the set threshold limit to discontinue treatment.

3.2.2 Results and Discussion

All three tiers discussed in the previous section together form the digital-twin of a patient. A total of five independently trained neural network models take the measured patient vitals and provide various severity indices as output. All models in this application are designed with ease of use in mind. Many healthcare units lack the state of the art IOT (Internet of Things) based health monitoring systems or face issues with platform compatibility. Manual inputting of data, including time dependent sequential inputs, would be necessary in units where electronic recording capabilities are unavailable. Thus, all inputs are designed to allow manual intervention (see supplementary information). The MLP models are designed to take, the most severe value for each input field, within a 24 hour period. All RNN based models require two types of inputs, discrete input fields once every 24 hour period, that are most severe, and all sequential input fields such as heart rate, SpO_2 , and blood pressures at regular time intervals. These models inherently take note of time elapsed from the start of care and use latest data for calculating severity indices. The two patient databases used for training the models are explained in the previous sections (see for example Table 3.1).

Performance measures: All models, performing classification to calculate probabilities, are evaluated using the Area Under Receiving Operating Characteristic Curve (AUROC), reported with corresponding 95% confidence interval (CI). Receiving Operating Characteristic (ROC)[96, 97] curve is a probability curve. Performance is measured using the AUROC. It represents the degree of separability between classes. In the context of the present work, this separability represents the difference between severe and not so severe cases, for each severity index. Higher AUROC represents better performance. The parameters used to estimate AUROC are true and false positive rates. The graphs representing ROC are plotted for false positive rate (1-specificity) vs true positive rate (sensitivity). At AUROC of 0.5, the model loses its discrimination capacity to distinguish between classes. It is represented by a dashed diagonal line in the figures below for reference.

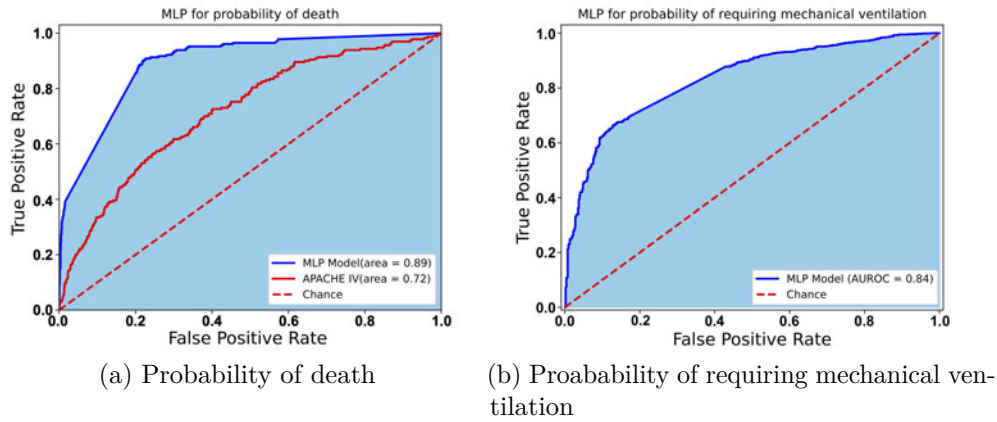


Fig. 3.10 AUROC (shaded area) curve for MLP models used to predict the probability of death and the probability of requiring mechanical ventilation support.

Tier One-"Identify"

Here, two MLP models are used to predict the probability of death and the probability of requiring mechanical ventilation using patient vital data, measured over a period of 24 hours. The AUROC obtained over the total dataset are respectively shown in Figures 3.10 (a) and (b). An AUROC of 0.89 (95% CI: 0.88-0.91) is obtained for the probability of death and 0.84 (95% CI: 0.82-0.86) is obtained for the probability of requiring mechanical ventilation. Cross-validated accuracy scores of 0.86 (SD: ± 0.005) and 0.70 (SD: ± 0.055), respectively, were obtained in these models on the training dataset. Furthermore, an accuracy score of 0.88 and 0.72 over the testing dataset. Figure 3.10 (a) also shows APACHE IV score with a predicted probability of death with an AUROC of 0.72. Thus, the proposed approach appears to be a substantially better predictor. The model shows that the probability of death and the probability of requiring ventilation with respectively 86% and 85% chances of accurate prediction. From the data computed, a patient prioritisation list for ITU admission may be created by calculating

- (a) Difference in probabilities of death with and without mechanical ventilation.
- (b) Probability of death with mechanical ventilation.
- (c) Probability of requiring mechanical ventilation support.

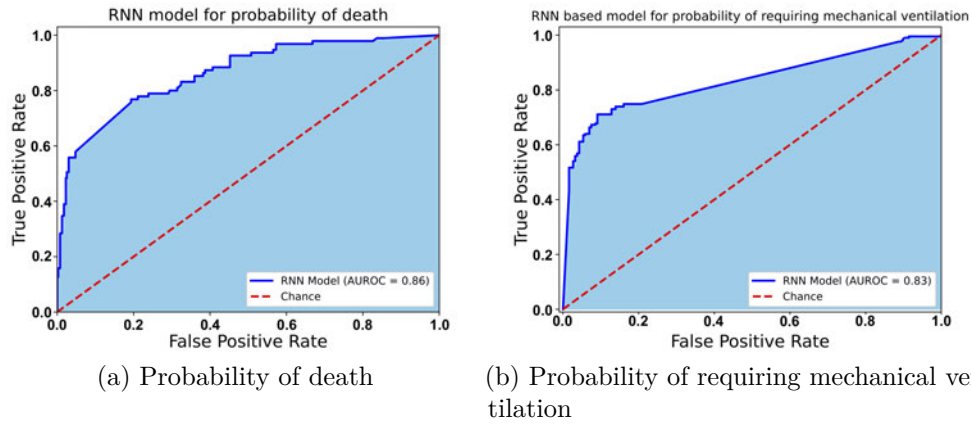


Fig. 3.11 AUROC (shaded area) curve for RNN based model results of the probability of death for patients and the probability of requiring mechanical ventilation support.

Tier Two-"Assign"

The inpatients within ITUs, whose vitals are continuously monitored, can be assessed for severity of lung disease periodically using the RNN model. As seen in Figure 3.11 (a), an AUROC of 0.86 (95% CI:0.81-0.90) is obtained from the model for the probability of death, over the entire dataset. The probability of requiring mechanical ventilation is calculated with an AUROC of 0.83 (95% CI: 0.79-0.86) as shown in Figure 3.11 (b). These models obtained a cross validated accuracy scores of 0.73 (SD: ± 0.04) and 0.74 (SD: ± 0.12) respectively. Furthermore, accuracy scores of 0.82 and 0.71 respectively were obtained over the testing dataset. This indicates that with continuous or regular inputs of measured vitals (heart rate, respiration rate, SpO_2 and blood pressures) and discrete inputs such as Haemoglobin, WBC, and sodium, need for mechanical ventilation can be identified with 83% chance. This calculation can be continued into Tier Three to discontinue ventilation as demonstrated below.

Tier Three-"Discontinue"

For patients in ITU an approach for the probability of death must be calculated by including the mechanical ventilation. Unlike the RNN based model used in Tier Two, the model here includes mechanical ventilator settings along with the other inputs to calculate the probability of death. As seen in Figure 3.12, the model performed classification with an AUROC of 0.89 (95% CI: 0.85-0.93) over the entire dataset. This model obtained a cross validated accuracy score of 0.81 (SD: ± 0.025) and testing

accuracy score of 0.80. This severity index is required to support the probability of still requiring mechanical ventilation support. A combined analysis of probability of requiring mechanical ventilation support and death is necessary to reduce the chances of erroneous decisions of early removal of support. If both indices are substantially low, the mechanical ventilation may be discontinued.

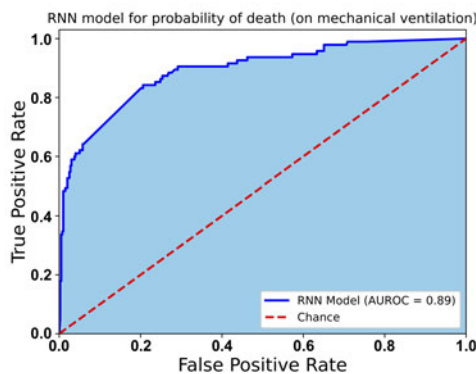


Fig. 3.12 ROC curve for RNN based model used to predict probability of death for patients in Tier Three

Comparison with other existing machine learning based models

As explained in Section 3.2, multiple machine learning based models exist in literature [78–80, 98, 99] for severity scoring. However, most of these models are designed or trained on larger patient datasets or for conditions other than pneumonia, thereby making them less suitable as a base upon which a prioritisation system can be built for patients with pneumonia-related characteristics, similar to those seen in COVID-19 patients. Nevertheless, these models may provide added benefits to clinicians if different or additional severity scoring is required as a result of non-pneumonia complications. Therefore, a comparison between the above proposed digital twin and some of the existing models is carried out here to provide a brief overview of their functionality. Ye *et al* [98], proposed a knowledge-guided CNN (Convolutional Neural Network) which predicted mortality in critically ill patients with diabetes with an AUROC of 0.97. This model used Unified Medical Language System (UMLS) resources and clinical notes as input. In the case of COVID-19, with diabetes patients at a higher risk of ICU admission [100], this model could be used as an additional tool for patient prioritisation in high patient volume areas. Barbieri *et al* [79], benchmarked the use of RNNs as well as attention-based networks for predicting readmission to the ICU within 30 days of

discharge, with the highest achieved AUROC of 0.739. This type of prioritisation adds well to the Tier-3 of the proposed digital twin. Since Tier-3 models predict the removal of mechanical ventilation support, this type of prioritisation based on readmission to ICU can assist clinicians in deciding discharge. Further, prediction of hospital length of stay using machine learning models, trained on larger patient datasets, has been proposed by Gentimis *et al* with an accuracy of 80%. An alternative for mortality prediction using a Super Learner Algorithm, known as Super ICU Learner Algorithm (SICULA), which has outperformed traditional SOFA and SAPS II score, was proposed and made available by Pirrachio *et al* [80]. SICULA predicted probabilities of death with a cross-validated AUROC of 0.85-0.88.

3.2.3 Conclusion

The digital-twin system proposed in the present study to construct a subject-specific digital twin appears to provide better results than existing scoring methods. Although the data used to train the models is for non-COVID-19 patients with pneumonia, the similarity of the data to COVID-19 patients appears to be strong. The symptoms, severity, the type of intensive care required and provided and the necessity of mechanical ventilation during care are fairly similar between pneumonia patients and COVID-19 patients. Thus, the proposed digital twin can be used as a starting point to further refine the scoring system. Overall, the accuracy of prediction is satisfactory with a minimum AUROC of 0.8 in all cases. By adapting transfer learning on emerging COVID-19 data, this accuracy may be substantially enhanced for severe COVID-19 patients.

The code used in this work is open to everyone to download, that could be found [here](#), and train on additional data. With further refinement by the community and our own research group, we believe that the model will serve the healthcare community to deal not only with the COVID-19 pandemic but any future influenza patient prioritisation.

3.3 Summary

This chapter provides an overview of state-of-the-art artificial intelligence and introduces the machine learning algorithms used in this thesis. Different types of algorithms described in this chapter will be employed in subsequent chapters for building different forms of digital twins for the cardiovascular system. In the second half of the chapter,

some of the machine learning algorithms explained are employed in developing a data-driven digital twin which will help in the three-tiered prioritisation of ITU care for pneumonia patients. This purely data-driven digital twin explores the concept of a digital twin that purely relies on artificial intelligence, unlike the different forms of digital twins proposed in the subsequent chapters which incorporate computational mechanics. The machine learning algorithms used in this twin are trained on ITU patient data from publicly available databases (eICU Collaborative Research Database v2.0 and MIMIC-III). The overall accuracy of prediction for patients' severity with this twin is satisfactory with a minimum AUROC of 0.8 at all levels of patient prioritisation.

Chapter 4

Passive Digital Twin

In this chapter, the first type of human digital twin, the passive digital twin, is explored through an application for calculating Fractional Flow Reserve (FFR). Passive digital twins are useful for offline analysis of any organ system and have no active components. The example presented in this chapter exemplifies offline geometrical and physiological replication of coronary artery system for calculating Fractional Flow Reserve (FFR), which provides the functional relevance of coronary atheroma.

The FFR guided strategy has been shown to reduce unnecessary stenting, improve overall health outcome, and to be cost-saving. The non-invasive, coronary Computerised Tomography (CT) angiography-derived FFR (cFFR) is an emerging method in reducing invasive catheter based measurements. This CFD based method is laborious as it requires expertise in multidisciplinary analysis of combining image analysis and computational mechanics. In this chapter, we present a rapid method, powered by unsupervised learning, to automatically calculate cFFR from CT scans with no manual intervention.

The chapter begins with an introduction to fractional flow reserve and a brief overview of published research in this field. Subsequent sections describe unsupervised geometry extraction from CT scans, mesh generation and computational haemodynamics used to calculate the FFR. The results obtained using the proposed method on CT scans from a cohort of 25 patients are presented and explained at the end of this chapter.

4.1 Introduction

In 2019, 218,032 people in the UK were affected by Coronary heart disease (CHD) and a 63,237 people died as a result of it [101]. These figures, however, reflect public health before the onset of COVID-19 pandemic. The living conditions as a result of this pandemic has in fact increased the risk of mortality. In Great Britain, 9 in 10 coronavirus deaths had a pre-existing condition and CHD was one of the most common ones [102]. Further, with over 7.6 million living with cardiovascular diseases in the UK and ever growing waiting lists, stress on healthcare is expected to increase astronomically. A rapid and automatic screening for functional relevance of coronary stenoses is one of the potential solutions for easing this situation. With such screening, patients with advanced deterioration of coronary haemodynamic state can be prioritised, thereby reducing mortalities.

Until recently, Coronary Computerised Tomography Angiography (CCTA) was the widely adopted screening tool for Coronary Artery Disease (CAD). However, detection of lesions and their severity, on its own, is insufficient to determine their functional relevance in oxygen supply to the cardiac tissue. Currently, invasive coronary catheter angiography-based measurements of Fractional Flow Reserve (FFR) has become the gold standard for the functional assessment of coronary artery obstructive lesions. The care planning, based on FFR, has shown to reduce unnecessary stenting and improve overall health of the patient.

Although measuring FFR is beneficial, invasive nature involved has its challenges. In terms of procedure, time involved and expertise required makes it an extremely laborious and slow procedure. A risk of failure, sometimes fatal in nature, is also present in this procedure. About 0.05% patients lose their life as a result of catheterization, due to complications such as vessel rupture and internal bleeding [103]. To reduce challenges in determining FFR values, a non-invasive CCTA based FFR (referred to simply as cFFR) calculation procedure has been proposed as passive digital twin to analyse the functional relevance of obstructive coronary lesions [104]. This approach, through mathematical modelling and computer simulation, integrates anatomical and physiological information. Until now, the majority of the approaches that use computational modelling incorporate semi-automated algorithms to segment the patient-specific coronary geometry. The blood flow simulations are conducted on the extracted geometry and the boundary conditions are calculated using patients' physiological conditions. These boundary conditions are usually expressed in terms of prescribed

flow rate and pressure at the proximal and distal interfaces created when isolating the vessels in the coronary network. There exist several cFFR approaches [104–115] which include

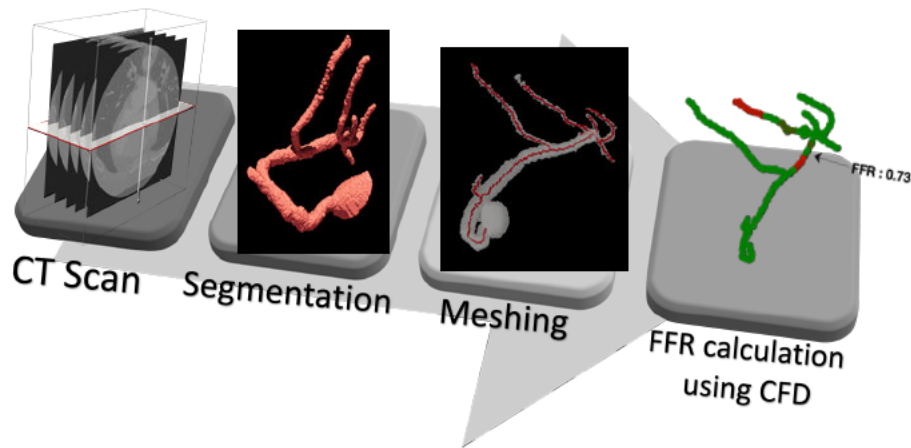


Fig. 4.1 Workflow proposed in the present work for automatic calculation of FFR from a CT Scan.

The critical components for cFFR are, (i) extraction of geometry from Computerised Tomography (CT) scan and (ii) selection of boundary conditions and CFD calculations. In order to obtain these components automatically, a three step process with CT scan as the input and calculated FFR as the output is presented in this work (see Figure 4.1). Firstly, to identify and segment coronary arteries from CT scans, an unsupervised-clustering based method is proposed alongside image filtration. Secondly, to extract geometrical values such as radii and centreline from the segmented geometry for mesh generation, another unsupervised method is proposed. Finally, to run blood flow simulations a coupled 1D-0D blood flow model is employed. The Table B1 in Appendix B lists all steps and sub-steps of the proposed automatic procedure. Following three sections respectively explain geometry extraction, meshing, CFD calculations and their integration. Section 4.5 provides detailed discussion on the performance of the automated cFFR calculation. Finally, Section 4.6 summarises the conclusions derived.

4.2 Geometry of coronary arteries

Computerised tomography (CT) scan, usually recorded in DICOM format, consists of a set of cross-sectional images taken along a patient's longitudinal axis. These slices,

usually two-dimensional grayscale images, use regions of different grey intensities to display various internal organs and tissues (Figure 4.1). A form of this scan, known as Coronary Computerised Tomography Angiography (CCTA) is used to image the blood supply to the heart. These scans are employed in the present work to extract the geometry of the coronary arteries. The extracted arteries are used in simulating and analysing haemodynamics within them.

In the present work, data acquisition was carried out from the same site as that of Carson *et al* [112]. All procedures were carried out according to standard CCTA protocols. To moderate heart rate and improve image quality during scanning, Metoprolol (Beta-blocker) was administered intravenously for some patients. The tube potential used in the scans ranged between 100 - 120kV with prospective gating and zero padding. The prospective gating uses an electrocardiograph as a trigger to scan at a particular point in the cardiac cycle. The average in-plane pixel spacing was 0.458 ± 0.051 mm and the slice-spacing was 0.625 mm. The CCTA data was provided in an anonymised DICOM format. The data made available is analysed in this chapter for coronary geometry, primarily using segmentation and lumen size estimation.

4.2.1 Segmentation

Image segmentation is a widely researched topic in computer vision and machine learning [116][117][118][119]. The applications of segmentation, within medical imaging, cover most parts of the human body i.e, from arteries to bones, brain to lungs, and other organs [120]. Geometries obtained from segmentation play a vital role in the diagnosis and monitoring of fatal conditions and diseases, such as malignant tumours and vascular stenoses [121].

Methods for segmentation using traditional image processing techniques have been popular amongst researchers from the late 20th century. A number of methods using techniques such as Hessian based filtering have been widely adopted to segment coronary arteries [122-125]. However, lately, the supervised learning approach using deep neural networks has gained popularity [126]. The convolutional neural networks (CNN) hold the capacity to learn various features from images using cascading filters with non-linear mapping. These networks are trained on vast amounts of data, thus can segment scans without pre-processing to remove issues such as noise and leaks in the images. However, this method has two major drawbacks, i) requirement for vast amount of data and ii) manual segmentation and labelling during the training phase. There are methods such

as transfer learning [127] to reduce data requirement, but manual segmentation and labelling takes a lot of work hours.

To reduce the time taken, an unsupervised approach for segmentation is adopted in the present work. Here, using a density based clustering, voxels relating to the coronary arteries are clustered. A similar approach has been proposed by Li *et al* [128]. However, significant variation lie in our workflow. The objective here can be divided into three parts, i) Pre-processing - Identifying all coronary size regions ii) Clustering - Clustering of voxel centres with similar intensity that are close to each other, to form clusters of voxels iii) Identification - Identifying the correct clusters corresponding to coronary arteries. These three steps are elaborated in the following subsections.

Pre-processing

To begin with, slices of the scan are automatically cropped to focus on the cardiac region and subsequently refined with de-noising and thresholding processes (Figure 4.2). This allows for unwanted artefacts to be removed from the images and convert them into binary images. For de-noising, non-local means method [129] with parameters shown in Table 4.1 is adopted. This method removes noise from the images but preserves the different textures present in various regions, making it an optimal choice for CCTAs. The non-local means works on the principle of finding different regions, usually disconnected, in the image that have similar grey intensities and averaging the pixel intensity within these regions.

Table 4.1 Filter settings used in de-noising and Frangi filters for preprocessing of images.

Non-local means de-noising filter parameters		Frangi filter parameters	
Filter strength	2σ	α	0.5
Template window size	5	β	0.5
Search window size	7	γ	15

In Table 4.1, σ is the standard deviation of Gaussian noise, calculated using wavelet based estimator from scikit-image library [130, 131]. In the present work, it is assumed that the noise in images follows a Gaussian distribution.

Following denoising, Frangi filter is used to preserve critical vessel features in the images. Frangi filter, which is a Hessian based filter, calculates eigenvectors of the Hessian matrix to compute the similarity of different regions in a given image to vessels [132]. The values used for filter's sensitivity to deviation from a plate-like structure,

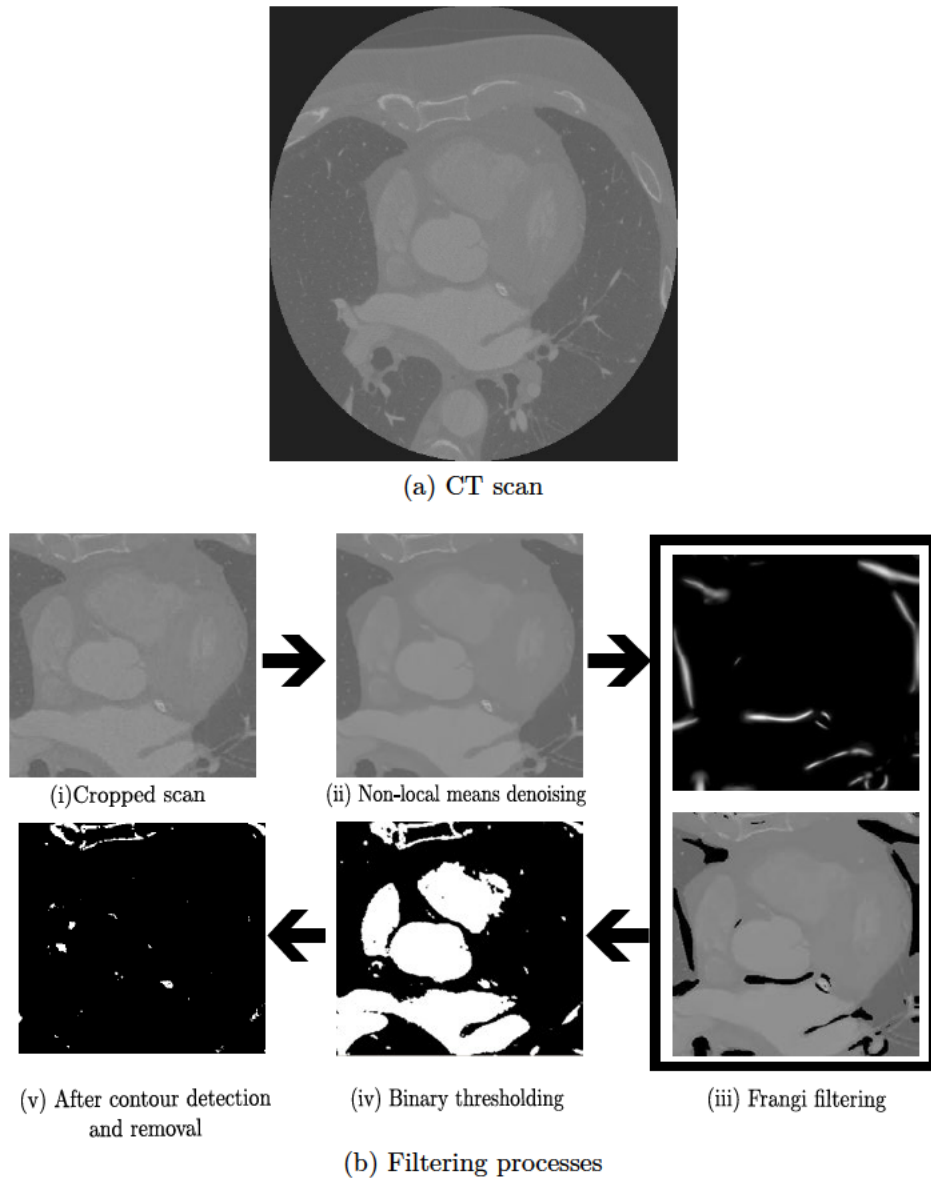


Fig. 4.2 Filtering processes carried out on each of the CCTA slices to extract pixels corresponding to coronary arteries. In subfigure [b], in clockwise order, Non-local means Denoising filtering, Frangi filtering, Binary thresholding, Contour detection and removal are carried out to extract parts of interest

represented by α , from a blob-like structure, represented by β , and its sensitivity to areas of high variance/texture/structures, represented by γ , are shown in Table 4.1. Filtered images are then subjected to global binary thresholding, in order to convert voxels with grey intensity above the selected threshold intensity value to white (255) and the rest to black(0). Following binarization, different regions in the images with white voxels are segmented using contour detection [133]. Countours corresponding to

components with area larger than the coronary are removed using an area threshold, which is set at 900 voxels. These steps allow for voxels corresponding to components in the size range of coronary arteries to be extracted. Figure 4.2 shows the entire pre-processing starting with cropping of the images.

Clustering

Before starting the clustering process, detection of aorta and coordinates of its centre is essential to calculate a spatial reference point. Such a reference point is later necessary to assist in identification of voxel clusters that belong to the coronary arteries. In order to detect aorta, hough circle transform [134] is chosen in this work (see Figure 4.3). This algorithm searches for circular regions in an image having radii within a prescribed range, using edges (regions of significant local change in the image intensity), detected with the help of canny edge algorithm [135].

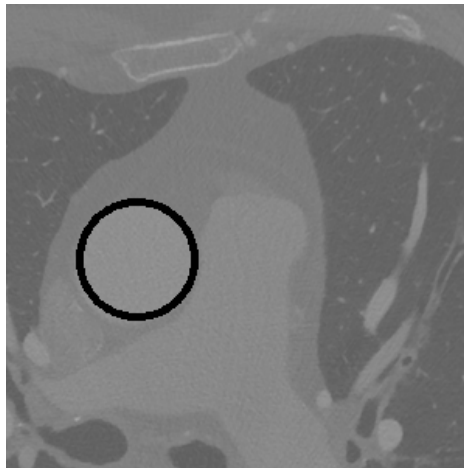


Fig. 4.3 Automatic detection of aorta using Hough circle transform. The detected aorta is encircled in black.

For this work, minimum radius to be detected is set to 25 pixels and max radius to be detected is set at 60 pixels. These values, chosen using trial and error, allow for the detection of only one circle closer to the heart. The centre of the detected circle is used as the reference point for cluster selection in the following subsection.

The filtered white voxels of the pre-processed image (with grey intensity of 255), need to be grouped in order to find different voxel clusters within the scan. In principle, two of these clusters will represent the left and right coronary arteries. Unsupervised method of clustering is one of the efficient and robust method to carry out such a grouping process. However, clustering works on the principle of grouping spatial points,

which in the case of voxels can only be represented by the voxel centres. Therefore, voxel centres are used as the spatial points here.

To perform clustering, many existing clustering algorithms are available, however, only those approaches that preserve the geometry of vessels be selected. The K-means, hierarchical and density based clustering, along with other variations of these methods, are a few of the widely used clustering algorithms. Amongst the three, K-means and hierarchical clustering are ill suited for our objective. In the K-means [136] clustering, a number of cluster centres are pre-selected, about which different points will be grouped iteratively. However, location for these cluster centres is usually chosen randomly. This is not preferable in our case as it allows for cluster centres to be selected outside the coronary arteries, which could lead to grouping of points that do not belong to the arteries or worse exclusion of those that actually belong to the arteries.

Further, in hierarchical clustering [137], nearby clusters are merged iteratively to create clusters at a higher level. The process starts with clusters of two points and then different clusters are merged iteratively based on their proximity to create clusters with increasing hierarchy. In order to get the clusters belonging to coronary, it is necessary to choose the correct hierarchy level. This selection is difficult to automate, especially if the scan contains discontinuities.

Thus, in the present work, a density-based spatial clustering of applications with noise (DBSCAN) [138], is adopted. This algorithm identifies clusters in an array of points based on their density in a given spatial region. Since points, representing centres of white voxels, corresponding to coronary arteries are densely packed, this algorithm is optimal to cluster them. Among the many clusters that emerge after DBSCAN clustering, two clusters will, in principle, represent the coronary geometry. In this algorithm, as shown in Figure 4.4, points that lie within each other's preset search radius, represented by ϵ , and also have a preset minimum number of points within this search area are grouped together (blue and grey points). Within such a group, points with more than preset minimum neighbouring points form the core points (blue points) and those which are reachable by the core points but have no further neighbouring points are considered outer points (grey points). Further, points with less than the preset minimum number of neighbouring points in the search area are considered as noise points (orange point).

For clustering of points belonging to the coronary arteries, ϵ , search radius, is chosen as 1.6 voxels and minimum points needed within the search area is chosen as 2.

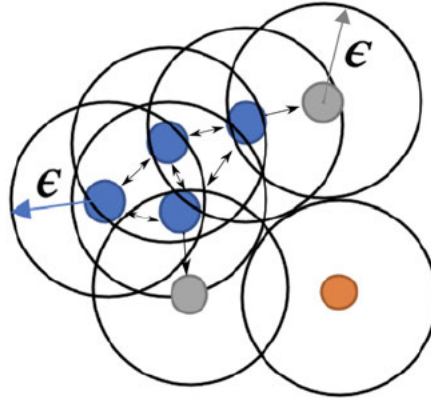


Fig. 4.4 Density-based spatial clustering of applications with noise (DBSCAN). Points within each other's vicinity, with a search radius of ϵ are grouped together as a single cluster. Blue and grey points belong to one cluster, where the former ones are core points. The grey points are reachable but make up the outer points of the cluster. The orange point is a noise point as it cannot be reached by any other point.



Fig. 4.5 Detected clusters of voxels of coronary arteries. The left cluster and right cluster are of right and left coronary arteries respectively.

Cluster identification

After clustering, various clusters of voxels (represented by their centres) emerge. However, only two of these clusters are the coronary arteries. In order to make our process automatic, two clusters corresponding to the left and right coronary arteries are chosen based on their proximity and orientation to the aorta (see Figure 4.5). By adopting this approach we eliminate the chances of incorrect cluster labelling, especially to avoid vessels in the pulmonary region, which sometimes can have geometry similar to that of the coronary arteries. Out of all clusters detected in Section 4.2.1, two clusters with points having least distance to the aortic centre, a spatial reference point identified in Section 4.2.1, are chosen as the coronary clusters.

4.3 Estimation of Lumen size for mesh generation

The voxel volume corresponding to coronary arteries, extracted from the above processes, is studied here for extracting geometrical values of the lumen. The coronary geometry is extracted using a combination of skeletonisation and surface meshing. However, before extracting the geometry, voxel volume is filtered to remove vessels smaller than a fixed size and also large volumes belonging to aortic root, thereby focusing on coronary vessels. To perform this DBSCAN is used. The density based clustering using DBSCAN was previously employed to detect coronary voxel volume from the filtered images. This algorithm is used again, however this time only on the selected voxel volume, with a setting of 7 voxel search radius, ϵ , and a minimum 700 points in this radius to detect and remove voxels from aortic root and a setting of 1.5 voxel search radius and a minimum 3 points in this radius to remove small vessels.

The skeletonisation algorithm, adopted from Scikit image [130], originally proposed by Lee *et al* [139], uses the logic of removing boundary voxels in order to thin down a volume of voxels until a middle voxel along the vessel axis is left out. These thinned down voxels make up the skeleton of vascular volume and act as the centreline for mesh generation (see Figure 4.6). The obtained centreline, which usually is a tree representing the coronary artery network, is split into individual branches for radii estimation in each of them. To split the skeleton into individual vessel branches, Skeleton network from ImagePy library [140][141] is used.

In order to extract radius from the volume, a surface Mesh is generated using marching cube algorithm [142](see Figure 4.6). This popular algorithm utilises a

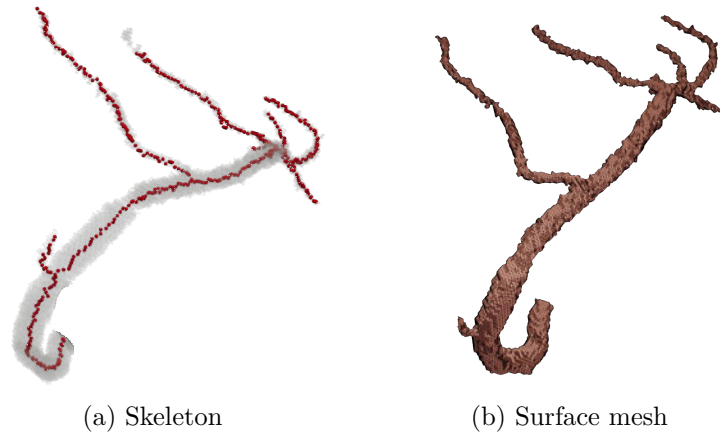


Fig. 4.6 Skeleton obtained from voxel cluster is used as centreline along which lumen radii is calculated.

traversing cube, in a volume discretised into cubes, for extracting a polygonal mesh of an iso-surface from voxels.

The cross-section of blood vessels are assumed to be circular for modelling purposes as explained in Section 4.4. Thus, an approximate circular radii needs to be calculated along the centreline. The vertices on the surface mesh are utilised to calculate such a vessel radius from the centre line. In the present work, the shortest normal distance between a point on the centreline to the wall vertices is chosen as the radius for that given point.

Finally, the points on the centreline and radii corresponding to them are interpolated using PCHIP, Piecewise Cubic Hermite Interpolating Polynomial, to generate an approximately uniform one-dimensional mesh along the vessel's centreline.

4.4 Haemodynamic modelling

The coronary lumen geometry extracted from CT scan is used to analyse blood flow using a coupled 1D-0D model, explained in Chapter 2 as the **ETM model**. The one dimensional model, formulated using Equations (4.1) and (4.2), is used to analyse vascular flow with the help of lumped models, to represent downstream resistance from the microvasculature or capillary beds. As explained in Chapter 2, the continuity and momentum equations are

$$C_A \frac{\partial P}{\partial t} + \frac{\partial Q}{\partial x} = 0, \quad (4.1)$$

and

$$\frac{\rho}{A} \frac{\partial Q}{\partial t} + \frac{\rho}{A} \frac{\partial (Q^2/A)}{\partial x} + \frac{\partial P}{\partial x} = -\frac{22\mu\pi Q}{A^2} \quad (4.2)$$

respectively, where C_A is the compliance, P is the hydrostatic pressure, Q is the volumetric flow rate, A is the cross-sectional area $\rho = 1.06g/cm^3$ is the density of blood, and $\mu = 0.04P$ (Poise) is the dynamic viscosity, t and x are the temporal and spatial coordinates, respectively. The viscous friction term on the right side of the momentum equation is responsible for predicting the pressure drop due to the vessel narrowing. The second term on the left side of this equation is also important for predicting the pressure drop, particularly if the area before and after a stenosis is different. A fine spatial mesh of 0.1 mm is required to accurately account for sudden changes in geometry. A non-linear visco-elastic constitutive law (Equation (4.3)) [30], is used to complete the system.

$$P - P_{ext} - P_0 = \frac{2\rho c_0^2}{b} \left(\left(\frac{A}{A_0} \right)^{b/2} - 1 \right) + \frac{\Gamma}{A_0\sqrt{A_0}} \frac{\partial A}{\partial t} \quad (4.3)$$

where P_{ext} is the external pressure, P_0 is a reference pressure, A_0 is the cross-sectional area at the reference pressure, and b is

$$b = \frac{2\rho c_0^2}{P_0 - P_{collapse}} \quad (4.4)$$

with $P_{collapse}$, collapsing pressure, and c_0 , reference wave speed of the vessel, which is calculated as

$$c_0 = \sqrt{\frac{2}{3\rho}(k_1 \exp(k_2 r_0) + k_3)} \quad (4.5)$$

with $k_1 = 2 \times 10^7 g^2/cm/s$, $k_2 = -22.53 cm^{-1}$, $k_3 = 8.65 \times 10^5 g^2/cm/s$ and r_0 being the reference radius of the vessel.

The boundary conditions, inlet conditions and ventricular pressures, for left and right coronary arteries are created using a closed-loop model, shown in Figure 4.7. In this figure, C_{art} and R_{beds} refer to arterial compliance and peripheral resistance from various capillary beds in the ETM model described in Chapter 2. R_{beds} is representative of various capillary beds across the arterial network in the ETM model and must not be confused with R_{cor} described below, which is the resistance pertaining to the coronary system. The heart lumped model from [30], is used to calculate ventricular pressures and flow in aorta, from which the boundary conditions for the coronary system, Q_{cor} , coronary inflow, P_{LV} , left ventricular pressures, and P_{RV} , right ventricular pressures

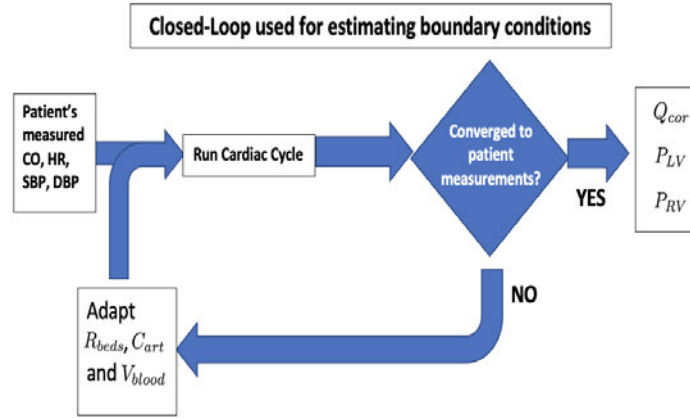


Fig. 4.7 The closed-loop used to estimate the boundary conditions for the coronary system. Detailed description is available in previous studies [143, 32, 144]. Here, CO is the cardiac output, SBP is the systolic blood pressure, DBP is the diastolic blood pressure, HR is the heart rate, C_{art} is the arterial compliance, R_{beds} is the peripheral resistance, V_{blood} is the blood volume, Q_{cor} is the coronary inflow, P_{LV} is the left ventricular pressure, and P_{RV} is the right ventricular pressure. R_{beds} and C_{art} refer to peripheral resistance from various capillary beds and arterial compliance in the ETM model (described in Chapter 2). R_{beds} is representative of various capillary beds across the arterial network in the ETM model and must not be confused with R_{cor} described below, which is the resistance pertaining to the coronary system. The cardiac cycle uses the heart lumped model proposed in [30].

are determined. However, the boundary conditions are chosen to be the same for all patients, as we have no additional patient information other than the CT data. The inflow rate of the left and right coronary arteries are shown in Figure 4.8. Due to this lack of patient data, coronary dominance was not considered in this modelling approach.

The coronary artery resistance is calculated as

$$R_{cor,i} = \frac{MAP}{Q_{cor,i}} \quad (4.6)$$

where MAP is a weighted average of an idealised diastolic and systolic pressure and $Q_{cor,i}$ is the inflow rate in the left (or right) coronary artery. The weighted average for MAP is $\frac{2}{3} \times$ diastolic pressure $+\frac{1}{3} \times$ systolic pressure, where diastolic pressure is 80mmHg, and systolic pressure is 120mmHg. The distribution of resistance throughout each branch is determined using a variant of Murray's power law, with a power of 2.27 as in van der Giessen *et al* [145], with vascular bed compliance distributed in a similar

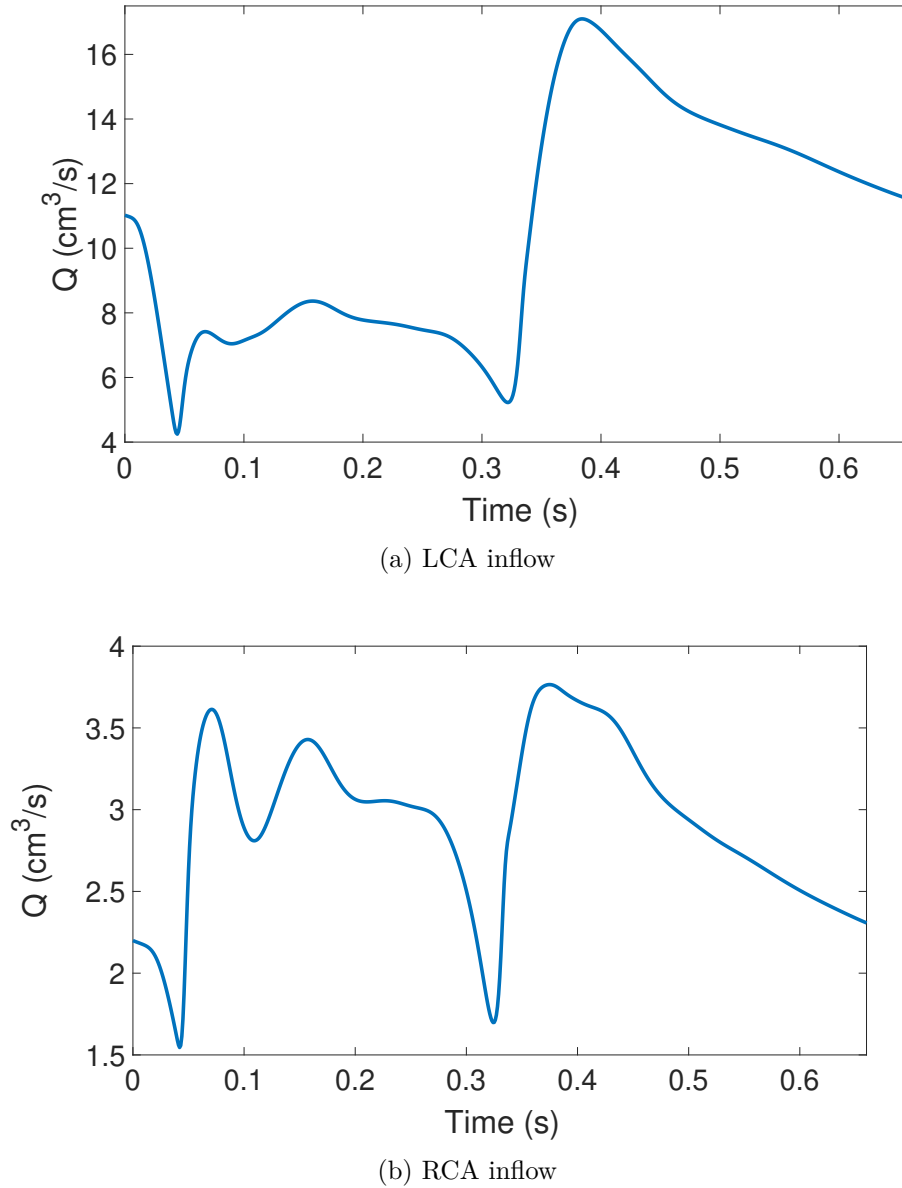


Fig. 4.8 Inflow boundary conditions used for left and right coronary arteries.

way [146]. The coronary vascular bed model is shown in Figure 4.9, which includes an external pressure acting from the heart ventricles. In Figure 4.9, the parameters of lumped-parameter model for each coronary vascular bed is calculated as $R_1 = \rho \frac{c_0}{A_{0,end}}$, $R_2 = 0.79 \times (R_{Tf} - R_1)$, $R_3 = 0.21 \times (R_{Tf} - R_1)$, where $A_{0,end}$ is the area at the end of the terminal vessel to which the vascular bed is connected and R_{Tf} is the resistance corresponding to the terminal vessel's fraction of total coronary resistance as per the distribution of resistance calculated using Murray's power law.

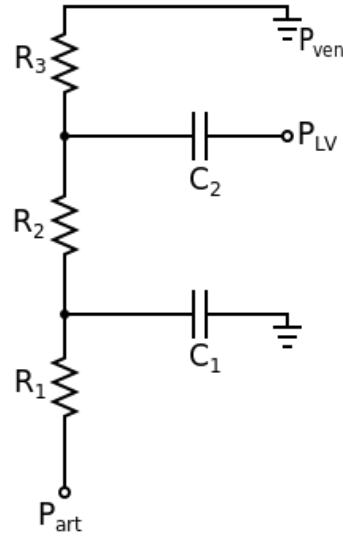


Fig. 4.9 A lumped-parameter model connected to the outlets of the patient specific coronary network to represent the micro-circulation. Part connects to the 1D domain, R_1 is the characteristic impedance, R_2 is the resistance of the micro-circulation at the arterial side, R_3 is the micro-circulatory resistance at the venous side, C_1 is the micro-circulatory arterial compliance, C_2 is the intra-myocardial compliance, P_{LV} is a scaled pressure from the left ventricle (or right ventricle for the right coronary artery [RCA]), and P_{ven} represents the pressure in the venous system which is set to 5mmHg

The full 1D-0D system is solved implicitly using a sub-domain collocation scheme referred to as the enhanced trapezoidal rule method [44][147]. The scheme uses a second-order backward difference temporal discretisation, and a composite trapezoidal rule for the spatial discretisation of the 1D domain. The steps taken in this section for haemodynamic modelling of coronary geometries have been summarised in Table 4.2.

4.5 Results and Discussions

The quintessence of methodology presented in this work is to process every step from CCTA scan to final cFFR value calculation without any manual intervention. Twenty five CCTAs, each belonging to different patients, were chosen to test the proposed automatic methodology. This section analyses the performance of the proposed workflow in terms of accuracy of segmented coronary geometry and the cFFR results obtained for the test patient cohort. Limitations to the degree of automation and their potential solutions have also been discussed in this section.

Table 4.2 A summary of steps followed in this chapter for haemodynamic modelling of the coronary artery geometries obtained using the proposed automatic method.

- Import 1D mesh
- Set boundary and initial conditions
 - Input inlet boundary conditions (as shown in Figure 4.8, calculated using closed-loop model)
 - Calculate total resistance
 - As per Murray's power law-
 - Distribute resistance throughout each branch
 - Distribute coronary vascular bed compliance
 - Calculate parameters for lumped-parameter models at each terminal vessel
- Solve full 1D-0D system using enhanced trapezoidal rule method
- Calculate cFFR using blood pressure values obtained.

Segmentation accuracy is one of the primary factors that will affect the accuracy of cFFR calculated using the proposed workflow. In order to estimate this accuracy, comparison with manually segmented coronary geometry is carried out for the CCTAs from the test patient cohort. The manual segmentation was carried out using widely available VMTK (Vascular Modelling toolkit) software. Table 4.3, summarises the results obtained from this geometry comparison, however, a detailed comparison for each case from the test patient cohort is made available to the readers in B2. In Table 4.3, it can be observed that the automatically segmented coronary geometry, using the proposed workflow, is similar to that of manually segmented geometry. The average vessel length (L), radii at the start of the vessel (R_0) and radii at the end of the vessel (R_f) of both left (LCA) and right (RCA) coronary arteries obtained automatically are similar or close to that of manually segmented geometry. However, the average length and final vessel radius obtained for left circumflex artery (LCX) and left anterior descending artery (LAD) using proposed workflow is higher than that of manual segmentation, providing an observation that automatic workflow can detect narrower vessels with ease. Further, the similarity in minimum vessel radius at the stenosis (R_s), provides confidence in geometry obtained automatically from CCTAs.

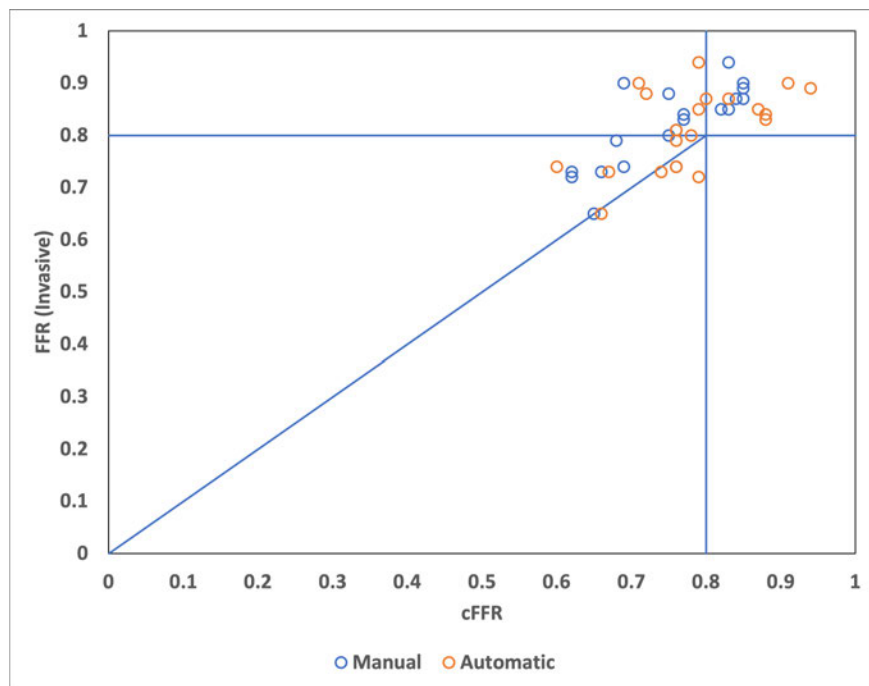


Fig. 4.10 cFFR values obtained from models using automatically and manually segmented coronary geometries are compared against invasively measured FFR. The cases for which invasive FFR values were not available have been excluded from the graph to avoid any confusion, however, cFFR values for such cases are available in Table 4.4.

Table 4.3 Coronary geometry detected from the proposed automatic segmentation workflow is compared against manually segmented coronary arteries. L , R_0 and R_f are average vessel length, radius at the start of the vessel and radius at the end of the vessel respectively. R_s is the average minimum vessel radius at the stenosis location. Detailed data for each patient case is available in B2.

	LCA		LAD		LCX		RCA	
	Automatic	Manual	Automatic	Manual	Automatic	Manual	Automatic	Manual
L (cm)	1.00 (SD: 0.50)	0.76 (SD: 0.54)	8.71 (SD: 2.75)	6.95 (SD: 2.60)	7.51 (SD: 3.02)	4.56 (SD: 2.13)	9.98 (SD: 2.58)	12.09 (SD: 2.26)
R_0 (mm)	1.60 (SD: 0.35)	1.63 (SD: 0.47)	1.38 (SD: 0.31)	1.40 (SD: 0.33)	1.35 (SD: 0.34)	1.35 (SD: 0.30)	1.52 (SD: 0.41)	1.57 (SD: 0.29)
R_f (mm)	1.55 (SD: 0.45)	1.53 (SD: 0.29)	0.66 (SD: 0.29)	0.88 (SD: 0.16)	0.69 (SD: 0.27)	1.03 (SD: 0.40)	0.96 (SD: 0.56)	0.92 (SD: 0.20)

R_s (mm)		
Left		Right
Automatic	Manual	Automatic
0.68 (SD: 0.30)	0.67 (SD: 0.21)	0.84 (SD: 0.50)
		0.70 (SD: 0.21)

In Table 4.4 and Figure 4.10, the cFFR values obtained are shown. In most of the cases, the cFFR value calculated are observed to be close to that of actual measured FFR, which is invasive in nature.

Though most of the results are in acceptable range, significant difference in patients 2, 6 and 12 can be observed. This could be attributed to either poor scan quality or incorrect selection of boundary conditions. It must be recollected that a fixed input boundary conditions for left and right coronary arteries are used in this work owing to lack of patient details. However, if a threshold of 0.8 is assumed as the critical value, none of the results have any false negatives. Thus, the proposed workflow produced satisfactory results, providing confidence towards using such a system in clinical environments.

4.5.1 Limitations

Proposed automatic method gives satisfactory cFFR values in most cases, however, in a small number of cases (20%), the automatic method either failed to produce or produced erroneous cFFR values. In all such cases, minor changes to the configuration, such as changes in filter settings, were observed to resolve any breakdown and satisfactory cFFR values were calculated without any further manual intervention. Since only minor adjustments to parameters were sufficient to resolve any problems, confidence is established in the core working principle of the proposed methodology. Majority of breakdowns in the automatic process occurred when analysis was carried out on scans of poor quality. Such scans usually had too many holes in them. In the process of making minor adjustments, the following challenges and their possible solutions were identified in the system.

During segmentation, binary thresholding is vital for identifying all voxels of interest so as to obtain their co-ordinates for clustering. The selection of the grey intensity threshold value is extremely vital for extraction of correct and complete vascular geometries. Various factors such as dye concentration, blood composition, calcification and pre-existing stents can affect the grey intensity in the scans. The intensity also decreases along the downstream direction of an artery. Since the orientation of arteries and patient parameters vary drastically, intensity-based thresholding methods in some cases either fail completely or partially in capturing the geometry. To alleviate this, 5-7 copies of the CCTA were simultaneously filtered and clustered individually. Each of these individual copies used a different grey intensity threshold varying within the range of 125 to 145. Upon completion, voxels from each individual copy classified as

Table 4.4 cFFR values calculated using geometries obtained automatically and manually on test patient cohort is compared against actual invasively measured FFR.

	Location	cFFR (automatic)	cFFR (manual)	FFR (invasive)
Patient 1	Left	0.76	0.69	0.74
Patient 2	Left	0.60	0.76	0.74
Patient 3	Left	0.66	0.65	0.65
Patient 4	Left	0.79	0.82	0.85
Patient 5	Left	0.76	0.68	0.79
Patient 6	Right	0.79	0.83	0.94
Patient 7	Left	0.78	0.75	0.80
Patient 8	Left	0.79	0.62	0.72
Patient 9	Left	0.73	0.78	NA
Patient 10	Left	0.91	0.69	0.90
Patient 11	Left	0.80	0.84	0.87
Patient 12	Left	0.71	0.85	0.90
Patient 13	Left	0.88	0.77	0.84
Patient 14	Right	0.83	0.85	0.87
Patient 15	Left	0.74	0.66	0.73
Patient 16	Left	0.58	0.62	NA
Patient 17	Left	0.75	0.77	NA
Patient 18	Left	0.67	0.62	0.73
Patient 19	Left	0.88	0.77	0.83
Patient 20	Left	0.72	0.75	0.88
Patient 21	Left	0.72	0.68	NA
Patient 22	Left	0.76	0.76	0.81
Patient 23	Right	0.87	0.83	0.85
Patient 24	Right	0.94	0.85	0.89
Patient 25	Left	0.51	0.42	NA

that of belonging to the coronary arteries, were combined. This approach, however, was not efficient in scans with discontinuities or inaccurate data. Since density based scanning identifies neighbouring points (voxel centres) using a search radius, incorrect voxels (from discontinuities) within this search area lead to major leaks. Interestingly, it was observed that most of the leaks occurred in regions closer to the aortic root. Manual intervention was required in order to select only those individual copies that had good quality cluster, which consequently was merged and analysed upon automatically.

The other issue faced was during cleaning/filtering of arterial voxel volume after clustering to remove small vessels. In some geometries, due to a presence of occlusion, lumen had cross-sectional area with very small voxel volume. These regions had a voxel density lower than the threshold values preset to remove small vessels, leading to loss of vessel geometry around the occlusion. This was undesirable as lowering the density threshold value in order to preserve geometry would allow for smaller vessels to be added to the mesh. Such geometry would reduce the performance of one dimensional code by delaying convergence and affecting approximations. In the two cases where this issue was observed, the density threshold had to be decreased and the smaller vessels had to be ignored during haemodynamic modelling.

The final issue faced was the deletion of initial few nodes in either of the coronary arteries. The section of coronary artery emerging from the aortic root is affected during filtering of coronary volume. This removal of geometry, belonging to aortic root, in some cases removed voxels disproportionately from the initial lumen region of the coronary arteries. This lead to smaller diameter being calculated for nodes in such regions. In turn it affected the complete cFFR calculation downstream. To alleviate this issue, first 4 to 6 nodes were not considered during haemodynamic analysis.

For future work, breakdowns like these can be avoided by training a supervised monitoring system. Such a system could intervene and adjust parameters if any of the above observed problems arise. A simple closed loop system or neural networks can be used for such control.

4.6 Conclusions

The proposed methodology, built on a combination of unsupervised learning and computational fluid dynamics, provides a robust platform to automatically calculate cFFR values. Satisfactory results observed by testing it on a patient cohort of twenty-five patients, with the average difference between the automatically calculated cFFR

and invasively measured FFR is 0.06, provides the required assurance that the method is reliable. Thus, it can be concluded that automating the process of calculating cFFR from CT scans is feasible and reliable. The entire workflow presented in this chapter take only between 12 to 25 minutes per patient. Thus, the automated method proposed is rapid and suitable for fast functional assessment of arteries.

In addition, it is worth noting that even though the working principle fundamentally varies from the popular rising trend of using supervised neural networks, present work provides a potential for future combination of such methodologies to enhance accuracy of cFFR calculation and computational performance.

4.7 Summary

In this chapter, the concept of a passive digital twin is explored by the development of an automatic workflow for calculating Fractional Flow Reserve (FFR) from CT scans, also known as coronary Computerised Tomography (CT) angiography-derived FFR (cFFR). The workflow begins with geometry extraction from the CT scan using filtering and density-based clustering. The extracted geometry is then used to build a one-dimensional mesh, using which the ETM model, a haemodynamic model described in Chapter 2, calculates the cFFR values in the coronary arteries. The proposed workflow is tested on CT scans from a cohort of twenty-five patients to calculate cFFR and compared against invasively measured FFR as well as cFFR calculated using manually segmented FFR. A satisfactory average difference of 0.06 is observed in values between the automatically calculated cFFR and invasively calculated FFR. The digital twin proposed in this chapter is an example of the first of the three forms of a human digital twin being explored in this thesis, wherein twins perform offline analysis of data that involves no active component.

Chapter 5

Semi-Active Digital Twin

To explore the concept of semi-active digital twin, in this chapter, we propose a methodology to detect the severity of carotid stenosis from a video of a human face with the help of a coupled blood flow and head vibration model. This semi-active digital twin model is an attempt to link non-invasive video of a patient face to the percentage of carotid occlusion. The pulsatile nature of blood flow through the carotid arteries induces a subtle head vibration. This vibration is a potential indicator of carotid stenosis severity and it is exploited in the present study. A head vibration model has been proposed in the present work that is linked to the forces generated by blood flow with or without occlusion. The model is used to generate a large number of virtual head vibration data for different degrees of occlusion. In order to determine the *in vivo* head vibration, a computer vision algorithm is adopted to use human face videos. The *in vivo* vibrations are compared against the virtual vibration data generated from the coupled computational blood flow/vibration model. A comparison of the *in vivo* vibration is made against the virtual data to find the best fit between *in vivo* and virtual data. The preliminary results on healthy subjects and a patient clearly indicate that the model is accurate and it possesses the potential for detecting approximate severity of carotid artery stenoses. The work presented in this chapter is available as a published journal paper [148].

5.1 Introduction

The digital twin concept is becoming a common theme in traditional engineering disciplines, and such a concept is yet to be completely realised in cardiovascular engineering. The digital twin concept can be broadly described by three characterisations: active,

where a digital replica (digital twin) of a physical system (physical twin) is continuously updated by information and data collected from the physical twin; semi-active, where time-varying data are collected, but rather than performing a continuous update, the information is analysed after the data are collected; and passive, where the digital twin utilises measurements from a physical twin which are not continuously updated, which may include some modelling assumptions. It is also possible to have a mix of active and passive digital twin models, where only specific sections or parameters of the digital twin are continuously updated via data collected from a physical twin, while other components of the model either use assumptions, or utilise measurements from a physical twin, but are not being continuously updated. The active and passive digital twin concepts of the systemic circulation are currently being considered by researchers [149, 150]. While the passive digital twin concept has been realised through off-line calculations in cardiovascular flow modelling, the active concept is fairly new. These passive concepts include off-line fractional flow reserve (FFR) calculations [151, 146, 147] and a large number of subject-specific blood flow calculations through aneurysms and stenoses. The active digital twin has all the ingredients to be the basis for future non-invasive diagnostic methods of cardiovascular problems, as we are increasingly making active and continuous online measurements of subject-specific cardiac signals. An active FFR calculation would require producing an FFR value instantaneously while a scan of the a coronary artery is being carried out. With the fast computational methods and emerging machine learning algorithms, we believe that such an active digital twin model is now plausible. In the present work we attempt a semi-active digital twin model for non-invasively detecting a carotid artery stenosis. In this method a time dependent face video of a subject is used to calculate the head vibration before comparing the *in vivo* value to computationally generated data, to approximately determine the severity of a carotid artery stenosis.

The carotid arteries are the main vessels that carry blood to the head. Due to ageing, hypertension, life style choices and injuries to the blood vessel wall, plaques build over time in the carotid artery wall layers. This is called atherosclerosis and it causes a progressive narrowing of carotid artery, known as carotid stenosis. As the plaque builds up, the inward growth of mass narrows the internal lumen diameter. Such a narrowing of the carotid artery can lead to reduced blood supply, and hence oxygen supply, to the brain. This reduction in oxygen supply may cause the death of brain tissue, leading to ischemic strokes or transient ischemic attacks (TIA). Annually, sixteen million people suffer from stroke around the globe [152], making it the third

highest cause of death in the world after cancer and coronary heart disease (CHD). In the UK alone, 85% of the 100,000 cases reported were ischaemic in nature [153]. In majority of the cases assessing the severity of carotid narrowing after a TIA is still a major challenge. The current assessment procedure of carotid duplex ultrasound often is delayed due to waiting time and other issues. Thus, development of other easier and non-invasive methods will add value to existing screening technologies. In other developing countries, availability of medical devices is very limited and a procedure like the one proposed can provide low cost screening of suspected TIA patients. Furthermore, there are other perceived barriers to the use of ultrasound in developing countries, which include lack of training or training opportunities; unable to afford the cost of obtaining, maintaining, or updating the equipment; lack of reliable electricity supply [154]. Furthermore, ultrasound is dependant on the Doppler, which can influence the peak systolic velocity value [155]. Thus development of a more consistent and reliable method would be useful to estimate stenosis severity. Conventionally carotid stenosis is clinically detected using either a doppler ultrasound of the neck, magnetic resonance angiography (MRA), CT angiography (CTA) of the neck, or a cerebral angiography. In the present work, a non-conventional method is proposed.

The forces generated as a result of pulsatile blood flow in major arteries lead to low amplitude vibrations of human body parts. These vibrations are potentially a vital sign for assessing the health of arteries. Many non-invasive methods to detect and analyze such vibrations have been developed, such as Seismocardiography, kinetocardiography, and ballistocardiography. Out of these, ballistocardiography (BCG) was once a topic researched upon extensively, but has been falling out of favour over time due to a lack of sophisticated and accurate measuring equipment, and techniques. A detailed analysis of the development of BCG, and the reasons for why it was discarded, have been well documented by Giovangrandi *et al* [156]. Proposed in the 19th century, BCG was given importance in 1940's to 1980's. Originally, setups such as sensitive vibration beds were developed to capture these vibrations. It has again gained momentum in 2010 after accurate and more sensitive sensors and vibration measuring devices have emerged. A type of BCG that records head movements or vibrations in the head due to blood flow, also known as head-BCG, was analyzed by He *et al* [157].

Blood flow, primarily in the carotid arteries, causes subtle head motions. Occlusion in these arteries can cause changes in this head motion due to a substantial change in amplitude of pressure waves in comparison to nonoccluded arteries. A procedure capable of detecting very subtle movements can be used for accurately capturing these

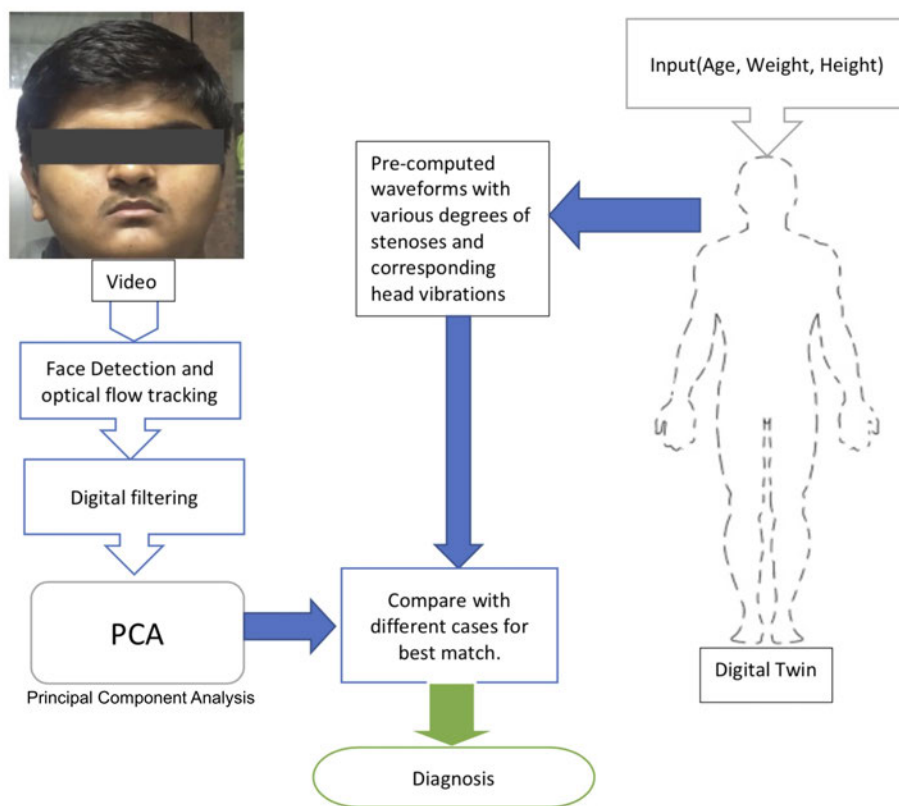


Fig. 5.1 Diagnosis of carotid stenosis by comparing results of computer vision and biomechanical model (digital twin).

motions, which cannot be sensed by our naked eye is essential to make progress. One such powerful tool is computer vision, which can analyse extremely small motions in a video. This has been made possible by advancements in camera technology and the raw power of processing. In Balakrishna *et al* [158], computer vision is used to capture this subtle head motion to determine heart rate and variability. In older computer vision algorithms, the pulse was detected using colour change in the skin. One of the future research possibilities mentioned in the past was to detect blockages in arteries, which provided a motivation to investigate the possibility of using cameras to detect the severity of carotid stenoses. This type of predictive methodology could potentially prevent strokes as widely accessible devices such as smart phones could be used for screening.

In the present work, we are attempting to mechanically model head vibrations and then use the model to predict vibrations corresponding to carotid stenoses. The proposed methodology has the following steps: (a) Generate synthetic head vibration data (computational) for different degrees of carotid artery occlusions by combining a systemic circulation blood flow model and a head vibration model; (b) Estimate the vibration of a human head as a result of blood flow by analysing the face video via a principal component analysis; and (c) Compare and match the measured vibration against the synthetic data to come to a conclusion on the severity of carotid artery occlusion. These steps are schematically presented in Figure 5.1. This chapter is organised into following sections. In the section that follows the introduction, analysis of face video is discussed. In Section 5.3, the methodology used to create the synthetic data is discussed in detail. This includes the blood flow model, vibration model, and the interface between these two models. In Sections 5.4 and 5.5 respectively some preliminary results and limitations of the present work are discussed and finally Section 5.6 provides some important conclusions and potential future research directions.

5.2 Detection of head oscillations

An algorithm proposed by Balakrishnan *et al.* [158] that uses computer vision to detect small motions in the head has been implemented in this work. A few modifications have been incorporated to enhance and simplify small motion analysis and help detect stenoses, such as changing the region of interest (ROI) from part of the face to only the forehead region. The proposed methodology analyses between 30 and 40 seconds of captured video. The analysis is not carried out in real time and thus we refer to the

method as "semi-active digital twin". A smart phone based camera is used to improve accessibility, which could eventually provide a low-cost and non-invasive technique for detection of carotid occlusion. The videos were captured on a Motorola G (2nd Generation) for android devices, which comes with an 8MP camera, and an iPhone 6s with a 12MP camera, for iOS devices. Due to its built-in features such as higher resolution, the iPhone 6s provides a better solution. In this work, samples are captured using both cameras.

5.2.1 Assumptions and guidelines

A basic assumption has been made that the subject remains still. Most of the involuntary actions such as respiration and blinking of eyes are removed digitally when the signal is passed through a bandpass filter. For an accurate detection of motion during the video recording, the following set of guidelines are followed:

1. The subject has been rested sufficiently before screening to ensure a relatively stable heart rate and respiration rate.
2. The video is shot in an environment with no direct lighting over the subject's face which ensures reliable feature tracking.
3. Neither the subject nor the camera is subjected to any small vibrations. For example, a camera placed on a table with a desktop computer can produce erroneous results.

5.2.2 Facial recognition and region of interest (ROI)

In order to detect the region of the video covered by the face, the Viola-Jones face detector is used [159][160]. This detector provides an object detection framework which allows competitive object detection rates in real-time. A small region, usually the central forehead or area below the eyes, is taken as the region of interest (although regions from other parts of the face may also work successfully). Unlike in Balakrishna *et al* [158], in which 50% to 60% of the face width and 60% to 70% of the face length is selected, only a small rectangular (forehead) region has been used in the present work (see Figure 5.2). This helps in maintaining a consistent average distance between the pivoting point at the base of the neck and the monitoring points, simplifies the conversion of angular displacement to linear displacement, as explained in Section 5.3.



Fig. 5.2 Region of interest.

5.2.3 Feature points tracking and filtering

OpenCV Lukas-Kanade optical flow [159] is used to track a number of points (N-points) within the region of interest. Since two components of motion, vertical and horizontal, can be detected during tracking, selection of a component for analysis and detection becomes necessary. It is noted by both Balakrishna *et al* [158] and He *et al* [157] that the horizontal motion is mainly due to dynamic equilibrium swaying. Thus, the horizontal component has been ignored in the present work. The vertical component of the signal is then passed through a Butterworth bandpass digital filter. The frequency band for this filter is chosen to be 0.75 to 2 Hz. This frequency range is derived from a spectral analysis, using fast Fourier Transforms, of predicted head-neck vibration from the mechanical model proposed in this work. The Figure 5.3 shows energy at different frequencies from the results of blood-flow-driven-head-neck vibration predicted by the proposed mechanical model. The frequencies being observed is above 0.5 Hz to avoid interference from very low frequency vibrations caused by different neurological activities and dynamic equilibrium swaying. Filtering of vertical signal (from the video) gave an output very close to that of the predicted results (from the mechanical model). This frequency range is also the same as a heart beat range, where 0.75 to 2 Hz can be related to 45 to 120 beats per minute.

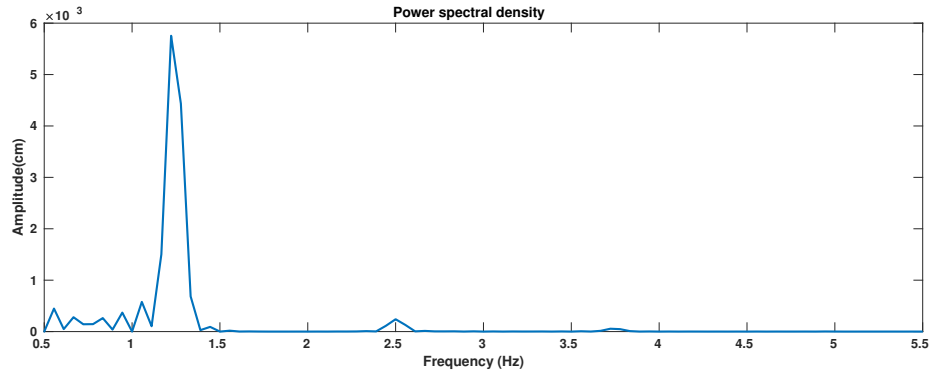


Fig. 5.3 Energy at different frequencies for the results of blood-flow-driven-head-neck vibration predicted by the proposed mechanical model.

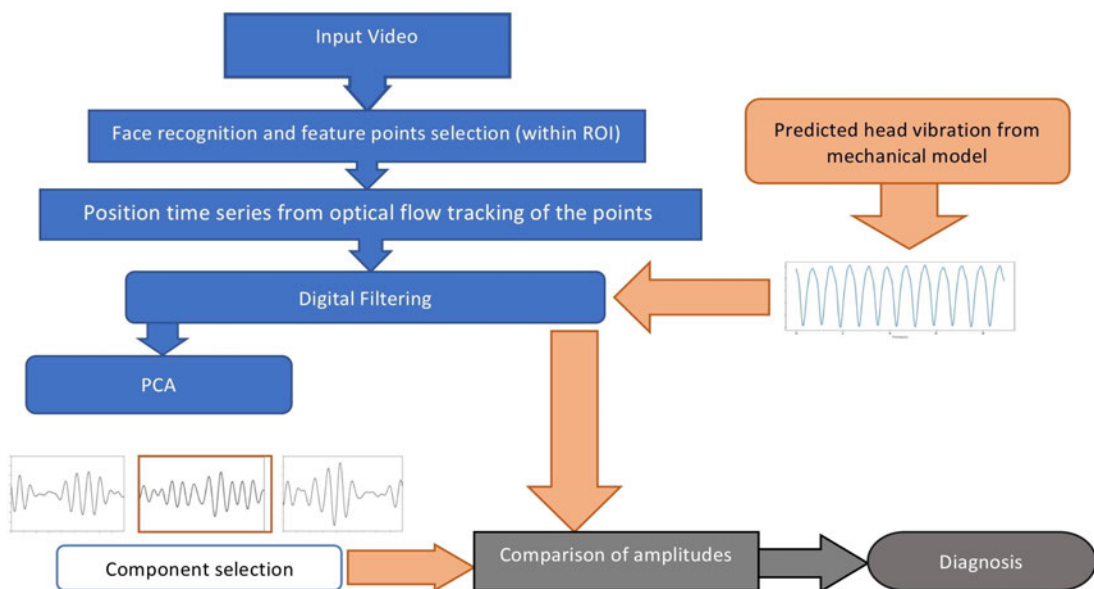


Fig. 5.4 Workflow used in the present work to detect carotid stenosis and its severity

5.2.4 Principal component analysis

In the present work, we are interested in head vibrations that are driven by haemodynamics. However, as head motion is caused by several factors, which includes blood flow, respiration, facial expressions, and neurological processes, it is necessary to separate the components of this mixed head motion into sub-motions in order to isolate blood flow driven vibration. This is carried out by performing a principal component analysis (PCA) using a similar technique to that of Balakrishna *et al* [158]. Later works (Haque *et al* [161], Li *et al* [162], Irani *et al* [163], Shan *et al* [164]) have implemented other methods, such as the discrete cosine transform, in order to isolate different types of motion. However, they generally gave results close to PCA, and thus PCA is chosen in the present work due to its simplicity (see Figure 5.4).

PCA is described by the following algorithm: let y_{fn} be the vertical displacement of the n th point at the f th frame: $n = \{1, \dots, N\}$ and $f = \{1, \dots, F\}$ where N is the number of points accounted and F is the total number of frames in the recording. We define the mean as

$$\mu_n = \frac{1}{F} \sum_{f=1}^F y_{fn} \quad (5.1)$$

and the matrix \mathbf{Y} of centred displacements with the entries as

$$Y_{fn} = y_{fn} - \mu_n. \quad (5.2)$$

We define the covariance matrix as

$$\mathbf{C} = \frac{1}{F-1} \mathbf{Y} \mathbf{Y}^T \quad (5.3)$$

The PCA finds the principal axes of variation of the position as the eigenvectors of the covariance matrix from

$$\mathbf{C} \mathbf{U} = \mathbf{\Lambda} \mathbf{U} \quad (5.4)$$

where $\mathbf{\Lambda} = \text{diag}\{\lambda_1, \dots, \lambda_N\}$ is a diagonal matrix of the eigenvalues and $\mathbf{U} = [\mathbf{u}_1, \dots, \mathbf{u}_N]$ is a matrix with each column of it being an eigenvector, \mathbf{u}_n , corresponding to the eigenvalue λ_n . In our work only the eigenvectors are of interest and not eigenvalues.

The final required signal, in the form of head displacement, can be written as follows:

$$S_i(t) = y_{fn} \mathbf{u}_i \quad (5.5)$$

where $t = f\Delta t$ with Δt being the time-step between two neighbouring frames and i in the above equation represents the eigenvector of interest.

The eigenvector (principal component) of interest is selected by analysing two properties of time series signals calculated from different eigenvectors. A signal having a frequency corresponding to the heart rate of the subject with good periodicity (reflecting a healthy heart rate variability) is chosen as the component of interest for the healthy condition, without the presence of a carotid stenosis.

However, since the majority of stenosis cases occur in older subjects and thus it is highly likely to be coupled with other cardiovascular diseases, an ambiguity may arise when choosing the eigenvector of interest for these subjects; thus a different technique must be performed. In these subjects, the head-neck vibration is not only affected by heart rate, but is also significantly affected by factors such as cardiac output, heart rate variability, and the occurrence of multiple stenosis or aneurysms. The heart rate variability, unlike in healthy conditions, leads to a non-periodic signal. For these cases, component selection requires more sophisticated and trial-tested techniques such as machine learning, where multiple input parameters can be used to select the required component. However, such techniques require substantial amounts of data that can only be collected through an extensive retrospective study; hence in this work the selection of components for all subjects, including the stenosis patient, is performed by analyzing only the frequency and heart rate variability of the subject. Although the same technique is implemented for the selection of eigenvectors for both healthy subjects and the stenosed subject, the stenosis patient was on medication for CVD and had been treated for irregular heartbeats, thus making the signal relatively periodic.

5.3 Mechanical modelling of head oscillations

A mechanical model is required to produce a database of virtual patients. The database surrogates the data required for developing an automated detection system, which otherwise would require a significant number of patients suffering from different forms of carotid stenoses. It also serves as a reference for choosing the number of filtration levels and types of digital filters, along with refinement of the virtual patient parameters.

The arterial network present in the head-neck system is extremely complicated and analysing each of the arteries for their contribution to the head-neck oscillations is a daunting task, particularly as there are anatomical variations of the cerebral

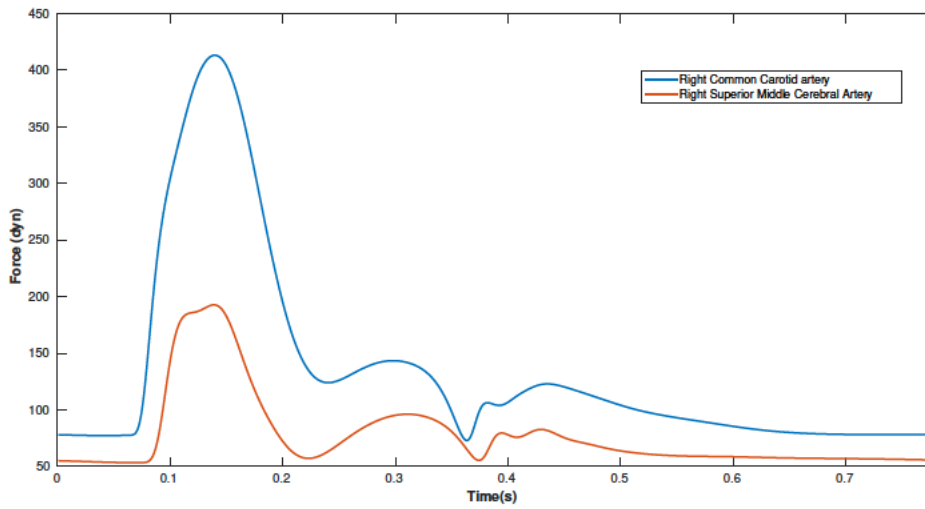


Fig. 5.5 Force exerted by blood flow in a single finite element of two major inter-cranial arteries with respect to time.

arteries. In order to reduce the complexity, forces imparted by various inter-cranial arteries are analysed using the one dimensional blood flow model, and it is observed that blood flow in the carotid arteries (Figure 5.5) have the most significant influence on the subtle head oscillations. The other smaller inter-cranial arteries had a very small influence when considered independently. However, when considered collectively they have a small but significant contribution to the head-neck vibration. Based on these observations, instead of accounting for the effect of each of these smaller arteries separately, we have mimicked their collective effect by scaling the force in the distal end of the internal carotid arteries. Since the majority of stenoses in this region develop in the carotid arteries, we chose to reduce the complexity of modelling by limiting the analysis to the carotid arteries. In the future, when more powerful graphic processing units and robust computer vision algorithms are available, the complexity of this model can be increased by including the individual effect of each of the other smaller arteries, especially those in the circle of Willis.

5.3.1 One dimensional haemodynamic model

The haemodynamic model adopted in this work is the **ETM model**, described in Chapter 2, a modified version of the model proposed by Mynard and Smolich [30]. The model considers 123 of the major vessels in the systemic arteries as 1-D vessel segments. As explained in Chapter 2, the inlet of the aorta is connected to a two

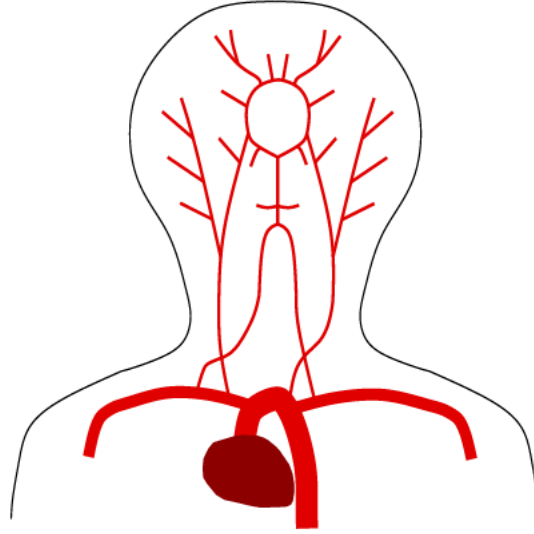


Fig. 5.6 Cerebral arteries used in the one dimensional model

chamber 0-D heart model, while the outlet of peripheral vessels connects to a three element Windkessel model, which accounts for the micro-circulation.

The length and diameter of common carotid arteries are modified according to Equations (5.6), by Passera *et al* [40], to approximate the vessel network that is specific to the subject. A part of the flow network used in the present study is shown in Figure 5.6.

$$L_{left\ carotid} = 1.26H \quad (5.6a)$$

$$L_{right\ carotid} = 1.05H \quad (5.6b)$$

$$D_{left\ carotid} = 6.61G + 5.82(1 - G) \quad (5.6c)$$

$$D_{right\ carotid} = 6.42G + 5.74(1 - G) \quad (5.6d)$$

In the above equations, H refers to the subject's height and G refers to subject's gender.

5.3.2 Determination of axial force on the wall

Only the axial or unbalanced components of fluid force is used for determining the force applied on the walls. The radial forces are imparted on the arteries uniformly along the radial direction and thus cancel out any vibration resulting from these radial forces (in the calculation of the moment of force). In order to estimate the axial force on the

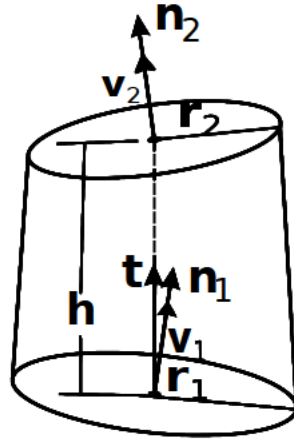


Fig. 5.7 Element of the vessel of length h . Here, \mathbf{t} is the unit vector acting along the element axis, \mathbf{n}_1 and \mathbf{n}_2 are the normals to the element inlet and outlet, respectively

wall, it is important to first discuss what is and what is not included in the model (or patient data), due to various necessary assumptions. There are significant variations in the range of parameters between individuals. This includes: cardiac output (stroke volume), systolic and diastolic pressures, length and orientation of arterial segments, vessel lumen diameters, vessel wall parameters such as wall thickness, and the elastic modulus. An assumption in the haemodynamic model is that the vessel wall only moves in the radial direction.

It is necessary to simplify the estimation of axial force in such a way that the method is generalised. In order to attempt this, it is assumed that the axial force on the occluded/healthy vessel wall will be proportional to the net force of the fluid in the axial direction. The force of the fluid can be derived from considerations on a control volume.

Consider an element of a vessel segment shown in Figure 5.7. Let the element length be h , inlet radius is R_1 and outlet radius be R_2 . Correspondingly, its inlet and outlet areas are $A_{1,2} = \pi R_{1,2}^2$. Let \mathbf{t} be a unit vector acting along the element axis, \mathbf{n}_1 and \mathbf{n}_2 be normal unit vectors to the element inlet and outlet, respectively. If a segment is curved or it is the first or last in the segment then direction of inlet and outlet may be different and do not coincide with the direction of the element axis. We assume that angle between \mathbf{n}_1 and \mathbf{n}_2 is small enough and we can consider an element as truncated cone (if the segment is tapering) or a part of a cylinder. Let v_1 and v_2 be velocities averaged over inlet and outlet, respectively. The axial forces encountered by the wall are:

1. Friction force \mathbf{F}_f acting in direction \mathbf{t}
2. Force \mathbf{F}_d caused by deflection of the flow in the element in the case $\mathbf{n}_1 \neq \mathbf{n}_2$
3. Force \mathbf{F}_t caused by vessel tapering.

The friction force can be calculated as

$$\mathbf{F}_f = F_f \mathbf{t}, \quad F_f = \tau A_w \quad (5.7)$$

where τ is the wall shear stress and A_w is the area of the element wall. The wall shear stress is given as

$$\tau = \gamma \mu \frac{v}{R} \quad (5.8)$$

Here γ is the friction coefficient, μ is dynamic viscosity, v is cross-sectional average velocity and R is the cross-section radius. The friction force per unit of length along the axis is τ times cross-sectional perimeter $2\pi R$:

$$\frac{dF_f}{dx} = \gamma \mu \frac{v}{R} \times 2\pi R = 2\pi \gamma \mu v \quad (5.9)$$

Integrating (5.9) by the trapezoidal rule, we have

$$F_f = \pi \gamma \mu (v_1 + v_2) h \quad (5.10)$$

The force acting on a curved pipe with the steady state flow is

$$\mathbf{F}_d = (\mathbf{v}_2 - \mathbf{v}_1) \dot{m} \quad (5.11)$$

where $\dot{m} = \rho \bar{Q}$ is the mass flow rate and $\bar{Q} = \frac{1}{2} (A_1 v_1 + A_2 v_2)$ is the average volumetric flow rate in the element. The normal component of this force can be approximated by

$$\mathbf{F}_d = (\mathbf{n}_2 - \mathbf{n}_1) \bar{v} \dot{m} = (\mathbf{n}_2 - \mathbf{n}_1) \rho \bar{v} \bar{Q}, \quad (5.12)$$

where $\bar{v} = \frac{1}{2} (v_1 + v_2)$. Finally,

$$\mathbf{F}_d = \frac{1}{2} (\mathbf{n}_2 - \mathbf{n}_1) \rho \frac{(v_1 + v_2)}{2} (A_1 v_1 + A_2 v_2) \quad (5.13)$$

Force associated with tapering is

$$\mathbf{F}_t = F_t \mathbf{t}, \quad F_t = \int_{A_2}^{A_1} p dA \quad (5.14)$$

where p is pressure and is written as $p = \frac{\rho \bar{Q}^2}{2} \left(\frac{1}{A_2^2} - \frac{1}{A^2} \right)$. Force due to taper is formulated as

$$F_t = \frac{\rho \bar{Q}^2}{2} \int_{A_2}^{A_1} \left(\frac{1}{A_2^2} - \frac{1}{A^2} \right) dA \quad (5.15)$$

$$F_t = \rho \bar{Q}^2 \frac{(A_1 - A_2)^2}{2A_1 A_2^2} \quad (5.16)$$

Total force acting on the the element can now be written as

$$\mathbf{F}_e = \mathbf{F}_f + \mathbf{F}_d + \mathbf{F}_t \quad (5.17)$$

$$\mathbf{F}_f = \mathbf{t} \pi \gamma \mu (u_1 + u_2) h \quad (5.18)$$

$$\mathbf{F}_d = \frac{1}{2} (\mathbf{n}_2 - \mathbf{n}_1) \rho (v_1 + v_2) \bar{Q} \quad (5.19)$$

$$\mathbf{F}_t = \mathbf{t} \rho \bar{Q}^2 \frac{(A_1 - A_2)^2}{2A_1 A_2^2} \quad (5.20)$$

This force, calculated in each element of the vessel, contributes to the total force being applied on the head due to blood flow.

Spatial mapping of elements

In order to link the blood flow and vibration models, all the individual finite elements in the carotid artery are identified with respect to the origin $C7$ in Figure 5.8. This is essential in order to calculate the moments about the origin for the vibration model, around which the head pivots. A CAD model developed from a scan is used to locate the relative locations of the finite elements along the carotid artery with respect to the pivot point [165].

The morphology of carotid arteries vary among the general population, making patient specific spatial mapping of elements an impossible task without a CT-scan of the head. By incorporating scans, the primary goal of developing a low cost and fast detection system goes unaccomplished. In order to solve this issue, the CAD model chosen is such that the morphology of carotids, by their relatively closer distance to the base of neck and smaller angle with respect to the reference axes (see Figure 5.8), produces the least amplitude possible for different stenoses conditions. By producing

the least possible amplitudes, false negatives (subjects suffering from stenoses but detected to be healthy) can be minimized, as lower threshold values are chosen for categorizing severity.

5.3.3 Dynamic equation of head-neck system

A mathematical formulation is required to calculate the head-neck motion. The dynamic equation formulated by Wang and Rahmatalla [166] is used to analyse the head-neck vibration induced by forces created from blood flow. The equation consists of the I_s matrix representing moments of inertia of the head and the first seven vertebral discs about the three primary axes (See Figure 5.8). Moments are applied by blood flow in the carotid arteries about X_0 at $C7$. An assumption is made that the subject rests their back on a backrest allowing only for the head-neck vibration to take place. This assumption helps to simplify the modelling, which would otherwise need a complex estimation of forces imparted in body parts below $C7$. For example, the force due to blood flow in major arteries such as the abdominal aorta, pumping of heart, and breathing. The dynamic equation used in the present study is

$$I_s \ddot{\theta} + C_s \dot{\theta} + K_s \theta = M_b \quad (5.21)$$

where the inertia and stiffness matrices, I_s and K_s are defined as follows [166]:

$$I_s = \begin{bmatrix} LL_c m \cos^2 \theta_{20} + I_{11} & 0 & -\frac{1}{2} L_c m L \cos \theta_{10} \sin(2\theta_{20}) \\ 0 & L_c m L + I_{22} & L_c m L \sin \theta_{10} \\ -\frac{1}{2} L_c m L \cos \theta_{10} \sin(2\theta_{20}) & L_c m L \sin \theta_{10} & b_{33} \end{bmatrix}$$

where b_{33} is,

$$b_{33} = \frac{3LL_c m}{4} - \frac{1}{4} m \cos(2\theta_{10}) LL_c - \frac{1}{8} m \cos(2(\theta_{10} - \theta_{20})) LL_c - \frac{1}{4} m \cos(2\theta_{10}) LL_c - \frac{1}{8} m \cos(2(\theta_{10} + \theta_{20})) L_c L + I_{33}$$

and

$$K_s = \begin{bmatrix} \frac{1}{2}(2K_{11} - 2gL_c m \cos \theta_{10} \cos \theta_{20}) & \frac{1}{2}(2K_{12} + 2gL_c m \sin \theta_{10} \sin \theta_{20}) & K_{13} \\ \frac{1}{2}(2K_{12} + 2gL_c m \sin \theta_{10} \sin \theta_{20}) & \frac{1}{2}(2K_{22} - 2gL_c m \cos \theta_{10} \cos \theta_{20}) & K_{23} \\ K_{13} & K_{23} & K_{33} \end{bmatrix}$$

L_h and L_n are length of the head and neck respectively, L is the distance between C_0 and C_7 , $L_c = m_n \times L_n + m_h \times L/m$, and m is the sum of m_h and m_n , masses of

Table 5.1 Values for K_s and C_s from Wang and Rahmatalla [166]

Stiffness (Nm/rad)	k_{11}	k_{12}	k_{13}	k_{22}	k_{23}	k_{33}
	10.121	2.86	1.609	8.238	3.989	6.9867
Damper (Nms/rad)	c_{11}	c_{12}	c_{13}	c_{22}	c_{23}	c_{33}
	0.096	0.304	0.127	0.778	0.3034	-0.0689

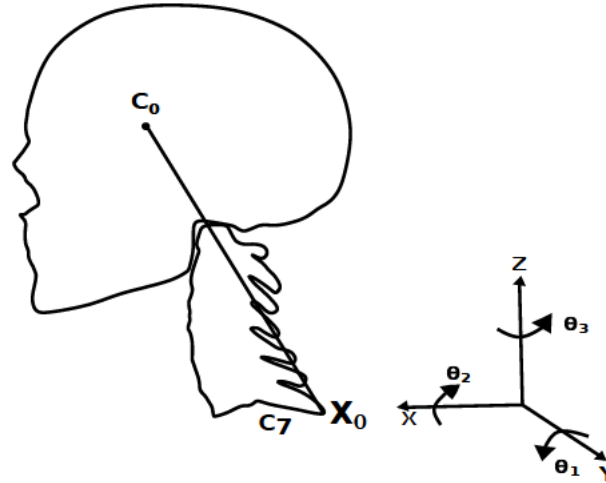


Fig. 5.8 The head-neck system employed in the present work.

head and neck respectively. In the present work, m_h is kept constant (4.6 Kg) but m_n is varied with body mass index (BMI). A linear change in mass of fat in the neck is adopted based on the change in neck circumference with BMI [167].

The experimentally derived values for K_s and C_s (shown in Table 5.1) are adopted from Wang and Rahmatalla [166]. Values for I_{ii} , where $i = 1, 2, 3$, are calculated from Himmetoglu *et al* [168]. The subject's measured neck length (L_n) and mass of the neck (m_n) varied from 10-14 cm and 1.2-2 Kg respectively. The θ values depended on the orientation of the subject's head.

5.3.4 Coupling moments calculated from haemodynamic model with the dynamic equation

Forces in each element are calculated from the haemodynamic model, and are resolved into components parallel to the three axes. The forces in the cerebral arteries and other inter cranial arteries are accounted in our work by scaling the forces in last four elements situated in the end leading to the cerebral arteries. The force in these elements is scaled by seven times their original force. These elements are chosen to reflect an approximate

distance of the cerebral arteries, the next major force contributing arteries after the carotid arteries, from X_0 . They are then used to find out moments, M_1 , M_2 and M_3 at X_0 about the three principal axes. The calculated values form the moments matrix $M_b = [M_1, M_2, M_3]^T$ are substituted into the dynamic equation, Equation (5.21). The completed dynamic equation is then solved for angular displacement using MATLAB's inbuilt ode solvers. The calculated angular displacements are further converted into linear displacements using the fixed distance between the forehead and X_0 , which are then projected onto a two-dimensional plane using trigonometric relations, $Y - Z$ (face). This projection is necessary to predict head-neck motion along two axes as a single lens camera can capture only two dimensional arrays, leading to the tracking of points along two directions. An overview of the full algorithm from the video capture and modelling components, to the prediction is given in Figure 5.4.

5.3.5 Modeling stenoses

Deweese *et al* [169] observed that the plaque build up starts about 1 cm before the bifurcation in the common carotid artery, and extends up to 1.5 cm into the internal carotid artery. The haemodynamic model is modified to artificially represent the occlusion by altering the vessel geometry. In the 1D haemodynamic model, the diameter in the last centimetre in the common carotid arteries and the first one and a half centimetres of the internal and external carotid arteries, are changed to values calculated from the following equation that depends on the percentage of blockage being analysed. The length and location of the stenosis are kept constant in this work, however, for future clinical application, scenarios with different lengths and locations of stenosis must also be considered during analysis as the force being exerted upon the head-neck system will vary for each scenario. The blockage in the left and right set of carotid arteries are set independently to accommodate different percentage of blockage in the respective arteries.

$$\% \text{ Blockage} = \frac{(\text{internal diameter of vessel} - \text{diameter of lumen at maximum occlusion point}) \times 100}{\text{internal diameter of the vessel}}. \quad (5.22)$$

Treatment of a stenosis in this manner assumes the most severe case possible, with the stenosis being treated a step decrease in the vessel area, which leads to the highest resistance estimation possible for a stenosis of a specific % blockage. The **ETM model** (Chapter 2), used in this work, has previously been compared with three-dimensional blood flow models for fractional flow reserve, in which the pressure drop across a

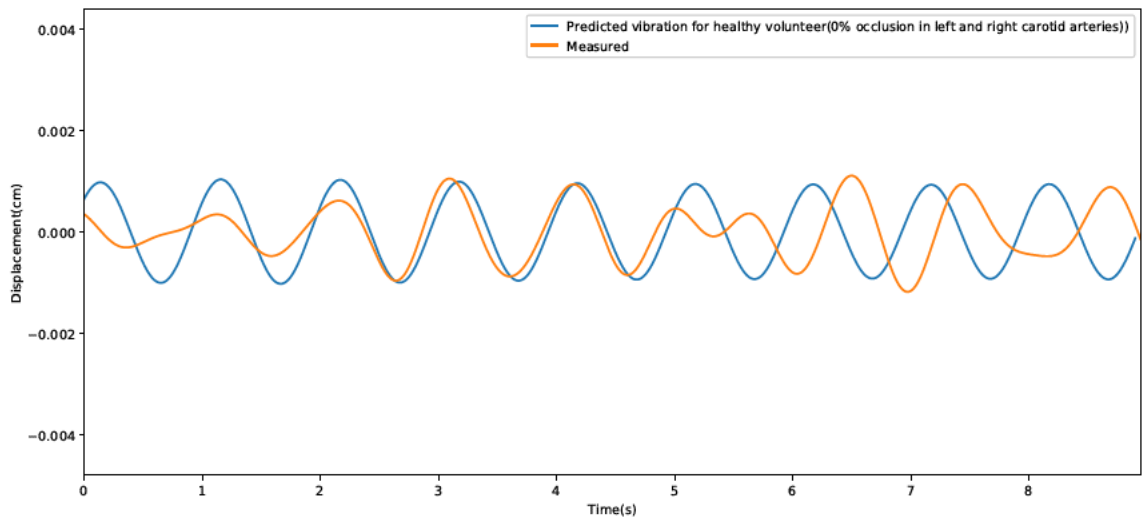
coronary artery stenosis is estimated. Satisfactory agreement is observed between these 1D and 3D modelling methodologies [170, 147]. During the simulation of the 1D blood flow model, the axial force is calculated as described in Section 5.3.2 which is coupled to the dynamic equation of the head-neck system, which is described in Section 5.3.3.

5.4 Results and discussions

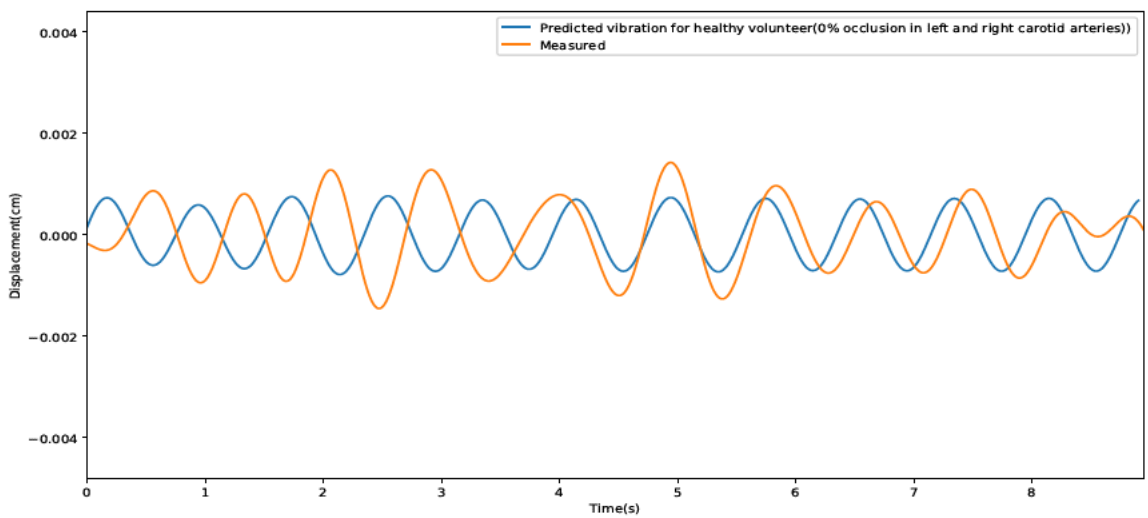
The results presented here are the first attempt to validate the proposed model. Although a precise match of head vibration against synthetic data is unlikely, the clinically relevant data required may simply be the amplitude of the head vibration. If the amplitude of a head vibration can be linked directly to the severity of carotid stenosis, the impact on the patient treatment pathway could be hugely significant. For example, the technique could be used to prioritise patient treatment when screening patients who are at risk of stroke. Considering the potential of such a technique to separate healthy and unhealthy individuals, we have provided two categories of results in this work. In the first category, the proposed procedure is applied to a group of healthy volunteers, while the second category involves a patient with a severe carotid stenosis.

The healthy subjects are chosen with the assumption that volunteers aged between 20 and 30 years do not suffer from carotid stenoses. We believe that this assumption is valid in most cases (95.5%) [171]. In addition to healthy volunteers, we also had access to the data of a single patient with a severe carotid stenosis, left untreated. This patient previously suffered from a stroke, as a result of the carotid stenosis, and in order to access the data, we obtained the required signed consent from the patient via the treating clinician. All the data used is anonymous and no personal information is disclosed at any point. The results of the model implemented in this work was not used in any way to inform patient treatment.

For both healthy subjects and the patient, individual face videos, weight, age and height are recorded with their consent. Once the basic data is collected, the computed systemic arterial circulation and vibration models of the individuals are scaled to closely resemble reality. The synthetic data is then generated for normal and stenosed carotid arteries. When dealing with stenosed arteries, the severity of the stenosis is varied between 50 and 92%. The synthetic data thus generated is presented in the form of time-dependent head vibrations. The synthetic vibrations are then compared against the measured vibrations to determine the approximate severity of the stenosis.



(a) Healthy volunteer A



(b) Healthy volunteer B

Fig. 5.9 Comparison of synthetic and measured head vibration for healthy volunteers

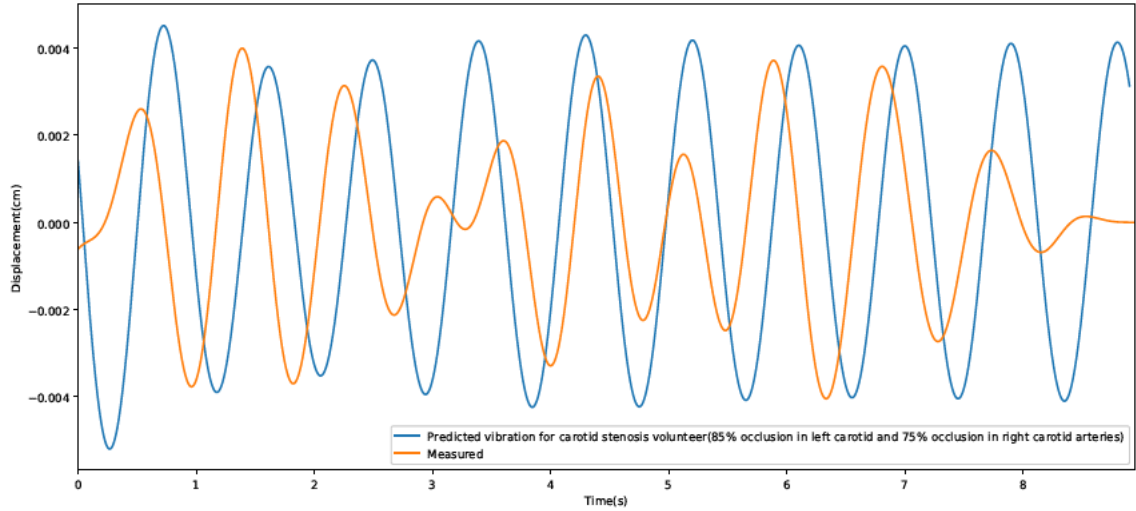


Fig. 5.10 Comparison of synthetic and measured head vibration for a patient suffering from severe carotid occlusions.

Figure 5.9 shows a comparison of head vibrations between synthetic and measured data. A satisfactory agreement is observed for both the magnitude and frequency of head vibrations. This indicates that the proposed method is correctly predicting the anticipated oscillations of the individual. Although not precise, an indicative prediction of severity is the starting point in non-invasively determining carotid occlusion. To further confirm the applicability of the proposed methodology, a video recording of a patient with a known carotid artery occlusion was taken. The comparison of *in vivo* measurements and synthetic data is shown in Figure 5.10. All occlusions below 50% may be classified as minor. Any blockage above this value is considered detectable using the proposed method. However, the signal from blockages above 70% may be harder to distinguish due to other cardiovascular issues such as cardiomyopathy. Thus, we categorise any occlusion above 70% as ‘requires attention’. In addition to assuming occlusions in only one of the carotid arteries, we require synthetic data that represents different combinations of occlusions in both left and right carotid arteries. Such data is created before the patient case mentioned is studied. The results as shown in Figure 5.10 matches satisfactorily for frequency and magnitude. This patient has nearly 70% blockage in both left and right carotid arteries, and thus is classified in the category of patients that require immediate attention.

5.4.1 Sensitivity analysis

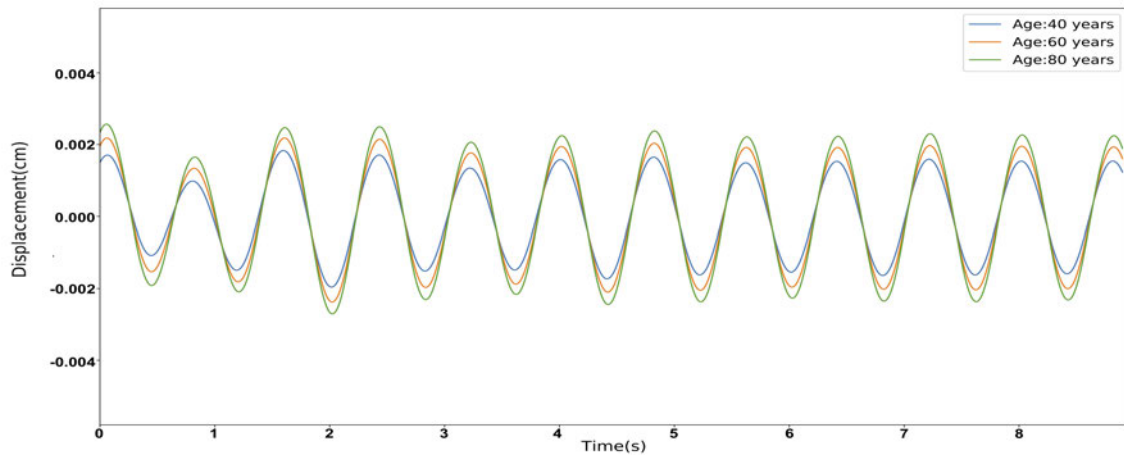
An analysis of the effect of each main input parameter on head-neck vibration is necessary in order to understand their interactions within the model. Among the main parameters, three that need to be analyzed critically are the input of age, neck length, and percentage of blockage. Age, which primarily affects the compliance of arteries, tends to cause a directly proportional increase in amplitude as the pulse wave velocity increases leading to increase in the friction force. Neck length, accounted in the dynamic equation, affects the amplitude by a significant amount. Variation of the blockage percentage is required to show how the mechanical model reacts to different severities of the stenosis. Figure 5.11 displays the effect of age, height, percentage of blockage (in the case of stenosis) when varied independently. For all simulations the heart rate is kept consistently at 72 beats-per-minute, allowing a straightforward comparison of the cases considered.

The input for the age sensitivity tests are shown in Table 5.2. For the age related simulations, it is assumed that all individuals are healthy, and do not have a stenosis. The pulse wave velocity estimation in the haemodynamic model increases with age. The amplitude of head oscillations predicted by the model in the virtual patient aged 80 years old are larger in magnitude than the 60 year old, which in turn are larger in magnitude than the 40 year old. This occurs even with a decrease in cardiac output for older individuals.

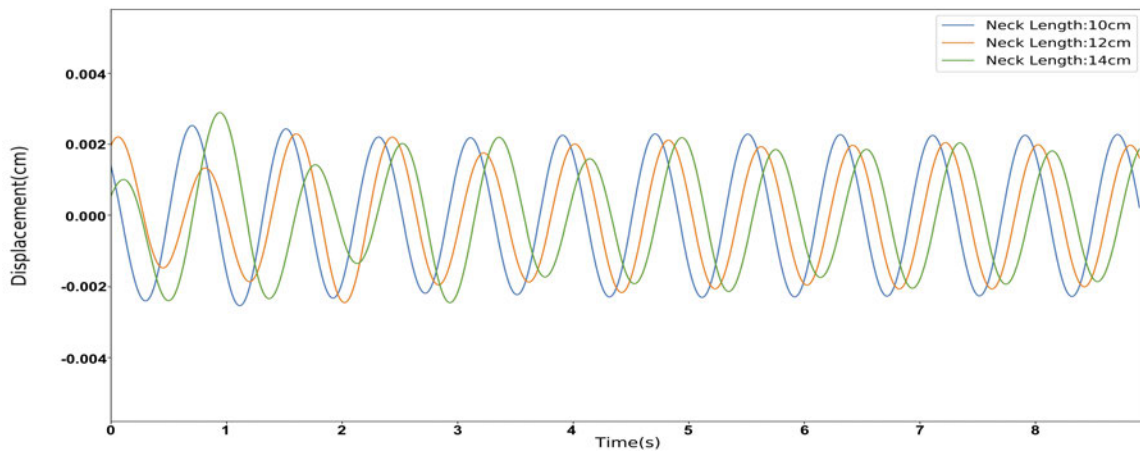
The neck length varies the model predicted amplitude of vibration for the head-neck system, and a phase shift is observed in Figure 5.11(b). This indicates that an accurate measure of the neck length could be crucial for the dynamic model to accurately predict the magnitude of head-neck oscillations. As expected the amplitude of vibration increases with an increased percentage blockage. The amplitude increase from 0.0034 cm in the case of a 50 % blockage, to 0.0041 cm in the case of an 80 % blockage. Noting the significant increase in estimation from approximately a 0.002 cm (or less) amplitude of the head-neck vibration in the healthy case, to over 0.003 for a 50% blockage, the model shows significant promise in potentially estimating the severity of a blockage in the carotid artery.

5.4.2 Discussions

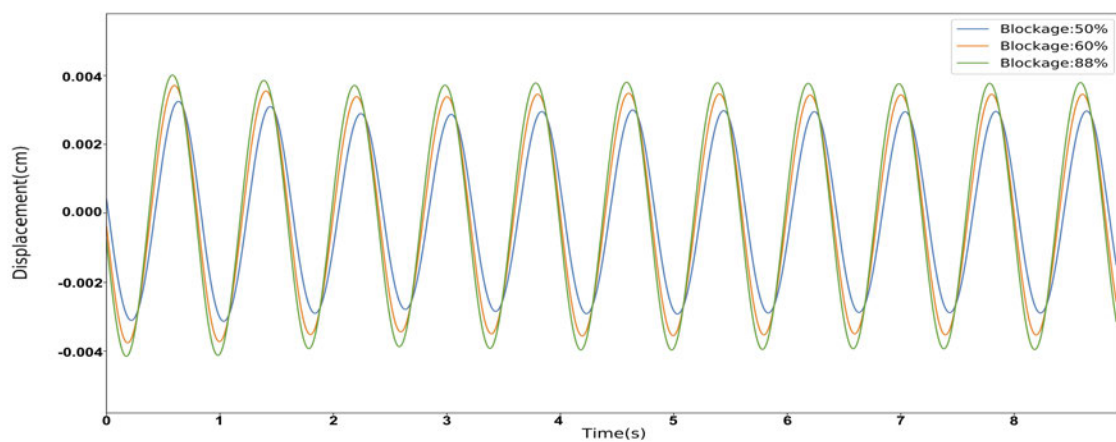
The preliminary results presented in the previous section require further refinement. Although promising, the insufficient number of patients do not allow us to produce a



(a) Head-neck vibration that can be observed when age is varied keeping other parameters constant. The neck length is kept constant at 12 cm and no stenosis is considered.



(b) Effect of subject's Neck length on vibration. The age is kept constant at 60 years and no stenosis is considered.



(c) Effect of blockage percentage in case of stenosis on vibration. The selected age is 80 years and neck length is 10 cm.

Fig. 5.11 Sensitivity analysis of different input parameters on head-neck vibration when other quantities have been kept constant

Table 5.2 Parameters of the sensitivity analysis for different ages, where PWV is the pulse wave velocity [172], MAP is the mean arterial pressure, and HR is the heart rate

Age	Cardiac Output (L/min)	PWV (m/s)	MAP ($mmHg$)	HR (bpm)
40	7.57	7.09	95.5	72
60	7.25	8.88	92.9	72
80	6.98	10.72	90.6	72

precise categorisation at this stage. Another important observation made is that only blockages above 60% gave significantly higher vibration amplitudes than unblocked arteries. This rise in vibration amplitude is due to the increase in force imparted by the fluid on the plaque.

Another point that requires refinement is the location of the occlusions. The synthetic data generated assumes that the locations of stenoses (both left and right side) have been fixed. By varying the locations of the stenoses, a large number of synthetic data can be generated but a manual comparison will then no longer be plausible. Thus more advanced methods such as well trained machine learning methods to find the right match between synthetic and measured data would be required.

Another difficulty that arises in this work is the selection of components from the PCA for models with stenosis. The selection of the correct component for analysis is an absolute necessity as the magnitude of signal is important here for estimation of the blockage percentage. The most efficient way this selection can be performed is by re-training a machine learning algorithm using cardiac output, arterial condition and physiological values from various patients as parameters. This will be possible only with the help of a large number of patient data, which will help us to produce a more accurate digital patient twin model.

5.5 Limitations

In this exploratory study, data from only one patient suffering from a stenosis was available. Typically someone suffering from a stenosis would undergo treatment to rectify this, and thus it is extremely difficult to get access to patients between the diagnostic and the treatment stages. This limits the number of classifications we can generate, given the small cohort size. To approximately circumvent this, we have created virtual patients with artificial stenosis to indicate what the proposed methodology works in terms of head vibrations. In the 1D blood flow equations a

stenosis is currently added in the common, internal, and external carotid arteries via a step decrease in vessel diameter. This is a simplistic representation of what are often complex geometries. In reality the stenoses may have varying geometric profiles that need more complex force estimations. There is a potential use for a scaling factor, which may aid in improving the accuracy of estimating these complex forces, and possibly take into account different geometries of plaque build up. However, this scaling factor needs to be calculated retrospectively by screening of TIA patients and potentially estimated by using machine learning techniques. The CAD model implemented is the same for all subjects. This is necessary as otherwise a scan for each patient would be required, which would defeat the purpose of this study, which is to investigate an inexpensive and fast technique to detect carotid stenosis. However, we have chosen the geometry in such a way as to minimize the number of false negative predictions. This is achieved by choosing a geometry which would produce the least amplitude possible for the head-neck vibration for both healthy and stenosed subjects.

5.6 Conclusions

A preliminary and very first attempt has been made to demonstrate that a coupled computer vision and computational mechanics model may be employed in the non-invasive detection of severe carotid stenosis. The results clearly indicate that the method proposed is viable but it has room for substantial improvements. Both the healthy subject cases and a patient case presented provide us with sufficient confidence that the proposed non-invasive procedure is simple and fairly effective. Further development is required in order for the method to move towards a clinically usable platform. We believe that there are many steps that require development to realise the clinical potential and use of the proposed method. For example, a deep learning based automatic detection system is required in order to eliminate the manual comparison between synthetic head vibration data from the model and the *in-vivo* head vibration captured through a video. The idea proposed here has a potential to non-invasively capture a large number of other blood flow related diseases if more sophisticated setups, such as multiple camera, accelerometer-camera, and thermal imaging cameras can be used. Like any other new methodologies, a substantial study using patient data is necessary to proceed from research to implementation. With further progress, the proposed procedure can move towards an active human digital twin, in which continuous monitoring of carotid stenosis/stroke potential may take place.

5.7 Summary

In this chapter, the concept of a semi-active digital twin is explored through an analysis of face videos for the detection of carotid stenosis and its severity. The amplitude of subtle head vibration caused by the pulsatile nature of blood flow in the carotid arteries is exploited in this chapter as it is a potential indicator of carotid stenosis. The process begins initially by capturing head vibrations of a patient from their face video, captured using a smartphone camera, and then comparing against expected head vibrations in that patient for healthy and various severities of carotid stenosis, calculated using a digital twin of the patient built using a personalised haemodynamic model coupled with a dynamic equation. The calculated vibration that best matches the measured vibrations allow for the detection of carotid stenosis and provide an estimation of its severity. This system is tested on a small cohort of healthy adults and one carotid stenosis patient, and satisfactory results are obtained providing confidence in the proposed methodology. This is the second form of digital twin being explored in this thesis, wherein the components being analysed by the twin are active but the analysis itself is carried out offline.

Chapter 6

Active Digital Twin

The concept of an active human digital twin is to replicate the functioning and physiology of an organ or organ system continuously. This concept is explored in this chapter for online haemodynamic analysis and monitoring. To begin with, a data-driven inverse analysis of the cardiovascular system using *in silico* data is proposed in the first part. Such an inverse analysis will assist in non-invasive haemodynamic monitoring with the least amount of input data. This section is available as a published peer-reviewed paper in the public domain [17]. The second part of this chapter begins by exploring the data-driven prognosis of arterial blood pressure waveforms, another crucial parameter for monitoring and predicting outcomes to allow for medical preparedness. The final section of the second part will propose a method to couple computational mechanics with artificial intelligence, using methods proposed in the previous sections. The chapter ends with a discussion on results obtained for the active digital twin method using waveforms taken from MGH/MF database.

Part I

Enabler model

6.1 Inverse analysis of human systemic circulation

An exponential rise in patient data provides an excellent opportunity to improve existing healthcare infrastructure. In this section, a method to enable cardiovascular digital twin is proposed using inverse analysis. Conventionally, accurate analytical solutions for inverse analysis in linear problems have been proposed and used. However, these methods fail or are not efficient for non-linear systems, such as blood flow in the cardiovascular system (systemic circulation) that involves high degree of non-linearity. To address this, a methodology for inverse analysis using recurrent neural network for the cardiovascular system is proposed in this section, using a virtual patient database. Blood pressure waveforms in various vessels of the body are inversely calculated with the help of Long Short-Term Memory (LSTM) cells by inputting pressure waveforms from three non-invasively accessible blood vessels (carotid, femoral and brachial arteries). The inverse analysis system built this way is applied to the detection of Abdominal Aortic Aneurysm (AAA) and its severity using neural networks.

6.2 Introduction

Data driven analysis and monitoring are key drivers for the evolution of state-of-the-art healthcare. With increase in patients requiring medical care [173], data generation and accumulation is also increasing at an alarming rate [174]. This increase has put additional stress on an already challenging medical cyber-infrastructure. In addition to data accumulation, increase in number of patients is also causing unprecedented delays in critical care, as a result of rise in waiting lists. It is also important to note that late diagnosis is a significant reason for medical complications. Since a significant number of diagnosing and monitoring tools employed in critical care are invasive in nature, time consuming, expensive and labour-intensive, rise in these delays have become inevitable. This has given rise to a need for alternative but robust diagnosis and monitoring tools that can non-invasively detect medical conditions or diseases and help to monitor them with minimal amount of data. A potential key towards development of such tools is artificial intelligence, owing to its capacity to perform complex analyses.

With recent advancements in artificial intelligence, especially in the area of deep learning, medical applications are being extensively developed with the help of neural networks and other deep learning algorithms. Many of these applications have shown promising results [175] and are indicating a future of better and faster tools that will

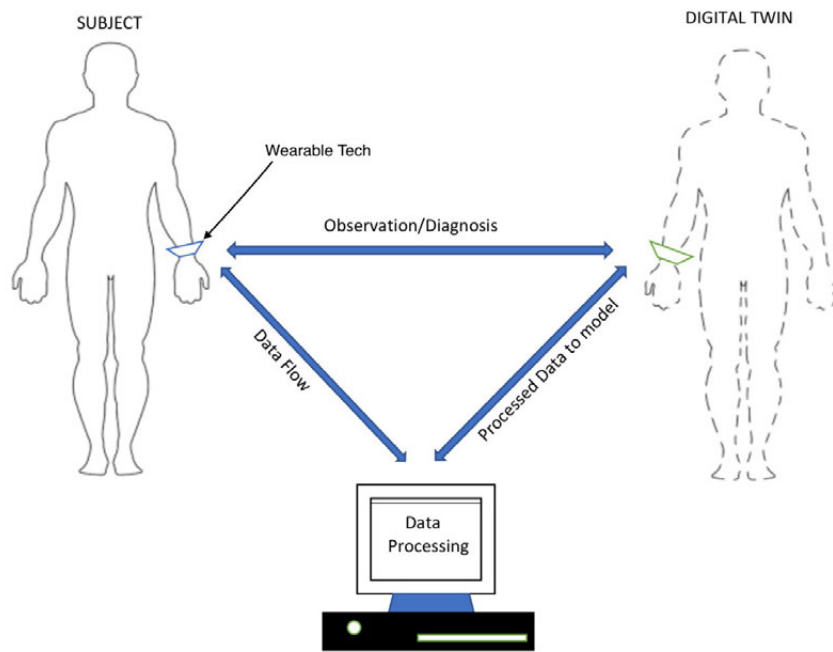


Fig. 6.1 A schematic representation of envisaged digital twin.

not only detect and monitor medical conditions and diseases but also prevent them before they set in. However, a major issue plaguing this advancement is the treatment of deep learning algorithms as ‘black boxes’. Logical justification of results generated by these algorithms are difficult owing to the complexity of non-linear transformations involved, leading to growing distrust amongst medical personnel and academicians [176]. Majority of these deep learning algorithms use supervised learning, a method wherein the algorithms are trained using samples obtained from general patient population. This leads to an observation that high chances of misdiagnosis still exist as the analysis is not patient specific. To overcome the above challenges, a digital twin is envisaged as a potential solution as shown in Figure 6.1.

A digital twin, virtual representation of an individual, can help perform patient oriented analysis, using continuous feed of data, thereby increasing the accuracy. This twin can take many forms ranging from investigating only a part of the body to a comprehensive model to study the body in its entirety. The process of making a digital twin can be classified into active, passive and semi-active digital twins. In an active digital twin model, a systemic circulation model is continuously adjusted by continuously monitoring the circulation, at accessible locations and feeding real data into the model as shown in Figure 6.1. This type of digital twin has potential

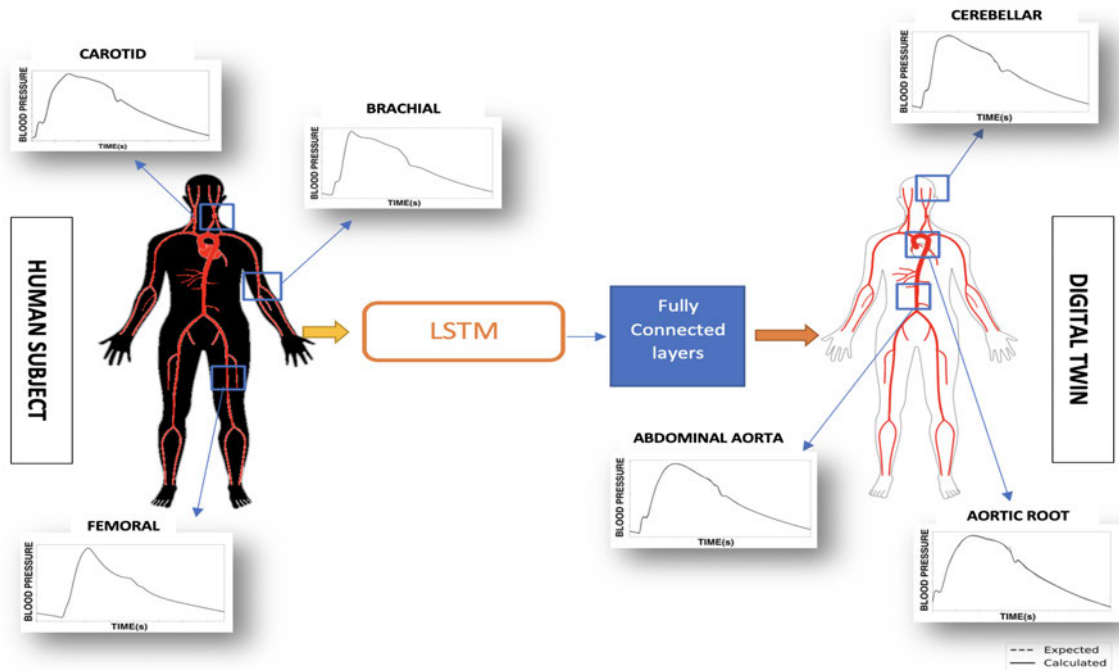


Fig. 6.2 Schematic of inverse analysis to determine wave-forms at different locations using three measurements at accessible locations as input.

applications to diagnosis and monitoring of cardiovascular diseases such as stroke, cardiomyopathy, arrhythmia, aneurysms, stenoses or a combination of these problems occurring at the same time. The passive digital twins (Chapter 4) are the ones in which we use the data obtained to create an off-line model (Chapter 5). This is very common in many of the subject-specific blood flow modelling studies. Some examples of such study include fractional flow reserve (FFR) calculations, understanding rupture potential of aneurysms and stenoses, etc. These passive digital twins can be enhanced to make active or semi-active digital twins by carrying out calculations online while measurements supplied to the underlying model. A semi-active digital twin may have components that have some dynamic nature built in as shown by [16].

Active digital twins work on the principle that the parameters of numerical model being used are updated continuously. This requires constant monitoring of different characteristics within a human system for estimating the parameters of the model. In a human systemic circulation, such monitoring will be fast and cost effective if it can be carried out non-invasively at the peripheral arteries. Since pressure wave forms at the peripheral arteries are easily accessible, determining the waveforms inversely

in the remainder of the systemic circulation may provide an easy way of assessing the health of an individual. Thus, inversely estimating the pressure waveforms at various locations of the systemic circulation is key to building an active digital twin. Therefore, an inverse analysis using deep learning is proposed in this chapter. Inverse analysis will help in estimating blood pressure waveforms at different locations of the human body by using minimal number of input pressure waveforms. These inversely calculated waveforms can further help in parameter estimations required for updating the systemic circulation model. However, one of the complexities involved in performing inverse calculation or inverse modelling, especially in non-linear problems, is the potential of obtaining non-unique solutions. However, with the aid of deep learning and appropriate constraints, it is now possible to obtain unique solutions [177].

As a demonstration of possible applications of inverse analysis in a cardiovascular system, an example of Aortic Abdominal Aneurysm (AAA) detection and severity classification is also described. An aortic aneurysm is a progressively growing dilation of the aorta with a risk of potentially lethal rupture. Successful treatment of an aneurysm depends on how early it is detected, as the post rupture mortality rate is around 80% [178]. To detect an AAA in time, a continuous and expensive screening programme is necessary. The existing methods of detection of AAA have several drawbacks. Ultrasound echography is currently considered the most practical and inexpensive modality in AAA screening, but it has limitations due to the fact that the aorta is buried deep in the body. The Ultrasound measurement can be obstructed by bowel gas, obesity, calcification, and other artefacts [179]. The shape and size of the aneurysm can be determined accurately by 3D CT or MRI methods but they are substantially more expensive and require injection of a contrast agent. Therefore, they are mainly applied at the latter stages of AAA evolution [180][181]. Besides the aneurysm size, its rupture time depends on mechanical properties of the vessel wall that cannot be determined from the above modalities directly [182]. Since the diameter of aneurysm is one of the key factors in assessing the severity of the condition, a neural network model may be used to detect and classify the severity of this problem using computed diameters. Various recent studies, such as Wang *et al* [183] and Jones *et al* [184], have shown promising results for AAA detection using machine learning algorithms such as neural networks. In [183], pulse waves have been successfully used for detection of AAA using Bidirectional Recurrent Neural Networks (BRNN), built using Long Short-Term Memory (LSTM) cells. In [184], multiple traditional machine learning algorithms have been analysed to detect AAA using six haemodynamic measurements

from the common carotid, brachial, and femoral arteries. However, in this chapter, an upstream blood pressure waveform is first calculated near the end of abdominal aorta using deep learning powered inverse analysis and the result obtained is then analysed using Convolutional Neural Network (CNN) for detection and classification of AAA. This is one of the several potential applications of inverse analysis, proposed in this chapter.

In this chapter, three key steps are followed to build and demonstrate the use of deep learning in inverse analysis. Firstly, a database containing computationally generated, realistic blood pressure waveforms is produced using a reduced order model and machine learning. Secondly, a neural network is built and trained to predict unknown blood pressure wave forms using accessible waveforms as input data, as shown in Figure 6.2. As seen in the figure, the data inputted at accessible locations (left) is employed to predict pressure wave forms at other locations (right). Finally, an additional neural network is trained to analyse the waveforms predicted by the inverse model to detect Abdominal Aortic Aneurysms (AAA) and their severity.

Briefly, as an essential step to realize the concept of a digital twin, following objectives are proposed. 1) Demonstrate the idea of inverse modelling using the neural networks on human systemic circulations, and 2) Propose the idea of using inverse analysis for the detection of an Abdominal Aortic Aneurysm (AAA) and its severity.

6.3 Methodology

In this chapter, the primary objective is to develop a system capable of performing inverse analysis on cardiovascular time sequences such as blood pressure waveforms. To demonstrate this, aortic blood pressure waveform, which is a critical parameter to assess the cardiac state of a person, is inversely calculated with the help of deep learning methods. This is carried out using blood pressure waveforms from easily accessible and measurable arteries such as radial, femoral and carotid arteries as inputs.

Supervised learning approach is adopted to perform this deep learning based inverse analysis. Since the usage of an existing database is a key component to this approach, access to large amounts of data becomes a necessity. However, for biomedical applications, access to large amounts of data means access to thousands of patients and their medical records, which is challenging given the time required and feasibility. To circumvent this problem, in this chapter, a method to generate virtual patients, a close approximation of human patients, is proposed. These virtual patients are

used to build the database required to train deep learning algorithms. The inverse method demonstrated in this chapter may be extended to real patients using wearable technology.

6.3.1 Virtual Patient Database

The objective of virtual patient generation for a cardiovascular system is to build a numerical model for blood flow that closely resembles a human patient in terms of blood flow parameters and vascular network. Previous research in virtual patient database generation methods can be found in references [185–187]. Two key components are required to build such realistic models, a validated one-dimensional haemodynamic model and realistic arterial networks based on anthropometric and haemodynamic parameters to represent a reliable human cohort.

One Dimensional haemodynamic model

The haemodynamic model used in this work is the **ETM model** explained in Chapter 2, which considers a vascular network of 123 of the major vessels in the systemic circulation.

Scaling vascular network and cardiac outflow parameters to create realistic human models

Prior to the generation of a synthetic patient database, a personalised model generation process is proposed to realistically and physically represent human systemic circulation. The personalised model of the systemic circulation for a human patient is generated by adapting geometric and haemodynamic parameters using nominal and ordinal inputs, such as gender, age, weight and height. This type of adaptation on the above 1D model has been validated against *in vivo* data in previous publications [143, 144, 44].

To achieve a realistic representation of arteries in the systemic circulation model, the geometrical parameters of the vascular network used in the above haemodynamic model are scaled using validated empirical relations (such as Eqs. (6.1), observed or derived by various studies [40–43] on general population, that are functions of parameters such as weight, height and age (left half of Figure 6.3). These relations lead to the geometry and mesh for a patient. Some of the equations used for scaling are:

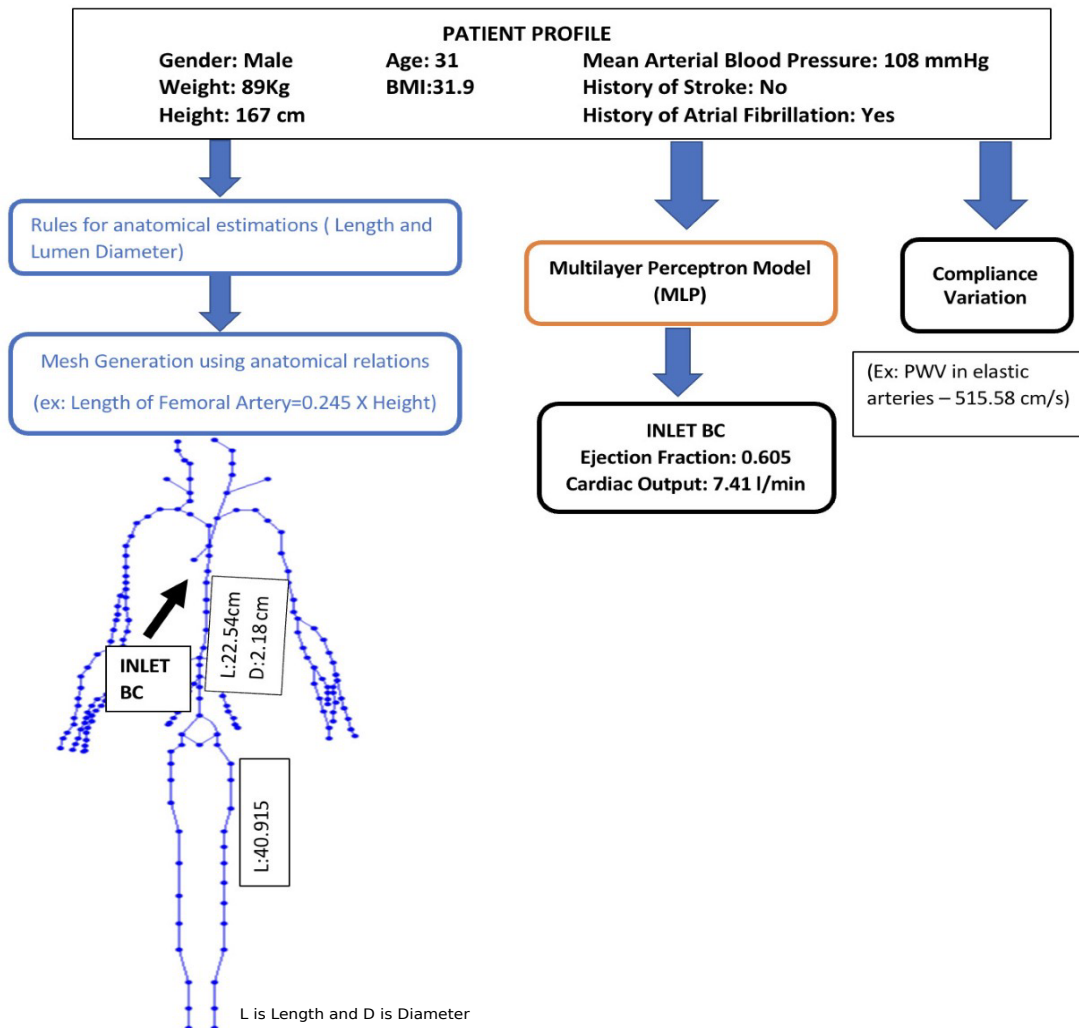


Fig. 6.3 Example of personalised model generation using patient profiles. This includes three parallel workflows: for generation of the geometrical mesh parameters (left), for generation the inlet boundary conditions (centre) and for generation of elastic parameters of the mesh segments

$$L_{\text{femoral}} = 0.245H \quad (6.1a)$$

$$L_{\text{descending aorta}} = -2.6235 + 0.1507H \quad (6.1b)$$

$$D_{\text{abdominal aorta}}(\text{begin}) = 14.10 + 0.13A + (-1.09 + 0.04A)G + 5.8 \text{BSA} \quad (6.1c)$$

where A is the age in years, H is the height in cm, G is the gender (1 for male, 0 for female), BSA is the body surface area in m^2 . Parameter ranges of the scaling are described in Section 6.4.1.

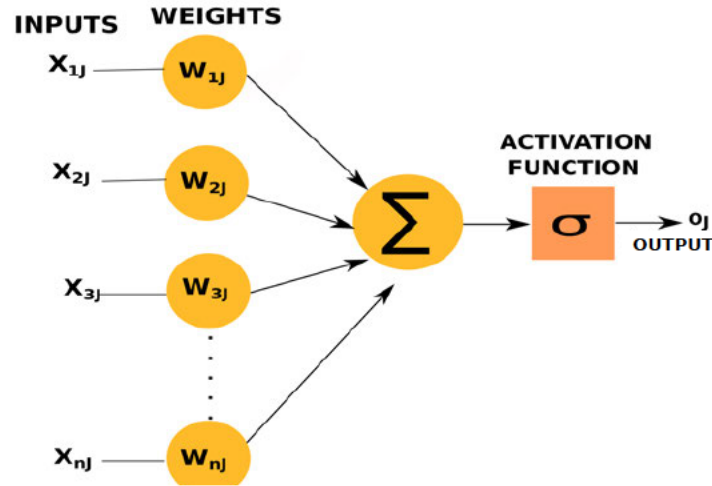


Fig. 6.4 An artificial neuron used in Multilayer Perceptron model (MLP).

The cardiac outflow parameters such as ejection fraction and cardiac output are used to modify inlet flow boundary conditions at the aortic root. These values are calculated using multilayer perceptron (MLP) models [188], as shown in Figure 6.4. Multilayer perceptron model is a type of neural network, as explained in Chapter 3. Every node of this network represents a connected unit called artificial neuron or perceptron. In Figure 6.4, x_{nj} are the discrete input values, w_{nj} are their corresponding weights. The weighted inputs are summed up and the sum is non-linearly mapped using an activation function σ to obtain an output O_j . One neural layer confines a certain number of these neurons. A cascaded setup of several of these hidden neural layers, along with an input layer and an output layer, constitute the neural network.

For calculating inlet flow boundary conditions, the MLP models are trained using a public medical database [189, 91] with inputs such as the mean arterial pressure, pre-existing heart conditions and so on as shown in central workflow in Figure 6.3.

These MLP models have an architecture of three to four hidden layers, with each layer having the number of neurons varying between 2 and 32, along with an input layer with the number of neurons varying between 4 and 7, and an output layer of one neuron for predicting the value of interest. The hidden layers have ‘TanH’ or hyperbolic tangent as activation function and output layer has either ‘sigmoid’ or ‘ReLU’ (Rectified Linear Unit) depending on the output being predicted. For example, in the case of ejection fraction, since the expected value is between 0 and 1, the sigmoid function is the suitable activation function for the output layer. All models are trained with Mean Squared Error (MSE) as the cost function and ‘Adam’ optimizer [64].

Haemodynamic parameters of the mesh, such as compliance of the vessels, calculated using pulse wave velocity (PWV), is adjusted for ageing related changes using equations from literature [190], as shown in the rightmost workflow in Figure 6.3.

In order to create a realistic virtual patient database and obtain a closer approximation of actual human patients, the above described personalised model generation is adopted to create patient profiles of the required number of virtual patients, as shown in Figure 6.3.

To train machine learning algorithms with better accuracy, virtual patient databases need to be chosen such that it covers a wide range of data, accounting for various combinations of input parameters (Age, weight, height, gender, blood pressure and pre-existing heart/medical conditions). The input parameters in personalised model generation, representing anatomical and haemodynamic input parameters of a patient, is referred to as a patient profile in this work (see Figure 6.3). Based on required number of virtual patients, a number of such patient profiles are generated by randomising the input parameters, by sampling a uniform distribution of these parameters. Each of these patient profiles are used to generate the required number of virtual patients, each representing a unique cardiovascular system. A sample of one such virtual patient is shown in Figure 6.3. Here, the three parallel processes for mesh generation, calculating inlet boundary conditions and haemodynamic parameters are represented by three workflows. In total, a database of 4137 such healthy virtual patients are generated. Healthy virtual patients refer to patients without any Abdominal Aortic Aneurysm (AAA), to be described in the next section. More details of generation of the database are presented in Section 6.4.1.

6.3.2 Application of inverse analysis in Abdominal Aortic Aneurysm (AAA) detection

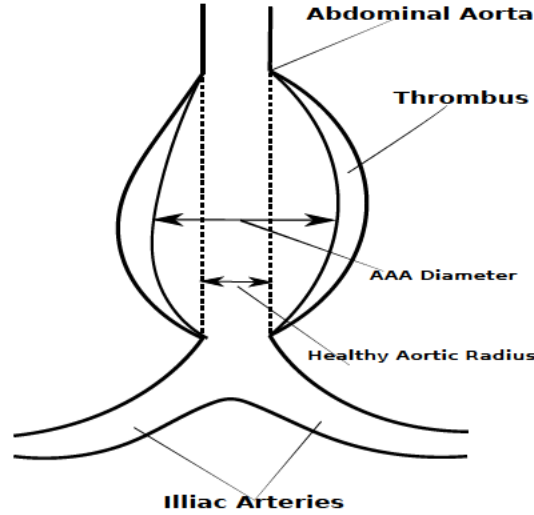


Fig. 6.5 A model of an Abdominal Aortic Aneurysm.

Abdominal Aortic Aneurysm (AAA) mainly occurs above the junction where aorta branches out into iliac arteries (see Figure 6.5). Various factors such as ageing, smoking, etc. can conduce decrease of the elastin fibers, that can result in a significant increase in vessel wall stiffness in this part of aorta. The enhanced blood pressure, along with the increased vessel stiffness, can cause the expansion of the vessel beyond the elastic deformation, leading to localised increase in diameter of the vessel.

The increase in diameter leads to decrease of the characteristic impedance of arteries, which is an essential parameter for propagation and reflection of pulse waves in the arterial system [191]. The characteristic vessel impedance can be evaluated from the equation,

$$Z = \frac{\rho c_0}{A_0} = \frac{4}{\pi} \frac{\sqrt{2\rho \left(\frac{4}{3} Eh\right)}}{D_0^{5/2}}. \quad (6.2)$$

where E is the Young's modulus, D_0 is a reference lumen diameter, h is the wall thickness. As it is seen from Equation ((6.2)), the characteristic impedance decreases proportionally with $D_0^{-5/2}$ if the wall stiffness does not change with increase in aneurysm size. Nevertheless, the characteristic impedance can stay constant if the vessel wall stiffness $\frac{4}{3} Eh$ increases dramatically with the aneurysm diameter (of the order of D^5).

In vivo measurements of effect of AAA diameter on the wall stiffness appears to show that the wall stiffness can increase with the growth of aneurysm [192], which is not confirmed by [193]. This makes dependence of $\frac{4}{3}Eh$ on D questionable. Some studies [194] indicate that aneurysm ruptures are caused by localized degradation and weakening of the wall. Therefore, at least in a number of critical cases, when the vessel is about to rupture, we could assume that the wall stiffness, and hence the characteristic impedance, at the location of rupture are almost non-existent. In this case, the aneurysm will lead to a significant wave reflection that can be detected during the waveform analysis.

Virtual patients with AAA are modelled with fusiform aneurysms in the abdominal aorta. The diameter is varied sinusoidally along the length of the aneurysm [195], with the widest area occurring at mid-length. The aneurysms are classified into Small AAA (3 cm - 4.4 cm), Medium AAA (4.5 cm - 5.4 cm) and Large AAA (> 5.5 cm) aneurysms. Within each category, diameter for each AAA virtual patient was randomly chosen. However, post database generation, at least one occurrence of all diameters within one decimal place between 3 cm to 6.9 cm was verified in order to account for every possible diameter. As the wall stiffness is of crucial importance in large aneurysms, it is indirectly modified using pulse wave velocity (PWV). In order to mimic critical cases, where rupture of vessel wall is imminent, in few personalised models the stiffness is made very low by decreasing PWV drastically at randomised locations along the aneurysm. In these locations, local PWV of 5 elements are reduced to values between 14% to 30% of their original PWV. The local stiffness for small and medium AAAs are not modified. This allowed for wide range of possible AAA cases to be simulated. AAA virtual patients are added to the database using their generated personalised models. The range used for randomised selection of input parameters, required for calculating anatomical and haemodynamic parameters, is similar as that of healthy (non-AAA) cases (see Section 6.4.1). Generating all possible combinations of input parameters and AAA sizes is not feasible. Hence, a randomised selection of their combinations is chosen to generate as many different combinations as possible in the database.

In total, a database of 8659 virtual patients is created with 4137 healthy (or non-AAA) cases and 4522 AAA cases.

Understanding blood waveforms in AAA

The database generated in subsections 6.3.1 and 6.3.2 consists of a collection of pressure waveforms, each of which represents a different vascular geometry and aneurysm

parameters. In order to give the reader an insight in to the variation of waveforms captured in the database, a detailed analysis of these waveforms is presented in this section. The pulse wave velocity (PWV) in the ascending aorta, an elastic vessel, varies between 5 m/s and 10 m/s, depending on age, and increases towards the peripheral arteries. Analysis of a typical *in vivo* waveform, in the frequency domain, shows that the first 5 harmonic components contain 95% of the pulse energy.

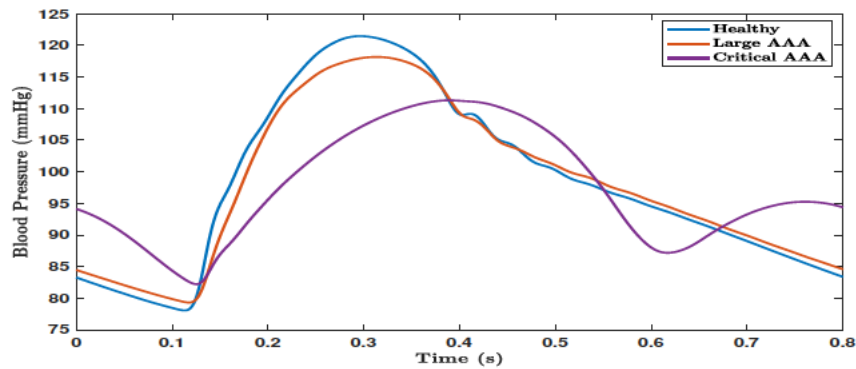


Fig. 6.6 Blood pressure waveforms (simulated) in abdominal aorta computed close to its distal end for healthy, Large AAA and critical AAAs (where the vessel is about to rupture) cases.

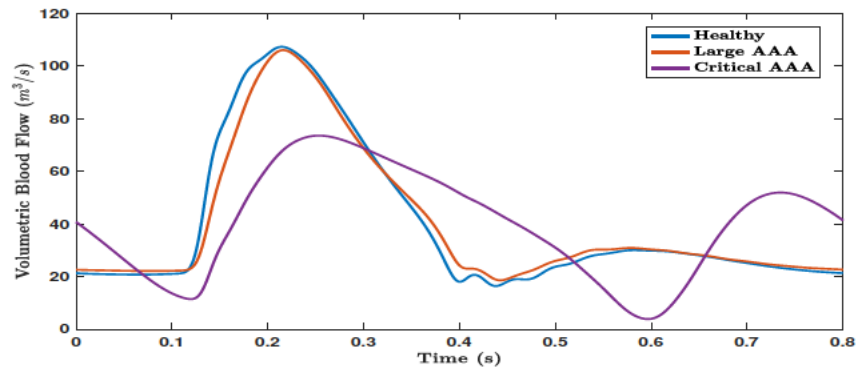


Fig. 6.7 Volumetric Blood Flow Rate (simulated) in abdominal aorta computed close to its distal end for healthy, Large AAA and critical AAA (where the vessel is about to rupture) cases.

Figures 6.6 and 6.7 respectively show the variation in pressure and flow rate waveforms for healthy and aneurysmal aortas. Large AAA refers to aneurysms with AAA diameter greater than 5.4 cm and critical AAA refers to large AAA which is about to rupture, with critical points on vessel wall where stiffness is close to zero. In Figures 6.6

and 6.7, a small phase shift can be observed in volumetric blood flow rates between healthy, large AAA and critical AAA conditions. These observations make this medical condition a suitable application for deep learning, where parameters can be observed in compounded non-linear domains. In this chapter, only blood pressure waveforms are used for deep learning applications.

6.3.3 Deep learning for inverse pressure wave form calculation and AAA classification

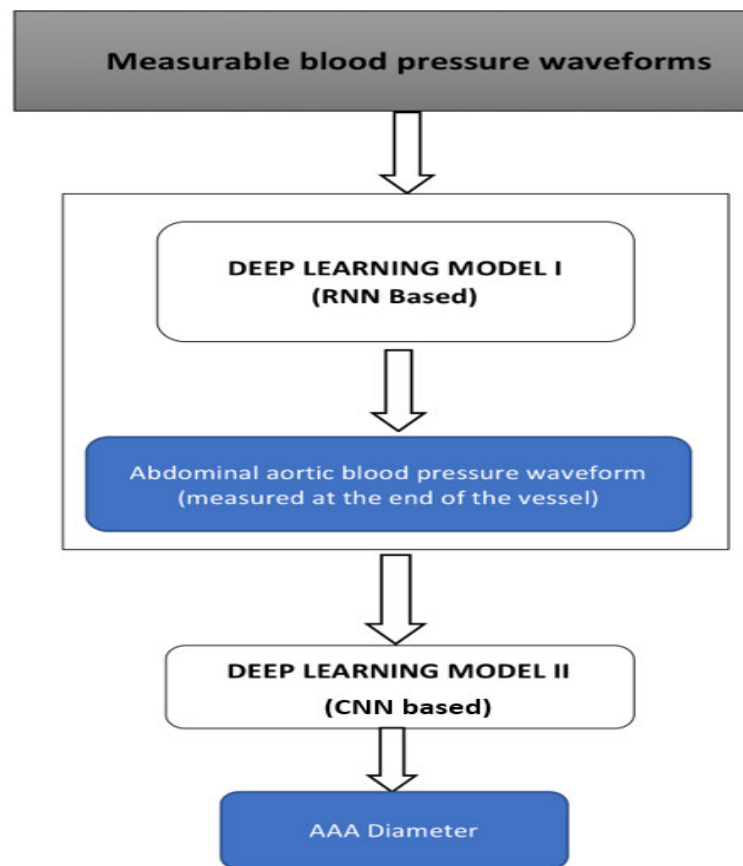


Fig. 6.8 LSTM based inverse analysis and AAA classification.

Deep learning, a type of machine learning, involving multiple layers of non-linear transformation is the method chosen in this work to perform supervised learning. Major part of deep learning involves usage of artificial neural networks. Basic building blocks

of these networks are nodes or connected units called artificial neurons or perceptrons, which incorporate a non-linear mapping of weighted inputs, as shown in Figure 6.4.

The patients' database described in Section 6.3.1 is used to train deep learning algorithms for performing inverse analysis. Upon completion of such an inverse model, deep learning is further used in the development of AAA classification tool to calculate the parameters of interest, which in this example is the diameter, using outputs generated by the inverse model (See Figure 6.8). In summary, a deep neural network is first used to determine waveforms at various locations of a blood flow network and then an additional neural network of a different configuration is employed to analyse AAA diameter.

Long Short-Term Memory (LSTM) based Neural Network for Inverse Analysis

The primary objective of inverse analysis, shown in Figure 6.8, is carried out using a Recurrent Neural Network (RNN) [196]. RNNs are a form of neural networks designed to handle sequential data, which use a concatenated input consisting of output from previous step and input from current time step. Output from previous time step refers to the prediction made by the RNN cell for input values of the previous time step. Input from current time step refers to the value present in external input data provided to the RNN cell, at that particular time step. Since the input data of interest is sequential in nature (pressure waveforms from available sites such as carotid, femoral and brachial arteries), an RNN is found to be the most robust and computationally viable option. Amongst the different types of RNNs, the most suitable form is a Long Short Term Memory (LSTM) cell [66] [65]. Regular RNN cells perform well, especially when the short duration data is processed. However, they fail when this duration increases. This issue is solved in an LSTM cell of the kind shown in Figure 6.9 that keeps track of dependencies between elements in the input sequence using a cell state.

A cell state is a parallel flow of data in an LSTM cell. It allows for certain information to be carried in parallel to actual data to track various dependencies between elements. For example, in the context of blood pressure wave forms, prediction of dichrotic notch depends on information from peak blood pressure, predicted several time steps before the notch. Such long term dependencies can be retained in the cell state. In Figure 6.9, the cell state (C_i) is passed through the upper channel and a concatenated signal, consisting of input from current step (X_i) and output from previous step (Y_{i-1}), is passed through the lower channel. Gates F_i , I_i , C , are used

to learn from previous steps and predict the next one. Each of these gates refers to a combination of neural layer connected to the cell state through a logical operator or combination of logical operator and other gates. Based on the logical operation carried at the end of their respective neural layer, gates can be identified for their functions such as to forget, retain, select or modify cell state which in turn affects the output value.

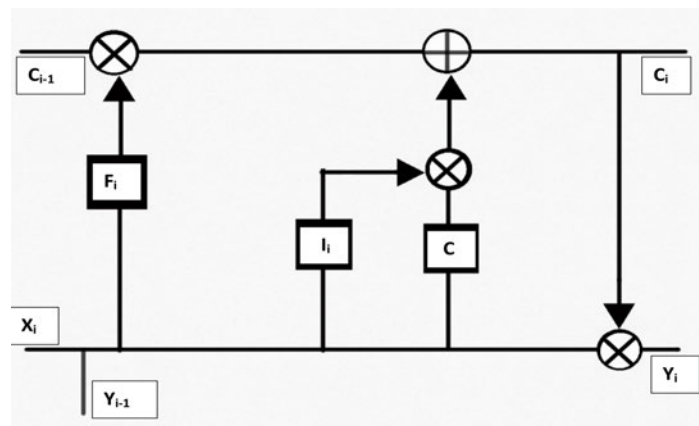


Fig. 6.9 Long Short-Term Memory (LSTM) cell consisting of cell state as well as forget, input and output gates

Using blood pressure waveforms measured for one cardiac cycle at three locations, carotids, brachial and femoral arteries, the above neural network model calculates time sequences, which here are the blood pressure waveforms, from various arteries of the body, some of which are located upstream. It is observed that only one or two input blood pressure waveforms, with different combinations between carotid, femoral and brachial arteries, failed to predict with the same level of accuracy as that from three inputs. Thus, it can be inferred that a minimum of three input blood pressure waveforms and their time sequences are required to achieve acceptable levels of accuracy. The neural network architecture used is detailed in Table 6.1. The model is compiled with Mean Squared Error(MSE) as the cost function and trained with ‘Adam’ optimizer, a modified gradient descent method [64]. The data is split into training (80%) and testing data sets (20%). During training, the training dataset is further split into training (80%) and validation subsets (20%).

Convolutional Neural Network for AAA Classification

In AAAs, the blood pressure waveform close to the distal end of abdominal aorta is a superimposed wave that includes reflections and negative pressures. This waveform

Table 6.1 Architecture of Deep learning model I

Type of RNN cell	Long Short Term Memory
Number of hidden layers	2
Number of cells in hidden layers	32
Number of inputs	3
Number of fully connected layers	1(output layer)
Cost Function	Mean Squared Error
Optimiser	ADAM
Batch size	300
Number of Epochs	1400

contains effects of any vessel enlargement. It is important for us to extract these features from the waveform in order to detect and analyse the severity. Traditionally, signal processing techniques such as Fast Fourier Transforms [191] and CEPSTRUM analyses are considered as suitable options for such feature extraction. However, with deep learning, these features can be extracted with compounded non-linear mapping, thereby extracting higher number of features compared to the traditional methods. The most suitable neural network for such application is a Convolutional Neural Network (CNN) [197]. CNNs use convolution to extract features from the data. The weights or coefficients in the filters, or convolutional layers, used for these convolutions are trained using a gradient descent based optimiser to extract the features affecting the parameter of interest, which in this work is the AAA diameter.

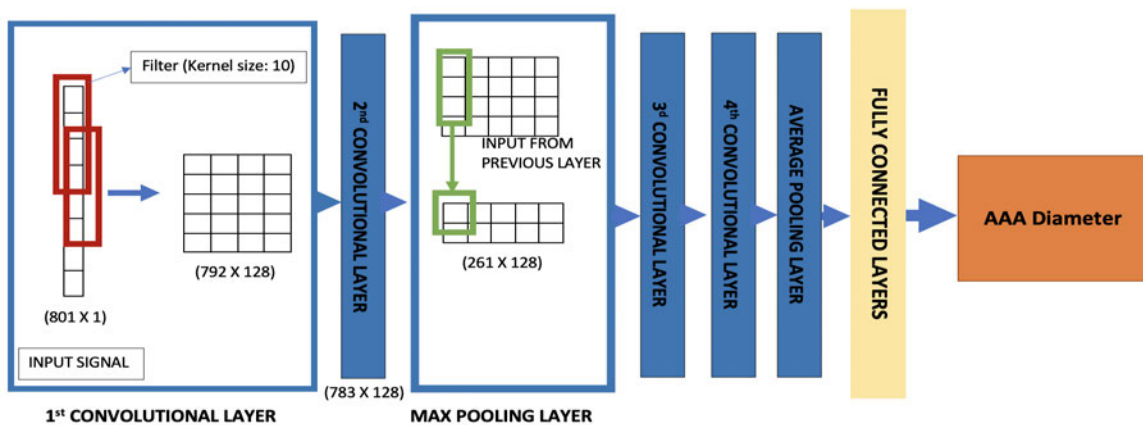


Fig. 6.10 1D Convolutional Neural Network used to detect severity of AAA.

The waveform inversely calculated by the RNN model at a location on the abdominal aorta close to the distal end, about 3cm downstream, is the input set to a 1D-CNN (see Figure 6.10) classifier which is trained to extract features from the signal and classify the severity of the aneurysm into categories based on the AAA diameter. The categories or classes chosen in this work are healthy (<3cm), small AAA (3cm - 4.4cm), medium AAA (4.5cm - 5.4cm) and large AAA (>5.4cm). The architecture of the 1-D CNN model is detailed in Table 6.2.

The convolutional neural networks employed here utilize convolutional filters in first two layers to capture features from the signal. Convolutional filters use the operation of convolution, multiplication of predetermined weight matrix of a chosen size, to highlight or extract certain aspects in the data provided. Features extracted from them are then compressed using maximum pooling layer, which chooses the maximum amongst extracted features in a given window. To perform with better accuracy, the output from maximum pooling layer is further passed onto another set of convolutional layers before pooling the features using global average (see Figure 6.10). The pooled features are then used by fully connected layers, perceptron layers, to estimate the severity of AAA. This network is compiled with ‘categorical crossentropy’, a combination of softmax function and cross entropy [198], as the cost function. Since classification uses probability distribution, categorical crossentropy uses softmax function i.e,

$$f(s)_i = \frac{e^{s_i}}{\sum_{j=1}^C e^{s_j}}, i = 1, \dots, C \quad (6.3)$$

to calculate a probability distribution. Here s are the output scores, a value in the range of 0 to 1, calculated by the neural network for each of the C number of categories. Equation (6.3) is used to calculate loss as

$$CE = -\sum_i^C t_i \log(f(s)_i) \quad (6.4)$$

Here CE is the cross entropy with t_i being the target or expected probabilities and $f(s)_i$ is the calculated probabilities. In training, the data is split into training (80%) and testing data sets (20%). Stratified K-fold cross validation method is used to train and evaluate the model. In K-fold cross validation method, the data is split into K subsets, and the model is iteratively trained by holding out one of the subsets as the validation set. Each subset is marked as the validation set only once during the iterations. Here, the number of folds, K, is 10. This approach is adopted in order to mitigate the problem of overfitting, as it allows for tuning of hyperparameters within

Table 6.2 Architecture of Deep learning model II

Type of Neural Network	Convolutional Neural Network (CNN)
Number of hidden layers	8
Number of filters	128 (1 st and 2 nd convolutional layers) 256 (3 ^d and 4 th convolutional layers)
Kernel sizes (Convolutional layers)	10 (All layers)
Number of pooling layers	2 (1 max pooling and 1 average pooling)
Number of fully connected layers	3
Number of cells in fully connected layers	16,8,4
Number of input sequences	1

the training dataset by iteratively holding out one of the ten folds as validation set. The only difference between K-fold cross validation and stratified K-fold cross validation is that the subsets are chosen such that there is equal representation of data from each of the categories in a multi-class classification.

6.4 Results and Discussion

In this section, results observed for inverse analysis using LSTM based neural network (RNN) and the example of application of inverse analysis to detection of Aortic Abdominal Aneurysm (using CNN) are presented and discussed in some detail. A brief analysis of the above generated virtual database is also presented to give the readers an overview of the baseline characteristics amongst the virtual patients.

6.4.1 Analysis of the virtual database

The virtual database generated consisted of a total 8516 patients, with 4137 healthy cases and 4392 AAA cases.

Table 6.3 shows the average values as well as minimum and maximum values seen in virtual database for healthy patients. The pulse wave velocity (PWV) recorded in

Table 6.3 Baseline characteristics of virtual patients (without AAA) used in the virtual database [199, 200, 172, 201].

	Average [95% CI] [n=4137] (Females=1734)	Minimum value	Maximum value
Age (years)	61.39 [60.87-61.90]	30.00	89.00
Weight (Kg)	96.11 [95.62-96.59]	40.00	120.00
Height (cm)	174.94 [174.47-175.41]	150.00	200.00
Ejection Fraction (%)	61.82 [61.74-61.91]	57.00	66.99
Pulse Pressure (mmHg)	53.46 [53.09-53.83]	28.08	87.81
Cardiac Output (L/min)	5.72 [5.70-5.75]	4.50	7.00
Pulse Wave Velocity (m/s)	9.20 [9.16-9.23]	6.80	11.96

this table refers to heart-femoral pulse wave velocity. The average value of PWV and different parameters in the 1D model, which include both inputs and measured values upon convergence, are observed to be within acceptable ranges for general human population [201][172]. Furthermore, extreme cases within physiologically acceptable range for each parameter, as shown in minimum and maximum values, have also been generated and recorded in the database. These cases allow for the neural networks, upon which the objective of present work is primarily based on, to be trained on a wide variety of physiologically possible cases for achieving higher accuracies.

Table 6.4 shows the average values (with 95% Confidence Interval) of key parameters in AAA virtual patients. The maximum and minimum input values for the AAA patients are similar to that of non-AAA patients (See Table 6.3). Values in Tables 6.3 & 6.4 are chosen for close physiological representation of general human population. However, since several approximations and assumptions are made in the 1D model, a lot of features may be lost with respect to real human patient data. Thus, any system trained on these databases must be bolstered with real human data, using transfer learning or other methods before being tested in clinical settings.

6.4.2 Inverse analysis using Neural Networks

As mentioned previously, inverse analysis is performed to predict blood pressure wave forms at various locations in the arterial network using virtual measurement at peripheral arteries. The inverse analysis model developed using LSTM based neural network, during training, calculated blood pressure waveforms at arteries located

Table 6.4 Baseline characteristics (average, 95% CI in brackets) of virtual patients (with AAA) used in the virtual database.

	Small AAA [n=1958] (Females=915)	Medium AAA [n=1164] (Females=455)	Large AAA [n=1400] (Females=436)
Age (years)	67.29 [66.70-67.87]	74.40 [73.81-74.98]	77.80 [77.47-78.13]
Weight (Kg)	95.47 [94.74-96.19]	97.25 [96.3-98.21]	87.71 [87.13-88.29]
Height (cm)	174.18 [173.49-174.87]	176.11 [175.20-177.02]	177.95 [177.20-178.70]
Ejection Fraction (%)	61.85 [61.50-62.21]	62.45 [62.00-62.89]	60.44 [60.22-60.66]
Cardiac Output (L/min)	4.72 [4.67-4.77]	4.68 [4.62-4.74]	6.77 [6.70-6.83]
Pulse Pressure (mmHg)	42.04 [41.45-42.63]	42.73 [42.02-43.44]	70.53 [69.76-71.29]
Pulse Wave Velocity (m/s)	8.97 [8.92-9.02]	9.45 [9.39-9.50]	10.54 [10.51-10.57]
AAA Diameter (cm)	3.97 [3.96-3.98]	4.98 [4.96-4.99]	5.97 [5.95-5.98]
AAA Length (cm)	5.31 [5.27-5.35]	5.79 [5.74-5.83]	7.75 [7.71-7.80]

upstream to the points of input measurement, such as aortic root and abdominal aorta, with an acceptable levels of accuracy. The results from this model is analysed primarily for two aspects. Firstly, its capacity to predict important features of the waveform such as dichrotic notch in aortic root. Secondly, the accuracy with which the blood pressure values at each time step is calculated. In order to explain different aspects of this analysis, results from one healthy virtual subject (from the virtual patient database) is described in this section.

The input blood pressure waveforms are measured in carotid, femoral and brachial arteries as shown in Figure 6.11. These waveforms are obtained from the haemodynamic model of a virtual subject. The measurements are taken from nodes located midway along the length of the arteries.

Figure 6.12 shows the waveforms at abdominal aorta, left cerebral artery, and aortic root. Both calculated (solid line) and expected (dotted line) are shown. The dichrotic notch (occurring at approximately 0.36s), peak pressure (occurring at approximately 0.25s), minimum pressure (at the start of the cardiac cycle), and shape of waveform for different arteries are calculated. As seen, both calculated and expected pressure wave forms agree excellently apart from minor differences observed in the aortic root. This accuracy extends also to the case of a virtual patient suffering from AAA (see

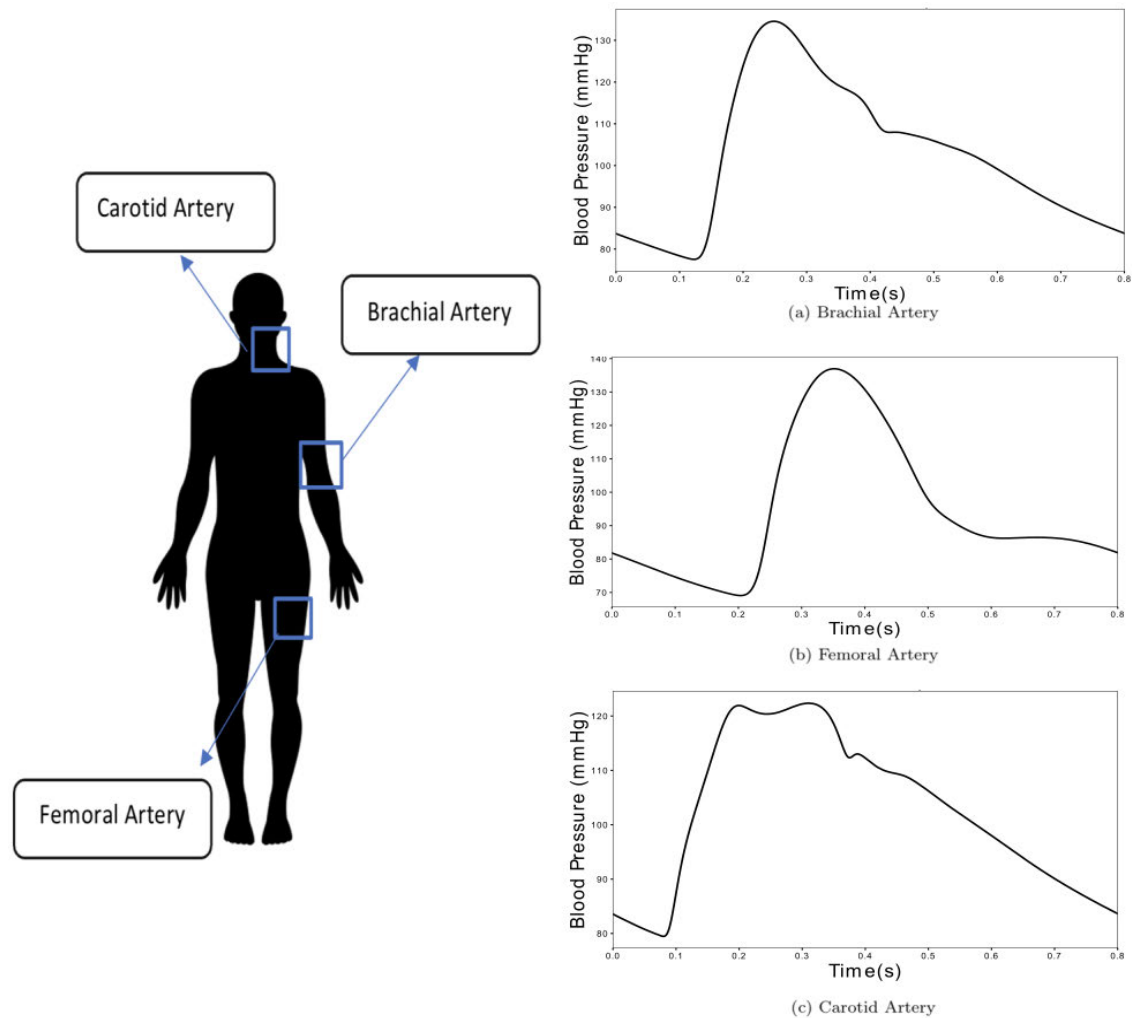


Fig. 6.11 Input blood pressure waveforms measured at three different locations.

Figure 6.13). The only significant deviation found in these output waveforms, which is also observed in other virtual patients, occur slightly before the dichrotic notch.

When observed on the entire virtual patient database, proposed procedure performs with promising results. Blood pressure waveforms in arteries upstream to the input vessels (carotid, brachial and femoral) such as aortic root, abdominal aorta and iliac arteries (see Figure 6.12) are calculated with an acceptable lowest accuracy of 98.81%, amongst the arteries. As mentioned in 6.3.3, the data is split into 80% for training dataset and 20% testing dataset. The lowest accuracy observed amongst the waveforms predicted for testing dataset, which is not used during training, is 94.16%. An acceptable accuracy, is assumed when averaged error between expected and calculated pressure wave forms over a cardiac cycle is less than 0.5 mmHg.

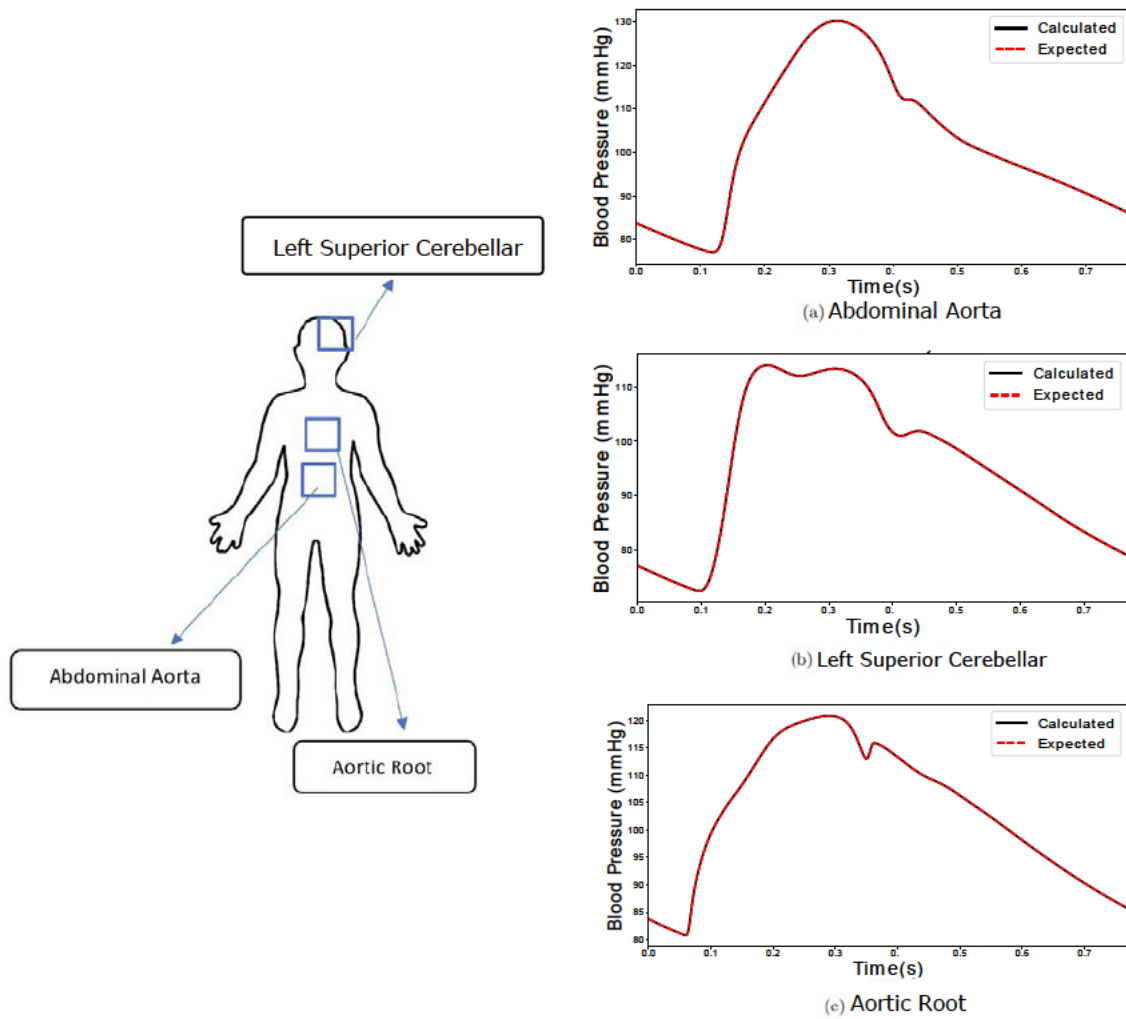


Fig. 6.12 Outputs calculated for inputs in Figure 6.11 by RNN in healthy subjects at different locations.

6.4.3 Application of inverse analysis to the classification of Aortic Abdominal Aneurysm (AAA)

In this section, Convolutional Neural Network (CNN) is used to classify AAA severity based on diameter into categories (Healthy (<3cm), Small AAA (3cm - 4.4cm), Medium AAA (4.5cm - 5.4cm), Large AAA (>5.5cm)), with an accuracy of 97.79%, when observed over the entire database. On testing dataset, data not used for training, network is observed to perform with an accuracy of 90.58%.

Characteristics such as relatively higher pressure in femoral artery compared to brachial artery in healthy patients, a contrast to AAA cases, could be one of the

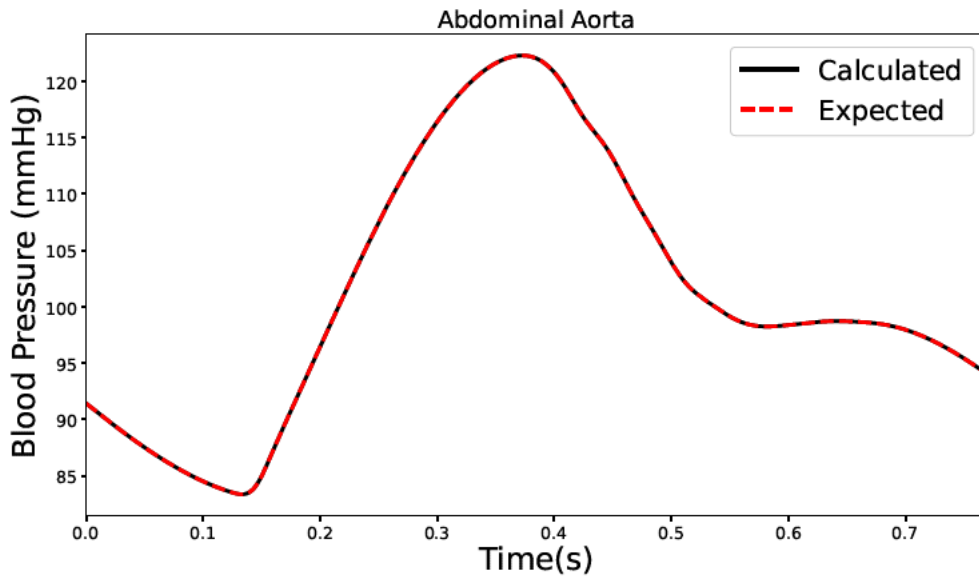


Fig. 6.13 Output calculated at the distal end of abdominal aorta by LSTM based neural network for inverse analysis in a human patient for Large AAA condition.

important features picked up by the CNN using pressure waveform calculated at the distal end of abdominal aorta (see Figure 6.13). The CNN, using convolutional filters in cascaded non-linear domains, captures various features of this waveform to detect AAA and classify its severity. Figure 6.14, a confusion matrix, displays the performance of the classifier with respect to multi-classification [97].

In the confusion matrix (Figure 6.14), it can be observed that true positives (4332 patients) and true negatives (4136 patients) make up the highest number of outputs calculated, making it a potential system with high reliability.

Furthermore, when only detection of AAA and not its severity to be considered, close to ideal performance of 99.91% accuracy can be observed. It must be noted that in Figure 6.14, all miss-classified cases below their actual severity (lower diagonal) are treated as false negatives and the ones above (upper diagonal) as false positives. However, when only detection of AAA is considered, only the cases miss-classified as healthy are considered as false negatives. With very low number of false negatives, proposed method may be seen as a reliable method when used as a detector of aneurysms.

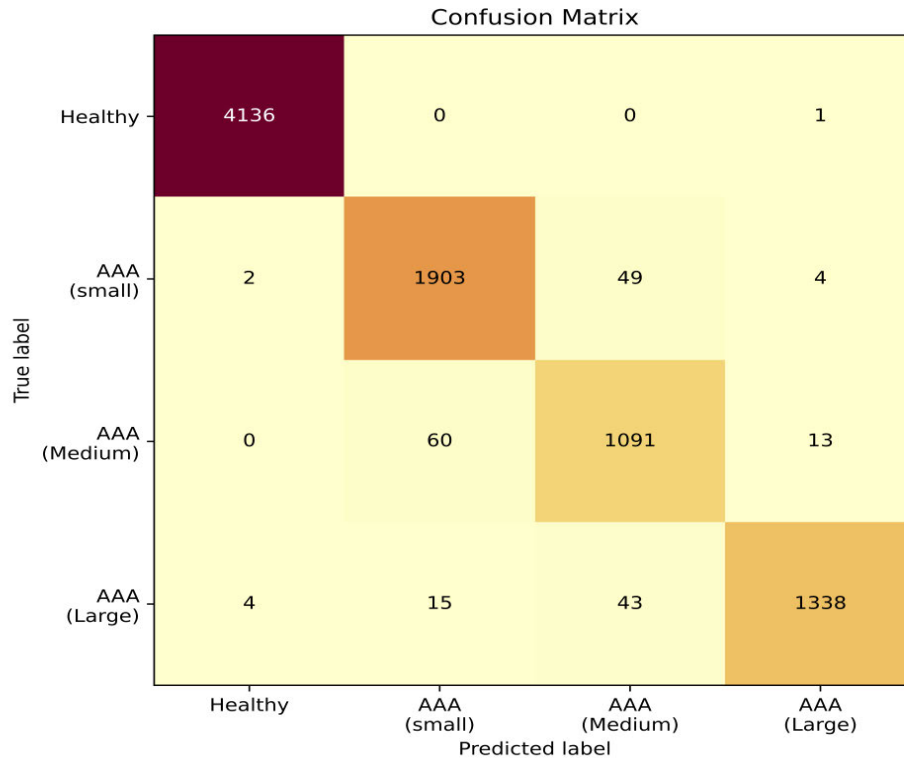


Fig. 6.14 Confusion matrix to understand the performance of the model for virtual patients in the entire database.

6.5 Conclusions

The proposed approach of inverse analysis makes development of an active digital twin, capable of continuously monitoring, and preventing medical conditions from developing or further aggravating feasible. This approach for biomedical applications with the help of non-invasive or minimally invasive measuring tools has the potential to reduce dependencies on sophisticated and invasive diagnostic tools.

In the case of a cardiovascular system, this approach is potentially implementable in clinical environments and aids in monitoring critical vessels and cardiovascular parameters. The method presented in this work can perform inverse analysis with high accuracy. It detected problems such as AAA with an accuracy as high as 99.91% and classified its severity with acceptable accuracy of 97.79%. With these results obtained in this work, it can be concluded that this approach may be used to monitor parameters

with on-par accuracy to that of conventional diagnostic tools if the real system behaves according to the physics employed in this chapter.

However, two key issues still need to be resolved before deployment in clinical environments. Firstly, since only one cardiovascular condition is modelled, the possibility of multiple other conditions or diseases generating the same output waveforms still exist. This is a common problem faced in inverse analysis, where multiple solutions for a given problem are possible. This work proposes the idea of using deep learning technique for inverse analysis in biomedical applications. However, a solution of using probability distribution for identifying the cause, when multiple clinical conditions gives rise to the same output, needs to be developed to avoid false diagnosis.

Secondly, since the deep learning model is trained on a virtual patient database, possibility of decrease in accuracy of the system is possible when exposed to clinical environments. To avoid this, the system must be additionally trained using transfer learning on real human patient data.

Part II

Truly active model

6.6 Data driven forecasting

The continuous monitoring of cardiovascular state using digital twins incorporates a replication of cardiovascular parameters, such as systemic vascular resistance and cardiac output, and the cardiovascular geometry. The idea of inverse analysis presented in Part I provides a way to assess cardiovascular parameters. However, idea of active digital twin extends beyond simple prediction of parameters, but continuous online estimation of current and future states of the system it replicates to make a decision. In this section, a deep-learning powered method is proposed to perform such a forecast for blood pressure waveforms using publicly available waveform datasets.

It is important to note that the concept of inverse analysis presented in the previous part, though ideal for active digital twins, is not feasible for *in vivo* application within the scope of this thesis. The lack of availability of data or datasets containing *in vivo* measurements of all the three required input blood waveforms, measured simultaneously, makes it difficult to use it within this thesis for further concept building. Gathering such data will require a large amount of time and funds to conduct clinical trials, which is out of the scope for this thesis. However, since the objective of this thesis is not just to propose different forms of human digital twins but also provide a proof of their functionality in real life (*in vivo*), further concepts required for an active digital twin is explored in this part of the chapter using a publicly available large clinical database.

6.6.1 Data selection and processing

The Massachusetts General Hospital (MGH)/ Marquette Foundation (MF) waveform database [202, 91] is chosen for the development of active digital twin concepts here. The MGH/MF wave form database consists of electronic recordings of haemodynamic and electrocardiographic waveforms of stable and unstable patients in critical care units, operating rooms and cardiac catheterisation laboratories. This database is publicly available and it consists of recordings from 250 patients.

Here, the arterial blood pressure wave forms from 203 of the 250 patients, with arterial line readings are used to train simple forecasting models to predict or forecast short term systolic, diastolic, and mean arterial blood pressure. In the recordings for each patient, 15% of the BP waveform data at the beginning and the end of the recordings are removed (as shown in Figure 6.15). Then, the waveform is split into smaller samples, with each sample having a length of 10 minutes. The systolic BP

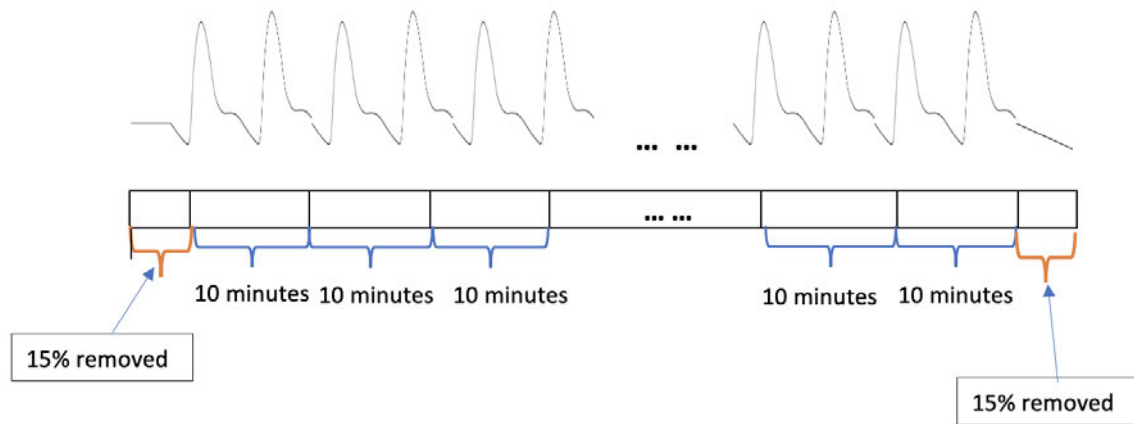


Fig. 6.15 Preprocessing of blood pressure waveform data to split it into samples of 10 minutes.

value, at peaks of each cardiac cycle, (identified using find peaks function from SciPy library [203]); diastolic blood pressure, at the trough of each cardiac cycle; and mean arterial pressure (MAP), calculated over each cardiac cycle, are extracted and recorded.

Each of these parameters recorded over a 10 minute sample is used to predict or forecast their values for 3-10 cardiac cycles that will occur 10 minutes after the end of the last cardiac cycle in the sample.

6.6.2 Neural network architecture and training

‘Shallow’ neural networks with one LSTM layer and two dense layers are used to predict each of these three parameters. Since the number of input points are small and simple, shallow networks are preferred over deep neural networks in this case. In Table 6.5, all training parameters used to train these neural networks are described.

Table 6.5 Parameters used to train neural networks for forecasting of BP values.

Number of inputs	1 waveform
Number of layers	3 (1 LSTM and 2 dense layers(MLP))
Number of output neurons	10 (for max. 10 cardiac cycles)
Activation function(dense layers)	‘Relu’ (hidden layer) & sigmoid (output)
Optimiser	Adam [64]
Number of epochs	500
Batch size	5
Total number of samples	529
Training-validation split	80%-20%

After training, following accuracy levels (considering a case as accurate overall error is less than 5 mmHg) were observed, for each of the desired parameters:

- Neural network for systolic blood forecasting- Training accuracy of 62.2% and Testing accuracy of 61.3%
- Neural network for diastolic blood pressure forecasting- Training accuracy of 73.9% and Testing accuracy of 70.8%
- Neural network for mean arterial blood pressure forecasting- Training accuracy of 69.3% and Testing accuracy of 67.5%

The final concept of combining the system proposed in this section along with continuous monitoring of haemodynamic system through 1D haemodynamic model is described in the following section.

6.7 Continuously adapting 1D haemodynamic modelling system

In this section, a system for continuously adapting parameters of a 1D haemodynamic model to replicate the haemodynamic state of a patient, using measured blood pressure waveform forms, is proposed. This section begins by describing the system and principles behind each step. Then, an example of diagnosing and monitoring sepsis is described to demonstrate the functioning of the proposed system in cardiovascular monitoring. Further, this section also describes the coupling of the forecasting system proposed in the previous section with the continuous monitoring proposed in this section before concluding the chapter with discussions of the results obtained for the sepsis example.

6.7.1 Closed loop system

The continuous modification of a 1D haemodynamic model, so as to replicate the haemodynamic state of a patient, requires modification of boundary conditions for fluid parameters. The boundary conditions can widely be divided into the inlet flow, characterised by cardiac functioning and outflow, vascular capillary bed resistance and external pressures, applied on vessels. Since only the cardiac vessels are subjected to significant amounts of pressure from surrounding tissue, external pressures in all other

elastic vessels are ignored in this work. In this subsection, a method to continuously alter the inlet boundary conditions and capillary bed resistance is proposed and discussed.

Vascular geometry may alter over a long period of time but small changes over a short period of time can be ignored. However, as in any other object in nature, there are exceptions to this assumption, for example during vascular repair surgery. In this work, scenarios with changes in vascular geometry over a short period of time are avoided and the mesh is assumed to be constant for the complete period of monitoring.

Ideally, inlet boundary conditions are best suited to be estimated using inverse analysis, using measured wave forms from peripheral vessels as explained in Part I. However, to build and test a system with such an estimation using available *in vivo* measurements from public databases is difficult. Such a system is not reliable with just one blood pressure waveform, since only one arterial line BP measurement is captured and recorded in publicly available databases. Hence, an alternative way is explored using just one BP waveform to estimate the inlet boundary conditions here.

In this work, for demonstrating active digital twins, continuous modifications of 1D haemodynamic model (**LCG model** described in Chapter 2) is carried out by altering the following control parameters within the 1D model -

- Left ventricular peak pressure
- Relaxation time (in ventricular pressure)
- Vascular compliance (altered using β , representing the material properties of the vessel wall)
- Systemic vascular resistance (capillary bed resistance, altered by varying area gradient(taper) in terminal vessels)
- Heart rate

These parameters are chosen as they are crucial to model the haemodynamic state during sepsis, an example described in the next section. In the case of sepsis, the systemic vascular resistance decreases with the severity of sepsis, causing the heart to adjust for maintained circulation. Heart rate, left ventricular peak pressure, and relaxation time are necessary to replicate cardiac activity. Vascular compliance and systemic vascular resistance are necessary to replicate vascular characteristics and downstream resistance respectively during sepsis.

Table 6.6 Range of physiological values used to generate the reference waveform database . * A_{0i} is the initial area at the start of the terminal vessels.

Parameters	Value range
Left ventricular peak pressure	55-125(mmHg)
Relaxation time	0.20-0.32 s
Vascular compliance	adjusted according to age (25-85 years)
Systemic vascular resistance	$0.4A_{0i}$ - $0.9A_{0i}$ *
Heart rate	50-185 BPM

In addition, the system is also designed to alter the mesh for personalised digital twin representation of the patient. However, since some of the required data, height and weight of the patients, is not available in the MGH/MF database, data used to test the system, this feature is not used for the problem presented in the following subsection. The estimation of above control parameters over time in two phases, warm-up phase and active phase.

Warm-up phase : In this phase, the system is exposed to the patient’s arterial blood pressure waveform for the first time. An initial approximation of the above control parameters are made in this phase. In this work, to perform such an estimation, a large reference database with waveforms calculated using the 1D model, for various combinations of control parameters using values chosen over a range shown in Table 6.6, is generated. The second cardiac cycle, from the beginning of the patient’s BP waveform data, is extracted and compared with waveforms from the reference waveform database, to find the closest resembling pre-calculated waveform. The parameter used in the generation of the best-matched waveform is used as the initial estimate for the control parameters. To match similarities between two waveforms, the Dynamic Time Warping (DTW) method is used to measure the cost or error between any two waveforms. It is an algorithm capable of measuring similarity between two temporal sequences, that may or may not be of same speed. The initial estimate for control parameters are then fine tuned to generate a ‘mature digital twin’ (1D model) capable of generating the closest resembling BP waveform to that of measured input. In this work, fine tuning or calibration of 1D model is carried out by running simulations with small variations of the control parameters and choosing the combination of parameters that generates waveform with highest similarity to the input.

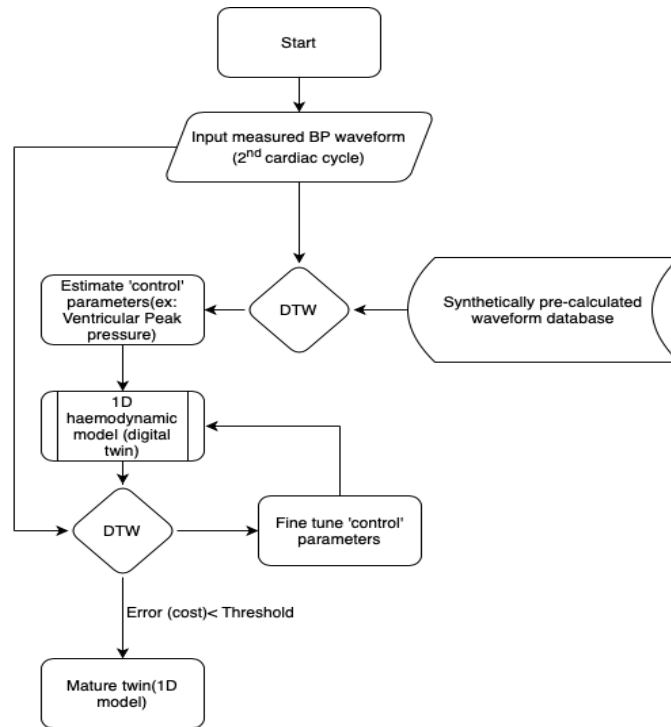


Fig. 6.16 Flowchart for the warm-up phase.

Active phase: Further on, continuous blood pressure waveform data from the patient, starting approximately one minute after the beginning of reading is intermittently utilised for further updating of the model, obtained from the warm-up phase. Approximately 12 continuous cardiac cycles are extracted every 10 minutes from the continuously arriving BP waveform data. Out of the 12 cardiac cycles extracted, n individual cardiac cycles (consequent or non-consequent) are selected and the control parameters are modified individually adapted for replication of each of the n waveforms. The parameters estimated over n cardiac cycles are averaged to represent the cardiovascular state of the patient in that particular 10-minute time period. Higher values of n allow for better averaging of the cardiovascular state as more pulse pressure variation can be captured. The computational capacity to simulate n cycles within 10 minutes dictates the value of n . Thus based on computational speed available, n is chosen as 3 for this work. Further, the waveform data in that particular 10-minute time period is also used to forecast or predict the patient's cardiac state after 10 minutes. This process is continuously repeated every 10 minutes until either manually stopped or no input waveform data is provided.

Figure 6.17 shows the complete workflow followed in the active phase. This phase can be subdivided into two parts, updating of the digital twin model (1D model) using

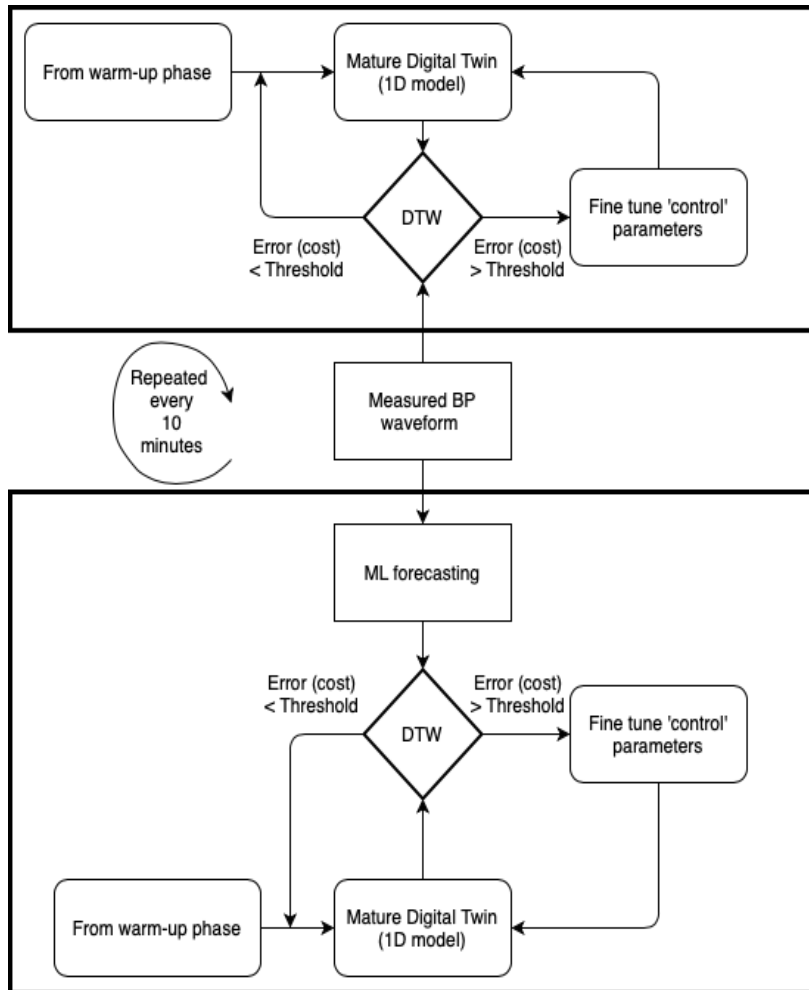


Fig. 6.17 Flowchart for the active phase.

measured data (with recently measured 10 minute time period) and forecasting of blood pressure, to be observed after 10 minutes, and calibrating the model to match forecasted BP values. In the figure, the first loop shown at the top shows the updating of the digital twin model using recently measured data. The second loop at the bottom shows forecasting of BP values in near future (after 10 minutes) and calibration of the digital twin model to match those values.

6.7.2 An example of sepsis

To demonstrate the proposed system, arterial BP wavforms from nine patients with sepsis, from the MGH/MF database, are used to replicate active monitoring of haemodynamic state. Since number of parameters being controlled in the above proposed

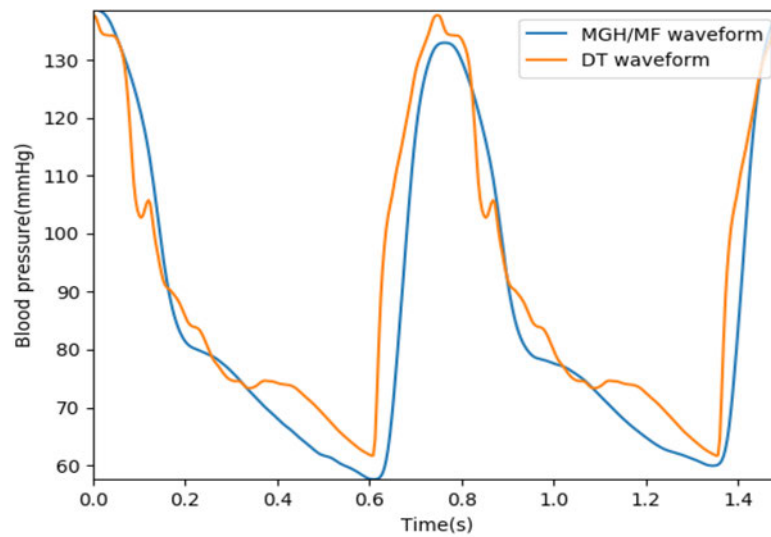


Fig. 6.18 An example of best matched waveform generated by digital twin model(1D model), after fine tuning the control parameters, with the input (MGH/MF waveform).

active digital twin is minimal, the case of sepsis is well-suited for replicating such a system.

In the MGH/MF waveform database, 14 patients have been diagnosed to have sepsis, out of which 5 patients undergoing treatment are used as samples for active monitoring. The exclusion of patients is carried out if the patient diagnosis is shown to have either other cardiovascular complications with sepsis, such as cardiac diseases or vascular surgery, or have readings that are beyond the capacity of replication by the 1D model. Compounded cardiovascular cases are avoided in this work for the following reasons:

- The control parameters used in this example are not sufficient enough to model cardiac diseases, such as endocarditis.
- Lack of data on exact geometry changes made during vascular procedures and lack of patient details make it difficult to generate personalised mesh, required for admissible replication of the patient's cardiovascular state.
- With a single input waveform and compounded cardiovascular problems, various combinations of cardiovascular conditions can generate approximately similar looking waveforms. To handle such combinations, a multimodal system is required. Since the objective of the proposed system is to demonstrate the active

modification of 1D model for continuous monitoring, only 1D model configurations (built with assumptions and approximations) with parameters that generate the waveform with highest similarity to that of the input is used. The selected model may or may not be the correct representation if more than one cardiovascular disease is present. Therefore, we mitigate the issue by selecting cases with only sepsis and no cardiovascular disease for this demonstration. However, two cases with past history of coronary disease were included to allow for analysis of how well the proposed system can adapt to the best of its capacity.

The patients chosen for this demonstration from the MGH/MF waveform database are, ‘mgh76’, ‘mgh86’, ‘mgh136’, ‘mgh152’, ‘mgh166’.

For each patient, initially the warm-up phase is conducted using the second cardiac cycle after start of recording (approximately 15% of recording at the beginning is removed from starting point of the recording). Then, three consecutive samples of 10 minutes period is extracted. The three samples are used to test the active calibration phase of the proposed system. The first sample is used as an input to the active forecasting phase to predict the cardiac state in the third sample, and the results are compared with the actual values.

6.7.3 Results and discussions

In this subsection, results obtained by applying on 5 patient waveforms from the MGH/MF database is presented. Tables 6.7, 6.8 and 6.9 show the BP values generated by fine tuned digital twin model (1D model) for three consecutive 10 minute long time periods. The columns show the results obtained after updating the digital twin in every time period (Period 1, Period 2 and Period 3). The values obtained are within acceptable range of actual values, showing that the active human digital twins for the cardiovascular system can be built on the same lines as that of the proposed system for continuous replication of a patient’s cardiac state.

The fine tuned models in each time period is used to calculate cardiac output (CO) for that period, shown in Table 6.10. This parameter allows for understanding on how well sepsis characteristics are replicated by the proposed system. In sepsis, patients usually have normal or elevated cardiac output, low systemic vascular resistance, and also low diastolic BP (for non-severe sepsis with normal MAP) [204]. In this work, a patient is considered to be suffering from or under treatment for sepsis if the diastolic blood pressure is approximately 60 or lower, pulse pressure is higher than 70 and

Table 6.7 Systolic blood pressure obtained after fine tuning digital twin models for three 10-minute periods, with values averaged over 3 cardiac cycles chosen within a 10 minute time period.

Systolic Blood pressure (mmHg)									
Patient	Period 1			Period 2			Period 3		
	DT	Actual	Error	DT	Actual	Error	DT	Actual	Error
mgh076	173	175	2	168	175	7	165	179	13
mgh086	94	92	2	98	100	2	100	100	0
mgh136	100	101	1	99	103	4	99	104	5
mgh152	136	142	6	139	138	1	136	142	6
mgh166	161	160	1	184	186	2	189	188	1

Table 6.8 Diastolic blood pressure obtained after fine tuning digital twin models for three 10-minute periods, with values averaged over 3 cardiac cycles chosen within a 10 minute time period.

Diastolic Blood pressure (mmHg)									
Patient	Period 1			Period 2			Period 3		
	DT	Actual	Error	DT	Actual	Error	DT	Actual	Error
mgh076	78	73	5	74	73	1	73	67	6
mgh086	55	61	6	60	59	1	56	61	5
mgh136	68	70	2	69	70	1	69	72	3
mgh152	59	67	8	58	62	4	67	60	7
mgh166	91	93	2	96	93	3	103	93	10

cardiac output is above 4 L/min. By analysing the cardiac output, systemic vascular resistance (measured as MAP/ CO), MAP and diastolic blood pressure, it can be seen that digital twins for ‘mgh152’ and ‘mgh166’ clearly show signs of sepsis or sepsis related care using vasopressors. In ‘mgh076’, neither BP and CO from digital twin nor BP from recorded waveforms show signs of sepsis, however, the digital twin has approximately 10% decrease reduced area taper gradient in terminal vessels (within the 1D model), which could signify a mild or early sepsis. ‘mgh136’ has a very low cardiac output, and since no data is available to validate it as well as lack of patient data, capturing of sepsis characteristics can only be assumed by the fact that this model has 40% reduced area taper gradient in terminal vessels(within the 1D model). Measured cardiac output values is not available for the selected patients except for a static measurement for ‘mgh086’, time of recording for which is also not available. In the case of ‘mgh086’, the observed cardiac output values is less than the recorded value from the patient record (5.4 L/min), this may be attributed to history of coronary

Table 6.9 Mean arterial blood pressure (MAP) obtained after fine tuning digital twin models for three 10-minute periods, with values averaged over 3 cardiac cycles chosen within each 10 minute time period.

Mean Arterial Blood pressure (mmHg)									
Patient	Period 1			Period 2			Period 3		
	DT	Actual	Error	DT	Actual	Error	DT	Actual	Error
mgh076	101	107	6	102	101	1	94	96	2
mgh086	70	69	1	76	71	5	74	73	1
mgh136	77	83	6	78	83	5	72	85	13
mgh152	96	90	6	87	90	3	96	88	8
mgh166	115	109	6	122	125	3	124	130	6

disease, replication of which is difficult with the current control parameters. Both ‘mgh136’ and ‘mgh086’ have a history of coronary disease.

Table 6.10 Estimated cardiac outputs calculated from tuned digital twin models for three 10-minute periods.

Cardiac output (L/min)			
Patient	Period 1	Period 2	Period 3
mgh076	4.83	4.28	3.18
mgh086	3.24	3.57	3.68
mgh136	1.62	1.64	1.63
mgh152	7.37	11.2	11.17
mgh166	6.17	6.60	6.60

The forecasting capacity of the active phase is tested by using Period 1 data to predict BP values (systolic BP, diastolic BP and MAP) in Period 3 for 3 cardiac cycles using neural networks trained in the previous section. Further, the mature twin model from warm-up phase is calibrated to closely match the values thus obtained. The results obtained are shown in Table 6.11. The values obtained show that the proposed system has the capacity to forecast cardiac state of a patient in the near future.

6.8 Conclusions

The truly active model presented in this part demonstrates the fact that continuous monitoring of patients through active digital twins is possible. Systems can be built to continuously update any numerical models for patient monitoring using a similar workflow like that of the proposed one. Capturing of haemodynamic parameters

Table 6.11 BP values forecasted and that obtained by calibrating digital twin using the forecasted values, compared against actual measured BP values from Period 3.

Patient	Systolic			Diastolic			MAP		
	Forecasted	Actual	DT	Forecasted	Actual	DT	Forecasted	Actual	DT
mgh076	172	179	175	75	73	76	105	96	101
mgh086	90	100	93	56	56	62	71	74	73
mgh136	102	103	98	72	72	69	81	85	77
mgh152	145	135	144	59	60	67	90	88	95
mgh166	180	188	187	101	103	92	136	130	124

through replication of blood pressure waveforms using digital twins can allow for a more detailed analysis of the patient's cardiovascular state and personalised care can be planned for faster recovery and prevention of damages to vital organs. The forecasting capacity of digital twins also demonstrates the potential to allow early intervention and medical preparedness in case the patient's cardiovascular state is predicted to deteriorate rapidly.

With further advancements to the proposed system, such as the introduction of multimodal analysis, active digital twins can successfully monitor, adapt and forecast to prevent deterioration of any cardiovascular state and promote faster recovery through personalised care.

6.9 Summary

In this chapter, the concept of active digital twin is explored in two parts, first an enabler model using inverse analysis and second a truly active model for continuous monitoring. In Part I :

- The enabler model uses inverse analysis carried out using deep learning algorithms trained on a virtual patient database. The virtual patient database used in this chapter is developed using realistic arterial networks developed based on anthropometric and haemodynamic parameters observed or derived by various population studies to represent a reliable human cohort. The database totally consists of 8659 virtual patients, with 4137 healthy (non-AAA) cases and 4522 AAA cases.

- The enabler model utilises blood pressure waveform measurements from three peripheral arteries to calculate upstream blood pressure waveforms inversely, such as those observed in the aorta, using deep learning.
- This model is applied in the detection of Abdominal Aortic Aneurysm (AAA) and classification of its severity, using an additional convolutional neural network. During testing, it detected problems such as AAA with an accuracy as high as 99.91% and classified its severity with acceptable accuracy of 97.79%.

In part II:

- The truly active model utilises a deep learning powered method to replicate and forecast the cardiovascular state of a patient.
- This model comprises of a warm-up phase and an active phase, the former phase is required at the beginning of monitoring to obtain an initial estimate of the control parameters of the haemodynamic model that help replicate the cardiovascular state of the patient. The latter phase is used to continuously update the control parameters at the end of every 10-minute period as well as to match the patient's cardiovascular state forecasted after 10 minutes. The forecasting is carried out using a neural network.
- The model is tested on waveform data of five sepsis patients from the MGH/MF database for three 10-minute periods. The cardiovascular state was successfully continuously replicated and forecasted with parameters such as blood pressures and cardiac output within an acceptable difference from the measured values.

Chapter 7

Conclusions and future research

In this chapter, conclusions for different forms of digital twins proposed in this thesis are described along with potential future research for each of the applications. An effective route to establish each of these digital twin forms in the healthcare system and also a description of a possible future where these twins are already a part of regular medical care is provided to highlight the importance of digital twins.

7.1 Passive digital twins

In the passive digital twin chapter (Chapter 4), by proposing and testing the workflow for automatic calculation of fractional flow reserve, it is shown that using passive data, such as scans and other medical images along with static patient details, vascular haemodynamics in the coronary system can be modelled and assessed automatically. With acceptable results from retrospective data, this system now needs to be tested in clinical environments in the form of clinical trials. There also exists an opportunity to enhance diagnosis capabilities using a data-driven deep learning approach for flow calculations, just as the work shown in [83]. A similar supervised deep learning based approach is also possible with image segmentation of vessels. Such ML based systems will reduce computational time to seconds.

Similar to the FFR application, vascular imaging and modelling of cerebral or peripheral arteries can allow for offline diagnosis and prognosis of vascular diseases such as aneurysms and stenoses, in different parts of the body. Furthermore, recent studies have shown that vascular geometry can be used as a biomarker for identifying not only diseases pertaining to the cardiovascular system but also to others such as cancer [205]. Upon the development of various other automatic systems to analyse the

functioning of other cardiovascular segments (such as the ventricles and atria), using scans, a comprehensive passive digital twin system can be developed in the future that uses a single scan of any given patient to automatically analyse all possible problems all at once. This would lead to a simplified diagnostic system and allow for an early medical intervention especially for cases where compounded problems can be observed.

Currently, the proposed FFR system requires CT scans that in turn require imaging hardware that cost in the range of hundreds of thousands of pounds. With advancements in imaging systems, cheap and reliable handheld imaging tools, such as mobile-app based ultrasound, are emerging. By adapting passive digital twins to work with data from these kinds of imaging tools could allow for a wider reach of care, especially in poorer countries. If a futuristic scenario is to be imagined, where passive digital twins are being used widely within healthcare then the following example would describe how these twins would help save more lives. A patient in their late 30 arrives at a healthcare facility with light-headedness, fatigue and arrhythmia. These symptoms did not occur suddenly, in fact, they were negligible in the beginning but deteriorated over a long period of time. A clinician suspects that the patient might be suffering from cardiomyopathy. Based on suspicion, the clinician uses a handheld imaging device and detects cardiomyopathy. Then the images are uploaded to the passive digital twin system where the system not only confirms that the patient has cardiomyopathy but also detects a lesion in the coronary arteries where the FFR is less than 0.8. With such information, clinician's can plan for better care by taking precautionary measures to avoid cardiac arrest. The further development of passive digital twins is expected to handle situations like these.

7.2 Semi-active digital twins

The semi-active digital twin system proposed in Chapter 5 to detect carotid stenosis and its severity from a face video demonstrates the capacity of non-invasive simple tools to detect life-threatening conditions. Basic mobile phone cameras can be used to detect carotid stenosis and prevent strokes. Further, the semi-active digital twin proposed in this system sets a basic methodology to be followed for generating semi-active digital twins that could process active data, such as videos, in an offline manner and compare it with results from numerical systems to diagnose medical conditions in a patient.

The proposed system relies on previous generation cameras and traditional machine learning for analysing videos for head vibration. However, with recent advancements

in mobile phone camera technology such as multi-camera and LiDAR models, facial vibrations can be detected with a higher accuracy. Further, by incorporating deep learning methods, this system could detect carotid stenosis in seconds and can be deployed on mobile platforms as applications. This kind of system is also possible for handling 4D flow MRI scans where a time-based representation of 3D volumes is recorded. In future, with advancements in the proposed system, when a face recording of a patient is analysed using semi-active digital twins it would not only check for carotid stenosis but also for cardiac conditions such as arrhythmia and hypertension.

7.3 Active digital twins

The proposed system for active digital twins in Chapter 6 provides proof that continuous monitoring of patients' cardiovascular state is possible. It also provides confidence in the forecasting of patients' cardiovascular state, which could help warn clinicians of an impending deterioration of patients' condition. However, there are limitations in the presented work. Ideally, the proposed system should use inverse analysis to calculate inlet flow conditions. For this to happen, the neural networks used in the inverse model must first be bolstered with clinical data, where all three input waveforms (brachial, femoral and carotid) and cardiac outflow are available. Only then the inverse model can be integrated with the active digital twin system. Further, the system proposed is unimodal in nature, in other words only the best-matched waveform is used to determine the cardiovascular state of a patient, which may not be correct in every situation as a similar waveform can be generated by other combinations of cardiovascular parameters. Thus this system must be enhanced to become a multimodal system for better cardiovascular monitoring.

In the future, when this kind of a system in combination with a non-invasive BP monitoring system is used in general settings, such as in a GP surgery, these systems could not only provide the overall cardiovascular condition of the patient but also pick up signs of sepsis as well as other cardiovascular conditions such as aneurysms. Additionally, if used on the patient for a long period (several hours), the rate of deterioration of a condition can be predicted early to help clinicians prioritise treatment.

7.4 Final remarks

Each of the three forms of digital twin proposed in this thesis, passive, active and semi-active digital twins, can replicate the functioning of the cardiovascular system using different forms of medical data. The three different applications proposed, one each for the three forms of digital twins, are all tested with *in vivo* data, thereby providing proof that these systems can be applied in clinical environments after further clinical trials. With further research, these platforms can be expanded to detect multiple cardiovascular conditions and diseases, and could potentially become one-stop solution for advanced and automatic diagnosis, prognosis and monitoring of the cardiovascular system.

Appendix A

Neural network architectures used for prioritising pneumonia patients

A1: MLP models

The neural network architecture of the MLP models used in Tier 1 and the parameters employed during training are presented in this section. Table A1.1 describes the training parameters used along with the activation functions employed. Figure A1.1 are graphical representations of the two models used in the first tier.

Table A1.1 Neural network parameters used in architecture and training of MLP models

Activation Functions: Hidden layers: ReLU Output layer: Sigmoid
Number of epochs: 100
Batch size: 150
Cost function: Binary cross-entropy
Optimizer: Adam
Regularisers used: L1 & L2

In Figure A1.1, L1 ($\lambda = 0.0003$) is an activity regulariser in the first hidden layer of MLP model used for predicting probability of death. L2 with $\lambda = 0.0038$ and $\lambda = 0.0018$ respectively are weight regularisation and activity regularisation, in the first hidden layer of MLP model to predict probability of requiring mechanical ventilation (See supplementary material). First and second dropout layers of MLP model for predicting probability of death has 50% and 40% dropouts respectively. Similarly, both

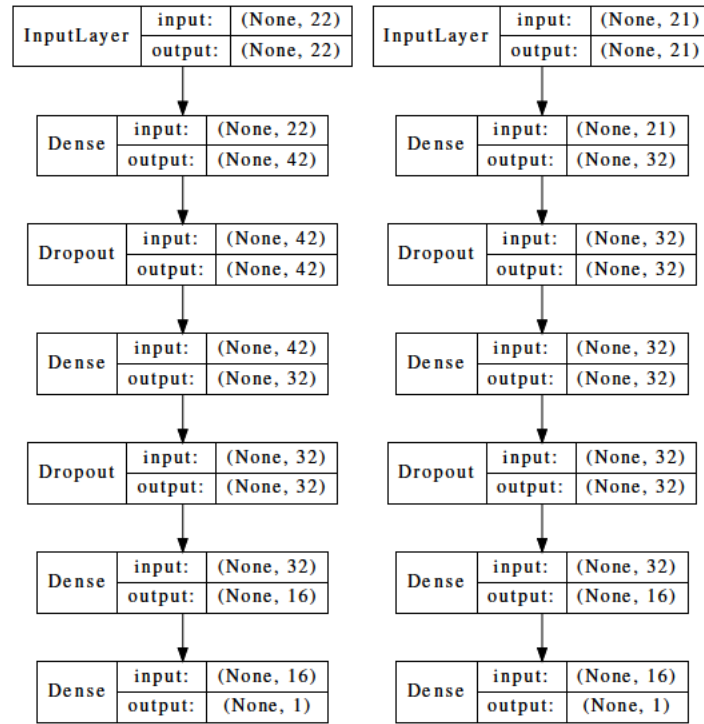


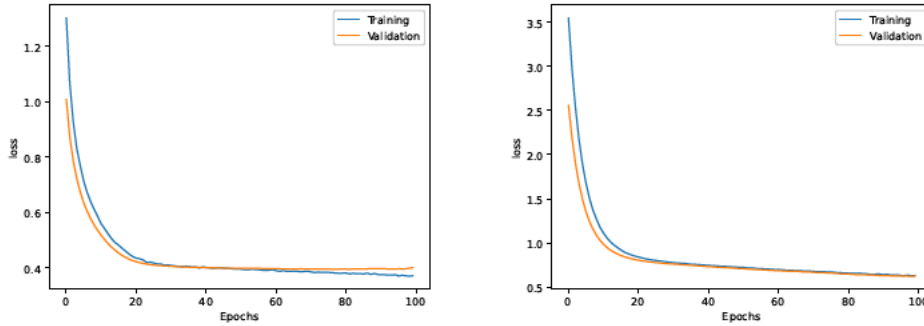
Fig. A1.1 Neural network architecture used for MLP models.

dropout layers in MLP for predicting probability of requiring mechanical ventilation have a dropout of 50%.

The performance of the model is shown in Figure A1.2. This figure shows the loss seen over epochs, averaged over 10 folds, during training. The convergence of training and validation losses confirm an optimal fitting of the model. Figure A1.3 shows the calibration curve for the three models, showing close to a perfect calibration.

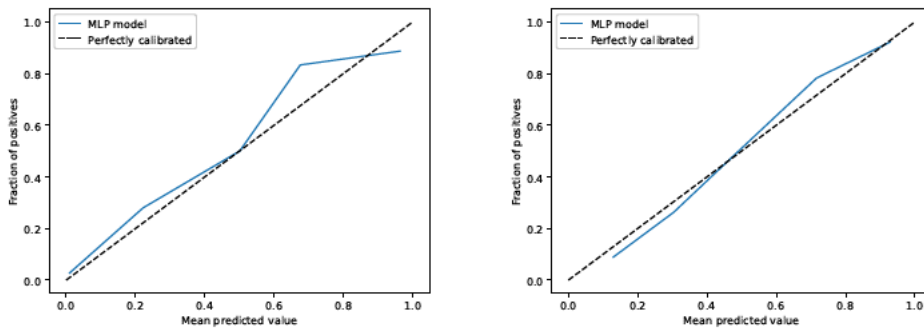
A2: RNN based models

The neural network architecture of the MLP models used in tiers 2 and 3, and the parameters employed during training are presented in this section. Table A2.2 describes the training parameters used along with the activations functions employed. Figures A2.1 and A2.2 are graphical representations of the three RNN models used in the tiers 2 and 3.



(a) Tier 1: MLP model for predicting probability of death
 (b) Tier 1: MLP model for predicting probability of requiring mechanical ventilation

Fig. A1.2 Loss observed over epochs during training.



(a) Tier 1: MLP model for predicting probability of death
 (b) Tier 1: MLP model for predicting probability of requiring mechanical ventilation

Fig. A1.3 Calibration curves for MLP models.

The performance of the model is shown in Figure A2.3. This figure shows the loss seen over epochs, averaged over 10 folds, during training. The convergence of training and validation losses confirm an optimal fitting of the model. Figure A2.4 shows the calibration curves for the three models, showing close to a perfect calibration.

In Figures A2.1 and A2.2, all dropout layers have 30% dropout except for the RNN model used in predicting probability of requiring mechanical ventilation in which the dropout is 50%. All weights were initialised, during training, with Glorot Normal function.

Table A2.2 Neural network parameters used in architecture and training of RNN based models.

<u>Activation functions:</u> Dense hidden layers: ReLU Output layer: Sigmoid LSTM: Tanh & Sigmoid (Recurrent activation) (Default for CuDNNLSTM)
Number of epochs: 100
Batch size: 10
Cost function: Binary cross-entropy
Optimizer: Adam
Regularizers: L1 ($\lambda = 0.02$)(All LSTM layers)

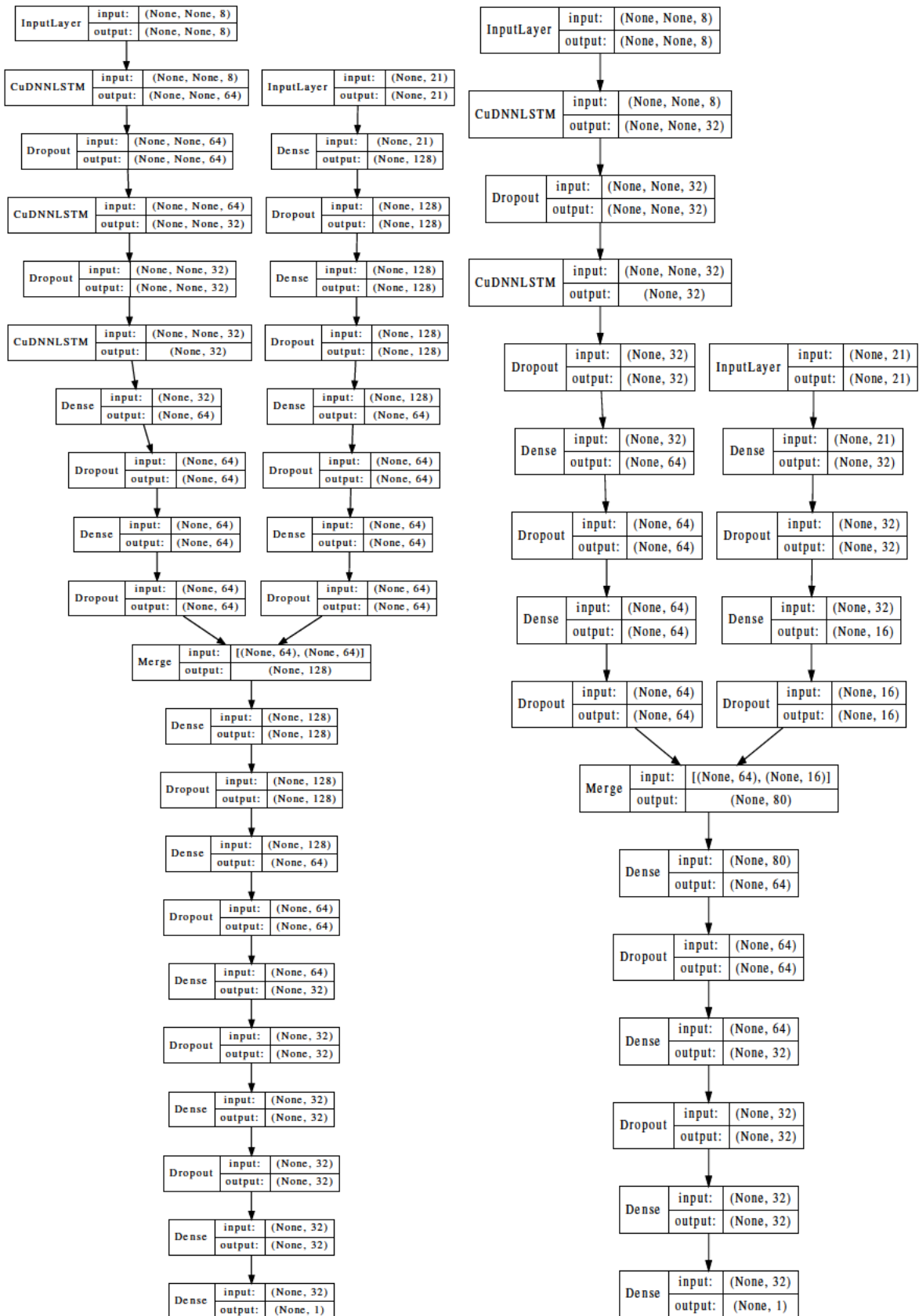


Fig. A2.1 Neural network architecture used for RNN based models in Tier 2)

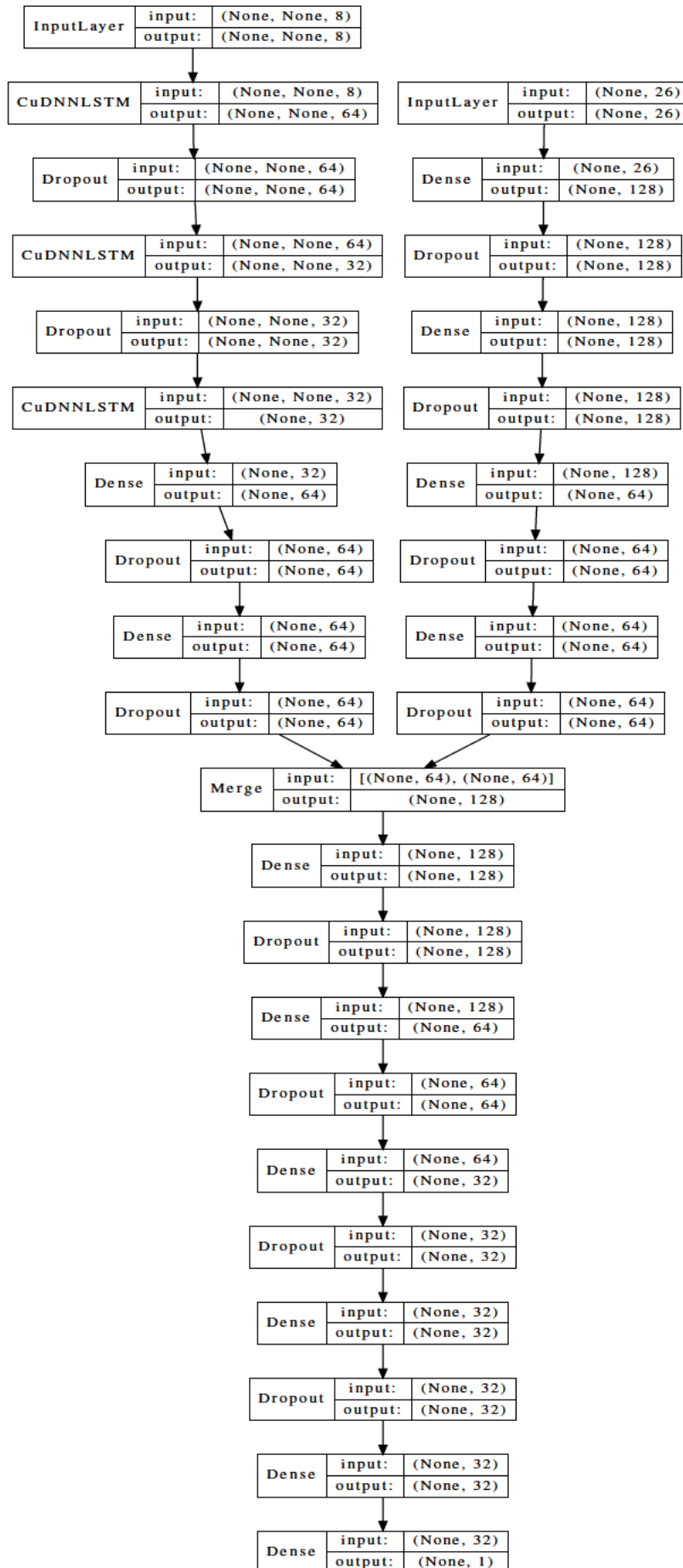
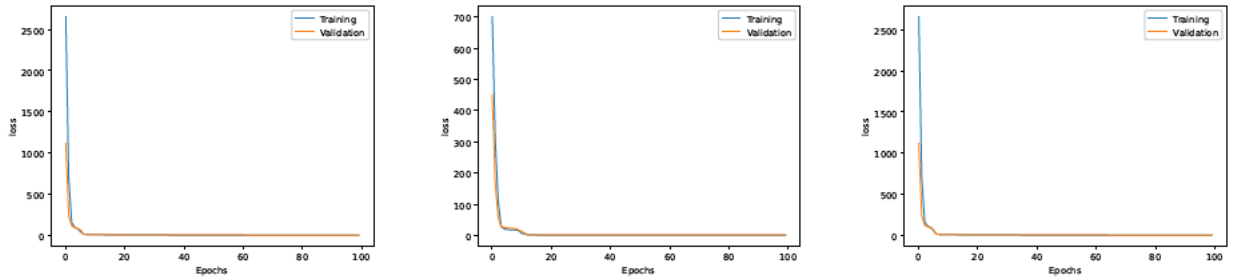
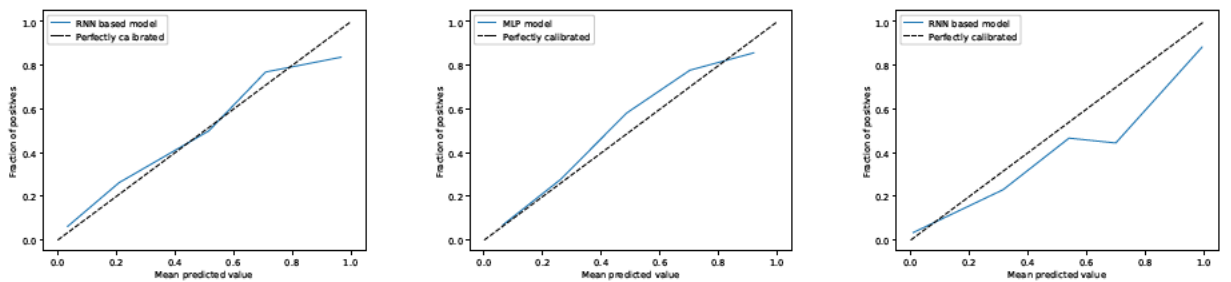


Fig. A2.2 Neural network architecture used for RNN based models in Tier 3



(a) Tier 2: RNN based model for predicting probability of death (b) Tier 2: RNN based model for predicting probability of requiring mechanical ventilation (c) Tier 3: RNN based model for predicting probability of death

Fig. A2.3 Loss observed over epochs during training.



(a) Tier 2: RNN based model for predicting probability of death (b) Tier 2: RNN based model for predicting probability of requiring mechanical ventilation (c) Tier 3: RNN based model for predicting probability of death

Fig. A2.4 Loss observed over epochs during training.

Appendix B

Workflow proposed and vascular dimensions observed for Fractional Flow Reserve application in Chapter 4

B1 : Workflow summary

The workflow proposed in the present work to automate cFFR calculation from CT scans is summarised in Table B1.

B2 Vessel geometry of coronary arteries with stenosis

Table B1 Workflow proposed in the present work to automate cFFR calculation from CT scans.

- **Segmentation**

- ▲ Pre-processing (to identify regions having area similar to the coronary arteries)

- Denoising (using Non-local means algorithm)

- Frangi filtering

- Binary thresholding

- Contour detection and removal

- ▲ Clustering

- Aorta detection (using Hough circle transform)

- Density based clustering of white voxels (using DBSCAN algorithm)

- ▲ Identification of cluster.

- **Estimation of lumen size**

- Skeletonisation (to obtain the centerline)

- Surface mesh generation (using marching cube algorithm)

- Splitting of centreline into individual vessels

- Radii calculation along the centreline

- 1D mesh generation (using centreline and radii along it)

- **Computational Fluid Dynamics** (to calculate cFFR using a 1D-0D blood flow model)

- Import 1D mesh

- Set boundary and initial conditions:

- ◊ Input inlet boundary conditions (as shown in Figure 4.8, calculated using closed-loop model)

- ◊ Calculate total resistance

- ◊ As per Murray's power law-

- Distribute resistance throughout each branch

- Distribute coronary vascular bed compliance

- ◊ Calculate parameters for lumped-parameter models at each terminal vessel

- ◊ Set initial boundary conditions

- Solve full 1D-0D system using enhanced trapezoidal rule method

- Calculate cFFR using blood pressure values obtained.

Table B2 Values obtained from the proposed workflow for left coronary geometry is compared against values obtained from manual segmentation carried out using VMTK(Vascular Modelling toolkit).

	Length (cm)								
	LCA			LAD			LCX		
	Automatic	Manual	Error	Automatic	Manual	Error	Automatic	Manual	Error
Patient 1	1.46	0.91	0.55	11.12	5.10	6.02	3.88	2.06	1.82
Patient 2	0.89	0.90	0.01	7.23	9.53	2.30	4.03	1.31	2.72
Patient 3	1.51	0.63	0.88	9.34	9.05	0.29	7.08	6.96	0.12
Patient 4	1.12	1.04	0.08	4.93	13.30	8.37	7.15	4.70	2.45
Patient 5	1.01	0.34	0.67	4.00	4.28	0.28	6.50	4.67	1.83
Patient 7	0.21	0.63	0.42	8.58	6.11	2.47	10.69	3.42	7.27
Patient 8	0.88	2.12	1.24	5.33	7.56	2.23	2.57	4.89	2.32
Patient 9	0.51	0.58	0.07	11.17	9.39	1.78	12.11	3.43	8.68
Patient 10	1.35	1.98	0.63	10.42	8.47	1.95	10.22	3.76	6.46
Patient 11	0.81	0.96	0.15	10.70	7.608	3.09	12.17	9.61	2.56
Patient 12	1.41	0.67	0.74	9.78	1.01	8.77	6.71	6.24	0.47
Patient 13	0.75	0.41	0.34	5.56	5.61	0.05	7.16	2.07	5.09
Patient 15	1.20	0.20	1.00	8.96	4.18	4.78	5.60	4.27	1.33
Patient 16	0.97	0.40	0.57	13.21	6.58	6.63	11.63	6.23	5.4
Patient 17	0.67	0.46	0.21	3.60	8.58	4.98	6.37	2.21	4.16
Patient 18	0.51	1.01	0.5	11.61	7.53	4.08	9.74	6.34	3.40
Patient 19	2.42	1.49	0.93	8.31	6.07	2.24	2.35	1.34	1.01
Patient 20	0.54	0.33	0.21	8.76	4.28	4.48	8.98	4.03	4.95
Patient 21	0.37	0.32	0.05	10.16	5.09	5.07	6.24	5.77	0.47
Patient 22	1.53	0.43	1.10	12.28	8.97	3.31	5.94	6.83	0.89
Patient 25	0.91	0.26	0.65	7.94	7.70	0.24	10.67	5.62	5.05

Table B3 Initial vessel radius obtained from the proposed workflow for left coronary geometry is compared against values obtained from manual segmentation carried out using VMTK(Vascular Modelling toolkit).

	R_0 (mm)								
	LCA			LAD			LCX		
	Automatic	Manual	Error	Automatic	Manual	Error	Automatic	Manual	Error
Patient 1	1.51	1.46	0.05	1.21	1.01	0.2	1.03	1.19	0.16
Patient 2	1.80	1.73	0.07	1.31	1.20	0.11	1.07	1.41	0.34
Patient 3	1.24	1.38	0.14	1.10	1.41	0.31	1.30	1.42	0.12
Patient 4	2.31	1.97	0.34	1.79	2.30	0.51	1.89	2.13	0.24
Patient 5	1.23	1.04	0.19	0.77	1.08	0.31	0.75	1.22	0.47
Patient 7	1.40	1.34	0.06	1.30	1.39	0.09	1.44	1.34	0.10
Patient 8	1.96	1.59	0.37	1.46	1.83	0.37	1.63	1.57	0.06
Patient 9	1.96	2.01	0.05	1.60	1.45	0.15	1.65	1.36	0.29
Patient 10	1.60	3.22	1.62	1.14	1.69	0.55	0.82	1.98	1.16
Patient 11	1.88	2.17	0.29	1.61	1.50	0.11	1.38	1.43	0.05
Patient 12	1.87	1.51	0.36	1.69	1.32	0.37	1.71	1.26	0.45
Patient 13	1.64	1.61	0.03	1.65	0.94	0.71	1.64	0.93	0.71
Patient 15	1.71	1.99	0.28	1.42	1.53	0.11	1.13	1.38	0.25
Patient 16	1.39	1.09	0.30	1.20	1.43	0.23	1.18	0.91	0.27
Patient 17	1.49	1.38	0.11	1.70	1.47	0.23	1.88	1.40	0.48
Patient 18	1.00	1.18	0.18	1.80	1.24	0.56	1.71	1.36	0.35
Patient 19	1.71	1.68	0.03	1.67	1.32	0.35	1.12	1.02	0.10
Patient 20	1.09	1.33	0.24	0.79	1.02	0.23	1.06	1.22	0.16
Patient 21	1.20	1.59	0.39	0.95	1.26	0.31	1.29	1.28	0.01
Patient 22	2.10	1.55	0.55	1.44	1.88	0.44	1.60	1.56	0.04
Patient 25	1.51	1.46	0.05	1.46	1.03	0.43	1.13	0.95	0.18

Table B4 Final vessel radius obtained from the proposed workflow for left coronary geometry is compared against values obtained from manual segmentation carried out using VMTK(Vascular Modelling toolkit).

	R_f (mm)								
	LCA			LAD			LCX		
	Automatic	Manual	Error	Automatic	Manual	Error	Automatic	Manual	Error
Patient 1	1.61	1.21	0.40	0.54	0.99	0.45	0.96	1.02	0.06
Patient 2	1.60	1.37	0.23	0.63	1.00	0.37	0.60	0.98	0.38
Patient 3	1.33	1.42	0.09	0.83	0.76	0.07	0.85	1.15	0.30
Patient 4	2.68	2.25	0.43	1.36	0.98	0.38	1.15	1.03	0.12
Patient 5	0.94	1.64	0.70	0.53	0.96	0.43	0.34	0.77	0.43
Patient 7	1.33	1.53	0.20	0.62	0.99	0.37	0.53	1.24	0.71
Patient 8	1.63	1.80	0.17	0.83	0.96	0.13	0.62	1.32	0.70
Patient 9	2.07	2.01	0.06	0.51	0.55	0.04	0.97	1.10	0.13
Patient 10	1.33	1.69	0.36	0.34	0.67	0.33	0.26	0.87	0.61
Patient 11	1.88	1.26	0.62	0.27	0.71	0.44	0.46	0.85	0.39
Patient 12	0.90	1.46	0.56	0.60	1.24	0.64	0.84	0.70	0.14
Patient 13	1.51	1.49	0.02	1.25	0.95	0.3	0.36	0.67	0.31
Patient 15	1.72	1.70	0.02	0.85	0.83	0.02	0.72	0.98	0.26
Patient 16	1.41	1.11	0.30	0.50	0.85	0.35	0.88	0.91	0.03
Patient 17	1.61	1.59	0.02	0.48	0.90	0.42	0.67	1.20	0.53
Patient 18	1.17	1.45	0.28	0.44	0.78	0.34	0.84	0.88	0.04
Patient 19	1.80	1.59	0.21	0.46	0.97	0.51	1.02	0.89	0.13
Patient 20	1.04	1.30	0.26	0.45	0.69	0.24	0.24	0.61	0.37
Patient 21	1.38	1.05	0.33	0.47	0.83	0.36	0.92	0.85	0.07
Patient 22	2.46	1.72	0.74	1.10	1.07	0.03	0.78	2.59	1.81
Patient 25	1.20	1.40	0.20	0.87	0.83	0.04	0.41	1.00	0.59

Table B5 Minimum vessel radius at stenosis location obtained from the proposed workflow for left coronary geometry is compared against values obtained from manual segmentation carried out using VMTK(Vascular Modelling toolkit).

	R_s (mm)		
	LCA		
	Automatic	Manual	Error
Patient1	0.42	0.91	0.49
Patient2	0.72	0.69	0.03
Patient3	0.63	0.56	0.07
Patient4	0.91	0.63	0.28
Patient5	0.52	0.64	0.12
Patient 7	0.64	0.61	0.03
Patient 8	1.57	0.64	0.93
Patient9	0.43	0.65	0.22
Patient10	0.62	0.69	0.07
Patient 11	0.36	0.69	0.33
Patient 12	0.57	0.53	0.04
Patient 13	0.76	0.55	0.21
Patient 15	1.00	1.15	0.15
Patient 16	0.32	0.61	0.29
Patient 17	0.48	0.61	0.13
Patient 18	1.15	0.61	0.54
Patient 19	0.96	0.87	0.09
Patient 20	0.31	0.58	0.27
Patient 21	0.71	0.56	0.15
Patient 22	0.59	0.94	0.35
Patient 25	0.65	0.41	0.24

Table B6 Values obtained from the proposed workflow for left coronary geometry is compared against values obtained from manual segmentation carried out using VMTK(Vascular Modelling toolkit).

	Length (cm)		
	RCA		
	Automatic	Manual	Diff
Patient6	6.11	9.97	3.86
Patient 14	11.44	10.30	1.14
Patient 23	11.28	14.09	2.81
Patient 24	11.09	13.99	2.90

Table B7 Initial vessel radius obtained from the proposed workflow for right coronary geometry is compared against values obtained from manual segmentation carried out using VMTK(Vascular Modelling toolkit).

	R_0 (mm)		
	RCA		
	Automatic	Manual	Error
Patient 6	0.92	1.72	0.80
Patient 14	1.63	1.89	0.26
Patient 23	1.75	1.26	0.49
Patient 24	1.78	1.39	0.39

Table B8 Final vessel radius obtained from the proposed workflow for right coronary geometry is compared against values obtained from manual segmentation carried out using VMTK(Vascular Modelling toolkit).

	R_f (mm)		
	RCA		
	Automatic	Manual	Error
Patient 6	0.54	0.96	0.42
Patient 14	0.43	0.86	0.43
Patient 23	1.57	1.18	0.39
Patient 24	1.31	0.69	0.62

Table B9 Minimum vessel radius at stenosis location obtained from the proposed workflow for right coronary geometry is compared against values obtained from manual segmentation carried out using VMTK(Vascular Modelling toolkit).

	R_s (mm)		
	RCA		
	Automatic	Manual	Error
Patient 6	0.41	0.53	0.12
Patient 14	0.47	0.51	0.04
Patient 23	1.06	0.92	0.14
Patient 24	1.45	0.84	0.61

Appendix C

Peer-reviewed journal papers published during PhD candidature

- **Chakshu, NK**, Carson, J, Sazonov, I, Nithiarasu, P. A semi-active human digital twin model for detecting severity of carotid stenoses from head vibration – A coupled computational mechanics and computer vision method. *Int J Numer Meth Biomed Engng.* 2019; 35:e3180. <https://doi.org/10.1002/cnm.3180>
- **Chakshu, NK**, Sazonov, I & Nithiarasu, P Towards enabling a cardiovascular digital twin for human systemic circulation using inverse analysis. *Biomech Model Mechanobiol* 20, 449–465 (2021). <https://doi.org/10.1007/s10237-020-01393-6>
- Carson, JM, **Chakshu, NK**, Sazonov, I, Nithiarasu, P. Artificial intelligence approaches to predict coronary stenosis severity using non-invasive fractional flow reserve. *Proceedings of the Institution of Mechanical Engineers, Part H: Journal of Engineering in Medicine.* 2020;234(11):1337-1350. doi:10.1177/0954411920946526
- Tamaddon-Jahromi HR, **Chakshu NK**, Sazonov I, Evans LM, Thomas H, Nithiarasu P. Data-driven inverse modelling through neural network (deep learning) and computational heat transfer. *Computer Methods in Applied Mechanics and Engineering.* 2020 Sep 1;369:113217.

References

- [1] Piascik, R., Vickers, J., Lowry, D., Scotti, S., Stewart, J. and Calomino, A. (2010), ‘Technology area 12: Materials, structures, mechanical systems, and manufacturing road map’, *NASA Office of Chief Technologist* pp. 15–88.
- [2] Grieves, M. and Vickers, J. (2017), *Digital Twin: Mitigating Unpredictable, Undesirable Emergent Behavior in Complex Systems*, pp. 85–113.
- [3] Tuegel, E. J., Ingraffea, A. R., Eason, T. G. and Spottswood, S. M. (2011), ‘Reengineering aircraft structural life prediction using a digital twin’, *International Journal of Aerospace Engineering* 2011, 154798.
URL: <https://doi.org/10.1155/2011/154798>
- [4] Armstrong, M. M. (2020), ‘Cheat sheet: What is digital twin? internet of things blog’. (Accessed on 3 August 2021).
URL: <https://www.ibm.com/blogs/internet-of-things/iot-cheat-sheet-digital-twin/>
- [5] Zhao, L., Fang, Y., Lou, P., Yan, J. and Xiao, A. (2021), ‘Cutting parameter optimization for reducing carbon emissions using digital twin’, *International Journal of Precision Engineering and Manufacturing* 22(5), 933–949.
- [6] Thies, L., Stamminger, M. and Bauer, F. (2020), Learning kinematic machine models from videos, in ‘2020 IEEE International Conference on Artificial Intelligence and Virtual Reality (AIVR)’, IEEE, pp. 107–114.
- [7] Joos, J., Buchele, A., Schmidt, A., Weber, A. and Ivers-Tiffée, E. (2021), ‘Virtual electrode design for lithium-ion battery cathodes’, *Energy Technology* p. 2000891.
- [8] Rjabtšikov, V., Rassölkin, A., Asad, B., Vaimann, T., Kallaste, A., Kuts, V., Jegorov, S., Stepień, M. and Krawczyk, M. (2021), Digital twin service unit for ac motor stator inter-turn short circuit fault detection, in ‘2021 28th International

- Workshop on Electric Drives: Improving Reliability of Electric Drives (IWED)', IEEE, pp. 1–5.
- [9] Uhlemann, T. H.-J., Lehmann, C. and Steinhilper, R. (2017), 'The digital twin: Realizing the cyber-physical production system for industry 4.0', *Procedia CIRP* 61, 335–340.
URL: <https://www.sciencedirect.com/science/article/pii/S2212827116313129>
- [10] Qi, Q. and Tao, F. (2018), 'Digital twin and big data towards smart manufacturing and industry 4.0: 360 degree comparison', *IEEE Access* 6, 3585–3593.
- [11] Vachálek, J., Bartalský, L., Rovný, O., Šišmišová, D., Morháč, M. and Lokšík, M. (2017), The digital twin of an industrial production line within the industry 4.0 concept, in '2017 21st International Conference on Process Control (PC)', pp. 258–262.
- [12] Shirowzhan, S., Tan, W. and Sepasgozar, S. M. E. (2020), 'Digital twin and cyberGIS for improving connectivity and measuring the impact of infrastructure construction planning in smart cities'.
- [13] Ford David, N. and Wolf Charles, M. (2020), 'Smart cities with digital twin systems for disaster management', *Journal of Management in Engineering* 36(4), 04020027.
URL: [https://doi.org/10.1061/\(ASCE\)ME.1943-5479.0000779](https://doi.org/10.1061/(ASCE)ME.1943-5479.0000779)
- [14] Jonsson, H., Magnusdottir, E., Eggertsson, H. P., Stefansson, O. A., Arnadottir, G. A., Eiriksson, O., Zink, F., Helgason, E. A., Jonsdottir, I., Gylfason, A., Jonasdottir, A., Jonasdottir, A., Beyter, D., Steingrimsdottir, T., Norddahl, G. L., Magnusson, O. T., Masson, G., Halldorsson, B. V., Thorsteinsdottir, U., Helgason, A., Sulem, P., Gudbjartsson, D. F. and Stefansson, K. (2021), 'Differences between germline genomes of monozygotic twins', *Nature Genetics* 53(1), 27–34.
URL: <https://doi.org/10.1038/s41588-020-00755-1>
- [15] Liu, Y., Zhang, L., Yang, Y., Zhou, L., Ren, L., Wang, F., Liu, R., Pang, Z. and Deen, M. J. (2019), 'A novel cloud-based framework for the elderly healthcare services using digital twin', *IEEE Access* 7, 49088–49101.
- [16] Chakshu, N. K., Carson, J., Sazonov, I. and Nithiarasu, P. (2019), 'A semi-active human digital twin model for detecting severity of carotid stenoses from

- head vibration – a coupled computational mechanics and computer vision method’, *International journal for numerical methods in biomedical engineering* 35(5), e3180.
- [17] Chakshu, N. K., Sazonov, I. and Nithiarasu, P. (2021), ‘Towards enabling a cardiovascular digital twin for human systemic circulation using inverse analysis’, *Biomechanics and Modeling in Mechanobiology* 20(2), 449–465.
URL: <https://doi.org/10.1007/s10237-020-01393-6>
- [18] Raines, J., Jaffrin, M. and Shapiro, A. (1974), ‘A computer simulation of arterial dynamics in the human leg’, *Journal of Biomechanics* 7(1), 77–91.
- [19] Avolio, A. (1980), ‘Multi-branched model of the human arterial system.’, *Medical & Biological Engineering & Computing* 18, 709–718.
- [20] Stergiopoulos, N., Young, D. and Rogge, T. (1992), ‘Computer simulation of arterial flow with applications to arterial and aortic stenoses’, *Journal of Biomechanics* 25(12), 1477–1488.
- [21] Wan, J., Steele, B., Spicer, S., Strohsand, S., Feijóo, G., Hughes, T. and Taylor, C. (2002), ‘A one-dimensional finite element method for simulation-based medical planning for cardiovascular disease’, *Computer Methods in Biomechanics and Biomedical Engineering* 5(3), 195–206.
- [22] Sherwin, S. J., Formaggia, L., Peiró, J. and Franke, V. (2003), ‘Computational modelling of 1D blood flow with variable mechanical properties and its application to the simulation of wave propagation in the human arterial system.’, *International Journal for Numerical Methods in Fluids* 43(6-7), 673–700. b.
- [23] Formaggia, L., Nobile, F. and Quarteroni, A. (2002), A one dimensional model for blood flow: Application to vascular prosthesis, in B. I., M. T. and C. P.G., eds, ‘Mathematical Modeling and Numerical Simulation in Continuum Mechanics, Lecture Notes in Computational Science and Engineering’, Springer-Verlag, Berlin.
- [24] Urquiza, S. A., Blanco, P. J., Vénere, M. J. and Feijóo, R. A. (2006), ‘Multidimensional modelling for the carotid artery blood flow’, *Computer Methods in Applied Mechanics and Engineering* 195, 4002–4017.
- [25] Smith, N., Pullan, A. and Hunter, P. (2002), ‘An anatomically based model of transient coronary blood flow in the heart.’, *SIAM Journals on Applied Mathematics* 62, 990–1018.

-
- [26] Alastruey, J., Parker, K. H., Peiró, J. and Sherwin, S. (2006), ‘Can the modified allen’s test always detect sufficient collateral flow in the hand? a computational study’, *Computer Methods in Biomechanics and Biomedical Engineering* 9(6), 353–361.
- [27] Alastruey, J., Parker, K. H., Peiró, J., Byrd, S. M. and Sherwin, S. J. (2007), ‘Modelling the circle of willis to assess the effects of anatomical variations and occlusions on cerebral flows’, *Journal of biomechanics* 40(8), 1794–1805.
- [28] Franke, V., Peiró, J., Sherwin, S., Parker, K., Ling, W. and Fisk, N. M. (2002), Computational modelling of 1D blood flow and its applications, in M. Thiriet, ed., ‘ESAIM Proceedings’, Vol. 12, pp. 48–54.
- [29] Mynard, J. P. and Nithiarasu, P. (2008), ‘A 1D arterial blood flow model incorporating ventricular pressure, aortic valve and regional coronary flow using the locally conservative Galerkin (LCG) method’, *Communications in Numerical Methods in Engineering* 24, 367–417.
- [30] Mynard, J. P. and Smolich, J. J. (2015), ‘One-dimensional haemodynamic modeling and wave dynamics in the entire adult circulation’, *Ann Biomed Eng* 43 (6)(DOI: 10.1007/s10439-015-1313-8), 1443–60.
- [31] Sherwin, S., Franke, V., Peiró, J. and Parker, K. (2003), ‘One-dimensional modelling of a vascular network in space-time variables’, *Journal of Engineering Mathematics* 47(3), 217–250.
- [32] Carson, J. M. (2019), Development of a cardiovascular and lymphatic network model during human pregnancy, PhD thesis, Swansea University.
- [33] Rammos, K., Koullias, G., Papou, T., Bakas, A., Panagopoulos, P. and Tsangaris, S. (1998), ‘A computer model for the prediction of left epicardial coronary blood flow in normal, stenotic and bypassed coronary arteries, by single or sequential grafting’, *Cardiovascular Surgery* 6(6), 635–648.
- [34] Müller, L. O. and Toro, E. F. (2014), ‘A global multiscale mathematical model for the human circulation with emphasis on the venous system’, *International Journal for Numerical Methods in Biomedical Engineering* 30, 681–725.
- [35] Formaggia, L., Lamponi, D. and Quarteroni, A. (2003), ‘One-dimensional models for blood flow in arteries’, *Journal of Engineering Mathematics* 47, 251–276.

- [36] Čanić, S. (2002), ‘Blood flow through compliant vessels after endovascular repair: Wall deformations induced by the discontinuous wall properties’, *Comput. Vis. Sci.* 4(3), 147–155.
URL: <https://doi.org/10.1007/s007910100066>
- [37] Smith, N. P., Pullan, A. J. and Hunter, P. J. (2002), ‘An anatomically based model of transient coronary blood flow in the heart’, *SIAM Journal on Applied Mathematics* 62(3), 990–1018.
- [38] Alastruey, J., Khir, A. W., Matthys, K. S., Segers, P., Sherwin, S. J., Verdonck, P. R., Parker, K. H. and Peiró, J. (2011), ‘Pulse wave propagation in a model human arterial network: Assessment of 1-d visco-elastic simulations against in vitro measurements’, *Journal of biomechanics* 44(21724188), 2250–2258.
URL: <https://www.ncbi.nlm.nih.gov/pmc/articles/PMC3278302/>
- [39] Boileau, E., Nithiarasu, P., Blanco, J., Muller, L., Fossans, F. E., Helleviks, L., Doners, W., Huberts, W., Willemet, M. and Alastruey, J. (2015), ‘A benchmark study of 1-d numerical schemes for arterial blood flow modelling’, *International Journal for Numerical Methods in Biomedical Engineering* e02732(DOI: 10.1002/cnm.2732).
- [40] Passera, K., Manini, S., Antiga, L. and Remuzzi, A. (2013), ‘Patient-specific model of arterial circulation for surgical planning of vascular access’, *The journal of vascular access* 14(2), 180–192.
- [41] Sandgren, T., Sonesson, B., Åsa Rydén Ahlgren and Länne, T. (1999), ‘The diameter of the common femoral artery in healthy human: Influence of sex, age, and body size’, *Journal of Vascular Surgery* 29(3), 503–510.
URL: <http://www.sciencedirect.com/science/article/pii/S074152149970279X>
- [42] Sonesson, B., Länne, T., Hansen, F. and Sandgren, T. (1994), ‘Infrarenal aortic diameter in the healthy person’, *European Journal of Vascular Surgery* 8(1), 89–95.
URL: <http://www.sciencedirect.com/science/article/pii/S0950821X05801276>
- [43] Chiaganam, N. O., Ekpo, E. U., Egbe, N. O., Okwara, K. and Nzotta, C. (2013), ‘Aging and the average diameter of the renal artery using computed tomography angiography (cta): peer reviewed original article’, *South African Radiographer* 51(1), 23–25.

- [44] Carson, J. and Van Loon, R. (2017), ‘An implicit solver for 1d arterial network models’, *International Journal for Numerical Methods in Biomedical Engineering* 33(e2837).
- [45] Thomas, C. (2006), A locally conservative Galerkin (LCG) finite element method for convection-diffusion and Navier-Stokes equations, PhD thesis, University of Wales Swansea.
- [46] Thomas, C. and Nithiarasu, P. (2007), ‘An element-wise, locally conservative galerkin (LCG) method for solving diffusion and convection-diffusion problems’, *International Journal for Numerical Methods in Engineering* .
- [47] Kroon, W., Huberts, W., Bosboom, M. and van de Vosse, F. (2012), ‘A numerical method of reduced complexity for simulating vascular hemodynamics using coupled 0d lumped and 1d wave propagation models’, *Computational and Mathematical Methods in Medicine* Article ID 156094, 10 pages.
- [48] Ozcift, A. (2012), ‘Svm feature selection based rotation forest ensemble classifiers to improve computer-aided diagnosis of parkinson disease’, *Journal of medical systems* 36(4), 2141–2147.
- [49] Tsien, C. L., Fraser, H. S., Long, W. J. and Kennedy, R. L. (1998), Using classification tree and logistic regression methods to diagnose myocardial infarction, in ‘MEDINFO’98’, IOS Press, pp. 493–497.
- [50] Khalilia, M., Chakraborty, S. and Popescu, M. (2011), ‘Predicting disease risks from highly imbalanced data using random forest’, *BMC medical informatics and decision making* 11(1), 1–13.
- [51] Nguyen, C., Wang, Y. and Nguyen, H. N. (2013), ‘Random forest classifier combined with feature selection for breast cancer diagnosis and prognostic’.
- [52] Atkeson, C. G., Moore, A. W. and Schaal, S. (1997), ‘Locally weighted learning’, *Artificial Intelligence Review* 11(1), 11–73.
URL: <https://doi.org/10.1023/A:1006559212014>
- [53] Si, Y., Du, J., Li, Z., Jiang, X., Miller, T., Wang, F., Jim Zheng, W. and Roberts, K. (2021), ‘Deep representation learning of patient data from electronic health records (ehr): A systematic review’, *Journal of Biomedical Informatics*

- 115, 103671.
URL: <https://www.sciencedirect.com/science/article/pii/S1532046420302999>
- [54] Ayala Solares, J. R., Diletta Raimondi, F. E., Zhu, Y., Rahimian, F., Canoy, D., Tran, J., Pinho Gomes, A. C., Payberah, A. H., Zottoli, M., Nazarzadeh, M., Conrad, N., Rahimi, K. and Salimi-Khorshidi, G. (2020), ‘Deep learning for electronic health records: A comparative review of multiple deep neural architectures’, *Journal of Biomedical Informatics* 101, 103337.
URL: <https://www.sciencedirect.com/science/article/pii/S1532046419302564>
- [55] Shen, D., Wu, G. and Suk, H.-I. (2017), ‘Deep learning in medical image analysis’, *Annual review of biomedical engineering* 19, 221–248.
- [56] Fakoor, R., Ladhak, F., Nazi, A. and Huber, M. (2013), Using deep learning to enhance cancer diagnosis and classification, in ‘Proceedings of the international conference on machine learning’, Vol. 28, ACM, New York, USA, pp. 3937–3949.
- [57] Bychkov, D., Linder, N., Turkki, R., Nordling, S., Kovanen, P. E., Verrill, C., Walliander, M., Lundin, M., Haglund, C. and Lundin, J. (2018), ‘Deep learning based tissue analysis predicts outcome in colorectal cancer’, *Scientific reports* 8(1), 1–11.
- [58] Kather, J. N., Krisam, J., Charoentong, P., Luedde, T., Herpel, E., Weis, C.-A., Gaiser, T., Marx, A., Valous, N. A., Ferber, D. et al. (2019), ‘Predicting survival from colorectal cancer histology slides using deep learning: A retrospective multicenter study’, *PLoS medicine* 16(1), e1002730.
- [59] Chen, H., Engkvist, O., Wang, Y., Olivecrona, M. and Blaschke, T. (2018), ‘The rise of deep learning in drug discovery’, *Drug discovery today* 23(6), 1241–1250.
- [60] Gawehn, E., Hiss, J. A. and Schneider, G. (2016), ‘Deep learning in drug discovery’, *Molecular informatics* 35(1), 3–14.
- [61] Albawi, S., Mohammed, T. A. and Al-Zawi, S. (2017), Understanding of a convolutional neural network, in ‘2017 International Conference on Engineering and Technology (ICET)’, Ieee, pp. 1–6.
- [62] Heimes, F. (1998), Extended kalman filter neural network training: experimental results and algorithm improvements, in ‘SMC’98 Conference Proceedings.

- 1998 IEEE International Conference on Systems, Man, and Cybernetics (Cat. No.98CH36218)', Vol. 2, pp. 1639 1644 vol.2.
- [63] Lee, D.-H., Zhang, S., Fischer, A. and Bengio, Y. (2015), Difference target propagation, *in* A. Appice, P. P. Rodrigues, V. Santos Costa, C. Soares, J. Gama and A. Jorge, eds, 'Machine Learning and Knowledge Discovery in Databases', Springer International Publishing, Cham, pp. 498 515.
- [64] Kingma, D. P. and Ba, J. (2014), 'Adam: A method for stochastic optimization', *arXiv preprint arXiv:1412.6980* .
- [65] Gers, F. A., Schmidhuber, J. and Cummins, F. (1999), 'Learning to forget: Continual prediction with lstm'.
- [66] Hochreiter, S. and Schmidhuber, J. (1997), 'Long short-term memory', *Neural Computation* 9(8), 1735 1780.
URL: <https://doi.org/10.1162/neco.1997.9.8.1735>
- [67] Graves, A. (2012), Long short-term memory, *in* 'Supervised sequence labelling with recurrent neural networks', Springer, pp. 37 45.
- [68] Adhanom, T. (2020), 'WHO director-general's opening remarks at the media briefing on COVID-19 - 11 march 2020'. (Accessed on 03 April 2020).
URL: <https://www.who.int/dg/speeches/detail/who-director-general-s-opening-remarks-at-the-media-briefing-on-covid-19-11-march-2020>
- [69] Meares, H. D. and Jones, M. P. (2020), 'When a system breaks: a queuing theory model for the number of intensive care beds needed during the COVID-19 pandemic', *The Medical Journal of Australia* 212(10), 1.
- [70] Nacoti, M., Ciocca, A., Giupponi, A., Brambillasca, P., Lussana, F., Pisano, M., Goisis, G., Bonacina, D., Fazzi, F., Naspro, R. et al. (2020), 'At the epicenter of the covid-19 pandemic and humanitarian crises in italy: Changing perspectives on preparation and mitigation', *NEJM Catalyst Innovations in Care Delivery* 1(2).
- [71] Vincent, J.-L., Moreno, R., Takala, J., Willatts, S., De Mendonça, A., Bruining, H., Reinhart, C., Suter, P. and Thijs, L. G. (1996), 'The SOFA (sepsis-related organ failure assessment) score to describe organ dysfunction/failure'.

- [72] Zimmerman, J. E., Kramer, A. A., McNair, D. S. and Malila, F. M. (2006), ‘Acute physiology and chronic health evaluation (APACHE) IV: hospital mortality assessment for today’s critically ill patients’, *Critical care medicine* 34(5), 1297 1310.
- [73] Le Gall, J.-R., Lemeshow, S. and Saulnier, F. (1993), ‘A new simplified acute physiology score (SAPS II) based on a european/north american multicenter study’, *Jama* 270(24), 2957 2963.
- [74] Ferreira, F. L., Bota, D. P., Bross, A., Mélot, C. and Vincent, J.-L. (2001), ‘Serial Evaluation of the SOFA Score to Predict Outcome in Critically Ill Patients’, *JAMA* 286(14), 1754 1758.
URL: <https://doi.org/10.1001/jama.286.14.1754>
- [75] Aegerter, P., Boumendil, A., Retbi, A., Minvielle, E., Dervaux, B. and Guidet, B. (2005), ‘SAPS II revisited’, *Intensive care medicine* 31(3), 416 423.
- [76] Beck, D. H., Smith, G. B., Pappachan, J. V. and Millar, B. (2003), ‘External validation of the SAPS II, APACHE II and APACHE III prognostic models in south england: a multicentre study’, *Intensive care medicine* 29(2), 249 256.
- [77] Ledoux, D., Canivet, J.-L., Preiser, J.-C., Lefrancq, J. and Damas, P. (2008), ‘SAPS 3 admission score: an external validation in a general intensive care population’, *Intensive care medicine* 34(10), 1873.
- [78] Gentimis, T., Alnaser, A. J., Durante, A., Cook, K. and Steele, R. (2017), Predicting hospital length of stay using neural networks on mimic iii data, *in* ‘2017 IEEE 15th Intl Conf on Dependable, Autonomic and Secure Computing, 15th Intl Conf on Pervasive Intelligence and Computing, 3rd Intl Conf on Big Data Intelligence and Computing and Cyber Science and Technology Congress(DASC/PiCom/DataCom/CyberSciTech)’, pp. 1194 1201.
- [79] Barbieri, S., Kemp, J., Perez-Concha, O., Kotwal, S., Gallagher, M., Ritchie, A. and Jorm, L. (2020), ‘Benchmarking deep learning architectures for predicting readmission to the icu and describing patients-at-risk’, *Scientific reports* 10(1), 1 10.
- [80] Pirracchio, R., Petersen, M. L., Carone, M., Rigon, M. R., Chevret, S. and van der Laan, M. J. (2015), ‘Mortality prediction in intensive care units with the super

- icu learner algorithm (sicula): a population-based study’, *The Lancet Respiratory Medicine* 3(1), 42–52.
- [81] Rapid Risk Assessment (2020), ‘Detection of new SARS-CoV-2 variants related to mink’, *Eur. Cent. Dis. Prev. Control*. (Accessed on 14 November 2020).
- [82] Bakator, M. and Radosav, D. (2018), ‘Deep learning and medical diagnosis: A review of literature’, *Multimodal Technologies and Interaction* 2(3), 47.
- [83] Carson, J. M., Chakshu, N. K., Sazonov, I. and Nithiarasu, P. (2020), ‘Artificial intelligence approaches to predict coronary stenosis severity using non-invasive fractional flow reserve’, *Proceedings of the Institution of Mechanical Engineers, Part H: Journal of Engineering in Medicine* 234(11), 1337–1350. PMID: 32741245. **URL:** <https://doi.org/10.1177/0954411920946526>
- [84] Amigo, N., Valencia, A., Wu, W., Patnaik, S. and Finol, E. (2021), ‘Cerebral aneurysm rupture status classification using statistical and machine learning methods’, *Proceedings of the Institution of Mechanical Engineers, Part H: Journal of Engineering in Medicine* 235(6), 655–662. PMID: 33685288. **URL:** <https://doi.org/10.1177/09544119211000477>
- [85] Singh, K., Singh, S. and Malhotra, J. (2021), ‘Spectral features based convolutional neural network for accurate and prompt identification of schizophrenic patients’, *Proceedings of the Institution of Mechanical Engineers, Part H: Journal of Engineering in Medicine* 235(2), 167–184. PMID: 33124526. **URL:** <https://doi.org/10.1177/0954411920966937>
- [86] Torrey, L. and Shavlik, J. (2010), Transfer learning, *in* ‘Handbook of research on machine learning applications and trends: algorithms, methods, and techniques’, IGI Global, pp. 242–264.
- [87] Johnson, A., Pollard, T. and Mark, R. (2016), ‘Mimic-III clinical database (version 1.4)’, *PhysioNet*.
- [88] Johnson, A. E., Pollard, T. J., Shen, L., Li-wei, H. L., Feng, M., Ghassemi, M., Moody, B., Szolovits, P., Celi, L. A. and Mark, R. G. (2016), ‘Mimic-III, a freely accessible critical care database’, *Scientific data* 3, 160035.
- [89] Pollard, T. J., Johnson, A. E., Raffa, J. D., Celi, L. A., Mark, R. G. and Badawi, O. (2019), ‘eICU collaborative research database (version 2.0)’, *PhysioNet*.

- [90] Pollard, T. J., Johnson, A. E., Raffa, J. D., Celi, L. A., Mark, R. G. and Badawi, O. (2018), ‘The eICU collaborative research database, a freely available multi-center database for critical care research’, *Scientific data* 5, 180178.
- [91] Goldberger, A. L., Amaral, L. A., Glass, L., Hausdorff, J. M., Ivanov, P. C., Mark, R. G., Mietus, J. E., Moody, G. B., Peng, C.-K. and Stanley, H. E. (2000), ‘Physiobank, physiotoolkit, and physionet: components of a new research resource for complex physiologic signals’, *circulation* 101(23), e215 e220.
- [92] Shi, H., Han, X., Jiang, N., Cao, Y., Alwalid, O., Gu, J., Fan, Y. and Zheng, C. (2020), ‘Radiological findings from 81 patients with COVID-19 pneumonia in wuhan, china: a descriptive study’, *The Lancet Infectious Diseases* 20(4), 425 434.
URL: <http://www.sciencedirect.com/science/article/pii/S1473309920300864>
- [93] Abadi, M., Agarwal, A., Barham, P., Brevdo, E., Chen, Z., Citro, C., Corrado, G. S., Davis, A., Dean, J., Devin, M., Ghemawat, S., Goodfellow, I., Harp, A., Irving, G., Isard, M., Jia, Y., Jozefowicz, R., Kaiser, L., Kudlur, M., Levenberg, J., Mané, D., Monga, R., Moore, S., Murray, D., Olah, C., Schuster, M., Shlens, J., Steiner, B., Sutskever, I., Talwar, K., Tucker, P., Vanhoucke, V., Vasudevan, V., Viégas, F., Vinyals, O., Warden, P., Wattenberg, M., Wicke, M., Yu, Y. and Zheng, X. (2015), ‘TensorFlow: Large-scale machine learning on heterogeneous systems’. Software available from tensorflow.org.
URL: <https://www.tensorflow.org/>
- [94] Chollet, F. et al. (2015), ‘Keras, <https://keras.io>’.
- [95] Johnson, A. E., Stone, D. J., Celi, L. A. and Pollard, T. J. (2018), ‘The mimic code repository: enabling reproducibility in critical care research’, *Journal of the American Medical Informatics Association* 25(1), 32 39.
- [96] Fawcett, T. (2006), ‘An introduction to roc analysis’, *Pattern recognition letters* 27(8), 861 874.
- [97] Pedregosa, F., Varoquaux, G., Gramfort, A., Michel, V., Thirion, B., Grisel, O., Blondel, M., Prettenhofer, P., Weiss, R., Dubourg, V., Vanderplas, J., Passos, A., Cournapeau, D., Brucher, M., Perrot, M. and Duchesnay, E. (2011), ‘Scikit-learn: Machine learning in Python’, *Journal of Machine Learning Research* 12, 2825 2830.

- [98] Ye, J., Yao, L., Shen, J., Janarthanam, R. and Luo, Y. (2020), ‘Predicting mortality in critically ill patients with diabetes using machine learning and clinical notes’, *BMC Medical Informatics and Decision Making* 20(11), 295.
URL: <https://doi.org/10.1186/s12911-020-01318-4>
- [99] Kim, S. Y., Kim, S., Cho, J., Kim, Y. S., Sol, I. S., Sung, Y., Cho, I., Park, M., Jang, H., Kim, Y. H., Kim, K. W. and Sohn, M. H. (2019), ‘A deep learning model for real-time mortality prediction in critically ill children’, *Critical Care* 23(1), 279.
URL: <https://doi.org/10.1186/s13054-019-2561-z>
- [100] Roncon, L., Zuin, M., Rigatelli, G. and Zuliani, G. (2020), ‘Diabetic patients with covid-19 infection are at higher risk of icu admission and poor short-term outcome’, *Journal of clinical virology : the official publication of the Pan American Society for Clinical Virology* 127(32305882), 104354 104354.
URL: <https://www.ncbi.nlm.nih.gov/pmc/articles/PMC7195018/>
- [101] Foundation, B. H. (2021), ‘British heart foundation heart and circulatory disease statistics 2021’, *British Heart Foundation* .
- [102] Samani, N. (2021), ‘British heart foundation health coronavirus and heart circulatory diseases factsheet’, *British Heart Foundation* .
- [103] Manda, Y. R. and Baradhi, K. M. (2018), ‘Cardiac catheterization, risks and complications’.
- [104] Koo, B.-K., Erglis, A., Doh, J.-H., Daniels, D. V., Jegere, S., Kim, H.-S., Dunning, A., DeFrance, T., Lansky, A., Leipsic, J. et al. (2011), ‘Diagnosis of ischemia-causing coronary stenoses by noninvasive fractional flow reserve computed from coronary computed tomographic angiograms: results from the prospective multicenter discover-flow (diagnosis of ischemia-causing stenoses obtained via noninvasive fractional flow reserve) study’, *Journal of the American College of Cardiology* 58(19), 1989 1997.
- [105] Min, J. K., Leipsic, J., Pencina, M. J., Berman, D. S., Koo, B.-K., Van Mieghem, C., Erglis, A., Lin, F. Y., Dunning, A. M., Apruzzese, P. et al. (2012), ‘Diagnostic accuracy of fractional flow reserve from anatomic ct angiography’, *Jama* 308(12), 1237 1245.

- [106] Nørgaard, B. L., Leipsic, J., Gaur, S., Seneviratne, S., Ko, B. S., Ito, H., Jensen, J. M., Mauri, L., De Bruyne, B., Bezerra, H. et al. (2014), ‘Diagnostic performance of noninvasive fractional flow reserve derived from coronary computed tomography angiography in suspected coronary artery disease: the next trial (analysis of coronary blood flow using ct angiography: Next steps)’, *Journal of the American College of Cardiology* 63(12), 1145–1155.
- [107] Papafaklis, M. I., Muramatsu, T., Ishibashi, Y., Lakkas, L. S., Nakatani, S., Bourantas, C. V., Ligthart, J., Onuma, Y., Echavarria-Pinto, M., Tzirka, G. et al. (2014), ‘Fast virtual functional assessment of intermediate coronary lesions using routine angiographic data and blood flow simulation in humans: comparison with pressure wire-fractional flow reserve’, *EuroIntervention* 10(5), 574–583.
- [108] Tu, S., Barbato, E., Köszegi, Z., Yang, J., Sun, Z., Holm, N. R., Tar, B., Li, Y., Rusinaru, D., Wijns, W. et al. (2014), ‘Fractional flow reserve calculation from 3-dimensional quantitative coronary angiography and timi frame count: a fast computer model to quantify the functional significance of moderately obstructed coronary arteries’, *JACC: Cardiovascular Interventions* 7(7), 768–777.
- [109] Zhang, J.-M., Zhong, L., Luo, T., Lomarda, A. M., Huo, Y., Yap, J., Lim, S. T., Tan, R. S., Wong, A. S. L., Tan, J. W. C. et al. (2016), ‘Simplified models of non-invasive fractional flow reserve based on ct images’, *PloS one* 11(5), e0153070.
- [110] Shi, C., Zhang, D., Cao, K., Zhang, T., Luo, L., Liu, X. and Zhang, H. (2017), ‘A study of noninvasive fractional flow reserve derived from a simplified method based on coronary computed tomography angiography in suspected coronary artery disease’, *Biomedical engineering online* 16(1), 1–15.
- [111] Morris, P. D., Ryan, D., Morton, A. C., Lycett, R., Lawford, P. V., Hose, D. R. and Gunn, J. P. (2013), ‘Virtual fractional flow reserve from coronary angiography: modeling the significance of coronary lesions: results from the virtu-1 (virtual fractional flow reserve from coronary angiography) study’, *JACC: Cardiovascular Interventions* 6(2), 149–157.
- [112] Carson, J. M., Pant, S., Roobottom, C., Alcock, R., Javier Blanco, P., Alberto Bulant, C., Vassilevski, Y., Simakov, S., Gamilov, T., Pryamonosov, R., Liang, F., Ge, X., Liu, Y. and Nithiarasu, P. (2019), ‘Non-invasive coronary ct angiography-derived fractional flow reserve: A benchmark study comparing the

- diagnostic performance of four different computational methodologies', *International Journal for Numerical Methods in Biomedical Engineering* 35(10), e3235. e3235 cnm.3235.
URL: <https://onlinelibrary.wiley.com/doi/abs/10.1002/cnm.3235>
- [113] Gamilov, T. M., Kopylov, P. Y., Pryamonosov, R. A. and Simakov, S. S. (2015), 'Virtual fractional flow reserve assessment in patient-specific coronary networks by 1d hemodynamic model', *Russian Journal of Numerical Analysis and Mathematical Modelling* 30(5), 269–276.
URL: <https://doi.org/10.1515/rnam-2015-0024>
- [114] Gognieva, D., Mitina, Y., Gamilov, T., Pryamonosov, R., Vasilevskii, Y., Simakov, S., Liang, F., Ternovoy, S., Serova, N., Tebenkova, E., Sinitsyn, V., Pershina, E., Abugov, S., Mardanian, G., Zakarian, N., Kirakosian, V., Betelin, V., Shchekochikhin, D., Syrkin, A. and Kopylov, P. (2021), 'Noninvasive assessment of the fractional flow reserve with the ct ffr 1d method: Final results of a pilot study', *Global heart* 16(33598381), 1–1.
URL: <https://www.ncbi.nlm.nih.gov/pmc/articles/PMC7792469/>
- [115] Huo, Y., Svendsen, M., Choy, J. S., Zhang, Z.-D. and Kassab, G. S. (2012), 'A validated predictive model of coronary fractional flow reserve', *Journal of The Royal Society Interface* 9(71), 1325–1338.
URL: <https://doi.org/10.1098/rsif.2011.0605>
- [116] Kaymak, Ç. and Uçar, A. (2019), 'A brief survey and an application of semantic image segmentation for autonomous driving', pp. 161–200.
- [117] Treml, M., Arjona-Medina, J., Unterthiner, T., Durgesh, R., Friedmann, F., Schubert, P., Mayr, A., Heusel, M., Hofmarcher, M., Widrich, M. et al. (2016), 'Speeding up semantic segmentation for autonomous driving'.
- [118] Bana, S. and Kaur, D. (2011), 'Fingerprint recognition using image segmentation', *International Journal of Advanced Engineering Sciences and Technologies* 5(1), 12–23.
- [119] Pham, D. L., Xu, C. and Prince, J. L. (2000), 'Current methods in medical image segmentation', *Annual review of biomedical engineering* 2(1), 315–337.

- [120] Wang, G., Li, W., Zuluaga, M. A., Pratt, R., Patel, P. A., Aertsen, M., Doel, T., David, A. L., Deprest, J., Ourselin, S. and Vercauteren, T. (2018), ‘Interactive medical image segmentation using deep learning with image-specific fine tuning’, *IEEE Transactions on Medical Imaging* 37(7), 1562–1573.
- [121] Bauer, S., Wiest, R., Nolte, L.-P. and Reyes, M. (2013), ‘A survey of mri-based medical image analysis for brain tumor studies’, *Physics in Medicine & Biology* 58(13), R97.
- [122] Kerkeni, A., Benabdallah, A., Manzanera, A. and Bedoui, M. H. (2016), ‘A coronary artery segmentation method based on multiscale analysis and region growing’, *Computerized Medical Imaging and Graphics* 48, 49–61.
URL: <https://www.sciencedirect.com/science/article/pii/S0895611115001913>
- [123] Schaap, M., van Walsum, T., Neefjes, L., Metz, C., Capuano, E., de Bruijne, M. and Niessen, W. (2011), ‘Robust shape regression for supervised vessel segmentation and its application to coronary segmentation in cta’, *IEEE Transactions on Medical Imaging* 30(11), 1974–1986.
- [124] Wang, C. and Smedby, Ö. (2009), ‘Integrating automatic and interactive methods for coronary artery segmentation: let the pacs workstation think ahead’, *International Journal of Computer Assisted Radiology and Surgery* 5, 275–285.
- [125] Yang, G., Kitslaar, P., Frenay, M., Broersen, A., Boogers, M. J., Bax, J. J., Reiber, J. H. and Dijkstra, J. (2012), ‘Automatic centerline extraction of coronary arteries in coronary computed tomographic angiography’, *The international journal of cardiovascular imaging* 28(4), 921–933.
- [126] Wolterink, J. M., van Hamersvelt, R. W., Viergever, M. A., Leiner, T. and Išgum, I. (2019), ‘Coronary artery centerline extraction in cardiac ct angiography using a cnn-based orientation classifier’, *Medical Image Analysis* 51, 46–60.
URL: <http://www.sciencedirect.com/science/article/pii/S1361841518308491>
- [127] Chen, C., Qin, C., Qiu, H., Tarroni, G., Duan, J., Bai, W. and Rueckert, D. (2020), ‘Deep learning for cardiac image segmentation: A review’, *Frontiers in Cardiovascular Medicine* 7, 25.
URL: <https://www.frontiersin.org/article/10.3389/fcvm.2020.00025>

- [128] Li, Z., Zhang, Y., Gong, H., Liu, G., Li, W. and Tang, X. (2017), ‘An automatic and efficient coronary arteries extraction method in ct angiographies’, *Biomedical Signal Processing and Control* 36, 221–233.
URL: <https://www.sciencedirect.com/science/article/pii/S1746809417300812>
- [129] Buades, A., Coll, B. and Morel, J.-M. (2011), ‘Non-Local Means Denoising’, *Image Processing On Line* 1, 208–212. https://doi.org/10.5201/ipol.2011.bcm_nlm.
- [130] Van der Walt, S., Schönberger, J. L., Nunez-Iglesias, J., Boulogne, F., Warner, J. D., Yager, N., Gouillart, E. and Yu, T. (2014), ‘scikit-image: image processing in python’, *PeerJ* 2, e453.
- [131] Donoho, D. L. and Johnstone, I. M. (1994), ‘Ideal spatial adaptation by wavelet shrinkage’, *Biometrika* 81(3), 425–455.
URL: <https://doi.org/10.1093/biomet/81.3.425>
- [132] Frangi, A. F., Niessen, W. J., Vincken, K. L. and Viergever, M. A. (1998), Multiscale vessel enhancement filtering, in ‘International conference on medical image computing and computer-assisted intervention’, Springer, pp. 130–137.
- [133] Suzuki, S. and be, K. (1985), ‘Topological structural analysis of digitized binary images by border following’, *Computer Vision, Graphics, and Image Processing* 30(1), 32–46.
URL: <https://www.sciencedirect.com/science/article/pii/0734189X85900167>
- [134] Rhody, H. (2005), ‘Lecture 10: Hough circle transform’, *Chester F. Carlson Center for Imaging Science, Rochester Institute of Technology* .
- [135] Canny, J. (1986), ‘A computational approach to edge detection’, *IEEE Transactions on Pattern Analysis and Machine Intelligence* PAMI-8(6), 679–698.
- [136] Lloyd, S. (1982), ‘Least squares quantization in pcm’, *IEEE Transactions on Information Theory* 28(2), 129–137.
- [137] Nielsen, F. (2016), *Hierarchical Clustering*, pp. 195–211.
- [138] Ester, M., Kriegel, H.-P., Sander, J., Xu, X. et al. (1996), A density-based algorithm for discovering clusters in large spatial databases with noise., in ‘Kdd’, Vol. 96, pp. 226–231.

- [139] Lee, T.-C., Kashyap, R. and Chu, C. (1994), ‘Building skeleton models via 3-d medial surface/axis thinning algorithms’, *CVGIP Graph. Model. Image Process.* 56, 462–478.
- [140] Wang, A., Yan, X. and Wei, Z. (2018), ‘ImagePy: an open-source, Python-based and platform-independent software package for bioimage analysis’, *Bioinformatics* 34(18), 3238–3240.
URL: <https://doi.org/10.1093/bioinformatics/bty313>
- [141] Polder, G., Hovens, H. and Zweers, A. (2010), ‘Measuring shoot length of submerged aquatic plants using graph analysis’, pp. 172–177. ImageJ User and Developer Conference 2010, Mondorf-les-Bains, Luxembourg ; Conference date: 27-10-2010 Through 29-10-2010.
- [142] Lewiner, T., Lopes, H., Vieira, A. W. and Tavares, G. (2003), ‘Efficient implementation of marching cubes’ cases with topological guarantees’, *Journal of Graphics Tools* 8(2), 1–15.
URL: <https://doi.org/10.1080/10867651.2003.10487582>
- [143] Carson, J., Warrander, L., Johnstone, E. and Van Loon, R. (2019), ‘Personalising cardiovascular network models in pregnancy: A two-tiered parameter estimation approach’, *International Journal for Numerical Methods in Biomedical Engineering* p. e3267.
- [144] Carson, J., Lewis, M., Rassi, D. and Van Loon, R. (2019), ‘A data-driven model to study utero-ovarian blood flow physiology during pregnancy’, *Biomechanics and modeling in mechanobiology* 18(4), 1155–1176.
- [145] Van der Giessen, A. G., Groen, H. C., Doriot, P.-A., De Feyter, P. J., Van der Steen, A. F., Van de Vosse, F. N., Wentzel, J. J. and Gijzen, F. J. (2011), ‘The influence of boundary conditions on wall shear stress distribution in patients specific coronary trees’, *Journal of biomechanics* 44(6), 1089–1095.
- [146] Boileau, E., Pant, S., Roobottom, C., Sazonov, I., Deng, J., Xie, X. and Nithiarasu, P. (2018), ‘Estimating the accuracy of a reduced-order model for the calculation of fractional flow reserve (ffr)’, *International journal for numerical methods in biomedical engineering* 34(1), e2908.

- [147] Carson, J., Pant, S., Roobottom, C., Alcock, R., Blanco, P., Bulant, C., Vasilevski, Y., Simakov, S., Gamilov, T., Pryamonosov, R., Liang, F. and Nithiarasu, P. (2018), ‘Non-invasive coronary ct angiography-derived fractional flow reserve: A benchmark study comparing the diagnostic performance of four different computational frameworks’, *International Journal for Numerical Methods in Biomedical Engineering* .
- [148] Chakshu, N. K., Carson, J., Sazonov, I. and Nithiarasu, P. (2019), ‘A semi-active human digital twin model for detecting severity of carotid stenoses from head vibration – a coupled computational mechanics and computer vision method’, *International journal for numerical methods in biomedical engineering* 35(5), e3180.
- [149] Nithiarasu, P. (2018a), ‘Active and passive human digital twins based on reduced cardiovascular flow models’, *Bioengineering UK, Imperial College, UK* .
- [150] Nithiarasu, P. (2018b), ‘Active and passive human digital twins - future prospects’, *VAJRA Colloquium Series, IIT Madras* .
- [151] Boileau, E. and Nithiarasu, P. (2013), One-dimensional modelling of the coronary circulation. application to noninvasive quantification of fractional flow reserve (ffr), *in* J. Tarves and R. Jorge, eds, ‘Computational and experimental biomedical sciences: Methods and Applications’, Springer, pp. 137–156.
- [152] Mackay, J., Mensah, G., Mendis, S. and Greenlund, K. (2004), The atlas of heart disease and stroke, Technical report, WHO.
- [153] Stroke Association (2018), ‘Stroke association. state of the nation: Stroke statistics(2018).information guide.stroke association,london’. (Accessed on 26 January 2018).
URL: <https://www.stroke.org.uk/system/files/sotn2018.pdf>
- [154] Shah, S., Bellows, B. A., Adedipe, A. A., Totten, J. E., Backlund, B. H. and Sajed, D. (2015), ‘Perceived barriers in the use of ultrasound in developing countries’, *Critical Ultrasound Journal* 7(1), 11.
URL: <https://doi.org/10.1186/s13089-015-0028-2>
- [155] Klingelhöfer, J. (2014), ‘Ultrasonography of carotid stenosis’, *IJCNMH* 1(Suppl. 1):S04.

- [156] Giovangrandi, L., Inan, O. T., Wiard, R. M., Etemadi, M. and Kovacs, G. T. (2011), ‘Ballistocardiography – a method worth revisiting’, *Engineering in Medicine and Biology Society, EMBC, 2011 Annual International Conference of the IEEE* (10.1109/iembs.2011.6091062), 4279–4282.
- [157] He, D. D., Winokur, E. S. and Sodini, C. G. (2011), A continuous, wearable, and wireless heart monitor using head ballistocardiogram (BCG) and head electrocardiogram (ECG), *in* ‘2011 Annual International Conference of the IEEE Engineering in Medicine and Biology Society’, IEEE.
- [158] Balakrishnan, G., Durand, F. and Guttag, J. (2013), ‘Detecting pulse from head motions in video’, *Proceedings of the IEEE Conference on Computer Vision and Pattern Recognition* pp. 3430–3437.
- [159] Bradski, G. (2000), ‘The OpenCV Library’, *Dr. Dobb’s Journal of Software Tools* .
- [160] Viola, P. and Jones, M. (2001), ‘Rapid object detection using a boosted cascade of simple features’, *Proceedings of the 2001 IEEE Computer Society Conference on Computer Vision and Pattern Recognition. CVPR 2001* 1(10.1109/CVPR.2001.990517), I–I.
- [161] M.A. Haque, R. Irani, K. N. T. M. (2016), ‘Heartbeat rate measurement from facial video’, *IEEE Intell. Syst.* 31, 40–48.
- [162] Li, X., Chen, J., Zhao, G. and Pietikäinen, M. (2014), ‘Remote heart rate measurement from face videos under realistic situations’, *IEEE Conference on Computer Vision and Pattern Recognition Columbus, OH* pp. 4264–4271.
- [163] Irani, R., Nasrollahi, K. and Moeslund, T. (2014), ‘Improved pulse detection from head motions using dct’, *2014 International Conference on Computer Vision Theory and Applications (VISAPP) 3*, 118–124.
- [164] Shan, L. and Yu, M. (2013), ‘Video-based heart rate measurement using head motion tracking and ica’, *IEEE 6th International Congress on Image and Signal Processing (CISP) 1*, 160–164.
- [165] PrintHuman Org (Accessed on: Jan 2018), ‘Partial Brain Vascular Network, <https://3dprint.nih.gov/discover/3dpx-001277>’.

- [166] Wang, Y. and Rahmatalla, S. (2013), ‘Human head-neck models in whole-body vibration: Effect of posture’, *Journal of Biomechanics* 46, 702–710.
- [167] MR, H., MA, Q. and A, M. (2012), ‘Neck circumference as a useful marker of obesity: a comparison with body mass index and waist circumference’, *J Pak Med Assoc* 62(1) pp. 36–40.
- [168] Himmetoglu, S., A. M. e. a. (2007), ‘A multi-body head-and-neck model for simulation of rear impact in cars.’, *Proceedings of the Institution of Mechanical Engineering Part D-J. Automobile Engineering* 221, 15.
- [169] Dewese, J. A., May, A. G., Lipchik, E. O. and Rob, C. G. (1970), ‘Anatomic and hemodynamic correlations in carotid artery stenosis’, *Stroke* 1(3), 149–157.
- [170] Boileau, E., Pant, S., Roobottom, C., Sazonov, I., Deng, J., Xie, X. and Nithiarasu, P. (n.d.), ‘Estimating the accuracy of a reduced-order model for the calculation of fractional flow reserve (ffr)’, *International Journal for Numerical Methods in Biomedical Engineering* 10.1002/cnm.2908, e2908.
- [171] Sturlaugsdottir, R., Aspelund, T., Bjornsdottir, G., Sigurdsson, S., Thorsson, B., Eiriksdottir, G. and Gudnason, V. (2016), ‘Prevalence and determinants of carotid plaque in the cross-sectional refine-reykjavik study’, *BMJ Open* 2016 6:e012457(doi:10.1136/bmjopen-2016-012457).
- [172] Phan, T. S., Syed, A. A., Oldland, H. G., Sanchez, N., Hashmath, Z., Akers, S. R. and Chirinos, J. A. (2017), ‘Heart-femoral pulse wave velocity is a stronger marker of arterial aging than carotid-femoral pulse wave velocity’, *Journal of the American College of Cardiology* 69(11 Supplement), 1768.
URL: <https://www.onlinejacc.org/content/69/11supplement/1768>
- [173] Baker, C. (2020), ‘NHS key statistics’. Accessed on 2020-07-08.
URL: <http://researchbriefings.files.parliament.uk/documents/CBP-7281/CBP-7281.pdf>
- [174] Dinov, I. D. (2016), ‘Volume and value of big healthcare data’, *Journal of medical statistics and informatics* 4.
- [175] Bali, J., Garg, R. and Bali, R. T. (2019), ‘Artificial intelligence (ai) in healthcare and biomedical research: Why a strong computational/ai bioethics framework is required?’, *Indian journal of ophthalmology* 67(1), 3.

- [176] Bathaee, Y. (2017), ‘The artificial intelligence black box and the failure of intent and causation’, *Harv. JL & Tech.* 31, 889.
- [177] Tamaddon-Jahromi, H. R., Chakshu, N. K., Sazonov, I., Evans, L. M., Thomas, H. and Nithiarasu, P. (2020), ‘Data-driven inverse modelling through neural network (deep learning) and computational heat transfer’, *Computer Methods in Applied Mechanics and Engineering* 369, 113217.
- [178] Washington, C., Genovese, E., Singh, M., Chaer, R., Makaroun, M. and Hager, E. (2016), ‘Mortality rates of ruptured abdominal aortic aneurysm repair have not changed with increasing utilization of evar’, *Journal of Vascular Surgery* 63(6).
- [179] Wilmlink, A., Forshaw, M., Quick, C., Hubbard, C. and Day, N. (2002), ‘Accuracy of serial screening for abdominal aortic aneurysms by ultrasound’, *Journal of medical screening* 9(3), 125–127.
- [180] Litmanovich, D., Bankier, A. A., Cantin, L., Raptopoulos, V. and Boiselle, P. M. (2009), ‘Ct and mri in diseases of the aorta’, *American Journal of Roentgenology* 193(4), 928–940.
- [181] McBride, O. M., Berry, C., Burns, P., Chalmers, R. T., Doyle, B., Forsythe, R., Garden, O. J., Goodman, K., Graham, C., Hoskins, P. et al. (2015), ‘Mri using ultrasmall superparamagnetic particles of iron oxide in patients under surveillance for abdominal aortic aneurysms to predict rupture or surgical repair: Mri for abdominal aortic aneurysms to predict rupture or surgery – the ma3rs study’, *Open Heart* 2(1), e000190.
- [182] Vorp, D. A. (2007), ‘Biomechanics of abdominal aortic aneurysm’, *Journal of biomechanics* 40(9), 1887–1902.
- [183] Wang, T., Jin, W., Liang, F. and Alastruey, J. (2021), ‘Machine learning-based pulse wave analysis for early detection of abdominal aortic aneurysms using in silico pulse waves’.
- [184] Jones, G., Parr, J., Nithiarasu, P. and Pant, S. (2021), ‘Machine learning for detection of stenoses and aneurysms: application in a physiologically realistic virtual patient database.’, *Biomechanics and modeling in mechanobiology* .
- [185] Willemet, M., Chowienczyk, P. and Alastruey, J. (2015), ‘A database of virtual healthy subjects to assess the accuracy of foot-to-foot pulse wave velocities for

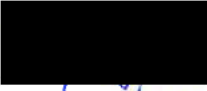
- estimation of aortic stiffness', *American Journal of Physiology-Heart and Circulatory Physiology* 309(4), H663 H675.
URL: <https://doi.org/10.1152/ajpheart.00175.2015>
- [186] Charlton, P. H., Mariscal Harana, J., Vennin, S., Li, Y., Chowienczyk, P. and Alastruey, J. (2019), 'Modeling arterial pulse waves in healthy aging: a database for in silico evaluation of hemodynamics and pulse wave indexes', *American Journal of Physiology-Heart and Circulatory Physiology* 317(5), H1062 H1085.
URL: <https://doi.org/10.1152/ajpheart.00218.2019>
- [187] Huttunen, J. M. J., Kärkkäinen, L., Honkala, M. and Lindholm, H. (2020), 'Deep learning for prediction of cardiac indices from photoplethysmographic waveform: A virtual database approach', *Int J Numer Meth Biomed Engng* 36(3), e3303.
URL: <https://doi.org/10.1002/cnm.3303>
- [188] Haykin, S. (1994), *Neural networks: a comprehensive foundation*, Prentice Hall PTR.
- [189] Melillo, P. (2015), Automatic risk evaluation in elderly patients based on Autonomic Nervous System assessment, PhD thesis, alma.
- [190] McEniery, C. M., Hall, I. R., Qasem, A., Wilkinson, I. B., Cockcroft, J. R., Investigators, A. et al. (2005), 'Normal vascular aging: differential effects on wave reflection and aortic pulse wave velocity: the anglo-cardiff collaborative trial (acct)', *Journal of the American College of Cardiology* 46(9), 1753 1760.
- [191] Sazonov, I., Khir, S., Hacham, W., Boileau, E., Carson, J., van Loon, R., Ferguson, C. and Nithiarasu, P. (2017), 'A novel method for non-invasively detecting the severity and location of aortic aneurysms.', *Biomechanics and modeling in mechanobiology* DOI 10.1007/s10237-017-0884-8.
- [192] Sekhri, A. R., Lees, W. R. and Adiseshiah, M. (2004), 'Measurement of aortic compliance in abdominal aortic aneurysms before and after open and endoluminal repair: preliminary results', *Journal of Endovascular Therapy* 11(4), 472 482.
- [193] Kolipaka, A., Illapani, V. S. P., Kenyhercz, W., Dowell, J. D., Go, M. R., Starr, J. E., Vaccaro, P. S. and White, R. D. (2016), 'Quantification of abdominal aortic aneurysm stiffness using magnetic resonance elastography and its comparison to aneurysm diameter', *Journal of vascular surgery* 64(4), 966 974.

- [194] Cebal, J. R., Vazquez, M., Sforza, D. M., Houzeaux, G., Tateshima, S., Scrivano, E., Bleise, C., Lylyk, P. and Putman, C. M. (2015), ‘Analysis of hemodynamics and wall mechanics at sites of cerebral aneurysm rupture’, *J NeuroIntervent Surg* 7(7), 530.
URL: <http://jn.is.bmj.com/content/7/7/530.abstract>
- [195] Low, K., van Loon, R., Sazonov, I., Bevan, R. L. T. and Nithiarasu, P. (2012), ‘An improved baseline model for a human arterial network to study the impact of aneurysms on pressure-flow waveforms’, *International Journal for Numerical Methods in Biomedical Engineering* 28, 1224–1246.
- [196] Rumelhart, D. E., Hinton, G. E., Williams, R. J. et al. (1988), ‘Learning representations by back-propagating errors’, *Cognitive modeling* 5(3), 1.
- [197] Zubair, M., Kim, J. and Yoon, C. (2016), An automated ecg beat classification system using convolutional neural networks, in ‘2016 6th International Conference on IT Convergence and Security (ICITCS)’, pp. 1–5.
- [198] Goodfellow, I., Bengio, Y. and Courville, A. (2016), *Deep Learning*, MIT Press.
<http://www.deeplearningbook.org>.
- [199] Waghlikar, K. B., Fischer, C. M., Goodson, A., Herrick, C. D., Rees, M., Toscano, E., MacRae, C. A., Scirica, B. M., Desai, A. S. and Murphy, S. N. (2018), ‘Extraction of ejection fraction from echocardiography notes for constructing a cohort of patients having heart failure with reduced ejection fraction (hfrf)’, *Journal of medical systems* 42(30255347), 209–209.
URL: <https://www.ncbi.nlm.nih.gov/pmc/articles/PMC6153777/>
- [200] Hudson, S. and Pettit, S. (2020), ‘What is ‘normal’ left ventricular ejection fraction?’, *Heart* 106(18), 1445.
URL: <http://heart.bmj.com/content/106/18/1445.abstract>
- [201] Asmar, R., Vol, S., Brisac, A.-M., Tichet, J. and Topouchian, J. (2001), ‘Reference values for clinic pulse pressure in a nonselected population’, *American Journal of Hypertension* 14(5), 415–418.
URL: [https://doi.org/10.1016/S0895-7061\(01\)01284-5](https://doi.org/10.1016/S0895-7061(01)01284-5)
- [202] Welch, J., Ford, P., Teplick, R., Rubsamen, R. et al. (1991), ‘The massachusetts general hospital-marquette foundation hemodynamic and electrocardiographic

- database comprehensive collection of critical care waveforms’, *Clinical Monitoring* 7(1), 96–97.
- [203] Virtanen, P., Gommers, R., Oliphant, T. E., Haberland, M., Reddy, T., Cournapeau, D., Burovski, E., Peterson, P., Weckesser, W., Bright, J., van der Walt, S. J., Brett, M., Wilson, J., Millman, K. J., Mayorov, N., Nelson, A. R. J., Jones, E., Kern, R., Larson, E., Carey, C. J., Polat, İ., Feng, Y., Moore, E. W., VanderPlas, J., Laxalde, D., Perktold, J., Cimrman, R., Henriksen, I., Quintero, E. A., Harris, C. R., Archibald, A. M., Ribeiro, A. H., Pedregosa, F., van Mulbregt, P. and SciPy 1.0 Contributors (2020), ‘SciPy 1.0: Fundamental Algorithms for Scientific Computing in Python’, *Nature Methods* 17, 261–272.
- [204] Holder, A. L., Gupta, N., Lulaj, E., Furgiuele, M., Hidalgo, I., Jones, M. P., Jolly, T., Gennis, P. and Birnbaum, A. (2016), ‘Predictors of early progression to severe sepsis or shock among emergency department patients with nonsevere sepsis’, *International Journal of Emergency Medicine* 9(1), 10.
URL: <https://doi.org/10.1186/s12245-016-0106-7>
- [205] Grizzi, F., Franceschini, B., Fiamengo, B., Russo, C. and Dioguardi, N. (2007), ‘Vascular architecture: is it a helpful histopathological biomarker for hepatocellular carcinoma?’, *Journal of Zhejiang University. Science. B* 8, 217–20.

Declarations

This work has not previously been accepted in substance for any degree and is not being concurrently submitted in candidature for any degree.

Signed: 

Date: 09/11/2021

This thesis is the result of my own investigations, except where otherwise stated. Other sources are acknowledged by footnotes giving explicit references. A bibliography is appended.

Signed: 

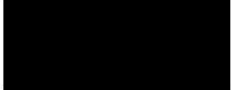
Date: 09/11/2021

I hereby give consent for my thesis, if accepted, to be available online in the University's Open Access repository and for inter-library loan, and for the title and summary to be made available to outside organisations.

Signed: 

Date: 09/11/2021

The University's ethical procedures have been followed and, where appropriate, that ethical approval has been granted.

Signed: 

Date: 09/11/2021